IMPACT OF STRUCTURAL COMPONENTS ON NATURAL VIBRATIONS

HOW THE INSPIRATION BY NATURE CAN HELP US IMPROVE VIBRATION PROPERTIES

Vom Fachbereich Produktionstechnik
der
UNIVERSITÄT BREMEN

zur Erlangung des Grades
Doktor der Ingenieurwissenschaften
(Dr.-Ing.)

genehmigte

DISSERTATION

von
M.SC. SIMONE ANDRESEN

Gutachter: Prof. i.R. Dr.-Ing. habil. Dr. h.c. Reinhold Kienzler
Universität Bremen

Prof. Dr.-Ing. habil. Dr. h.c. mult. Holm Altenbach
Otto-von-Guericke-Universität Magdeburg

Tag der mündlichen Prüfung: 26.11.2021

M.Sc. Simone Andresen: *Impact of structural components on natural vibrations,* How the inspiration by nature can help us improve vibration properties,
© 06 August 2021

This work is dedicated to my family:
Mauri, Ella Marie, and Pancho.

And - of course - to all people,
who are interested in this research work!

ZUSAMMENFASSUNG

Seit Jahrzehnten wird das Ziel verfolgt, durch ein optimiertes Design Resonanz zu vermeiden, was für viele technische Bereiche von großem Interesse ist. Vor allem Leichtbaustrukturen zeigen eine hohe Anfälligkeit gegenüber Schwingungen. Ein Ansatz hierbei ist die Erhöhung (Maximierung) der Struktureigenfrequenzen bzw. die „Verstimmung“ des Systems.

In dieser Arbeit wird eine detaillierte Literaturübersicht zu technischen Leichtbaustrukturen und Strukturoptimierung mit Fokus auf Schwingungseigenschaften gegeben. Anschließend untersuchen verschiedene Studien die Anwendung biologisch inspirierter Strukturen und Methoden zur Erhöhung von Eigenfrequenzen.

In den Schalen von Diatomeen ist eine Verformung nach den Eigenmoden nachgewiesen worden, was zu der Annahme einer Schwingungsoptimierung in den Schalenstrukturen führt. Inspiriert von dieser Tatsache werden in Axialrichtung verformungsbehinderte Balken (1D) und Platten (2D) nach ihren Eigenmoden vorverformt, was zu enormen Eigenfrequenzerhöhungen bei konstanter Masse führt. Ebenso lassen sich mehrere Eigenfrequenzen gleichzeitig erhöhen. Die Ergebnisse werden mit Optimierungen basierend auf der Evolutionsstrategie und – im Fall der Platte – mit Topographieoptimierungen verglichen. Die Optimierungen unter Verwendung kommerziell erhältlicher Optimierer führen zur Erhöhung der gewünschten Eigenfrequenzen. Während die Frequenzerhöhung einzelner Eigenfrequenzen jedoch geringer als bei der Strukturvorverformung nach den Eigenmoden ist, führen die Evolutionsstrategie-Optimierungen zu besseren Ergebnissen für die Optimierung mehrerer Eigenfrequenzen.

Im Hinblick auf komplexe Waben- und Gitterstrukturen, die in aquatischen Planktonorganismen zu finden sind, wird der Einfluss der Strukturkomplexität auf die Eigenfrequenzen untersucht. Die erste Eigenfrequenz einer 2D Wabenplatte erhöht sich signifikant durch die Nutzung unregelmäßiger Strukturen. Darüber hinaus führt die anschließende Vorverformung nach dem Eigenmode zu einer weiteren Frequenzerhöhung. Auch bezüglich der Gitterstrukturen kann eine starke Erhöhung der ersten Eigenfrequenz durch zunehmende Strukturkomplexität erreicht werden. Zusätzliche Einschränkungen im Design erlauben die Entwicklung von schwingungsoptimierten Gitterstrukturen, die ohne den Einsatz von Stützstrukturen additiv gefertigt werden können.

Als ein Anwendungsbeispiel für biologisch inspirierte Schwingungsoptimierung wird ein in einer Synchrotronstrahlungsquelle eingesetzter Magnetträger untersucht, der für die Stabilität des Teilchenstrahls von großer Bedeutung ist. Es handelt sich um eine Trägerstruktur der aktuell geplanten Aufrüstung der Synchrotronstrahlungsquelle PETRA IV bei DESY (Deutsches Elektronen-Synchrotron, Hamburg, Deutschland). Eine Parameterstudie untersucht den Einfluss verschiedener Randbedingungen wie veränderliche Lasten, Lagerdefinitionen und Materialeigenschaften des Trägers und der Stützen, auf den Magnetträgeraufbau. Im Anschluss wird ein Entwicklungsprozess für eine Trägerstruktur einer Synchrotronstahlungsquelle entwickelt. Basierend auf dem Ergebnis einer Topologieoptimierung lässt sich ein parametrisches Balken-Schalen-Modell erstellen, in das biologisch inspirierte Strukturen integriert werden. Die darauffolgende Querschnittsoptimierung unter Verwendung der Evolutionsstrategie führt zu einer optimierten Trägerstruktur. Die Eigenfrequenzmessungen der gegossenen Trägerstruktur erlauben eine Validierung der numerigen Ergebnisse. Zukünftige Änderungen in den technischen Vorgaben können in den Entwicklungsprozess eingepflegt werden, um eine angepasste Trägerstruktur zu erhalten.

Schlagwörter: Bionik, Gitter, Magnetträgerstruktur, Maximierung von Eigenfrequenzen, Strukturanpassung nach Eigenmoden, Strukturoptimierung, Strukturunregelmäßigkeiten, Wabenplatten

ABSTRACT

Finding the optimal structural design to avoid resonance has been a goal for decades as it is of high interest in many technical areas. Lightweight design structures, in particular, show a high susceptibility to vibration. One approach is to increase (maximise) the structural eigenfrequencies, i.e., to 'detune' the system.

In this work, a detailed literature review on technical lightweight structures and structural optimisations focusing on vibration characteristics is presented. Subsequently, different studies investigate the application of biologically inspired structures and methods to increase eigenfrequencies.

It has been observed that diatom shells are shaped according to their vibration mode shapes, which leads to the assumption that these structures are optimised for vibratory loads. Applying this mode shape adaptation strategy to axially constrained beams (1D) and plates (2D) results in strong eigenfrequency increases at constant mass. In addition, the increase of multiple eigenfrequencies is possible. The mode shape adaptation results are compared to evolutionary strategic optimisations and, in the case of the plate, also to topography optimisations. The optimisations using commercially available optimisers successfully increase the targeted eigenfrequencies. However, the single eigenfrequency increases are generally lower than those generated by the mode shape adaptation method, while the evolutionary strategic optimisations lead to higher multiple eigenfrequency increases.

With regard to the complex honeycomb and lattice structures found in aquatic plankton organisms, the impact of the structural complexity on the eigenfrequencies is studied. The 1^{st} eigenfrequency of a 2D cellular plate significantly rises using irregular structures. In addition, the application of the mode shape method to the studied cellular plates raises the 1^{st} eigenfrequency even further. Regarding lattice structures, a strong 1^{st} eigenfrequency increase with rising structural complexity is obtained likewise. Additional design constraints allow the development of vibration optimised lattices that can be additive manufactured without support structures.

As an example of biologically inspired vibration optimisation, a girder used in synchrotron radiation facilities to support the magnets and to assure a stable particle beam is studied. It is focused on the girder design for the currently planned synchrotron radiation facility upgrade PETRA IV at DESY (German Electron Synchrotron, Hamburg, Germany). In a parametric study, the impact of different boundary conditions on the magnet-girder assembly is investigated, involving varying loading conditions, girder support definitions, and material properties of the girder and bases. Afterwards, a development process for a girder structure installed in a synchrotron radiation facility is generated. Based on a topology optimisation, a parametric beam-shell model including biologically inspired structures is created. The subsequent cross section optimisation using evolutionary strategic optimisation reveals an optimum girder structure. Vibration experiments of the casted girder structure validated the numerical results. Future changes in the specifications can be implemented in the development process to obtain further adapted girder structures.

Keywords: Biomimetics, cellular plates, eigenfrequency maximisation, lattices, magnet-girder design, mode shape adaptation, structural irregularities, structural optimisation

PREFACE

The purpose of this work is to contribute to the complex and large research field of structural vibrations. In particular, it is focused on different methods to raise eigenfrequencies in structural parts for improved vibration properties. The here proposed approaches and methods are very interdisciplinary, including a glance into nature for inspiration in solving vibration problems.

The work is organised into five parts, each composed of different chapters:

Part 1 describes the motivation for this work and introduces the field of lightweight design structures, biomimetics, and different structural optimisation techniques. Relevant published studies are reviewed, in particular those dealing with vibration characteristics, before the objectives and the outline of the work are stated.

Part 2 summarises the theoretical background information on which the following studies are based. It focuses on mechanical vibrations and the finite element method.

In Part 3, different methods to increase eigenfrequencies inspired by biological structures and phenomena are studied. The methods include structural adaptations according to mode shapes, evolutionary strategic optimisations, and the impact of structural irregularities on the eigenfrequencies. The latter is applied to honeycomb plates and lattice structures. Finally, all methods are compared among each other and to other published approaches aiming at an eigenfrequency increase.

Regarding the application of biologically inspired vibration optimisation to a technical component, the design of a girder structure, which supports magnets in a synchrotron radiation facility, is generated in Part 4. After an introduction into synchrotron radiation facilities and the importance of girder structures, a parametric study focuses on the impact of different components and boundary conditions on the eigenfrequencies of a magnet-girder assembly. The last chapter develops a biologically inspired girder design. The design process includes different findings from Part 3, namely the implementation of biologically inspired structures and the conduction of evolutionary strategic optimisations. Finally, vibration experiments are conducted to validate the numerical results.

The last Part 5 summarises the work.

This dissertation contains studies, which combine different research and knowledge fields including mechanical engineering and mechanical vibrations, numerical simulations, biomimetics and biological inspiration, and synchrotron radiation facilities. The author hopes that this work will create interest for this interdisciplinary research field and that the findings might contribute to different investigations that build on the here presented findings.

Bremen, 06 August 2021
Simone Andresen

ACKNOWLEDGEMENTS

This thesis is the result of several years of work and I am deeply grateful to many people, who have supported me during my PhD project.
First, I would like to thank my professor and supervisor at the University of Bremen, Prof. Reinhold Kienzler. Prof. Kienzler, after the defense of my master thesis and the approval of my research project, you were the one encouraging me to do a PhD and offered your supervision. Thank you very much for your interest on this research topic, your support, your time for discussions and corrections on papers, and for motivating me in finishing my PhD project soon.
In addition, I would like to express my gratitude to Prof. Holm Altenbach, who also showed interest in my research and immediately agreed to be my second PhD supervisor. Thank you very much for your support during the last month, which allowed me to successfully finish my doctoral thesis project by the end of this year.
I am also very grateful to my supervisor at the Alfred Wegener Institute (AWI), Dr. Christian Hamm. He offered me to be the project leader of this interesting research project in collaboration with DESY, in which I got the opportunity to do my PhD project. Christian, I really appreciate that you have always supported my ideas, the research questions that came up into my mind and that I wished to answer, and you have always given me a lot of freedom in doing the research the way I wanted it to do. Thanks!
Furthermore, I am very appreciative for the support of my research group 'bionic lightweight design', now part of the AWI research section 'marine bioeconomy'. I am happy to be part of this interdisciplinary biomimetics team! Thanks also to my former colleague Robert Ciomber, who helped me out with errors I encountered in my parametric constructions and simulations.
Many thanks to my colleagues at DESY, Dr. Markus Körfer, Norbert Meyners, Daniel Thoden, and Claudia Engling. It has been a pleasure to lead our collaboration project and to discuss results and further research questions on our regular meetings. Norbert and Daniel, thank you also for performing the vibration measurements of the biologically inspired girder structure that I designed.
I would like to thank also the DLR Bremen, in particular the team responsible for the vibration measurements, for the collaboration regarding the vibration measurements of the regular and irregular lattice structures.
In addition, my gratitude goes to the graduate school POLMAR for allowing me to participate in different courses, which helped me

in developing my personal skills and in successfully finishing my PhD project.
On a personal level, I am deeply grateful to my husband Mauricio, for his deep love and his support. Mauri, thank you for reducing your working hours, so that we have both been able to work half-time and I could finish writing my thesis. You are a wonderful father to our lovely daughter Ella Marie and, of course, to our first 'son' Pancho. And about you, Ella Marie, you are the most wonderful gift that we have received in our life. We are so proud of you, so lucky to be your parents, and every smile from you makes us so indescribably happy!
I am also very thankful to my parents, who have always supported me in all my studies and in spending important years of my life abroad, which strongly shaped my personality and helped me in finding my path of life.
And what would life be without friends? My gratitude also goes to my dear friends, who mean so much to me and who have accompanied me in many years of my life. Thank you very much, especially to Laura, Lisa, Katrin, Viki, Lucie, Vanessa, Kevin, Alke, Lucia, and Karen!
Finally, a big 'Thank you!' to Prof. Kienzler, my friends, and my colleagues for reviewing my thesis and the helful comments and suggestions.

Sincerely yours,

Simone Andresen

PUBLICATIONS

Parts of the dissertation have appeared previously in the following publications:

- Peer-reviewed publications:
  - S. Andresen, A. Bäger, and C. Hamm. "Eigenfrequency maximisation by using irregular lattice structures." In: *Journal of Sound and Vibration* 465 (2020), p. 115027. DOI: `10.1016/j.jsv.2019.115027`
  - S. Andresen, L.M. Lottes, S.K. Linnemann, and R. Kienzler. "Shape adaptation of beams (1D) and plates (2D) to maximise eigenfrequencies." In: *Advances in Mechanical Engineering* 12 (2020), pp. 1–18. DOI: `10.1177/1687814020971903`
- Reviewed publications:
  - S. Andresen. "Optimizing the PETRA IV girder by using bio-inspired structures." In: *Proceedings of the* 10^{th} *Mechanical Engineering Design of Synchrotron Radiation Equipment and Instrumentation Conference* (Paris, France). Ed. by V.R.W. Schaa, K. Tavakoli, and M. Tilmont. Geneva (Switzerland): JACoW Publishing, 2018, pp. 297–301. DOI: `10.18429/JACoW-MEDSI2018-THOAMA01`
  - S. Andresen. "Impact of Bio-inspired Structural Irregularities on Plate Eigenfrequencies." In: *Proceedings of the* 14^{th} *International Conference on Vibration Problems. Lecture Notes in Mechanical Engineering*. Ed. by Sapountzakis E.J., Banerjee M., Biswas P., and Inan E. Singapore: Springer, 2021, pp. 1117–1125. DOI: `10.1007/978-981-15-8049-9_71`
- Not-reviewed publications:
  - S. Andresen. "Improving vibration characteristics by using bio-inspired structures." In: *Bionik: Patente aus der Natur, Innovationspotenziale für Technologieanwendungen, 9. Bremer Bionik-Kongress*. 9. Bionik-Kongress. Ed. by A.B. Kesel and D. Zehren. Bremen (Germany), 2019, pp. 30–42

CONTENTS

List of Figures xix
List of Tables xxv
Acronyms and Terms xxvii
List of Symbols xxxi

I INTRODUCTION 1
1 Motivation 3
2 Technical Lightweight Structures and Their Properties 5
3 Biomimetics - Inspired by Nature 9
4 Structural Optimisation to Improve Vibration Characteristics 15
5 Objectives and Outline 19

II THEORETICAL BACKGROUND INFORMATION 23
6 Mechanical Vibrations 25
  6.1 Introduction 25
  6.2 Vibration of Structures With One Degree of Freedom . 26
    6.2.1 Free Damped Vibration 26
    6.2.2 Free Undamped Vibration 28
    6.2.3 Forced Damped Vibration 30
    6.2.4 Frequency Response Function 33
  6.3 Vibration of Structures With Multiple Degrees of Freedom 34
    6.3.1 Free Vibration of an Undamped Structure With More Than Two Degrees of Freedom 34
    6.3.2 Modal Analysis 36
  6.4 Resonance Phenomena and How to Prevent Them . . . 37
7 Finite Element Method 39
  7.1 Introduction 39
  7.2 Theory of Linear Elasticity 39
  7.3 Principle of Virtual Work 41

III EIGENFREQUENCY INCREASE INSPIRED BY NATURE 45
8 Shape Adaptation According to Mode Shapes 47
  8.1 Material and Methods 48
    8.1.1 Slender Beam 48
    8.1.2 Squared Plate 52
  8.2 Results 54
    8.2.1 Slender Beam 55
    8.2.2 Squared Plate 61
  8.3 Discussion 69
    8.3.1 Slender Beam 69
    8.3.2 Squared Plate 71

8.3.3 Outlook 75
8.4 Conclusion 77
9 Shape Adaptation Based on Evolutionary Strategic Optimisations 79
9.1 Material and Methods 81
9.1.1 Slender Beam 81
9.1.2 Squared Plate 82
9.2 Results 83
9.2.1 Slender Beam 83
9.2.2 Squared Plate 87
9.3 Discussion 90
9.3.1 Slender Beam 90
9.3.2 Squared Plate 91
9.3.3 Methodology 92
9.4 Conclusion 94
10 Regular and Irregular Honeycomb Plates 95
10.1 Material and Methods 96
10.2 Results 99
10.3 Discussion 101
10.4 Conclusion 103
11 Regular and Irregular Lattice Structures 105
11.1 Material and Methods 106
11.1.1 Lattice Design and Optimisation 106
11.1.2 Lattice Vibration Measurements 109
11.1.3 Further Lattice Optimisation 111
11.2 Results 111
11.2.1 Lattice Design and Optimisation 111
11.2.2 Lattice Vibration Measurements 114
11.2.3 Further Lattice Optimisation 115
11.3 Discussion 117
11.3.1 Lattice Design and Optimisation 117
11.3.2 Lattice Vibration Measurements 119
11.3.3 Further Lattice Optimisation 120
11.4 Conclusion 121
12 Comparison of Different Methods to Increase Eigenfrequencies 123

IV GIRDER DESIGN FOR PETRA IV 131
13 Highly Brilliant PETRA IV Synchrotron Radiation Source 133
13.1 Synchrotron Radiation Facility 133
13.2 PETRA IV Project 134
13.3 Magnet-Girder Assemblies 137
13.4 Problem Definition, Specifications, and Model Assembly 141
14 Parametric Study on Components and Boundary Conditions 147
14.1 Material and Methods 147
14.1.1 Magnets 148
14.1.2 Girder Support 152

14.1.3 Material Properties 154
14.2 Results 154
14.2.1 Magnets 155
14.2.2 Girder Support 158
14.2.3 Material Properties 162
14.3 Discussion 163
14.3.1 Magnets 163
14.3.2 Girder Support 166
14.3.3 Material Properties 167
14.4 Conclusion 168
15 Development of a Biologically Inspired Girder Design 171
15.1 Material and Methods 171
15.1.1 Topology Optimisation 173
15.1.2 Abstraction and Cross Section Optimisation . . 174
15.1.3 Biologically Inspired Structures and Further Structural Adaptation 175
15.1.4 Manufacturing and Impact Testing 177
15.2 Results 178
15.2.1 Topology Optimisation 178
15.2.2 Abstraction and Cross Section Optimisation . . 178
15.2.3 Biologically Inspired Structures and Further Structural Adaptation 183
15.2.4 Manufacturing and Impact Testing 186
15.3 Discussion 189
15.3.1 Topology Optimisation 189
15.3.2 Abstraction and Cross Section Optimisation . . 190
15.3.3 Biologically Inspired Structures and Further Structural Adaptation 192
15.3.4 Manufacturing and Impact Testing 194
15.3.5 Outlook 195
15.4 Conclusion 196

V SUMMARY 197
16 Summary 199

VI APPENDIX 201
A Supplemental Material I
A.1 Shape Adaptation According to Mode Shapes I
A.2 Shape Adaptation Based on Evolutionary Strategic Optimisations II
A.3 Regular and Irregular Honeycomb Plates XI
A.4 Regular and Irregular Lattice Structures XII
A.5 Development of a Biologically Inspired Girder Design XIII

BIBLIOGRAPHY XV

LIST OF FIGURES

Figure 2.1 Regular lattices based on gyroid, diamond, and primitive cells . . . 7
Figure 3.1 Complex biological lightweight structures . . . 10
Figure 3.2 Diatoms and radiolaria . . . 12
Figure 3.3 Lightweight structures and stiff design principles of diatom shells . . . 13
Figure 3.4 Comparison of diatom shell deformation patterns and mode shapes . . . 14
Figure 4.1 Three categories of structural optimisation . . . 15
Figure 4.2 Macro structure composed of a regular micro structure . . . 18
Figure 5.1 Outline of this work . . . 21
Figure 6.1 SDOF spring-mass-damper model . . . 26
Figure 6.2 Vibration decay of an underdamped system . . . 29
Figure 6.3 SDOF spring-mass model . . . 29
Figure 6.4 SDOF spring-mass-damper model with harmonic excitation . . . 30
Figure 6.5 Dynamic amplification factor depending on the frequency ratio . . . 32
Figure 6.6 Vibration chain-type model . . . 35
Figure 6.7 Local and modal coordinates . . . 36
Figure 7.1 Normal and shear stresses of an infinitesimal element . . . 40
Figure 7.2 External forces acting on a 3D body . . . 42
Figure 8.1 Slender beam geometry, dimensions, and boundary conditions . . . 48
Figure 8.2 Circular arch dimensions . . . 50
Figure 8.3 Squared plate geometry and dimensions . . . 52
Figure 8.4 49 points distributed on the squared plate . . . 54
Figure 8.5 Pre-deformed squared plate . . . 55
Figure 8.6 Mesh study result of the slender beam . . . 56
Figure 8.7 Mode shapes of the slender beam . . . 56
Figure 8.8 Analytical and numerical results of the slender beam . . . 57
Figure 8.9 Eigenfrequencies of the slender beam pre-deformed according to mode 3 and 4 . . . 58
Figure 8.10 Eigenfrequencies of the slender beam pre-deformed according to mode 5 . . . 59
Figure 8.11 Eigenfrequencies of the slender beam pre-deformed according to weighted combinations of mode 1 and 2 . . . 61

Figure 8.12 Mesh study result of the squared plate 62
Figure 8.13 Mode shapes of the squared plate 62
Figure 8.14 Analytical and numerical results of the squared plate 62
Figure 8.15 Eigenfrequencies of the squared plate pre-deformed according to mode 1 64
Figure 8.16 Eigenfrequencies of the squared plate pre-deformed according to mode 2/3 65
Figure 8.17 Eigenfrequencies of the squared plate pre-deformed according to mode 4 66
Figure 8.18 Eigenfrequencies of the squared plate pre-deformed according to weighted combinations of mode 1 and 2 68
Figure 8.19 Mode 1 of the squared plate pre-deformed according to mode 1 74
Figure 8.20 Geometry and dimensions of the studied 3D beam structure 75
Figure 8.21 Mesh convergence study result for the 3D beam structure 75
Figure 8.22 Geometry and dimensions of the studied 3D beam structure 76
Figure 8.23 Eigenfrequencies of the 3D beam pre-deformed according to mode 1 76
Figure 9.1 Fitness landscape 79
Figure 9.2 Evolutionary strategic optimisation process . . 80
Figure 9.3 25 points distributed on the squared plate . . . 82
Figure 9.4 Eigenfrequencies of the slender beam based on evolutionary strategic optimisations 84
Figure 9.5 Beam structures obtained by evolutionary strategic optimisations 85
Figure 9.6 Eigenfrequencies and shapes of the squared plate based on evolutionary strategic optimisations . 87
Figure 9.7 Eigenfrequencies and shapes of the squared plate based on topography optimisations 89
Figure 9.8 Squared plate shapes based on optimisations of multiple eigenfrequencies 90
Figure 10.1 Sandwich panel with an irregular core structure 95
Figure 10.2 Diatom *Thalassiosira* sp. 96
Figure 10.3 Generation of Voronoi combs 97
Figure 10.4 Data interpolation algorithm 98
Figure 10.5 1st eigenfrequency depending on the Voronoi cell size 99
Figure 10.6 Optimisation results of the irregular Voronoi plate 100
Figure 10.7 1st eigenfrequency of different cellular plates pre-deformed according to mode 1 100

Figure 10.8 Shapes of different cellular plates pre-deformed according to mode 1 101
Figure 11.1 Overview of the study on lattices 105
Figure 11.2 Lattice design space 106
Figure 11.3 Design of lattice structures 107
Figure 11.4 Vibration test setup for the lattice structures . 109
Figure 11.5 Half power bandwidth method 110
Figure 11.6 Parametric study results for lattice 1 111
Figure 11.7 Optimisation results for lattice 2 and 3 112
Figure 11.8 Lattice structures L1, L2, and L3 113
Figure 11.9 Frequency response analysis curve for lattice L3 115
Figure 11.10 1st eigenfrequency of different lattices 116
Figure 11.11 Mass values of different lattices 117
Figure 11.12 Lattices L4, L2*, L3*, and L4* obtained by further lattice optimisations 117
Figure 12.1 Comparison of different methods to increase the 1st eigenfrequency 126
Figure 12.2 Multiple eigenfrequency increase based on the mode shape adaptation method and evolutionary strategic optimisations 128
Figure 13.1 Components of synchrotron radiation facilities 135
Figure 13.2 View on the DESY ground 136
Figure 13.3 PETRA IV layout 136
Figure 13.4 Planned girders for PETRA IV 137
Figure 13.5 Vibration transmission path to the particle beam 139
Figure 13.6 PETRA III girder 140
Figure 13.7 Ground vibration at the DESY campus 142
Figure 13.8 Casting process with additively manufactured cores 143
Figure 13.9 Dimensions of the 3 m PETRA IV magnet-girder assembly 144
Figure 14.1 Girder geometries of the parametric study . . 147
Figure 14.2 Parametric study model to analyse the magnet position 150
Figure 14.3 Frame composed of four elastic posts and a rigid bar with a mass 150
Figure 14.4 Force acting on a massless rod 151
Figure 14.5 1st eigenfrequency of the magnet-girder assembly depending on the girder support 152
Figure 14.6 Girder support point positions considered in the parametric study 153
Figure 14.7 Deflection of a cantilever beam 154
Figure 14.8 Mesh study results of the parametric study . . 155
Figure 14.9 Magnet-girder assembly eigenfrequencies depending on the magnet position 156

Figure 14.10 1st mode shape of the PETRA III girder with magnets positioned at 15 mm height 157
Figure 14.11 Impact of the magnet position height and connection on the 5th mode shape 157
Figure 14.12 Magnet-girder assembly eigenfrequencies depending on the magnet-girder connection stiffness 158
Figure 14.13 1st mode shape of the box girder for a varying magnet-girder connection stiffness 159
Figure 14.14 Magnet-girder assembly eigenfrequencies depending on the magnet mass 159
Figure 14.15 Impact of the magnet mass on the 1st magnet-girder assembly mode shape 160
Figure 14.16 1st eigenfrequency of the magnet-girder assembly depending on the support point position . 161
Figure 14.17 1st mode shape of the PETRA III girder with the optimum support point position 162
Figure 14.18 Magnet-girder assembly eigenfrequencies depending on the girder support stiffness 162
Figure 14.19 1st mode shape of the PETRA III girder depending on the girder support stiffness 163
Figure 14.20 1st magnet-girder assembly eigenfrequency depending on the material properties 164
Figure 15.1 Overview of the girder design procedure . . . 172
Figure 15.2 Topology optimisation result for the girder structure 172
Figure 15.3 Positioning of accelerometers for the girder impact testing 177
Figure 15.4 Topology optimisation result and the abstracted beam-shell model of the girder 179
Figure 15.5 Cross section optimisation convergence 180
Figure 15.6 Cross section optimisation result of the girder beam-shell model 181
Figure 15.7 Optimum parameter combination of the girder beam-shell model 182
Figure 15.8 Mode shapes of the magnet-girder assembly based on the cross section optimisation 183
Figure 15.9 Bio-inspired girder design 184
Figure 15.10 Mode shapes of the final unloaded bio-inspired girder 185
Figure 15.11 Mode shapes of the final bio-inspired magnet-girder assembly 185
Figure 15.12 Deformation due to gravity of the final bio-inspired magnet-girder assembly 186
Figure 15.13 Manufacturing (casting) process of the bio-inspired girder 186

Figure 15.14 Manufactured bio-inspired girder 187
Figure 15.15 PSD of the bio-inspired girder obtained by impact testing 188
Figure 15.16 PSD of the floor and the pedestal 188
Figure 15.17 Measured 1st mode shape of the bio-inspired girder 189
Figure 15.18 Beam-shell vs. volume model of the magnet-girder assembly: a detailed view 192
Figure A.1.1 Eigenfrequencies of the slender beam pre-deformed according to mode 1 and 2 I
Figure A.2.1 Convergence plot of the evolutionary strategic optimisation of the beam to maximise f_1 II
Figure A.2.2 Convergence plot of the evolutionary strategic optimisation of the beam to maximise f_2 III
Figure A.2.3 Convergence plot of the evolutionary strategic optimisation of the beam to maximise f_3 III
Figure A.2.4 Convergence plot of the evolutionary strategic optimisation of the beam to maximise f_4 IV
Figure A.2.5 Convergence plot of the evolutionary strategic optimisation of the beam to maximise f_1 & f_2 . IV
Figure A.2.6 Convergence plot of the evolutionary strategic optimisation of the beam to maximise f_1, f_2, and f_3 V
Figure A.2.7 Convergence plot of the evolutionary strategic optimisation of the plate to maximise f_1 V
Figure A.2.8 Convergence plot of the evolutionary strategic optimisation of the plate to maximise f_2 VI
Figure A.2.9 Convergence plot of the evolutionary strategic optimisation of the plate to maximise f_3 VI
Figure A.2.10 Convergence plot of the evolutionary strategic optimisation of the plate to maximise f_4 VII
Figure A.2.11 Convergence plot of the evolutionary strategic optimisation of the plate to maximise f_1 & f_2 . VII
Figure A.2.12 Convergence plot of the evolutionary strategic optimisation of the plate to maximise f_1, f_2, and f_3 VIII
Figure A.2.13 Convergence plot of the topography optimisation of the plate to maximise f_1 VIII
Figure A.2.14 Convergence plot of the topography optimisation of the plate to maximise f_2 IX
Figure A.2.15 Convergence plot of the topography optimisation of the plate to maximise f_3 IX
Figure A.2.16 Convergence plot of the topography optimisation of the plate to maximise f_4 X

Figure A.3.1 Convergence plot of the evolutionary strategic optimisation of the irregular Voronoi plate to maximise f_1 XI
Figure A.4.1 Frequency response analysis curve for lattice L1 XII
Figure A.4.2 Frequency response analysis curve for lattice L2 XII
Figure A.5.1 Girder topology optimisation convergence . . XIII

LIST OF TABLES

Table 8.1 Material properties of aluminium 48
Table 8.2 Beam eigenfrequency changes due to pre-deformations according to mode shapes 59
Table 8.3 Mode shape frequency changes of the beam due to pre-deformations according to single and multiple mode shapes 60
Table 8.4 Varying plate thickness due to pre-deformations 63
Table 8.5 Plate eigenfrequency changes due to pre-deformations according to mode shapes 67
Table 8.6 Eigenfrequency changes of the plate due to pre-deformations according to single and multiple mode shapes 68
Table 9.1 Octopus settings 81
Table 9.2 Overview of the evolutionary strategic optimisation objectives 82
Table 9.3 Plate thickness defined for topography optimisations 83
Table 9.4 Topography optimisation settings 83
Table 9.5 Beam eigenfrequency increases due to optimisation and mode shape adaptation 85
Table 9.6 Pre-deformation values of the optimised beams 86
Table 9.7 Multiple eigenfrequency increase results for the slender beam 86
Table 9.8 Plate eigenfrequency increases due to optimisations and mode shape adaptation 88
Table 9.9 Multiple eigenfrequency increase results for the squared plate 90
Table 10.1 Overview of the analyses of six cellular plates 97
Table 10.2 Irregular Voronoi plate optimisation parameters 98
Table 11.1 Strut cross section optimisation parameter for lattice L2 108
Table 11.2 Lattice and strut cross section optimisation parameter for lattice L3 108
Table 11.3 Lattice vibration test levels 110
Table 11.4 Defined parameter values for lattice L3 113
Table 11.5 1st eigenfrequency and mass of L1, L2, and L3 based on the beam and solid model 114
Table 11.6 Measured lattice eigenfrequencies and calculated damping ratios 115
Table 11.7 Comparison of the measured and simulated 1st lattice eigenfrequency 116
Table 13.1 Properties of the considered magnets 145

Table 14.1 Overview of the parametric study components and properties 149
Table 14.2 Material properties of girder and bases 154
Table 14.3 Optimum support point position for the girder 160
Table 15.1 Topology optimisation mesh properties 173
Table 15.2 Bio-inspired structures implemented in the designed PETRA IV girder 176
Table 15.3 Mesh properties of the final magnet-girder assembly 177
Table 15.4 Comparison of the beam-shell and the volume model of the girder 182
Table 15.5 Eigenfrequencies of the unloaded bio-inspired girder and the magnet-girder assembly 185
Table 15.6 Comparison of the measured and simulated bio-inspired girder eigenfrequencies 189

LIST OF ACRONYMS AND TERMS

ACRONYMS

APS	Advanced Photon Source
APS-U	Advanced Photon Source Upgrade
CAD	Computer-aided Design
CBEAM	Beam element
CTETRA	Solid element
CTRIA	Shell element
DESY	Deutsches Elektronen-Synchrotron (German Electron Synchrotron)
DLR	Deutsches Zentrum für Luft- und Raumfahrt (German Aerospace Centre)
DoE	Design of Experiments
EASy	Easy Alignment System
ELiSE®	Evolutionary Light Structure Engineering
ESRF	European Synchrotron Radiation Facility
ESRF-EBS	European Synchrotron Radiation Facility's Extremely Brilliant Source
FEM	Finite Element Method
FRF	Frequency Response Function
ID	Insertion Device
IIR	Infinite Impulse Response
LINAC	Linear Accelerator
MDOF	Multi Degree Of Freedom
NSLS	National Synchrotron Light Source
PETRA	Positron-Elektron-Tandem-Ring-Anlage (Positron Electron Tandem Ring Facility)
PSD	Power Spectral Density
PSHELL	Shell element

RBE3	Rigid Body Element
RF	Radio Frequency
S235	Structural Steel with a minimum yield strength of 235 MPa
SDOF	Single Degree Of Freedom
SEM	Scanning Electron Microscopy
SIMP	Solid Isotropic Micro structures with Penalisation
SPring-8	Super Photon ring-8 GeV
SSRF	Shanghai Synchrotron Radiation Facility

TERMS

ELISE	ELISE is a plug-in implemented in Grasshopper that was developed at the Alfred Wegener Institute to build the entire design and simulation process including technical specifications, pre- and post-processing, and the connection to the external solver, and to facilitate the generation and optimisation of complex, biologically inspired structures.
Excel	Microsoft Excel is a spreadsheet developed by Microsoft Corporation, which allows the evaluation of data.
Grasshopper	Grasshopper is a visual programming language and environment within Rhinoceros developed by Robert McNeel & Associates. It is mostly used to build generative algorithms and enables parametric modelling for structural engineering.
HyperMesh	Altair HyperMesh (Altair Engineering Inc.) is a finite element pre-processor. It allows the generation of large models based on an imported CAD geometry to export a final solver file.
HyperView	Altair HyperView (Altair Engineering Inc.) enables the post-processing of engineering simulations and the engineering data visualisation.
Inkscape	Inkscape is a free and open-source vector graphics editor, which is used to create vector images.
LaTeX	LaTeX ($\LaTeX$) is a free software system used for document preparation.

Octopus	The optimiser Octopus was developed for multi-objective evolutionary optimisations that is implemented in Grasshopper.
OptiStruct	Altair OptiStruct (Altair Engineering Inc.) is a structural for linear and nonlinear analyses and optimisations across statics and dynamics, vibrations, acoustics, fatigue, heat transfer, and multiphysics disciplines.
Rhinoceros	Rhinoceros is a 3D computer graphics and CAD software developed by Robert McNeel & Associates.
TeXstudio	TeXstudio is a cross-platform open-source LaTeX editor that can be used in combination with, for example, the TeX distribution MiKTeX to facilitate the document compilation with LaTeX.

LIST OF SYMBOLS

SYMBOL	DESCRIPTION	UNIT
a	Edge length of a squared plate	m
A	Cross section area	m^2
b	Width	m
B_n	Coefficients	–
c	Factor	–
d	Viscous damping coefficient	$N\,s\,m^{-1}$
$\boldsymbol{D}$	Differential operator	–
E	Young's modulus	$N\,m^{-2}$
$\boldsymbol{E}$	Elasticity tensor	$N\,m^{-2}$
f	Eigenfrequency	Hz
$f_{1,a}$	1st arch eigenfrequency	Hz
$f_{1,frame}$	1st frame eigenfrequency	Hz
$f_{2,a}$	2nd arch eigenfrequency	Hz
f_n	n-th eigenfrequency	Hz
$f_{n,b}$	n-th beam eigenfrequency	Hz
$f_{mn,p}$	mn-th plate eigenfrequency	Hz
$f_{mn,sss}$	mn-th eigenfrequency of a shallow spherical shell	Hz
$f_{n,ref}$	n-th eigenfrequency of a reference structure	Hz
f_{max}	Maximum frequency at the half-power amplitude of a resonance peak	Hz
f_{min}	Minimum frequency at the half-power amplitude of a resonance peak	Hz
Δf	Frequency deviation	–
F	Force	N
F_{input}	Input force	N
$\boldsymbol{F}$	Force vector	N
$\boldsymbol{F_b}$	Body forces vector	N
$\boldsymbol{F_c}$	Concentrated forces vector	N
$\boldsymbol{F_s}$	Surface forces vector	N
g	Acceleration due to gravity	$m\,s^{-1}$
G	Shear modulus	$N\,m^{-2}$

SYMBOL	DESCRIPTION	UNIT
$g_{arb,n}$	n-th arbitrary function	–
G_{arb}	Arbitrary function	–
h_a	Arch height	m
h_b	Beam height	m
h_p	Plate thickness	m
h_{post}	Height of a post	m
h_{sss}	Height of a shallow spherical shell	m
H	Dynamic amplification factor	–
H_{max}	Maximum dynamic amplification factor	–
i	Imaginary unit	–
I	Second moment of inertia	$\mathrm{m^4}$
Im	Imaginary part	–
k	Stiffness	$\mathrm{N\,m^{-1}}$
k_{frame}	Stiffness of a frame	$\mathrm{N\,m^{-1}}$
k_{post}	Stiffness of a post	$\mathrm{N\,m^{-1}}$
k_{rod}	Stiffness of a rod	$\mathrm{N\,m^{-1}}$
k_{shear}	Shear stiffness	$\mathrm{N\,m^{-1}}$
K	Plate bending stiffness	$\mathrm{N\,m}$
$\boldsymbol{K}$	Stiffness matrix	$\mathrm{N\,m^{-1}}$
$\boldsymbol{K_e}$	Element stiffness matrix	$\mathrm{N\,m^{-1}}$
l	Length	m
l_G	Girder length	m
l_{rod}	Length of a rod	m
Δl	Longitudinal expansion	m
L	Characteristic length	m
m	Index; Mass	–; kg
m_{L1}	Mass of the lattice structure L1	kg
m_{mag}	Magnet mass	kg
M_n	n-th mode shape	–
$\boldsymbol{M}$	Mass matrix	kg
$\boldsymbol{M_e}$	Element mass matrix	kg
n	Index; Natural number	–; –
$\boldsymbol{N}$	Shape function tensor	–
N_e	Number of elements	–
N_G	Number of generations	–
p	Cartesian modal coordinate	m
P	Population size	–

SYMBOL	DESCRIPTION	UNIT
q	Factor	–
q_d	Vibration reduction factor due to damping	–
q_{fofb}	Vibration reduction factor due to a fast orbit feedback	–
r	Radius	m
r_{sss}	Curvature radius of a shallow spherical shell	m
Re	Reynold's number; Real part	–; –
S	Surface of a body	m^2
t	Time	s
T_d	Oscillation period of a damped system	s
$TF_{gir-mag}$	Vibration transfer function from the girder to the magnet	–
TF_{gr-sl}	Vibration transfer function from the ground to the slab	–
$TF_{mag-beam}$	Vibration transfer function from the magnet to the beam	–
TF_{sl-gir}	Vibration transfer function from the slab to the girder	–
u	Displacement	m
$\boldsymbol{u}$	Displacement vector	m
$\delta\boldsymbol{u}$	Vector of the virtual displacement	m
$\ddot{\boldsymbol{u}}$	Acceleration vector	$\mathrm{m\,s^{-2}}$
u_{flow}	Fluid flow speed	$\mathrm{m\,s^{-1}}$
V	Body volume	m^3
V_e	Element volume	m^3
V_{mag}	Magnet volume	m^3
w	Deflection	m
w_{max}	Maximum deformation	m
$W_{n,b}$	n-th beam bending mode shape in the xz plane	–
$W_{mn,p}$	mn-th plate bending mode shape in the xz plane	–
δW_{ext}	Virtual external work	N m
δW_{int}	Virtual internal work	N m
x	Displacement, Cartesian (local) coordinate; Variable	m; –
$\boldsymbol{x}$	Displacement vector	m

SYMBOL	DESCRIPTION	UNIT
$\dot{x}$	Velocity	$\mathrm{m\,s^{-1}}$
$\ddot{x}$	Acceleration	$\mathrm{m\,s^{-2}}$
$\ddot{\boldsymbol{x}}$	Acceleration vector	$\mathrm{m\,s^{-2}}$
$\hat{x}$	Maximum vibration amplitude	m
$\hat{\boldsymbol{x}}$	Vector of the maximum vibration amplitude	m
x_d	Dynamic amplitude	m
x_{gr}	Ground vibrations	m
x_h	General solution of a homogeneous differential equation	–
x_p	Particular solution of an inhomogeneous differential equation	–
x_s	Static displacement due to a constant force	m
$\Delta\, x_{beam}$	Vibration amplitude at the particle beam in x direction	m
$\boldsymbol{x_N}$	Vector of the nodal displacement	m
$\boldsymbol{\delta x_N}$	Vector of the virtual nodal displacement	m
$\ddot{\boldsymbol{x}}_{\boldsymbol{N}}$	Vector of the nodal acceleration	$\mathrm{m\,s^{-2}}$
xy	xy plane	–
xz	xz plane	–
X	Vibration response	m
y	Variable, Cartesian coordinate	m
yz	yz plane	–
z	Variable, Cartesian coordinate	m
α	Central arch angle	radian
β	Interpolation decay factor	–
γ	Shear strain	–
δ	Maximum relative pre-deformation	–
δ_{max}	Maximum pre-deformation	m
δ_d	Damping coefficient	–
ε	Normal strain	–
$\boldsymbol{\varepsilon}$	Strain tensor	–
ζ	Damping ratio	–
η	Angular frequency ratio between the excitatory and the excited vibration	–
κ	Shear correction factor	–
λ	Coefficient; solution of a quadratic equation	–

SYMBOL	DESCRIPTION	UNIT
λ_s	Slenderness ratio	m^2
ω	Angular eigenfrequency	–
ω_d	Angular eigenfrequency of a damped system	–
ω_n	n-th angular eigenfrequency	–
Ω	Angular frequency of a harmonic vibration excitation	–
μ	Dynamic viscosity	$\mathrm{kg\,m^{-1}\,s^{-1}}$
ν	Poisson's ratio	–
ρ	Density	$\mathrm{kg\,m^{-3}}$
ρ_{mag}	Artificial magnet density	$\mathrm{kg\,m^{-3}}$
σ	Normal stress	$\mathrm{N\,m^{-2}}$
$\sigma_{x,beam}$	Particle beam size in x direction	m
$\boldsymbol{\sigma}$	Stress tensor	$\mathrm{N\,m^{-2}}$
τ	Shear stress	$\mathrm{N\,m^{-2}}$
φ	Phase angle	–
Φ	Angular phase difference	–

Part I

INTRODUCTION

Biologically inspired structures, such as irregular honeycomb and lattice structures, show improved mechanical properties compared to technical lightweight design structures. In the following chapters, the motivation for vibration optimised lightweight design structures is explained. Technical lightweight structures are presented and the published studies on this topic are reviewed, before introducing the field of biomimetics and biologically inspired structures. After that, a chapter is dedicated to published work on structural optimisations, before the outline and the objectives of this work are presented.

1

MOTIVATION

Finding the optimal structural design to avoid resonance has been a goal for decades as it is of high interest in many technical areas, e.g., in the car industry to minimise the occurring noise and vibration during operation or in the space industry to avoid coupling with the electronic control system [98]. Especially with recent demands for high performance structures with substantial weight reductions, the optimum vibration design in consideration of dynamic characteristics has become extremely important [90]. Also, the global goal to reduce emission motivates the development of improved lightweight structures.

The lightweight design technology aims at realising a structure of minimised mass and a certain service life combined with reliability considering the defined boundary conditions and load cases. For this, not only the appropriate construction/design method, but also the lightweight material, the joining technology, and the fabrication have to be taken into account. A compromise between technical and economic aspects has to be sought out, because the implementation of lightweight designs often results in increased financial expenses. Naturally, lightweight design will only be applied if the benefits exceed the costs [82].

With regard to a car, Klein and Gänsicke [82] estimated that a mass reduction of 100 kg results in a mean consumption reduction of 0.5 l per 100 km and a CO_2 reduction of 12 g per km. They state that cars still show a potential of mass reduction of about 35%. Thus, there is a high potential of lightweight structures to improve today's technologies. In addition, as the fabrication technology constantly improves a lot, especially in the last years, it is important to investigate lightweight design structures and further improve their mechanical properties, for example by optimising the structure.

Lightweight structures are susceptible to vibration because reduced masses are more easily excited by external influences (such as vibrations and individual shocks) than those of heavy, massive constructions [92]. In other words, lightweight structures tend to 'rattle' more than heavyweight structures. Traditional methods of reducing high vibration amplitudes include increasing the mass and/or structural damping [17]. However, this often contradicts the original design goal of generating lightweight structures. In addition, active damping systems are weak points of the system and 'react time-delayed'.

Other investigated passive methods to avoid resonance in technical structures are the alteration of boundary conditions, the implementation of internal supports, or the implementation of additional systems to a structure such as masses, springs, or dampers [6]. Also the use of alternative materials with different properties can generate an eigenfrequency shift out of the range of external exciting frequencies [7]. Moreover, the application of vibration isolation using springs is possible [86]. However, in many cases these methods cannot be applied due to fixed technical specifications. Thus, there is a high demand of methods to avoid high resonance that (1) are easily applicable, (2) do not involve adaptations of technical specifications (such as the design space), (3) are inexpensive, and (4) act passively.

In regard to lightweight structures, the change of a structure's geometry to shift its eigenfrequency (i.e., 'detuning' the system) shows high potential and has been subject of many studies. A vibrating system is defined by the mass, the elastic properties, and the damping properties. Detuning implies variations of the mass and/or the elastic properties (i.e., stiffness) to shift the eigenfrequency.

Until now, most published studies have been focusing on structural optimisations to find an optimum material distribution with the aim to maximise eigenfrequencies. In this work, however, the studied methodologies to increase eigenfrequencies are inspired by nature.

2

TECHNICAL LIGHTWEIGHT STRUCTURES AND THEIR PROPERTIES

Cellular structures including foams, honeycombs, and regular lattice structures have been a common subject of current research. They are usually divided into stochastic (foams) and periodic (honeycombs and regular lattices) cellular structures. Gibson and Ashby [53] summarised the structural characteristics and properties of different technical and biological cellular solids. An overview on the properties of foams and regular lattices was provided by Ashby [19]. Aside from these structures, non-stochastic irregular cellular structures are comparatively new and less studied. Besides their lightweight potential, cellular structures exhibit high energy absorption during compression [88, 209], good heat-dissipation (cooling) performance, and highly efficient cross-flow heat exchange [46, 179]. Several studies on periodic and stochastic cellular structures have emphasised the enhanced performance of periodic structures compared to stochastic structures of the same relative density, e.g., higher stiffness and strength [39, 46, 180].

Regarding the impact of structural irregularities on mechanical properties, Silva et al. [157] studied 2D cellular solids and demonstrated that the elastic properties of honeycombs almost conformed to those of irregular arranged cell walls of the same density. However, later studies by Van der Burg et al. [175], Zhu et al. [210], and Zhu et al. [211] revealed that the Young's modulus increased significantly with an increase in the irregularity of the cell arrangement. The potential to use irregular versatile structures for multi-functionality [46] makes them highly useful in a broad field of applications. The growing interest regarding cellular structures coincides with the recent advancements in additive manufacturing, which now allows the fabrication of these complex structures using a wide range of materials [172].

While most research has investigated the static mechanical properties of complex cellular structures, little is known about their dynamic properties, in particular, their vibration properties. Several studies have been conducted on sandwich beams. Sandwich structures are likely to have high eigenfrequencies because of their large bending stiffness per mass [46], which has been confirmed by comparing a solid beam with a sandwich beam of the same mass [95]. Ruzzene [144] studied the vibration and acoustic behaviour of sandwich beams with honeycomb truss cores. Several investigations showed that the eigenfrequencies of sandwich beams are sensitive to the lattice core design [21] and to other geometric parameters, e.g., to an increase in the core thickness of a sandwich beam with a lattice truss core [95, 96, 197].

Regarding 2D honeycomb structures, Dai et al. [35] studied the eigenfrequencies and mode shapes depending on different top and bottom layer thicknesses. An integral method to solve regular honeycombs under dynamic loads has been proposed by Wang and Stronge [186]. Sorokin et al. [160] actively shifted the eigenfrequency of a sandwich plate with a honeycomb core owing to parametric stiffness modulation by changing the orientation of cell elements. Banerjee and Bhaskar [20] showed that macroscopic cellular structures can be abstracted as a homogeneous continuum to calculate low eigenfrequencies, which helps to reduce computing effort in obtaining eigenfrequency values. Sandwich structures with gyroid lattice cores (figure 2.1a) were investigated regarding the impact of geometrical parameters (plate thickness, gyroid wall thickness) on the 1^{st} eigenfrequency by Simsek et al. [158].

Generally, although Ashby [19] defined a lattice as a connected network of struts, many cellular structures or lattices, which were investigated in the here reviewed studies, are composed of both struts and walls or are even based on only walls, e.g., the lattice structures displayed in figure 2.1. Helou and Kara [72] gave an overview of studies conducted on lattice structures focusing on design, analyses and optimisations, and manufacturing. The following listed studies mainly focused on larger-scaled lattices, which cannot be seen as cellular structures anymore.

Yan et al. [199] conducted compression tests on additively manufactured, stainless steel regular lattice structures based on different unit cells. Their results indicated a Young's modulus decrease with an increase in unit cell size. Ozdemir et al. [127] also conducted compression experiments on additive manufactured regular lattice structures showing that the structures reduced the peak impact stress by temporally spreading the impact loading. Maskery et al. [104] found that the cell size of a metal lattice structure has a significant impact on the failure mechanism under compression. Implementing post-manufacture heat-treatment leads to reduced peak stresses at the same amount of compressive deformation. The mechanical properties of different triply periodic lattice structures of the same mass based on gyroid, diamond, and primitive unit cells (figure 2.1) were analysed by Maskery et al. [106]. The additive manufactured structures made out of polymer were tested under tension and compression and were also simulated. They showed that the lattices deformed differently depending on their unit cell geometry. Aremu et al. [18] focused on the design method of lattice structures based on unit cells, which were characterised by a cross section diameter grading. Maskery et al. [105] showed that functionally graded regular lattice structures lead to far higher energy absorption during compression than non-graded regular lattice structures of the same mass. The effect of density and unit cell size grading on the stiffness and energy absorption in simulations and experiments on additively manufactured lattices was investigated by Plocher and Panesar [135]. Studies on functionally graded foams [29, 111] and honeycombs [30, 112] also demonstrated improved mechanical properties under compression and an enhanced capability of sound absorption.

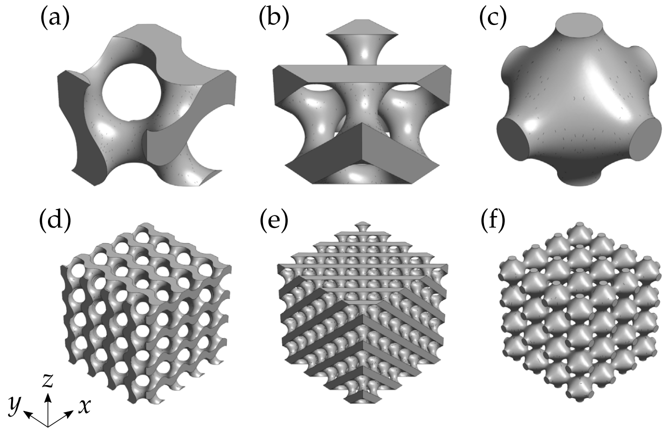

Figure 2.1: An individual gyroid (a), diamond (b), and primitive (c) cell as well as regular lattice structures based on 4x4x4 gyroid (d), diamond (e), and primitive (f) cells are displayed. The figure is reprinted from Maskery et al. [106], published under the CC BY 4.0 license. The characters are replaced by high-resoultion characters.

In terms of larger-scaled lattice structures, Nourbakhsh et al. [119] designed an optimised car chassis based on an irregular lattice structure (also called 'beam network') to reduce the overall mass. Also Hands et al. [65] reduced the mass of a steering arch by applying irregular lattice structures. Ferrari et al. [47] gave a numerical example of successfully increasing a torsional mode shape frequency by designing a 3D beam made of struts regularly oriented with 45° angles. Du Plessis et al. [45] also showed examples of irregular lattice structures, however, studies on the mechanical properties are not included.

Very few studies have investigated the vibration characteristics of lattice structures. Syam et al. [166] studied different regular lattice structures in vibration isolation applications. They conducted simulations and experiments of additively manufactured lattices and examined large differences in eigenfrequencies of regular lattice structures based on different unit cells. However, the masses of their models differed up to 20%, which might have had a significant impact on the eigenfrequency results. But also Zhao et al. [208] showed that the 1st eigenfrequency of a regular lattice depends on the unit cell design. Regarding graded lattice structures, Cheng et al. [32] showed that the 1st eigenfrequency of a 3D cantilever, a 3D clamped beam, and a 3D bracket-like structures composed of cubic lattices can be increased by 73%, 32%, and 25%, respectively, owing to the implementation of irregular lattice strut cross section diameters.

Besides the mentioned studies on graded lattice structures, all published works dealt with regular (periodic) lattice structures. Moreover, little effort has been made to analyse the vibration properties of irregular cellular structures or to maximise their eigenfrequencies. Also larger-scale lattice structures (‘beam networks’) have been rarely investigated. This work shall contribute to partly filling this knowledge gap by studying the impact of structural irregularities on the vibration properties, especially on the eigenfrequencies.

3

BIOMIMETICS - INSPIRED BY NATURE

Biomimetics is a scientific discipline that deals systematically with the technical implementation and application of constructions, processes, and development principles of biological systems. Thus, being a cross-border discipline, biomimetics brings the results of basic research to a technical application. In doing so, biological models are not copied, but investigated, understood, and applied to technical problems [114, 136].

The biomimetic approach is a three-step process involving research, abstraction, and implementation. While the 'biology push' process stands for the biological discovery based on basic research, which is applied to technological products, 'technology pull' is demand-driven allowing the improvement of a technological product due to the application of studied biological principles [136].

There are many biological functions that have been investigated and (partly) transferred to technical solutions, like for example:

- The salvinia effect: The floating leaves of *Salvinia molesta* are covered with hairs. Their superhydrophobic surface in combination with hydrophilic pins allows the air retention under water. Artificial surfaces based on this effect could exemplarily lead to drag reduction of ship coatings [22].

Salvinia molesta *is commonly known as 'Kariba weed' or 'Giant salvinia'.*

- Self-sharpening teeth: The teeth of a rodent incisor are made of dentin (bone-like, visco-elastic material) and the teeth front is covered by a thin layer of enamel (hardest material in living species). As both materials differ in their abrasive resistance, the enamel permanently covers the tip of the sharp tooth, which constantly grows. These principles have been transferred into industrial tool concepts [140].

Rodents *are mammals that have a single pair of continuously growing incisors in each of the upper and lower jaws.*

- Vault structures: The turtle shell structure is vaulted, which increases the load-bearing capacity [206]. Following this example and furnishing thin sheet metals with repetitively arranged bulges significantly rises the stiffness and the flexural strength [110].

For more biomimetics investigations refer to Pohl and Nachtigall [136]. In addition, Studart [164], and Du Plessis et al. [45] reviewed biomimetics and biologically-inspired materials and designs in connection with additive manufacturing. In the following, the focus will be on biologically inspired lightweight design structures.

Most technical lightweight structures, such as typical honeycomb sandwich constructions, lattice structures or steel girders used for planes, buildings, or cranes have mainly regular periodic geometries. However, natural lightweight structures are often complex and show good mechanical properties, like honeycombs of bees [53], the beak of toucans (figure 3.1a) [151, 152], cancellous bones (figure 3.1b) [52, 53], the southern giant horsetail (figure 3.1c) [161], or the shell structures of plankton organisms [142]. These structures are highly optimised during the process of evolution and usually fulfil different functions.

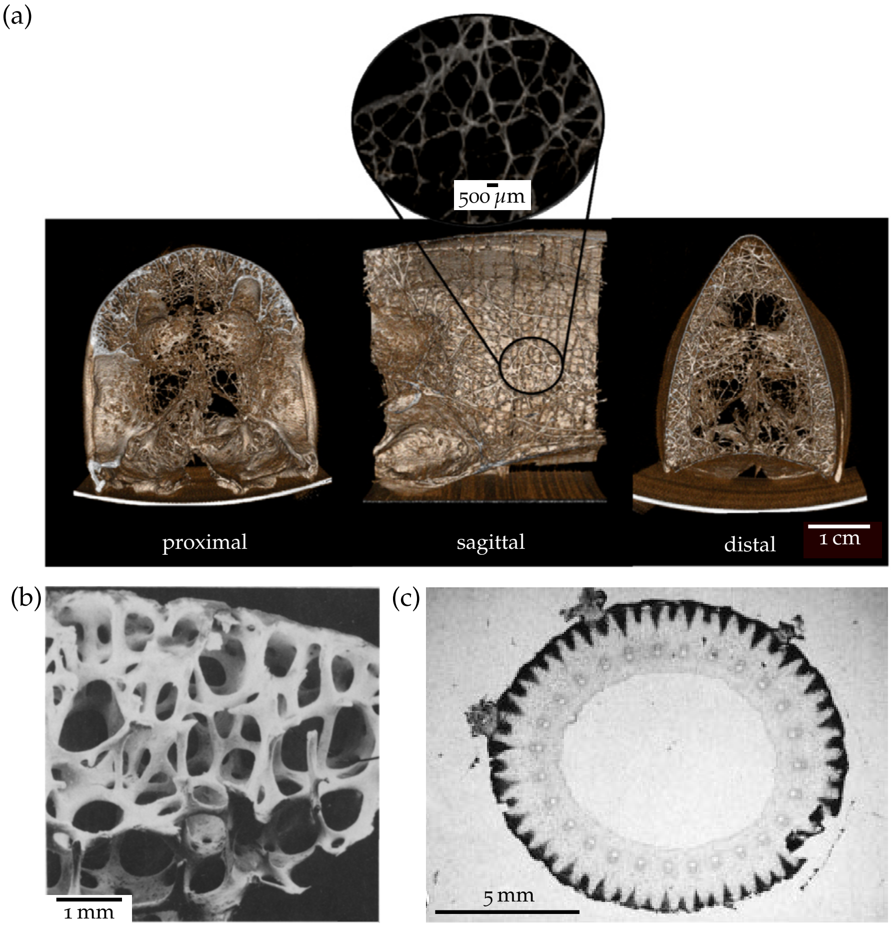

Figure 3.1: Different complex biological lightweight structures are displayed. A μCT-scan shows the inner foam structure of a Toco Toucan (*Ramphastos toco*) beak, reprinted from Seki et al. [151] with permission from Elsevier (a). The figure includes proximal and distal cross sections and a sagittal view of the mid-region of the beak. The scanning electron microsopic image of a low density cancellous bone (part of a femoral head) is composed of an asymmetric rod-like structure (b). The image is reprinted from Gibson [52] with permission from Elsevier. The third displayed biological lightweight structure is the cross section of a stem of a southern giant horsetail (*Equisetum giganteum*), reprinted from Spatz et al. [161] with permission from John Wiley and Sons. The characters and the scale bar of the three images are replaced to improve the resolution.

In particular, plankton organisms with biomineralised cell covers (such as diatoms and radiolaria, figure 3.2) have developed an extremely high diversity of irregular structures. In contrast to technical production processes (with the exception of 3D printing, to a certain extent) the natural process of morphogenesis in diatoms and radiolarians allows the production of almost any form, including irregular honeycomb and lattice structures [61, 142, 146]. As these organisms need to float in the nutritious upper water column to survive and, in particular in the case of diatoms, to also carry out photosynthesis, their silicate shells must be very light. At the same time, high structural stiffness and stability is essential to stand the attacks by their predators, the copepods. Thus, the combination of low mass and high stiffness leads to lightweight design principles that can be observed in these biological structures (figure 3.3) [51, 62–64].

Although these complex structures follow the same basic construction principles of technical structures using ribs, lattices, and honeycombs [62], they are highly multifunctional characterised by a high permeability [94], mechanical robustness [41], high energy absorption [64], and vibration optimisation [59]. The diatom shell's geometrical parameters (pores, layers) significantly influence their mechanical behaviour [60]. Thus, diatom shells are of high interest for many technical applications, e.g., improved nano-filtration [200], drug delivery systems [170], plastic deformation elements in automobiles [74], membrane holder for deep sea sample inlet systems [9], and optical sensing materials [36, 37] have been discussed. In regard to the good mechanical properties of planktonic shells, their lightweight design principles serve already as inspiration for lightweight construction and has been successfully applied to structures of different industrial sectors [71, 100, 101]. In addition, the systematic product development process Evolutionary Light Structure Engineering (ELiSE®), primarily based on the shells of diatoms and radiolaria, inspires engineers to improve technological products by applying biological lightweight design principles. The biomimetic process has been invented at the Alfred Wegener Institute Helmholtz Centre of Polar and Marine Research and is defined as an Industry Standard by the German Association of Engineers [177]. ELiSE® has been successfully applied to different technical areas involving automotive, aerospace, and space industry, medicine, offshore structures, civil engineering, and industrial housings [136].

Aside from the lightweight design principles observed in diatom shell structures, a high impact of these irregular structures on the vibration characteristics is expected, since the copepod's attacks do not only involve high point loads, but the predators also hammer on their prey with Reynold's numbers of 10^{-2} to 10^{-1}, or rather, the feeding tools move at rates of 20 to 80 Hz [83]. Consequently, the cell cover has to be resilient against vibrational load cases.

Diatoms *are single-celled algae worldwide present in oceans, waterways, and soils. The cell is protected by a stiff and lightweight silicate shell (silica:* SiO_2*).*

Radiolaria *are single-celled eukaryotes that have - similar to diatoms - a skeleton mostly composed of silica. They are part of the zooplankton present in oceans.*

Morphogenesis *is the generation of forms.*

Although the **density of silicate** *is about 2.2 to* $2.7\,\mathrm{g\,cm^{-3}}$*, diatoms and radiolaria are able to float in the upper water column (sea water density:* $1.03\,\mathrm{g\,cm^{-3}}$*).*

Copepods *are small crustaceans present in nearly every freshwater and saltwater habitat.*

The non-dimensional **Reynold's number** *Re is defined as*

$$Re = \rho\, u_{flow}\, L/\mu$$

including the fluid density ρ*, the fluid flow speed* u_{flow}*, a characteristic lengh L, and the dynamic viscosity of the fluid* μ*. A low Re value indicates a laminar flow, a high Re value a turbulent flow.*

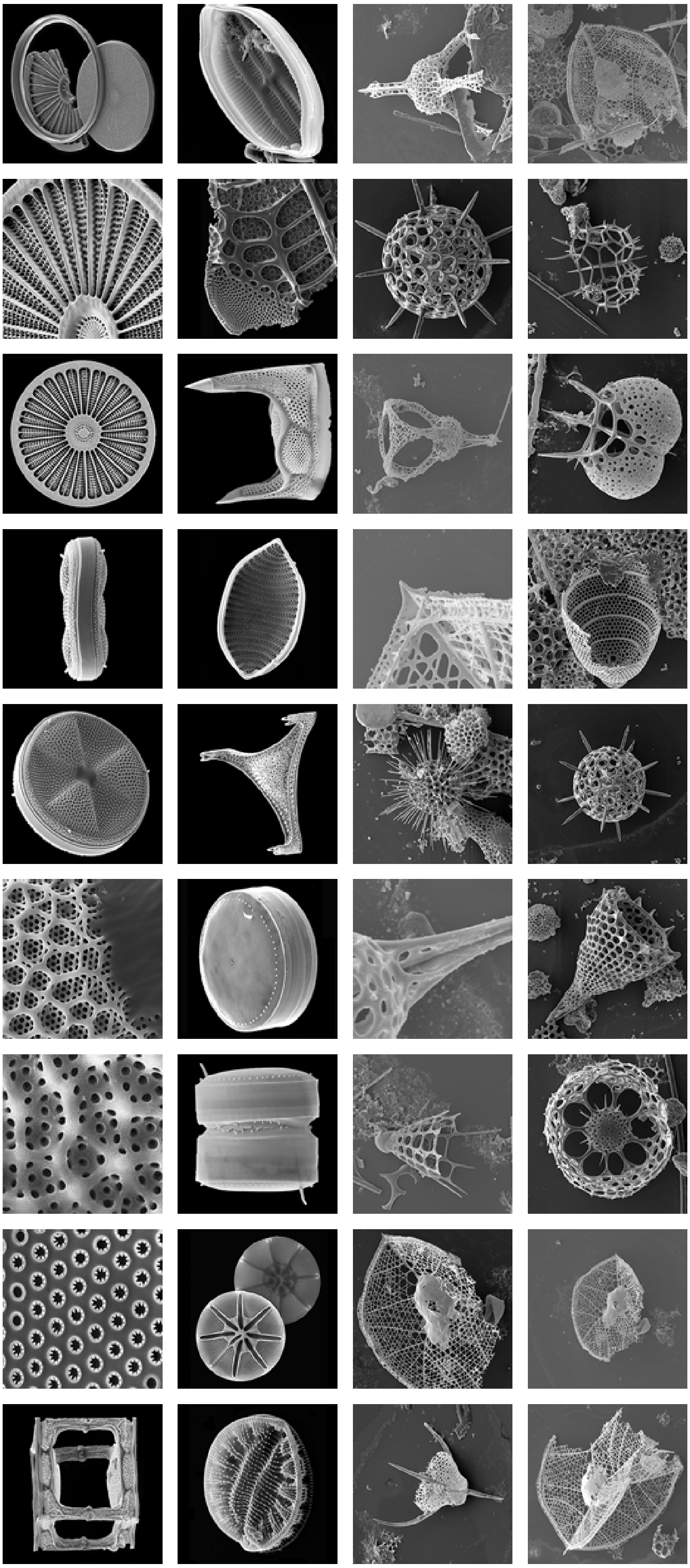

Figure 3.2: Scanning electron microscopic images of different diatom shells (first two rows) and exosceletons of radiolaria (last two rows). The figure is reprinted from Maier [100] with permission from the author.

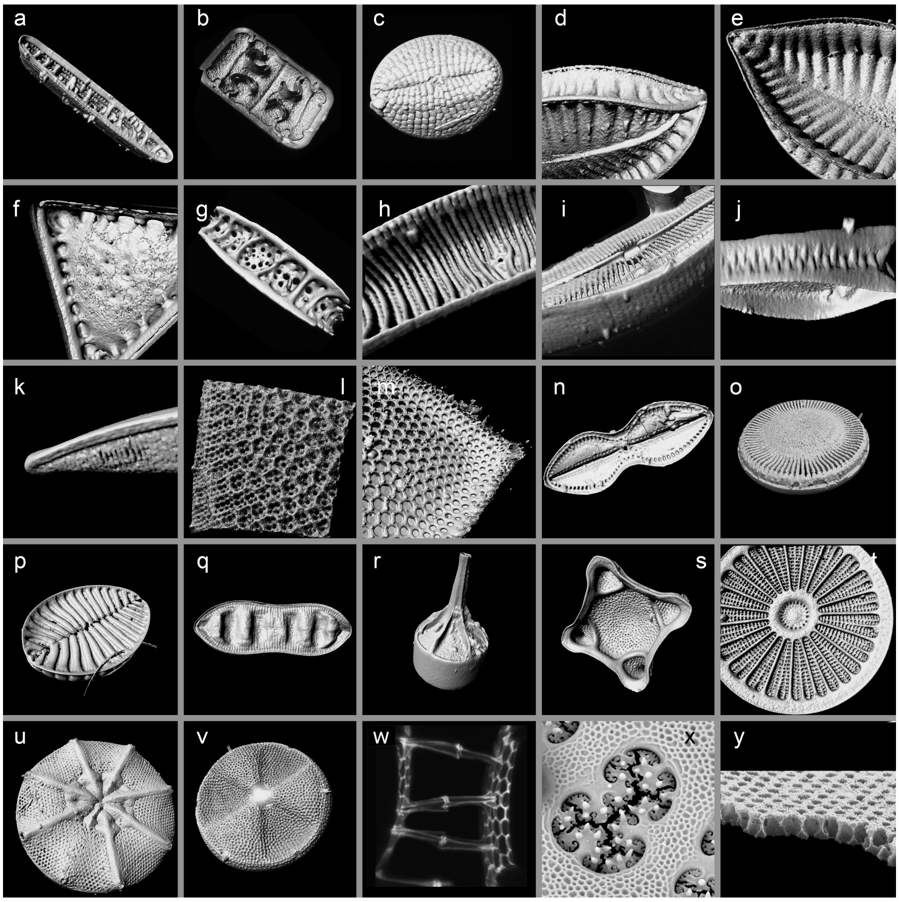

Figure 3.3: Confocal laser scanning microscopic (a-w) and scanning electron microscopic (x-y) images of lightweight structures and stiff design principles that can be observed in diatom shells including a beam construction (a), corrugated sheet stiffener (b), camber structures (c), stiffening fins with reinforced edges (d-e), reinforced edges (f), beam constructions (g-h), beam constructions with frame and fin (i), interlocking connections (j), notch stress minimising raphe design (k), pore constructions (l-m), fractal hierarchical structure (l), honeycomb with surface layer (m), multiple rippled and finned surfaces (n-q), stabilised tubes (r-s), combination of radial and concentric spokes (t), tube–like spokes as stiffening elements (u), radial curvatures (v), connecting interlocking elements (w), notch-stress minimising pore structure, and sandwich/honeycomb construction (y). The figure is reprinted from Friedrichs [51] with permission from the author. The characters have been partly replaced.

However, *in vivo* experiments to measure the diatom shell eigenfrequencies have not been possible up to now. Thus, construction and simulation of diatom shells are necessary to obtain more information about their vibration characteristics. First studies were published by Gutiérrez et al. [59], who performed numerical modal analyses of abstracted diatom shells (figure 3.4), and found that the diatom shell mode shapes correlated well with deformation patterns that can be observed in these shells. They stated that although most interactions in the environment, in which diatoms live, occur at low Reynold's numbers (e.g., the predators' attacks), dynamic stimulations are possible at micro- and nano-scale. Therefore, they suggested that the deformation patterns observed in diatom shells may be the result of mechanical interactions during morphogenesis. Gutiérrez et al. [59] estimated the 1st eigenfrequency of a diatom shell surrounded by air to be in the range of 7 to 10 kHz.

Aside from this, little is known about the purpose of diatom cell covers as a result of challenges related to acoustic properties. However, it is obvious that the concept to generate, optimise, and apply such highly complex irregular structures allows the substantial manipulation of vibration properties [79].

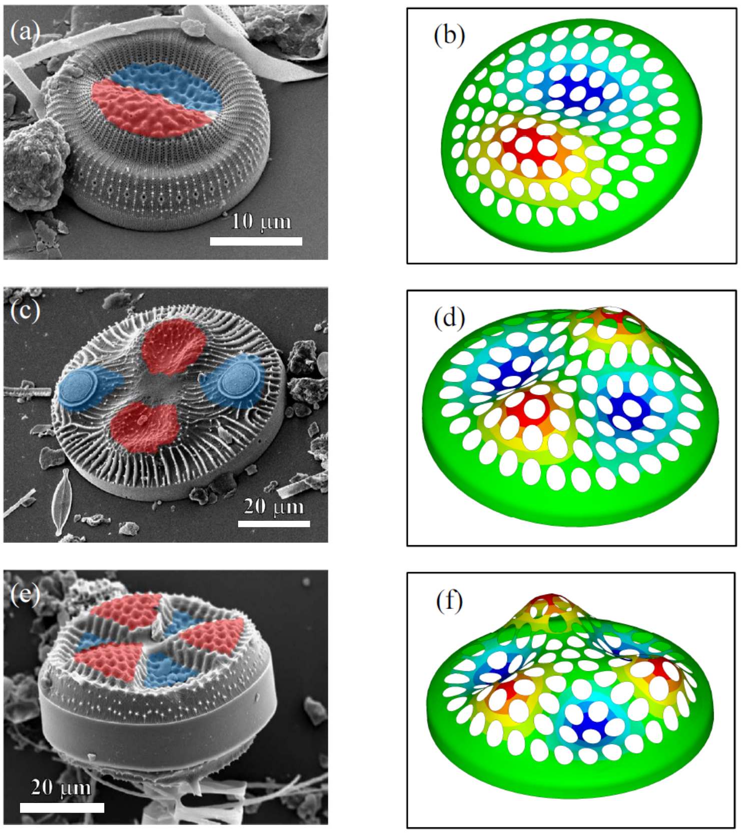

Figure 3.4: Comparison of deformation patterns of centric diatom shells to mode shapes obtained in modal analyses. The scanning electron microscopy images show *Cyclotella distinguenda* (a), *Auliscus sculptus* (c), and *Actinoptychus senarius* (e) that are compared to the 1st mode shape (b), the 2nd mode shape (d), and the 3rd mode shape (f), respectively, obtained by a finite element simulation of a abstracted centric diatom shell. The figures are reprinted from Gutiérrez et al. [59] published under the CC BY 3.0 license. The scale bar is replaced by a high-resoultion line.

4

STRUCTURAL OPTIMISATION TO IMPROVE VIBRATION CHARACTERISTICS

Structural optimisation implies the development of an optimum structure, i.e., an optimum material distribution. Sizing, shape, and topology optimisation are distinguished (figure 4.1).

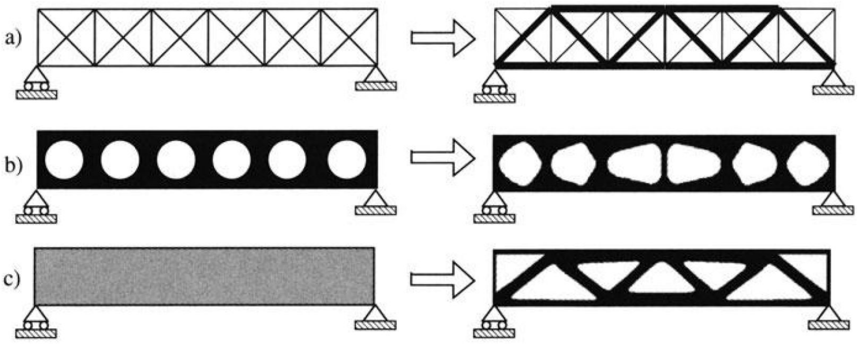

Figure 4.1: The three categories of structural optimisation are sizing optimisation (a), shape optimisation (b), and topology optimisation (c). The initial problems are displayed on the left hand side, while the optimum solutions are shown at the right. The figure is reprinted from Bendsøe and Sigmund [25] (page 2) with permission from Springer Nature.

In sizing optimisations, the optimum shell thickness or truss/beam cross section distribution of a given structure is searched to fulfil an objective function like for example minimising the static deflection. Whereas the design domain is known during this optimisation, the shape of this domain is the design variable and an optimum shape is searched for during a shape optimisation [25]. In a topography optimisation, which is a subset of a shape optimisation, the nodes of a structure are moved normal to the continuous surface to create an optimum structure [171]. A topology optimisation problem involves the determination of the physical size and the shape and connectivity of a structure, while the boundary conditions, the design space, and the targeted volume are predetermined [25].

In the following paragraphs, the history of structural optimisation and its recently published studies are presented, mainly focusing on vibration issues. The named studies are mostly dealing with 1D and 2D structures, which are also investigated in this work (see chapter 8 to chapter 10).

Numerical sizing optimisations of 1D and 2D structures under certain static or dynamic loading conditions to optimise specific single eigenfrequencies have already been studied starting from the 70s, e.g., Olhoff [123, 124] conducting cross section optimisation of beams or Olhoff [121, 122] focussing on thickness optimisation of circular and rectangular plates. Cheng and Olhoff [31] presented a regularised mathematical formulation of annular plates with the objective to maximise the 1^{st} eigenfrequency. Similarly, but taking dual optimisation problems into account, Haug et al. [67–69] studied beams, frames, and plates using a generalised steepest descent method to optimise the 1^{st} eigenfrequency with constraints on the deflection while keeping a minimum weight and varying the cross section of beams or frames or the thickness of plates. A summary of literature concerning sizing optimisation to increase frequencies of different 1D and 2D structures was given by Grandhi [56].

Next to the sizing optimisation, most focus has been put on topology optimisation that was first considered by Díaz and Kikuchi [40] using the homogenisation design method with focus on increasing the 1^{st} eigenfrequency of plates. The work was extended by Tenek and Hagiwara [169] focusing on single and multiple eigenfrequencies as well as isotropic and composite plates. Regarding other utilised optimisation methods, the Solid Isotropic Micro structures with Penalisation (SIMP) method was used by Pedersen [130] to increase single eigenfrequencies or by Tsai and Cheng [173] to create desired eigenmodes of plates. Du and Olhoff [44] applied the SIMP method on beams and plates to maximise the 1^{st} and also higher-order single eigenfrequencies, and to create eigenfrequency gaps. A topology optimisation method to increase the 1^{st} eigenfrequency by considering casting constraints was proposed by Xu et al. [196].

Single eigenfrequencies were also maximised by using evolutionary structural optimisation on beams and plates [195, 207] or bidirectional evolutionary structural optimisation on beams [73] and plates [73, 212]. Also Ma et al. [98] and Yaghoobi and Hassani [198] conducted topology optimisations to increase single eigenfrequencies of beams. In addition, Stanford et al. [163] used topology optimisation to design stiffening-structures targeting at a 1^{st} eigenfrequency increase. This study was extended by multiple biologically inspired algorithms, e.g., Ding and Yamazaki [42], introducing the bionic growth method based on a growing and branching tree model. All mentioned topology optimisations included multi-optimisation problems, mainly minimising mass or volume while maximising the targeted eigenfrequency.

Beside topology optimisation, also shape optimisation has been frequently used. Afonso and Hinton [1] changed the shape or thickness of various plates and shells to maximise their natural frequency, while using a structural optimisation algorithm with sequential quadratic programming and a constant volume. The parameter-free shape optimisation method based on the H gradient method (traction method) has been utilised by Liu and Shimoda [90] in order to optimise the vibration design of stiffened thin-walled shell structures, while both the stiffeners as well as the basic plate were optimised. The maximisation of an eigenvalue or the achievement of a specified eigenvalue was set as objective. Parametric investigations regarding topography optimisation have been applied by Alshabatat and Naghshineh [6] examining the optimal distribution of spherical dimples or cylindrical beads to optimise the natural frequency of plate-like structures. A genetic algorithm, which is a stochastic optimisation method, was used to perform the optimisation. Pedersen and Pedersen [132] conducted shape optimisations to increase single eigenfrequencies of plate membranes, whereas Meske et al. [107] also defined constraints on the volume. Shimoda and Liu [155] increased plate eigenfrequencies vía shell optimisation as well. Pedersen [131] optimised the shape of holes in plates to maximise eigenfrequencies or to obtain a specific eigenfrequency value. An optimum bead orientation was first investigated by Yang et al. [201] for the maximisation of the first five eigenfrequencies of a cantilever plate and continued by Luo and Gea [97] aiming at a 1^{st} eigenfrequency increase of 3D shell/plate structures by implementing an energy-based method. An optimum distribution of sinusoidal and trapezoidal corrugations was studied by Alshabatat [4] utilising a genetic algorithm in order to shift the 1^{st} eigenfrequency to maximum values. Park et al. [129] used surface-grooving to increase the 1^{st} eigenfrequency of L-shaped plates and hard disk drive covers. Applying topography optimisation to a bracket, Wang and Liao [181] optimised an automotive bracket increasing the 1^{st} eigenfrequency by 30% using the commercially available optimiser OptiStruct. Warwick et al. [189] studied the impact of a stiffener layout on the modal parameters of a bulkhead. Afterwards, topology optimisations were performed to increase the 1^{st} eigenfrequency of the pre-stiffened bulkhead using Altair HyperWorks [190].

While most of the mentioned work focused on maximising single eigenfrequencies, other studies investigated the maximisation of multiple plate eigenfrequencies [84, 169, 201] and the creation of desired eigenfrequency values (beams: [34, 98], plates: [99, 115]) or desired plate eigenmodes [99, 115, 173]. Another important topic has been the creation of eigenfrequency gaps to avoid resonance frequencies in the range of external, exciting frequencies (beams: [44, 93, 98, 125], plates: [6, 44, 77]). Moreover, Nakasone and Silva [115], Ansari et al. [16], Alshabatat et al. [5], and Shimoda and Liu [155] focused on the minimisation of vibration amplitudes of plates or shell structures. Other investigations dealt with the design of supports to increase specific single eigenfrequencies (beams: [3, 78, 182, 183], plates: [78, 183]). Also the design of stiffeners (beads, dimples, ribs, embossing) to increase eigenfrequencies has been part of passive structural dynamics modifications (plates: [4, 6, 42, 97, 201], other 2D structures: [90, 129, 163], 3D structures: [49, 181, 190]. Finally, the concurrent (two-scale) optimisation of cellular material composed of macro- and micro-structures, as exemplarily displayed in figure 4.2, has also been studied to maximise the 1^{st} eigenfrequencies [32, 118, 213] or to minimise the frequency response [178].

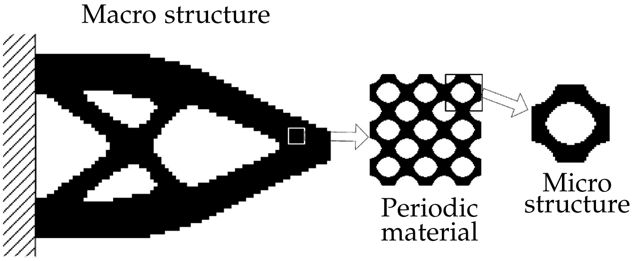

Figure 4.2: The arbitrary macro structure is composed of a regular micro structure. The image is reprinted from Zuo et al. [213] with permission from Elsevier. Some lines and the characters are replaced to improve the resolution.

Also other studies combined topology optimisations with lattice structures (also called 'lattice structure topology optimisation') to improve mechanical properties. Panesar et al. [128] compared uniform lattice structures to lattice structures derived from topology optimisation results and showed an up to 50% higher specific stiffness for the latter. Simsek et al. [158] integrated a homogenisation-based material penalisation formula into the SIMP algorithm to directly map the relative densities obtained from the topology optimisation in order to obtain functionally graded lattice structures. The application to a cantilever beam increased the eigenfrequencies. Wu et al. [193] studied irregular, porous infills for additive manufactured structures inspired by cancellous bones. They showed that the porous infills were 1.5 times stiffer than honeycomb structures and 1.1 times stiffer than optimised rhombic structures.

Altogether, the numerous published work regarding the vibration issue shows the relevance of this topic. As an increase in eigenfrequency can substantially reduce the dynamic response of a structure [156], an eigenfrequency maximisation is of great interest for many technical applications.

5

OBJECTIVES AND OUTLINE

Numerous studies on structural optimisations to improve the vibration characteristics of structures have been published, as presented in chapter 4. However, structural optimisations often require high computational effort, which is why efficient methods to significantly manipulate the vibration characteristics are in great demand. Regarding the use of cellular and lattice structures as efficient lightweight structures, many investigations highlighted the improved mechanical properties of those complex structures over solid (and often simple) geometries, which have been reviewed in chapter 2. Though, little is known regarding the impact of in particular irregular cellular and lattice structures on the vibration characteristics.

This work contributes to research on especially lightweight structures with improved vibration characteristics studying the impact of biologically inspired methods and structures on the vibration characteristics. Due to the large variety of methodological approaches that were considered, a thorough theoretical analysis on each of them was not practicable in the framework of this work. In addition, the studies included the development and testing of a prototype with a high potential for real application. As a consequence of these conditions, this work focused on a systematic empirical approach to get a comprehensive overview on biologically inspired methods to manipulate eigenfrequencies efficiently. Based on this approach, it was possible to apply and verify some of the results successfully by developing and testing a girder structure for the future synchrotron radiation facility Positron-Elektron-Tandem-Ring-Anlage (Positron Electron Tandem Ring Facility) (PETRA) IV at the Deutsches Elektronen-Synchrotron (German Electron Synchrotron) (DESY).

At first, theoretical background information is given in Part II focusing on mechanical (technical) vibrations (chapter 6) and the finite element method (chapter 7).

In the following broad and empirical approach (Part III), different methods inspired by nature to improve the vibration characteristics of structures were studied and compared among each other. The aim was to explore whether the different biologically inspired approaches result in a significant structural eigenfrequency maximisation. The investigated methods comprised

- the shape adaptation of a structure according to specific mode shapes, which can be observed in diatoms (chapter 8)
- the conduction of strategic optimisations following the principles of evolution (chapter 9)

- the application of complex and irregular cellular structures, also combined with the shape adaptation method studied in chapter 8 (chapter 10), and
- the application of complex and irregular lattice structures (chapter 11).

In chapter 12, the studied methods were compared among each other and to other published methods.

Based on the conducted studies, an optimised biologically inspired girder design for the synchrotron radiation facility PETRA IV was developed in Part IV of this work. This design process considered several findings of the investigated methods that were inspired by nature and included

- a general introduction into the topic and the problem definition including the technical specifications and the design space (chapter 13),
- a parametric study investigating the impact of different components and boundary conditions on the eigenfrequencies of a magnet-girder assembly (chapter 14), and
- the girder design process comprising a topology optimisation to indicate an optimum material distribution, an abstraction process and a cross section optimisation, the implementation of biologically inspired design principles, the manufacturing of the designed structure, and the eigenfrequency measurements to assess the numerical results (chapter 15).

Finally, the results of this work were summarised in Part V (chapter 16). Supplemental material is given in the appendix A. The outline of the whole work is displayed in figure 5.1.

To conduct the following studies, the software Rhinoceros (version 6 SR10, Robert McNeel & Associates) with its plug-In Grasshopper (version 1.0.0007, Robert McNeel & Associates) were used to generate parametric and algorithm-based constructions. The Grasshopper-based module ELISE (version 1.0.38, `www.elise.de`) provided algorithms to design biologically inspired structures and allowed the construction of the entire design and simulation process involving technical specifications, pre- and post-processing, and the connection to the external solver OptiStruct (version 2017, Altair Engineering Inc.). All topology and topography optimisations were performed using HyperMesh (version 2017, Altair Engineering Inc.) in combination with the solver OptiStruct. The result evaluation was based on HyperView as well as on Excel (Microsoft Office Standard 2013, Microsoft Corporation). Most figures were generated utilising Inkscape (version 0.92, `www.inkscape.org`). The dissertation was typesetted using LaTeX, based on a layout from André Miede, and the integrated writing environment TeXstudio (version 3.0.4, Benito van der Zander, Jan Sundermeyer, Daniel Braun, and Tim Hoffmann).

I INTRODUCTION

1. Motivation
2. Technical Lightweight Structures and Their Properties
3. Biomimetics - Inspired by Nature
4. Structural Optimisation to Improve Vibration Characteristics
5. Objectives and Outline

II THEORETICAL BACKGROUND INFORMATION

6. Mechanical Vibrations
7. Finite Element Method

III EIGENFREQUENCY INCREASE INSPIRED BY NATURE

8. Shape Adaptation According to Mode Shapes
9. Shape Adaptation Based on Evolutionary Strategic Optimisations
10. Regular and Irregular Honeycomb Plates
11. Regular and Irregular Lattice Structures
12. Comparison of Different Methods to Increase Eigenfrequencies

IV GIRDER DESIGN FOR PETRA IV

13. Highly Brilliant PETRA IV Synchrotron Radiation Source
14. Parametric Study on Components and Boundary Conditions
15. Development of a Biologically Inspired Girder Design

V SUMMARY

16. Summary

Figure 5.1: Outline of this work composed of five main parts (dark grey) that include 16 chapters (light grey).

Part II

THEORETICAL BACKGROUND INFORMATION

This part summarises theoretical background information relevant to the studies described within this work. First, it is focussed on technical/mechanical vibrations of single and multiple degree of freedom systems. Subsequently, the fundamental equations of the finite element analysis extensively applied in this work are given.

6

MECHANICAL VIBRATIONS

6.1 INTRODUCTION

Mechanical vibrations refer to the oscillating response of an elastic body to disturbances, which take the body off its equilibrium position. In general, all bodies having a mass and a finite stiffness are capable of vibrating. The studied parameters (e.g., displacement) change over time, so that certain characterics (e.g., specific displacement value) recur.[28, 147]

Vibration is the periodic exchange of stored (i.e., potential) energy and energy of motion (i.e., kinetic energy). All real, vibrating systems show damping, e.g., due to friction between moving elements, leading to energy dissipation by converting the potential and kinetic energy into heat. Thus, during vibration, there is a periodic transformation of kinetic and potential energy until all energy is lost because of damping. Based on the nature of the vibration excitation and the resulting motion and according to Schmitz and Smith [147], mechanical vibrations can be divided into the following three categories:

- Free vibration:
  Perturbating a body from its equilibrium position results in a free vibration characterised by an exponentially decaying, periodic response to the initial conditions. The body oscillates at its characteristic eigenfrequency (also called 'natural frequency'), until it is brought to a stop due to damping.

- Forced vibration:
  A body is excited by a continuing, periodic force. As a result, the body oscillates at the forcing frequency. If the exciting frequency corresponds to the body's eigenfrequency, a large vibration amplitude ocurrs. This phenomenon is called 'resonance'.

- Self-excited vibration:
  When a steady input force is modulated into vibration at a frequency close to the body's eigenfrequency, self-exciting vibration occurs. In contrast to free vibrations, the vibration amplitude can increase over time owing to the external force.

Each body can be characterised by its eigenfrequencies and mode shapes (also called 'eigenmodes' or 'eigenvectors'). Mode shapes are the characteristic relative motion of the individual degrees of freedom of a body. They are usually normalised to one of the degrees of freedom, because they only contain the ratio of the vibration amplitude between coordinates. Each mode shape is associated with a specific eigenfrequency. Modal analyses (see chapter 6.3.2) allow the determination of eigenfrequencies and mode shapes, which are ordered in ascending eigenfrequency values. Thus, if eigenfrequencies shift due to structural adaptation, the mode shapes can change their order, which is called 'mode switching'.[28, 147]

6.2 VIBRATION OF STRUCTURES WITH ONE DEGREE OF FREEDOM

This chapter presents the free damped and undamped vibration of a Single Degree Of Freedom (SDOF) system. In addition, the equation of motion for a forced damped vibration is solved. Afterwards, the frequency response function is derived and different measurement techniques are presented. The information is mostly based on Schmitz and Smith [147] and Gross et al. [58] with additional information according to Beards [24], Petyt [133], Freymann [50], and Brommundt and Sachau [28].

6.2.1 *Free Damped Vibration*

A spring-mass-damper model (figure 6.1) is analysed, in which the spring force kx with the stiffness k and the damping force $d\dot{x}$ with the viscous damping coefficient d act on the SDOF mass m. The application of Newton's 2nd law of motion leads to the equation of motion:

Newton's 2nd law of motion *states that the time rate of change of the momentum of a body is proportional to the sum of all forces acting on that body. The momentum is defined as the product of the body mass and the velocity.*

$$\downarrow: m\ddot{x} = -d\dot{x} - kx \quad \rightarrow \quad m\ddot{x} + d\dot{x} + kx = 0 \tag{6.1}$$

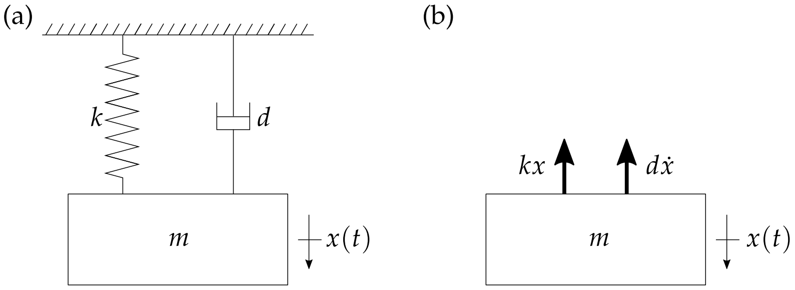

Figure 6.1: Spring-mass-damper model for a single degree of freedom vibration (a) and the corresponding free body diagram (b).

x, $\dot{x}$, and $\ddot{x}$ denote the displacement, the velocity, and the acceleration, respectively.

All structures or systems are able to dissipate energy. As mathematical expressions for the energy dissipation are quite complex, simplified models are usually utilised that involve viscous damping, structural damping, and internal damping.[137] Equation 6.1 considers viscous damping.

Inserting the equations:

$$2\delta_d = \frac{d}{m} \tag{6.2}$$

and:

$$\omega = \sqrt{\frac{k}{m}} \tag{6.3}$$

into equation 6.1 leads to:

$$\ddot{x} + 2\delta_d \dot{x} + \omega^2 x = 0 \tag{6.4}$$

δ_d is the damping coefficient and ω is the angular eigenfrequency of the undamped SDOF system. The general solution of this differential equation with constant coefficients is:

$$x(t) = B_1 e^{\lambda t} \tag{6.5}$$

with the time t and the unknown coefficients B_1 and λ resulting in the characteristic equation:

$$\lambda^2 + 2\delta_d \lambda + \omega^2 = 0 \tag{6.6}$$

This quadratic equation has two solutions:

$$\lambda_{1,2} = -\delta_d \pm \sqrt{{\delta_d}^2 - \omega^2} \quad \rightarrow \quad \lambda_{1,2} = -\delta_d \pm \omega\sqrt{1 - \zeta^2} \tag{6.7}$$

with the damping ratio ζ defined as:

$$\zeta = \frac{\delta_d}{\omega} \tag{6.8}$$

Thus, the solution of equation 6.4 depends on the damping ratio:

1. $\zeta > 1$: Overdamped System

   The solution of equation 6.4 is a linear combination of the two partial solutions in equation 6.7:

   $$x(t) = B_1 e^{\lambda_1 t} + B_2 e^{\lambda_2 t} \tag{6.9}$$

   The two coefficients B_1 and B_2 can be obtained from the initial conditions $x(0) = x_0$ and $\dot{x}(0) = \dot{x}_0$ with x_0 and $\dot{x}_0$ denoting the displacement and the velocity at $t = 0$, respectively.

2. $\zeta = 1$: Critical Damping

   In the case of critical damping, λ_1 and λ_2 are both equal to $-\delta_d$. Thus, the solution of equation 6.4 is:

   $$x(t) = B_1 e^{\lambda_1 t} + B_2 e^{\lambda_2 t} = (B_1 + B_2 t)\, e^{-\delta_d t} \tag{6.10}$$

3. $\zeta < 1$: Underdamped System

   The radicand in equation 6.7 is negativ. λ_1 and λ_2 are defined as:

   $$\lambda_{1,2} = -\delta_d \pm i\omega\sqrt{1-\zeta^2} = -\delta_d \pm i\omega_d \tag{6.11}$$

   with:

   $$\omega_d = \omega\sqrt{1-\zeta^2} \tag{6.12}$$

   Note that the angular eigenfrequency of the damped system ω_d is smaller than the angular eigenfrequency of the undamped system.

   The solution of equation 6.4 is:

   $$x(t) = B_1 e^{\lambda_1 t} + B_2 e^{\lambda_2 t} = e^{-\delta_d t}\left(B_1 e^{i\omega_d t} + B_2 e^{-i\omega_d t}\right) \tag{6.13}$$

   Inserting the relation:

   $$e^{\pm i\omega_d t} = \cos\omega_d t \pm i \sin\omega_d t \tag{6.14}$$

   into equation 6.13 leads to:

   $$x(t) = e^{-\delta_d t}\left[(B_1 + B_2)\cos\omega_d t + i\,(B_1 - B_2)\sin\omega_d t\right] \tag{6.15}$$

   Equation 6.15 can also be rewritten as:

   $$x(t) = B_3 e^{-\delta_d t}\cos\left(\omega_d t - \varphi\right) \tag{6.16}$$

   Both new coefficient B_3 and the phase angle φ can be obtained from the initial conditions.

   Figure 6.2 shows a vibration decay of an underdamped system. T_d denotes the period of the damped oscillation.

6.2.2 *Free Undamped Vibration*

All real structures dissipate energy while they vibrate, which is why undamped vibrations do not exist. However, the energy dissipation is often small. Thus, the equations of an undamped systems presented in this sub-chapter do sometimes apply. Moreover, in many engineering structures the damping ratio is equal to or less than 0.02.[24]

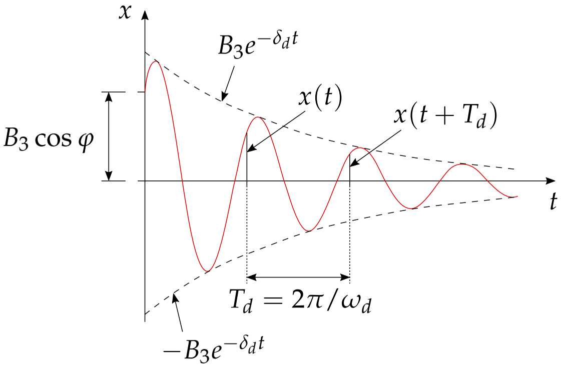

Figure 6.2: Vibration decay of an underdamped system.

Consequently, considering equation 6.12, the angular eigenfrequency of the undamped system corresponds to that of the damped system. In addition, as the majority of the studies within this work do not consider damping, the following equations for undamped vibrations are important to mention.

Figure 6.3 shows a spring-mass model composed of a SDOF mass that is affected by a spring force. The equation of motion results from Newton's 2nd law of motion:

$$\rightarrow: m\ddot{x} = -kx \quad \rightarrow \quad m\ddot{x} + kx = 0 \tag{6.17}$$

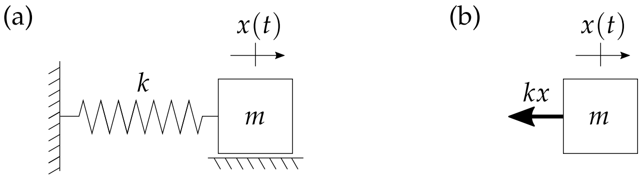

Figure 6.3: Spring-mass model for a single degree of freedom vibration (a) and the corresponding free body diagram (b).

Considering the definition of the angular eigenfrequency in equation 6.3 leads to:

$$\ddot{x} + \omega^2 x = 0 \tag{6.18}$$

The general solution of this linear and homogeneous differential equation of 2nd order is:

$$x(t) = B_1 \cos \omega t + B_2 \sin \omega t \tag{6.19}$$

Based on the initial conditions $x(0) = x_0$ and $\dot{x}(0) = \dot{x}_0$, the unknown coefficients B_1 and B_2 are determined:

$$B_1 = x_0 \qquad \text{and :} \qquad B_2 = \frac{\dot{x}_0}{\omega} \tag{6.20}$$

The eigenfrequency f can be considered with the following relation:

$$f = \frac{\omega}{2\pi} = \frac{1}{2\pi}\sqrt{\frac{k}{m}} \tag{6.21}$$

6.2.3 *Forced Damped Vibration*

Many real structures are affected by periodic excitation. Only some periodic forces are harmonic. However, as non-harmonic periodic forces can be described as a series of harmonic functions applying Fourier analysis techniques [24], harmonic vibration excitation is presented in this sub-chapter.

Applying Newton's 2nd law of motion to a SDOF spring-mass-damper model subjected to harmonic excitation (figure 6.4) leads to the corresponding equation of motion:

$$\uparrow: m\ddot{x} = -d\dot{x} - kx + F\cos\Omega t \quad \rightarrow \quad m\ddot{x} + d\dot{x} + kx = F\cos\Omega t \tag{6.22}$$

Ω is the angular frequency of the harmonic vibration excitation.

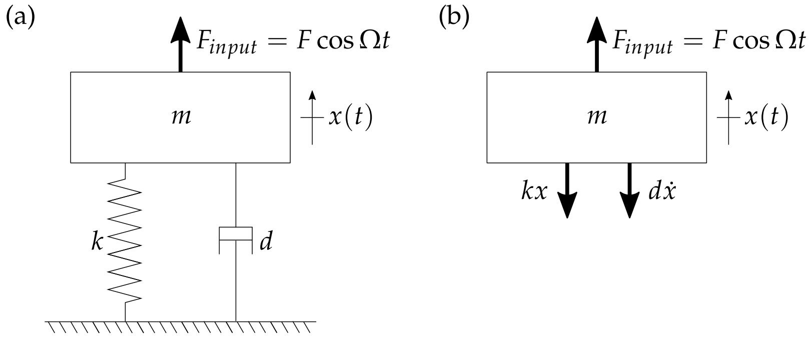

Figure 6.4: Spring-mass-damper model for a single degree of freedom vibration with harmonic excitation (a) and the corresponding free body diagram (b).

Considering the relation

$$x_s = \frac{F}{k} \tag{6.23}$$

in which x_s denotes the static displacement of the spring due to the constant force F, and the equations 6.2 and 6.3, results in the following inhomogeneous differential equation:

$$\ddot{x} + 2\delta_d\dot{x} + \omega^2 x = \omega^2 x_s \cos\Omega t \tag{6.24}$$

Dividing the equation by ω^2 and inserting equation 6.8 leads to:

$$\frac{1}{\omega^2}\ddot{x} + 2\frac{\zeta}{\omega}\dot{x} + x = x_s\cos\Omega t \tag{6.25}$$

The solution of this differential equation is composed of the general solution of the homogeneous (or transient) differential equation x_h and the particular (or steady-state) solution of the inhomogeneous differential equation x_p.

$$x(t) = x_h(t) + x_p(t) \tag{6.26}$$

The homogeneous differential equation $\frac{1}{\omega^2}\ddot{x} + 2\frac{\zeta}{\omega}\dot{x} + x = 0$ decays rapidly for damped systems. Its solution has been presented in chapter 6.2.1. The particular solution is defined as:

$$x_p(t) = x_s H \cos\left(\Omega t - \Phi\right) \tag{6.27}$$

H is the dynamic amplification factor (cf., equation 6.36) and Φ is the angular phase shift between the excitation and the response (cf., equation 6.34). Equation 6.27 can be rewritten to:

$$x_p(t) = x_s H \left(\cos\Omega t \cos\Phi + \sin\Omega t \sin\Phi\right) \tag{6.28}$$

Differenting equation 6.28 twice and inserting it into equation 6.25 leads to:

$$\begin{aligned} x_s H\frac{\Omega^2}{\omega^2}\left(-\cos\Omega t\cos\Phi - \sin\Omega t\sin\Phi\right) \\ +2\zeta x_s H\frac{\Omega}{\omega}\left(-\sin\Omega t\cos\Phi + \cos\Omega t\sin\Phi\right) \\ +x_s H\left(\cos\Omega t\cos\Phi + \sin\Omega t\sin\Phi\right) = x_s\cos\Omega t \end{aligned} \tag{6.29}$$

Dividing equation 6.29 by x_s, organising the items of the equation, and considering the angular frequency ratio between the excitatory and the excited vibration η defined as:

$$\eta = \frac{\Omega}{\omega} \tag{6.30}$$

results in:

$$\begin{aligned} \left[H\left(-\eta^2\cos\Phi + 2\zeta\eta\sin\Phi + \cos\Phi\right) - 1\right]\cos\Omega t \\ + \left[H\left(-\eta^2\sin\Phi - 2\zeta\eta\cos\Phi + \sin\Phi\right)\right]\sin\Omega t = 0 \end{aligned} \tag{6.31}$$

Equation 6.31 is only satisfied for all t, if the expressions in both brackets are equal to 0:

$$H\left(-\eta^2\cos\Phi + 2\zeta\eta\sin\Phi + \cos\Phi\right) = 1 \tag{6.32}$$

and:

$$\begin{aligned} &H\left(-\eta^2\sin\Phi - 2\zeta\eta\cos\Phi + \sin\Phi\right) = 0 \\ &\rightarrow \quad -\eta^2\sin\Phi - 2\zeta\eta\cos\Phi + \sin\Phi = 0 \end{aligned} \tag{6.33}$$

Equation 6.33 allows the calculation of the angular phase shift:

$$\tan\Phi = \frac{2\zeta\eta}{1-\eta^2} \tag{6.34}$$

Based on equation 6.32 and considering the relations:

$$\sin\Phi = \frac{\tan\Phi}{\sqrt{1+\tan^2\Phi}} \quad \text{and :} \quad \cos\Phi = \frac{1}{\sqrt{1+\tan^2\Phi}} \tag{6.35}$$

the dynamic amplification factor can be determined:

$$H = \frac{1}{\sqrt{\left(1-\eta^2\right)^2 + 4\zeta^2\eta^2}} = \frac{x_d}{x_s} \tag{6.36}$$

$$\text{with :} \quad \zeta \le \sqrt{0.5} \quad \rightarrow \quad H_{max} = H\left(\sqrt{1-\zeta^2}\right) = \frac{1}{2\zeta\sqrt{1-\zeta^2}}$$

$$\zeta << 1 \quad \rightarrow \quad H_{max} \approx H(1) = \frac{1}{2\zeta}$$

Thus, the dynamic amplification factor H can be calculated from the damping ratio ζ and the frequency ratio η. In addition, it is defined as the ratio between the dynamic amplitude x_d and the static displacement due to a constant force x_s. This ratio is also called 'receptance' [133].

Figure 6.5 shows how the dynamic amplification factor varies with the frequency ratio. The frequency ratio, at which the dynamic amplification factor reaches its maximum H_{max}, depends on the damping ratio (cf., equation 6.36). For small damping ratios, which are very common, the dynamic amplification factor is maximised at $\eta_{max} \approx 1$, which means that the excitatory frequency (nearly) matches the eigen-

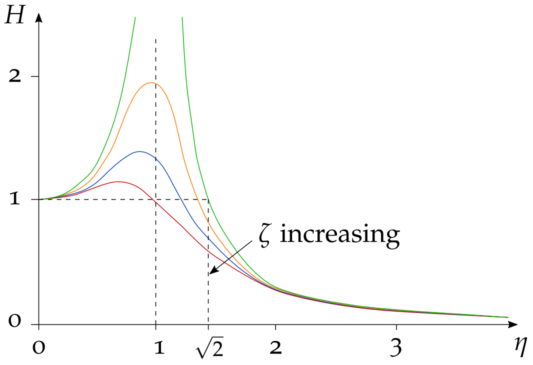

Figure 6.5: Dynamic amplification factor H depending on the ratio of the excitatory frequency and the eigenfrequency of the system η for different damping ratios ζ (based on Beards [24]).

frequency of the excited system. This phenomenon is called 'resonance' (cf., chapter 6.4).

6.2.4 *Frequency Response Function*

In the previous chapter 6.2.3, a SDOF mass is subjected to harmonic excitation. Here, the excitatory force is defined as a complex exponential equation in order to obtain the definition of the complex frequency response funtion according to Schmitz and Smith [147]:

$$F_{input} = Fe^{i\Omega t} \tag{6.37}$$

Thus, the equation of motion for a SDOF spring-mass-damper model (cf., equation 6.22) is changed to:

$$m\ddot{x} + d\dot{x} + kx = Fe^{i\Omega t} \tag{6.38}$$

As already been discussed in chapter 6.2.3, only the inhomogeneous part of equation 6.38 is further analysed. Its solution in form of a complex exponential function is based on the forcing function. Thus, if the above defined input force F_{input} acts on the system, the steady-state response x is

$$x(t) = Xe^{i\Omega t} \tag{6.39}$$

The velocity and the acceleration can be obtained by differentiating the response. Inserting these terms into the equation 6.38 results in:

$$\left(-m\Omega^2 + i\Omega d + k\right) Xe^{i\Omega t} = Fe^{i\Omega t} \tag{6.40}$$

After eliminating $e^{i\Omega t}$ and rewriting the equation, the Frequency Response Function (FRF) is obtained:

$$\frac{X}{F}(\Omega) = \frac{1}{-m\Omega^2 + i\Omega d + k} \tag{6.41}$$

Here, the response to an excitation is considered in the frequency domain, as the time t does no longer appear in the equation. The ratio of the output (vibration X) and the input (force F) depends on the mass, the stiffness, and the damping coefficient of the system as well as on the amplitude and the frequency of the excitation.

The eigenfrequencies of a system can be obtained by FRF measurements. In these experiments, the system is excited by a force based on a fixed frequency sine wave, a random signal, or an impulse:

- Fixed frequency sine wave:
  During this sine sweep test, the FRF is obtained one frequency at a time. The sinusoidal force is generated by a shaker and

Note that **complex exponential functions** *can represent sine and cosine functions (cf. equation 6.14):*
$e^{ix} = \cos(x) + i\,\sin(x)$
$= Re(e^{ix}) + i\,Im\,(e^{ix})$; *with the real part Re, the imaginary unit* $i^2 = -1$*, and the imaginary part Im.* [50]

applied to the studied structure at each frequency of a defined bandwidth.

- Random signal:
  A random frequency signal, either a broad-band (white noise) or limited range (pink noise), is generated by a shaker and applied to the analysed structure. Consequently, all frequencies within a specified bandwidth are excited in a single test.
- Impulse:
  A short duration impact excites the structure to measure the FRF. As for the random signal excitation, a broad range of frequencies are excited in a single test. The impact testing involves an impact hammer, which is used to hit the analysed structure. Thus, the input energy depends on the hammer mass.

Transducers with the required frequency bandwidth (e.g., accelerometers) record the vibration of the structure and other components that have to be taken into account (e.g., base plate to which the analysed structure is fixed). The analog signals are amplified and converted into digital signals using an analog-to-digital converter. Fourier transformation is utilised to convert these time-domain force and vibration signals to the frequency domain to be able to obtain the FRF.

6.3 VIBRATION OF STRUCTURES WITH MULTIPLE DEGREES OF FREEDOM

6.3.1 *Free Vibration of an Undamped Structure With More Than Two Degrees of Freedom*

The SDOF system presented in chapter 6.2 allows a basic understanding of where the eigenfrequencies are derived from. However, structures do normally show numeros degrees of freedom, which is why subsequently, the procedure will be applied to a Multi Degree Of Freedom (MDOF) system. It may be noted that the number of eigenfrequencies and eigenmodes of a system is equal to the number of degrees of freedom. The eigenfrequencies and eigenmodes of large MDOF systems (number of degrees of freedom $n> 2$) can usually only be obtained numerically.[50, 75, 147]

Figure 6.6 displays a vibration chain-type model for an undamped system with n degrees of freedom.

Based on equation 6.17 for the SDOF system, the following equations of motion can be stated for the n degrees of freedom system:

$$\boldsymbol{M}\ddot{\boldsymbol{x}} + \boldsymbol{K}\boldsymbol{x} = 0 \tag{6.42}$$

$$\text{with}: \quad \boldsymbol{M} = \begin{bmatrix} m_1 & 0 & ... & 0 \\ 0 & m_2 & ... & 0 \\ ... & ... & ... & 0 \\ 0 & 0 & ... & m_n \end{bmatrix} \quad ;$$

$$\boldsymbol{K} = \begin{bmatrix} k_1 + k_2 & -k_2 & ... & 0 \\ -k_2 & k_2 + k_3 & ... & 0 \\ ... & ... & ... & -k_n \\ 0 & 0 & ... & k_n + k_{n+1} \end{bmatrix}$$

$\boldsymbol{M}$ and $\boldsymbol{K}$ denote the mass matrix and the stiffness matrix, respectively. $\boldsymbol{x}$ is the displacement vector and $\ddot{\boldsymbol{x}}$ represents the acceleration vector.

The exact solution, in which $\hat{\boldsymbol{x}}$ symbolises the vibration amplitude vector and ω_n the n-th angular eigenfrequency, is:

$$\boldsymbol{x}(t) = \hat{\boldsymbol{x}} \sin(\omega_n t) \quad ; \quad n = 1, 2, 3, ... \tag{6.43}$$

Inserting equation 6.43 in equation 6.42 leads to:

$$\boldsymbol{M}\left[-\omega_n^2 \hat{\boldsymbol{x}} \sin(\omega_n t)\right] + \boldsymbol{K} \hat{\boldsymbol{x}} \sin(\omega_n t) = 0 \quad ; \quad n = 1, 2, 3, ... \tag{6.44}$$

Equation 6.44 can be rewritten in form of the eigenvalue problem:

$$\left(-\omega_n^2 \boldsymbol{M} + \boldsymbol{K}\right) \hat{\boldsymbol{x}} = 0 \quad ; \quad n = 1, 2, 3, ... \tag{6.45}$$

The roots of this equation are the eigenvalues. In order to determine those eigenvalues of the MDOF system, the determinant of the matrix form for the equations of motion is set equal to 0 (non-trivial solutions):

$$\det\left(-\omega_n^2 \boldsymbol{M} + \boldsymbol{K}\right) = 0 \quad ; \quad n = 1, 2, 3, ... \tag{6.46}$$

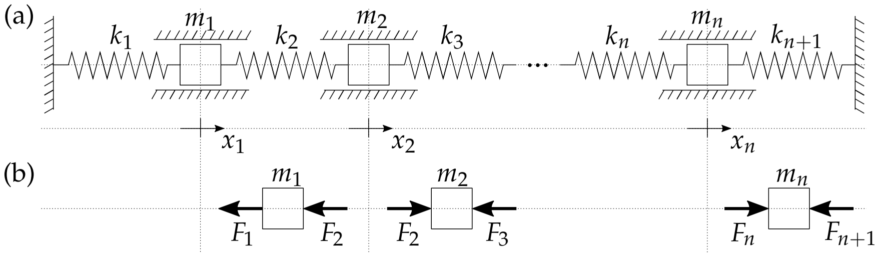

Figure 6.6: Vibration chain-type model for an undamped system with n degrees of freedom (a) and the corresponding free body diagram (b).

The resulting characteristic equation is a *n-th* degree polynomial, whose roots ω_1, ω_2, ..., ω_n are the angular eigenfrequencies:

$$a_n \left(\omega_n^2\right)^n + a_{n-1} \left(\omega_{n-1}^2\right)^{n-1} + ... + a_1 \left(\omega_1^2\right) + a_0 = 0 \;\; ; \;\; n = 1,2,3,... \tag{6.47}$$

To sum up, the characteristic equation 6.47 is derived from the equations of motion 6.42 and its roots are the eigenvalues ω_n^2, which identify the body's angular eigenfrequencies ω_n.

The eigenvectors (mode shapes) can be determined by substituting the eigenvalues back into the eigenvalue problem (cf., equation 6.45). Here, an undamped MDOF system was analysed. However, regarding a damped MDOF system, the mode shapes are always derived from the homogeneous solution presented here.

Both the eigenfrequencies and the mode shapes can be obtained from modal analyses (chapter 6.3.2).

6.3.2 *Modal Analysis*

The modal analysis approach involves a transformation of the local (i.e., model) coordinates into modal coordinates, in which the equations of motion are uncoupled. Thus, the MDOF system is 'decoupled' into separate SDOF systems.

According to Schmitz and Smith [147], figure 6.7 illustrates the concept of modal coordinates. The local coordinates show a dependency of the response of x_1 and x_2 illustrated by the non-zero off-diagonal terms in the stiffness matrix. In regard to the modal coordinates p_1 and p_2, the modal stiffness matrix is uncoupled and two separate SDOF systems are obtained. Thus, vibration solutions can be individually applied to each SDOF system (figure 6.1). Afterwards, the results obtained in modal coordinates are transformed back to local coordinates.

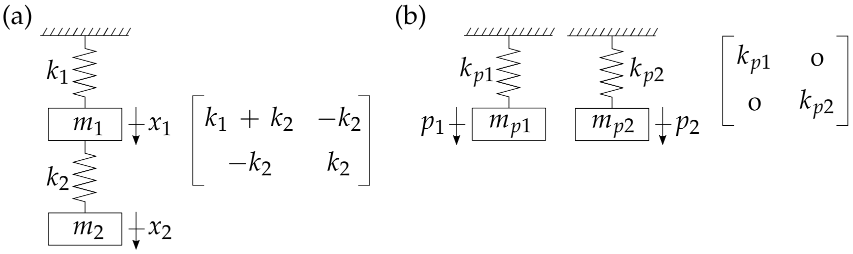
(a)
k_1
m_1
x_1
k_2
m_2
x_2
$\begin{bmatrix} k_1 + k_2 & -k_2 \\ -k_2 & k_2 \end{bmatrix}$
(b)
k_{p1}
k_{p2}
p_1
m_{p1}
m_{p2}
p_2
$\begin{bmatrix} k_{p1} & 0 \\ 0 & k_{p2} \end{bmatrix}$

Figure 6.7: Comparison of the local (a) and modal (b) coordinates of a two degree of freedom system. The subscripts p_1 and p_2 symbolise the modal coordinates. For both coordinates, the corresponding stiffness matrices are given.

A modal matrix (squared matrix) is used to transform the local coordinates into the modal coordinates and vice versa. The columns of the modal matrix are the ordered model's eigenvectors.

It may be noted that the modal analysis approach works because the eigenvectors are orthogonal with respect to themselves. In addition, modal analysis considers proportional damping, which means physically that the individual mode shapes reach their maximum values at the same time. This allows the damping matrix to be written as a linear combination of the mass and stiffness matrices. However, the modal analyses conducted within this work primarily aimed at determing the eigenfrequencies and mode shapes, hence, damping was neglected in all performed modal analyses.

6.4 RESONANCE PHENOMENA AND HOW TO PREVENT THEM

Resonance occurs when the exciting frequency conforms to the eigenfrequency of the system (cf., figure 6.5), which means that the system is excited at its eigenfrequency.[28, 50, 147]

For many technical applications, it is crucial to avoid resonance phenomena, as they lead to undesirable and large vibration amplitudes and – in the worst case - to structural failure. There are different ways to prevent high vibration amplitudes of an oscillating system including

- Isolation:

  By isolating a system from the vibration source (e.g., by using springs), the transmission of energy from the source to the system is prevented. For example, it is possible to position a strongly vibrating machine on springs, so that the high vibration amplitudes of the machine are not transmitted to the ground.

- Damping:

  Vibration energy dissipates due to damping. Additional damping devices can be implemented to increase the energy that is detracted from the system. Consequently, the vibration amplitudes decrease more rapidly. Damping can be applied either passively (e.g., using materials with high damping ratios) or actively. It is also possible to implement tuned mass dampers, which are additional components that adopt the vibration energy of the system.

- Detuning the system:

  The structural eigenfrequencies depend on the stiffness and the mass. Increasing the stiffness results in an eigenfrequency shift. Thus, if the system's eigenfrequencies do no longer coincide with the external exciting frequencies and resonance can be prevented.

Generally, a higher damping ratio or stiffness to mass ratio leads to a smaller response amplitude. In this work, it is mainly focused on raising the stiffness at a constant mass by changing the structure. A stiffness increase does not only reduce the vibration amplitude for any vibration forcing function, but it also increases the eigenfrequency, i.e., it detunes the system. Thus, as mentioned above, the forcing function does no longer conform with the system's eigenfrequency. Regarding a SDOF system, for example, a stiffness increase of Δk leads to a new angular frequency equal to $\omega = \sqrt{(k + \Delta k) / m}$ (cf., equation 6.3).

Structural optimisations with the aim to maximise eigenfrequencies (cf., chapter 4) mainly focus on increasing the 1^{st} (fundamental) eigenfrequency of a system above external exciting frequencies. Although structural adaptations certainly affect all eigenfrequencies and mode shapes, the objective to maximise the 1^{st} eigenfrequency typically leads to the best result.

A small example is given: the 2^{nd} eigenfrequency of a system coincides with the external exciting frequency. An optimisation to maximise the 2^{nd} eigenfrequency is carried out, which also raises the 1^{st} eigenfrequency, so that it matches the exciting frequency. Thus, the resonance phenomeno is not solved. A structural optimisation to increase the 1^{st} eigenfrequency, however, might have increased both the 1^{st} and the 2^{nd} (and also higher-order) eigenfrequencies above the exciting frequency. Hence, the maximisation of the 1^{st} eigenfrequency is widely-used as an optimisation objective.

Regarding the magnet carrier structure (girder) of a synchrotron radiation facility, which is analysed in the chapters 14 and 15, another reason for the performed optimisations to increase the 1^{st} eigenfrequency is that the ground vibration amplitudes decline with increasing frequency. Thus, all systems' eigenfrequencies should be as high as possible, and the most efficient ways to increase all eigenfrequencies is to raise the 1^{st} eigenfrequency, because all higher-order frequencies will also be increased.

In summary, finding the optimal structural design to avoid resonance is of high interest in many technical areas. In this work, it is focused on the eigenfrequency shift of a system owing to structural adaptations.

7

FINITE ELEMENT METHOD

7.1 INTRODUCTION

The majority of structures are very complex, which is why analyses via analytical techniques are not possible. In these cases, numerical analyses are widely used, especially the Finite Element Method (FEM). The FEM is a very useful and accurate method to solve large-scale structural problems involving a high complexity of geometries, load conditions, boundary conditions, material properties, and geometrical and material non-linearity.[137]

The FEM divides a geometric continuum into a finite number of smaller regions (i.e., finite elements) often characterised by simpler geometries than the original structure. Each element is described by a number of points (i.e., nodes), based on which the displacement within an element can be approximated. The approximation results from a linear combination of polynomial functions that have to be differentiated. Thus, as the displacement of an element depends on that of the nodes, only a finite number of differential equations of motion have to been written and solved.[137] The approximate solution of the differential equations of motion can be obtained using the virtual work principle as described below.

It is important to consider that the accuracy of numerical results using the FEM depends on the discretisation of the structural problem: the smaller the finite elements (i.e., the finer the FEM mesh), the higher the accuracy. However, a fine mesh involves a large number of algebraic equations that have to be solved and thus a high computational effort. Usually, mesh studies are carried out to obtain the sufficient element size for a reliable numerical result. Nevertheless, theoretical calculations based on abstracted models and/or experiments are carried out, if possible, to validate the numerical results.

7.2 THEORY OF LINEAR ELASTICITY

The following equations are according to Qu [137], Kienzler and Schröder [80], and Klein [81] and based on linear elastic bodies, whose deformations are small and continuous. Figure 7.1 shows the normal stresses σ and the shear stresses τ of an infinitesimal element within a 3D body.

The elasto-mechanical behaviour of a 3D body can be described using 15 equations.

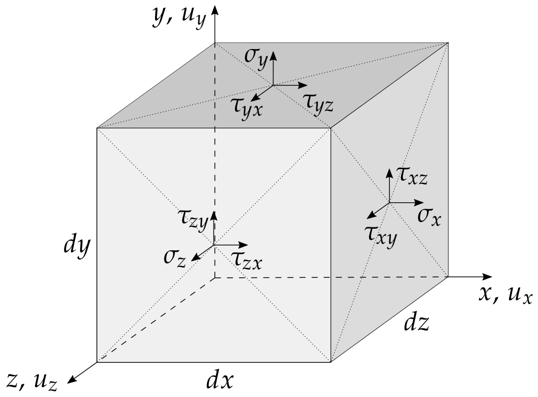

Figure 7.1: Normal (σ) and shear stresses (τ) of an infinitesimal element with edge length of dx, dy, and dz.

The first six equations involve the strain-displacement relationships. The strain vector $\boldsymbol{\varepsilon}$ contains the normal strains ε and the shear strains γ and is obtained by differentiating the displacement vector $\boldsymbol{u}$ that contains the displacement u in the directions x, y, and z. $\boldsymbol{D}$ denotes the differential operator.

$$\boldsymbol{\varepsilon} = \begin{bmatrix} \varepsilon_x \\ \varepsilon_y \\ \varepsilon_z \\ \gamma_{xy} \\ \gamma_{yz} \\ \gamma_{zx} \end{bmatrix} = \begin{bmatrix} \frac{\partial}{\partial x} & 0 & 0 \\ 0 & \frac{\partial}{\partial y} & 0 \\ 0 & 0 & \frac{\partial}{\partial z} \\ \frac{\partial}{\partial y} & \frac{\partial}{\partial x} & 0 \\ 0 & \frac{\partial}{\partial z} & \frac{\partial}{\partial y} \\ \frac{\partial}{\partial z} & 0 & \frac{\partial}{\partial x} \end{bmatrix} \cdot \begin{bmatrix} u_x \\ u_y \\ u_z \end{bmatrix} = \boldsymbol{D} \cdot \boldsymbol{u} \tag{7.1}$$

The following six equations describe the relation between the strain and the stresses (Hooke's law). Considering linear, isotropic material properties characterised by a Youngs modulus E and a Poisson's ratio ν, the stress vector $\boldsymbol{\sigma}$ depends on the elasticity matrix $\boldsymbol{E}$ and the strain vector:

$$\begin{bmatrix} \sigma_x \\ \sigma_y \\ \sigma_z \\ \tau_{xy} \\ \tau_{yz} \\ \tau_{zx} \end{bmatrix} = \boldsymbol{E} \cdot \begin{bmatrix} \varepsilon_x \\ \varepsilon_y \\ \varepsilon_z \\ \gamma_{xy} \\ \gamma_{yz} \\ \gamma_{zx} \end{bmatrix} \tag{7.2}$$

with :

$$\boldsymbol{E} = \frac{E\,(1+\nu)^{-1}}{(1-2\nu)} \begin{bmatrix} 1-\nu & \nu & \nu & 0 & 0 & 0 \\ \nu & 1-\nu & \nu & 0 & 0 & 0 \\ \nu & \nu & 1-\nu & 0 & 0 & 0 \\ 0 & 0 & 0 & \frac{1-2\nu}{2} & 0 & 0 \\ 0 & 0 & 0 & 0 & \frac{1-2\nu}{2} & 0 \\ 0 & 0 & 0 & 0 & 0 & \frac{1-2\nu}{2} \end{bmatrix}$$

Equations 7.1 and 7.2 can be summarised to:

$$\boldsymbol{\sigma} = \boldsymbol{E} \cdot \boldsymbol{\varepsilon} = \boldsymbol{E} \cdot \boldsymbol{D} \cdot \boldsymbol{u} \tag{7.3}$$

The following equations of motion contain the internal stresses of the body and the body forces $\boldsymbol{F_b}$ (e.g., dead load or centrifugal forces) acting on it. The equations are based on Newton's 2^{nd} law of motion.

Note that:
$\tau_{xy} = \tau_{yx}$,
$\tau_{yz} = \tau_{zy}$,
$\tau_{xz} = \tau_{zx}$.

$$\begin{bmatrix} \sigma_x \\ \sigma_y \\ \sigma_z \\ \tau_{xy} \\ \tau_{yz} \\ \tau_{zx} \end{bmatrix} \cdot \begin{bmatrix} \frac{\partial}{\partial x} & 0 & 0 & \frac{\partial}{\partial y} & 0 & \frac{\partial}{\partial z} \\ 0 & \frac{\partial}{\partial y} & 0 & \frac{\partial}{\partial x} & \frac{\partial}{\partial z} & 0 \\ 0 & 0 & \frac{\partial}{\partial z} & 0 & \frac{\partial}{\partial y} & \frac{\partial}{\partial x} \end{bmatrix} + \begin{bmatrix} F_{b,x} \\ F_{b,y} \\ F_{b,z} \end{bmatrix} = \rho \begin{bmatrix} \ddot{u}_x \\ \ddot{u}_y \\ \ddot{u}_z \end{bmatrix} \tag{7.4}$$

$$\rightarrow \quad \boldsymbol{\sigma} \cdot \boldsymbol{D}^T + \boldsymbol{F_b} = \rho \ddot{\boldsymbol{u}}$$

with the transpose of the differential operator $\boldsymbol{D}^T$, the material density ρ and the acceleration vector $\ddot{\boldsymbol{u}}$.

7.3 PRINCIPLE OF VIRTUAL WORK

According to Qu [137] and Klein [81], the principle of virtual work allows the solution of the differential equations of motion (equation 7.4). It states that the total work of internal and external forces, δW_{int} and δW_{ext}, respectively, on an infinitesimal, virtual displacement $\boldsymbol{\delta u}$ is zero, which leads to:

$$\delta W_{int} = \delta W_{ext} \tag{7.5}$$

The internal work is defined as:

$$\delta W_{int} = \int_V \delta \boldsymbol{\varepsilon}^{\mathrm{T}} \cdot \boldsymbol{\sigma} \, \mathrm{d}V \tag{7.6}$$

In figure 7.2, a general 3D body affected by body forces, surfaces forces $\boldsymbol{F_s}$, and concentrated forces $\boldsymbol{F_c}$ is displayed.

The intertia body forces depend on the acceleration vector $\ddot{\boldsymbol{u}}$ and the density ρ. Damping effects are neglected. The external work involves those forces acting on a 3D body characterised by a volume V and a surface S:

$$\delta W_{ext} = \int_V \delta \boldsymbol{u}^{\mathrm{T}} \cdot \boldsymbol{F_b} \,\mathrm{d}V + \int_S \delta \boldsymbol{u}^{\mathrm{T}} \cdot \boldsymbol{F_s} \,\mathrm{d}S + \delta \boldsymbol{u}^{\mathrm{T}} \cdot \boldsymbol{F_c} - \int_V \delta \boldsymbol{u}^{\mathrm{T}} \cdot \rho \ddot{\boldsymbol{u}} \,\mathrm{d}V \tag{7.7}$$

Inserting equations 7.6 and 7.7 into equation 7.5 leads to:

$$\begin{aligned} \int_V \delta \boldsymbol{\varepsilon}^{\mathrm{T}} \cdot \boldsymbol{\sigma} \,\mathrm{d}V = \int_V \delta \boldsymbol{u}^{\mathrm{T}} \cdot \boldsymbol{F_b} \,\mathrm{d}V + \int_S \delta \boldsymbol{u}^{\mathrm{T}} \cdot \boldsymbol{F_s} \,\mathrm{d}S + \delta \boldsymbol{u}^{\mathrm{T}} \cdot \boldsymbol{F_c} \\ - \int_V \delta \boldsymbol{u}^{\mathrm{T}} \cdot \rho \ddot{\boldsymbol{u}} \,\mathrm{d}V \end{aligned} \tag{7.8}$$

The strain vector and the stress vector can be replaced by the relations stated in equations 7.1 and 7.3 and it follows:

$$\begin{aligned} \int_V \delta \boldsymbol{u}^{\mathrm{T}} \cdot \boldsymbol{D}^{\mathrm{T}} \cdot \boldsymbol{E} \cdot \boldsymbol{D} \,\mathrm{d}V \cdot \boldsymbol{u} = \int_V \delta \boldsymbol{u}^{\mathrm{T}} \cdot \boldsymbol{F_b} \,\mathrm{d}V + \int_S \delta \boldsymbol{u}^{\mathrm{T}} \cdot \boldsymbol{F_s} \,\mathrm{d}S \\ + \delta \boldsymbol{u}^{\mathrm{T}} \cdot \boldsymbol{F_c} - \int_V \delta \boldsymbol{u}^{\mathrm{T}} \cdot \rho \ddot{\boldsymbol{u}} \,\mathrm{d}V \end{aligned} \tag{7.9}$$

Equation 7.9 contains the real virtual displacement vector $\boldsymbol{\delta u}$. However, this vector is unknown and will be approximated with the following relation:

$$\delta \boldsymbol{u}^{\mathrm{T}} = \delta \boldsymbol{x_N}^{\mathrm{T}} \cdot \boldsymbol{N}^{\mathrm{T}} \tag{7.10}$$

The tensor of the shape function $\boldsymbol{N}$ is the displacement interpolation between nodes and consists of, e.g., linear or quadratic functions.

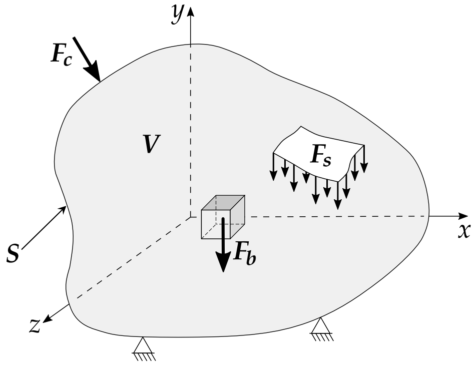

Figure 7.2: External forces acting on a general 3D body (surface S, volume V) including body forces $\boldsymbol{F_b}$, surfaces forces $\boldsymbol{F_s}$, and concentrated forces $\boldsymbol{F_c}$.

$\delta \boldsymbol{x_N}$ denotes the vector of the virtual nodal displacement. Applying the relation to equation 7.9 leads to:

$$\begin{aligned} &\int_V \delta \boldsymbol{x_N}^{\mathrm{T}} \cdot \boldsymbol{N}^{\mathrm{T}} \cdot \boldsymbol{D}^{\mathrm{T}} \cdot \boldsymbol{E} \cdot \boldsymbol{D} \cdot \boldsymbol{N} \, \mathrm{d}V \cdot \boldsymbol{x_N} \\ &= \int_V \delta \boldsymbol{x_N}^{\mathrm{T}} \cdot \boldsymbol{N}^{\mathrm{T}} \cdot \boldsymbol{F_b} \, \mathrm{d}V + \int_S \delta \boldsymbol{x_N}^{\mathrm{T}} \cdot \boldsymbol{N}^{\mathrm{T}} \cdot \boldsymbol{F_s} \, \mathrm{d}S \\ &+ \delta \boldsymbol{x_N}^{\mathrm{T}} \cdot \boldsymbol{N}^{\mathrm{T}} \cdot \boldsymbol{F_c} - \int_V \delta \boldsymbol{x_N}^{\mathrm{T}} \cdot \boldsymbol{N}^{\mathrm{T}} \cdot \rho \boldsymbol{N} \cdot \ddot{\boldsymbol{x}}_{\boldsymbol{N}} \, \mathrm{d}V \end{aligned} \tag{7.11}$$

As this applies to all virtual nodal displacements, the equation can be simplified:

$$\begin{aligned} \int_V (\boldsymbol{D} \cdot \boldsymbol{N})^{\mathrm{T}} \cdot \boldsymbol{E} \cdot (\boldsymbol{D} \cdot \boldsymbol{N}) \, \mathrm{d}V \cdot \boldsymbol{x_N} &= \int_V \boldsymbol{N}^{\mathrm{T}} \cdot \boldsymbol{F_b} \, \mathrm{d}V \\ + \int_S \boldsymbol{N}^{\mathrm{T}} \cdot \boldsymbol{F_s} \, \mathrm{d}S + \boldsymbol{N}^{\mathrm{T}} \cdot \boldsymbol{F_c} &- \int_V \boldsymbol{N}^{\mathrm{T}} \cdot \rho \boldsymbol{N} \cdot \ddot{\boldsymbol{x}}_{\boldsymbol{N}} \, \mathrm{d}V \end{aligned} \tag{7.12}$$

Equation 7.12 contains on the left side a stiffness multiplied with a displacement, on the right side external forces and the inertia body forces. These equilibrium equations of the structure corresponding to the nodal displacement vector $\boldsymbol{x_N}$ and the nodal acceleration vector $\ddot{\boldsymbol{x}}_{\boldsymbol{N}}$ can be rewritten in a concise form as

$$\boldsymbol{M} \cdot \ddot{\boldsymbol{x}}_{\boldsymbol{N}} + \boldsymbol{K} \cdot \boldsymbol{x_N} = \boldsymbol{F} \tag{7.13}$$

$$\text{with :} \quad \boldsymbol{M} = \sum_{n=1}^{N_e} \boldsymbol{M_e} = \sum_{n=1}^{N_e} \int_{V_e} \rho \boldsymbol{N}^{\mathrm{T}} \cdot \boldsymbol{N} \, \mathrm{d}V_e \;\; ;$$

$$\boldsymbol{K} = \sum_{n=1}^{N_e} \boldsymbol{K_e} = \sum_{n=1}^{N_e} (\boldsymbol{D} \cdot \boldsymbol{N})^{\mathrm{T}} \cdot \boldsymbol{E} \cdot (\boldsymbol{D} \cdot \boldsymbol{N}) \, \mathrm{d}V_e \;\; ;$$

$$\boldsymbol{F} = \boldsymbol{F_b} + \boldsymbol{F_s} + \boldsymbol{F_c}$$

Thus, the mass matrix $\boldsymbol{M}$ and the stiffness matrix $\boldsymbol{K}$ are the sum of all element mass matrices $\boldsymbol{M_e}$ and element stiffness marices $\boldsymbol{K_e}$, respectively. N_e denotes the number of elements, V_e the element volume. The force vector $\boldsymbol{F}$ contains the body forces, surface forces, and concentrated forces.

The nodal displacements in equation 7.13 can be obtained by applying iterative solving procedures. Differentiating the numerically determined displacement field leads to the strains and stresses according to the equations in chapter 7.2.

Finally, it may be noted that equation 7.13 conforms with equation 6.42 obtained by analysing a vibration chain-type model, with the exception of the force vector that is not included in the latter. In modal analyses, eigenfrequencies and mode shapes can be determined without applying external forces to the system. Other analyses concerning the vibrational properties, like for example frequency response analyses, do consider external forces (cf., equation 6.38). However, this type of numerical analysis was only once performed within this work to state the conformity of the experimental results with the numerically obtained values (cf., analysis of bio-inspired lattices in chapter 11).

Part III

EIGENFREQUENCY INCREASE INSPIRED BY NATURE

In this part of the dissertation, different studies evaluating the impact of biologically inspired structures and optimisation techniques on the vibration characteristics are studied. The overall objective is to investigate whether eigenfrequencies can be strongly shifted (maximised) using complex structures and optimisation techniques observed in nature. In a final chapter, all studies are compared among each other and to other published methods aiming at an eigenfrequency increase.

8

SHAPE ADAPTATION ACCORDING TO MODE SHAPES

Many different optimisation approaches to maximise eigenfrequencies of various structures have already been published (cf., chapter 4). However, structural optimisations, like topology and shape optimisations, are often time consuming and require high computational effort. In addition, the manufacturing of the optimised structures is often restricted to additive manufacturing, which, however, has become more promising in the last years, but still lacks in reproducibility, high costs and extended production time. Therefore, all mentioned studies led to good results, however, might not be applied in big scale or for low-cost parts. An efficient frequency optimisation method is therefore still in demand.

Adapting the shape according to eigenvectors (mode shapes), as it is apparently present in diatom shells (cf., figure 3.4), has the potential to be such an efficient optimisation technique [34]. In their parametric studies, Da Silva and Nicoletti [34] pre-deformed a Bernoulli beam according to its mode shapes. They concluded that it is possible to influence the n-th eigenfrequency of a beam by changing the beam shape according to its n-th eigenvectors, while all additional frequencies of lower order remain almost unaffected. First indications that the method also applies for plate-like structures was shown in the application to a cab floor [49]. In addition, the results from Lim and Lee [89], who performed a topology optimisation on a simply supported 3D beam to maximise the frequency of the 1st bending mode, indicate that the mode shape adaptation method might also work for 3D structures, because the resulting arch-like structure reminds of the 1st mode shape of an undeformed beam.

This chapter focuses on an extension of the work of Da Silva and Nicoletti [34] by further investigating the potential of the method. The pre-deformations applied to the simply supported beam were strongly increased beyond the values studied by Da Silva and Nicoletti [34] to analyse whether the mode shape adaptation method also applies for large pre-deformations. While Da Silva and Nicoletti only investigated the first three mode shapes, the beam was also pre-deformed according to the 4th and 5th mode shape.

Since Da Silva and Nicoletti [34] solely studied beams and little work has been published regarding the eigenfrequencies of pre-deformed plate-like structures, the mode shape adaptation method was additionally applied to squared plates. Small and large pre-deformations according to mode 1 to 4 were extensively studied.

The here presented study on beams and plates did not only investigate the potential of the mode shape adaptation method to raise single eigenfrequencies, but also studied the possibility to use the proposed pre-deformation method for the maximisation of multiple eigenfrequencies by applying several mode shapes.

8.1 MATERIAL AND METHODS

A slender beam, which has already been studied by Da Silva and Nicoletti [34], and a squared plate were pre-deformed according to their mode shapes. This was performed by conducting parametric studies to investigate the impact of the pre-deformations on the eigenfrequencies.

8.1.1 *Slender Beam*

The beam geometry and material properties were defined in analogy to Da Silva and Nicoletti [34] leading to a 600 x 30 x 3 mm reference beam (figure 8.1) made out of aluminium characterised by the properties listed in table 8.1.

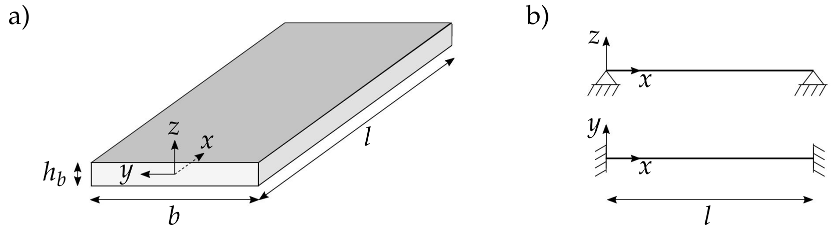

Figure 8.1: Slender reference beam with coordinate system (a) and the defined boundary conditions (b).

Table 8.1: Material properties of aluminium that were considered in the studies.

	Properties
Young's modulus E	69,000 MPa
Density ρ	$2.688 \cdot 10^{-9}$ t mm^{-3}
Poisson's ratio ν	0.34

Axial constraints are inevitable to increase eigenfrequencies by performing the here analysed shape adaptation [34], since the eigenfrequency increase is based on the improved loadbearing capacity (arch effect) resulting from the pre-deformation. Consequently, the beam was simply supported at both ends implying a restriction of all degrees of freedom except for the rotation around the y axis.

A modal analysis to calculate the first six eigenfrequencies and eigenmodes was conducted. The adequate mesh was obtained in a mesh convergence study varying the total number of nodes from 3 to 31. Since beam elements (CBEAM) were defined between two consecutive nodes, the number of beam elements varied from 2 to 30 within the mesh convergence study. A sufficient mesh fineness was reached as soon as the results differed less than 5% from the results of the following three finer meshes. The results were evaluated on the 1st and the 6th eigenfrequency. The numerically obtained results of the undeformed reference beam and the beam pre-deformed according to the 1st mode shape were compared to analytically obtained eigenfrequencies to confirm the plausibility of the numerical simulations.

The eigenfrequencies $f_{n,b}$ of a simply supported Bernoulli beam characterised by Young's modulus E, material density ρ, length l, rectangular cross section area A, and second moment of inertia I, both depending on the beam width b and the beam height h_b, are defined as follows [24]:

$$f_{n,b} = \frac{1}{2\pi} \frac{(n\pi)^2}{l^2} \sqrt{\frac{E\,I}{A\,\rho}} \quad ; \quad n = 1,2,3... \tag{8.1}$$

$$A = b\,h_b \tag{8.2}$$

$$I = \frac{b\,{h_b}^3}{12} \tag{8.3}$$

The n-th bending mode shape in the xz plane $W_{n,b}$ depending on the variable x can be described with the following equation [24]:

$$W_{n,b}(x) = \sin\left(\frac{n\,\pi\,x}{l}\right) \quad ; \quad n = 1,2,3... \tag{8.4}$$

According to Nicoletti [117], the approximation of a sinusoidal arch as a circular arch generates an error smaller than 1% of the length l for l/r ratios smaller than 1, which is valid for all here studied models. Therefore, formulae to calculate the 1st and 2nd eigenfrequency of a circular arch (figure 8.2) that have been published by Den Hartog [38] serve as approximation for sinusoidal beams.

The first two eigenfrequencies $f_{1,a}$ and $f_{2,a}$ can be calculated as follows:

$$f_{1,a} = \frac{1}{2\pi} \sqrt{\frac{1}{r^4} \left[0.82 \left(\frac{r}{\lambda}\right)^2 + \left(\frac{\pi^2}{\alpha^2} - 1\right)^2\right]} \sqrt{\frac{E\,I}{A\,\rho}} \tag{8.5}$$

$$f_{2,a} = \frac{1}{2\pi} \sqrt{\frac{1}{r^4\,\alpha^4} \frac{\alpha^4 - 8\,\pi^2\,\alpha^2 + 16\,\pi^4}{1 + 0.075\,\frac{\alpha^2}{\pi^2}}} \sqrt{\frac{E\,I}{A\,\rho}} \tag{8.6}$$

with the radius r of the arch curvature depending on the arch span length, which is equal to the undeformed beam length l, the arch height h_a, the central angle α (radian), and the slenderness ratio λ_s depending on a rectangular cross section:

$$r = \frac{1}{2\,h_a} \left[\left(\frac{l}{2}\right)^2 + {h_a}^2 \right] \tag{8.7}$$

$$\alpha = 2 \cdot \sin^{-1}\left(\frac{l}{2\,r}\right) \tag{8.8}$$

$$\lambda_s = \frac{I}{A} = \frac{{h_b}^2}{12} \tag{8.9}$$

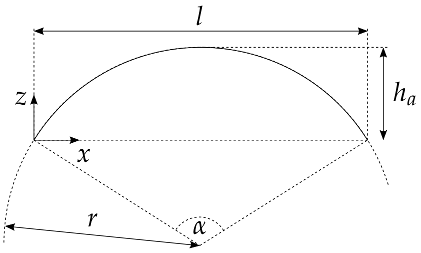

Figure 8.2: Dimensions of a circular arch.

8.1.1.1 *Maximisation of a Specific Eigenfrequency or Mode Shape Frequency*

A pre-deformation according to the 1st, 2nd, 3rd, 4th, and 5th mode shape was applied to the analysed beam. In analogy to Da Silva and Nicoletti [34], a maximum relative pre-deformation δ was defined as the quotient of the maximum pre-deformation of the beam δ_{max} (mm) and the beam height h_b (mm):

$$\delta = \frac{\delta_{max}}{h_b} \tag{8.10}$$

In parametric studies, δ_{max} was varied to analyse maximum relative pre-deformations from 0.0 to 5.0 mm with step sizes of 0.5 mm and from 5.0 to 20.0 mm with step sizes of 5.0 mm. The 5th mode shape showed a 1st transversal (i.e., out-of-plane) bending mode. Consequently, the height considered for the calculation of the maximum relative pre-deformation δ was the beam width b. During the pre-deformation according to mode 5, δ_{max} was varied up to 180 mm, which corresponded to a maximum relative pre-deformation of 6.0.

It may be mentioned that, although the pre-deformation was quite large, the analyses were still linear. The mechanical system, however, was changed considerably. Instead of beams (and plates), arches (and vaults or shells) were investigated. In linear beam theory, the natural eigenfrequencies do not depend on the axial constraint, whereas the axial constraint (hindered horizontal displacements at the ends) becomes essential for arches and shells as the membrane load-bearing capacity increases and so do the eigenfrequencies. Without the horizontal constraint, the frequency change is marginal [34]. Since the span length l was kept constant, the length of the arch changed with increasing pre-deformation. As the aim was to alter eigenfrequencies only due to the structural deformation without changing the mass (and also boundary conditions and material properties), the beam width b was adapted in all calculations to have a constant beam mass of 145 g. If a variation of mass would have been permitted, it would not have been possible to clearly state that the eigenfrequency increases were due to the structural deformations, because mass change would also have strongly manipulated the eigenfrequencies.

During the analyses, the first six eigenfrequencies and the mode shapes were recorded. The resulting eigenfrequencies were always ordered by their value. Consequently, the frequency increase of a specific mode shape can lead to an alternation of the mode shape order. Thus, if the mode shape that was adapted to the beam could not be found within the first six eigenmodes, higher-order mode shapes were searched for the corresponding mode shape.

The results of the parametric studies were compared to the reference beam. The obtained eigenfrequency increase Δf was calculated based on the n-th eigenfrequency f_n and the n-th eigenfrequency of the reference beam $f_{n,ref}$:

$$\Delta f = \frac{f_n - f_{n,ref}}{f_{n,ref}} \cdot 100\% \;\; ; \;\; n = 1, 2, 3, ... \qquad (8.11)$$

Equation 8.11 was also utilised to obtain the increase of specific mode shape frequencies.

8.1.1.2 *Maximisation of Multiple Eigenfrequencies*

The reference beam was pre-deformed according to linear combinations of different mode shapes to analyse whether a simultaneous maximisation of different eigenfrequencies was possible.

The effect of linear combinations of mode 1 and 2, mode 1, 2, and 3, and mode 1, 2, 3, and 4 of the reference beam were tested for maximum relative pre-deformations of 1.0, 3.0, and 5.0. For each beam node, the normalised eigenvectors of the considered mode shapes were added in equal parts.

The resulting sum was normalised to obtain a maximum amplitude of 1, which was multiplied by the maximum relative pre-deformation δ that was analysed. Additionally, weighted linear combinations of mode 1 and mode 2 were investigated considering also maximum relative pre-deformations of 1.0, 3.0, and 5.0. The normalised eigenvectors of mode 1 and mode 2 were multiplied with the factors c and $(1 - c)$, respectively, varying c from 0.0 to 1.0 in step sizes of 0.1. Also here, the sum of the resulting values was normalised and subsequently multiplied with the maximum relative pre-deformation δ. An adaptation of the beam width b permitted a constant beam mass of 145 g in all calculations.

8.1.2 *Squared Plate*

The considered plate was characterised by an edge length a of 100 mm and a constant thickness h_p of 2 mm (figure 8.3). The material properties were set analogue to the slender beam (table 8.1) resulting into a plate mass of 53.76 g. Concerning the boundary conditions, all degrees of freedom were restricted except for the rotations around the x axis for the edges parallel to the x axis, and for the rotations around the y axis for the edges parallel to the y axis. Thus, also here, axial constraints were considered, as otherwise a significant eigenfrequency increase due to the mode shape adaptation would not have been possible [15].

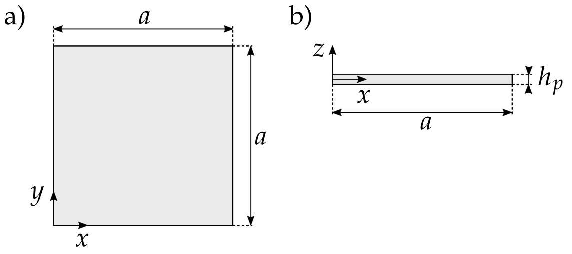

Figure 8.3: Top view (a) and front view (b) of the squared reference plate with coordinate system.

Similar to the investigated beam, a shell mesh convergence study was conducted varying the number of elements per plate edge from 4 to 200 to identify a sufficiently small element size. A modal analysis was performed in order to obtain the first six eigenfrequencies and the corresponding mode shapes.

As the thickness to length ratio of the reference plate was smaller than 10%, the plate could be considered as thin and the classic plate theory of Kirchhoff was applied to calculate the eigenfrequencies analytically [27]. The eigenfrequencies $f_{mn,p}$ of the simply supported, squared plate depend on the plate edge length a, the material density ρ, the plate height h_p and the plate stiffness K, which is based on Young's modulus E, the plate height, the Poisson's ratio ν, and the natural numbers m and n [24]:

$$f_{mn,p} = \frac{\pi}{2\,a^2}\left(m^2 + n^2\right)\sqrt{\frac{K}{\rho\,h_p}} \quad ; \quad m,n = 1,2,3,... \tag{8.12}$$

$$K = \frac{E\,{h_p}^3}{12\,(1-\nu^2)} \tag{8.13}$$

The following equations defined the mode shapes $W_{mn,p}$ of the squared plate:

$$W_{mn,p}(x,y) = \sin\left(\frac{m\,\pi\,x}{a}\right)\sin\left(\frac{n\,\pi\,y}{a}\right) \quad ; \quad m,n = 1,2,3,... \tag{8.14}$$

The reference plate pre-deformed according to mode 1 was alike a spherical shell. Thus, shallow spherical shell theory was used to validate the numerical calculations. Shallow spherical shell theory implies thin shells [27]. These thin shells are characterised by a shell wall length and width of less than 10% of the shell radius, a constant shell thickness, and a shell raise of less than about $1/8^{\text{th}}$ of its lateral dimension. During vibration, these shells deform primarily perpendicular to the shell surface. The eigenfrequencies of a shallow spherical shell $f_{mn,sss}$ can be obtained using the following equations, in which r_{sss} represents the curvature radius and h_{sss} the height of the spherical shell [159]:

$$f_{mn,sss} = \sqrt{{f_{mn,p}}^2 + \frac{1}{4\,\pi^2}\frac{E}{\rho\,{r_{sss}}^2}} \quad ; \quad m,n = 1,2,3,... \tag{8.15}$$

$$r_{sss} = \frac{1}{2\,h_{sss}}\left[\left(\frac{a}{2}\right)^2 + {h_{sss}}^2\right] \tag{8.16}$$

8.1.2.1 *Maximisation of a Specific Eigenfrequency or Mode Shape Frequency*

The plate was pre-deformed according to its first four mode shapes by calculating the z values of 49 regular distributed points on the plate (figure 8.4) using formula 8.14. As the analysed plate eigenmodes show only vertical deformations, the calculated mode shapes $W_{mn,p}$ can be considered as the z values of the distributed points, while the x and y values were like for the undeformed plate. The surface in between the points was interpolated to obtain the pre-deformed plate.

Analogue to the slender beam, the maximum relative pre-deformation δ was defined as the quotient between the maximum pre-deformation of the plate varied from 0.0 to 60 mm and the plate thickness. This time, the plate thickness was adapted to keep a constant mass. The first six eigenfrequencies and the corresponding mode shapes were recorded. If the mode shape that was adapted to the plate could not be found within the first six eigenmodes, higher-order mode shapes were searched for maximum relative pre-deformations of 3.0 and 5.0 to find the corresponding mode shape. The eigenfrequency deviation compared to the reference plate was calculated using formula 8.11.

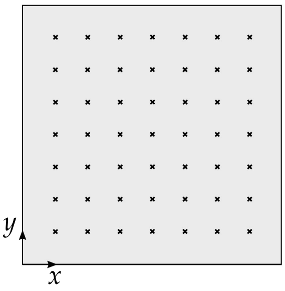

Figure 8.4: Regular distribution of points on the plate that were used for pre-deforming the plate according to its mode shapes.

8.1.2.2 *Maximisation of Multiple Eigenfrequencies*

According to the investigated beam, linear combinations of mode shapes were applied to the reference plate. As already described in the corresponding paragraph about the slender beam, mode 1 and 2 and mode 1, 2, and 3 were equally combined. Also here, weighted combinations of mode 1 and 2 were investigated. Both analyses were performed for maximum relative pre-deformations of 1.0, 3.0, and 5.0. The mesh properties and boundary conditions coincided with the previous investigations.

Figure 8.5 exemplarily shows the squared plate pre-deformed according to the first four mode shapes and a linear combination of the first two and the first three mode shapes. Here, a maximum pre-deformation of 10 mm was considered.

8.2 RESULTS

In the following, the results of the mode shape adaptation method applied to the slender beam and the squared plate are presented.

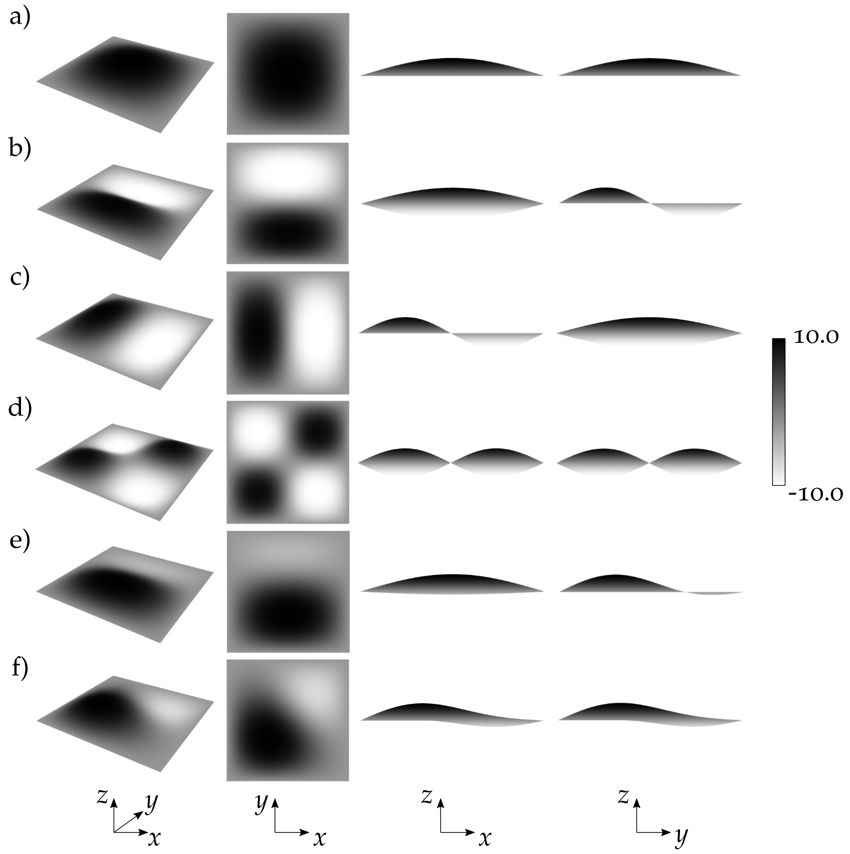

Figure 8.5: Squared plate pre-deformed according to the 1st (a), 2nd (b), 3rd (c), and 4th (d) single bending mode shape. (e) shows the pre-deformation according to a linear combination of the first two mode shapes (50% mode 1 and 50% mode 2) and (f) the linear combination of the first three mode shapes (33% mode 1, 33% mode 2, and 33% mode 3). The pre-deformed plates are displayed in four different views for $\delta = 5.0$ and the colours represent the maximum pre-deformation (mm).

8.2.1 *Slender Beam*

A beam mesh consisting of 24 elements (25 nodes) was chosen to allow the generation of complex beam deformations throughout all simulations, even though the mesh study results showed that the output values had already converged with a coarser mesh and coincided with the analytically obtained values (figure 8.6). The first six mode shapes of the reference beam are shown in figure 8.7. The 1st, 2nd, 3rd, 4th, and 6th mode shapes represented the 1st, 2nd, 3rd, 4th, and 5th bending mode shapes in the xz plane, while the 5th mode shape was the 1st bending mode in the xy plane (1st out-of-plane bending mode, cf., definition of boundary conditions in figure 8.1). Regarding the eigenfrequencies of the circular arch, the theoretical and numerical frequencies of the 1st and the 2nd mode coincided very well (figure 8.8).

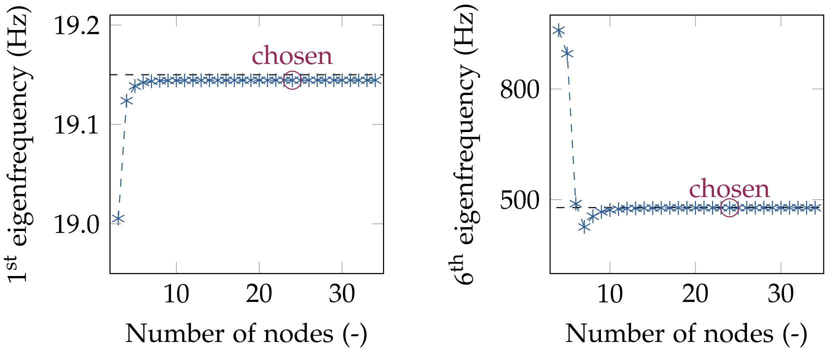

(a) 1st eigenfrequency (b) 6th eigenfrequency

Figure 8.6: Results of the beam mesh study involving the 1st (a) and the 6th (b) eigenfrequency depending on the number of nodes. The dashed black lines represent the analytically obtained results using Bernoulli beam theory. The red circled data points indicate the chosen mesh properties, which allowed the generation of complex beam pre-deformations in all simulations.

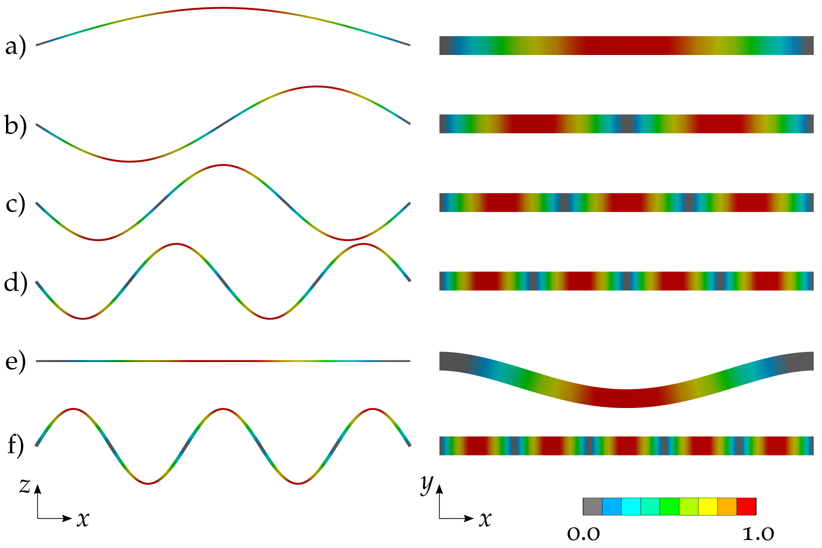

Figure 8.7: 1st (a), 2nd (b), 3rd (c), 4th (d), 5th (e), and 6th (f) bending mode shape of the analysed beam in the xz and the xy plane. The colours represent the absolute normalised vibration amplitude.

8.2.1.1 *Maximisation of a Specific Eigenfrequency or Mode Shape Frequency*

Shaping the beam according to the 1st, 2nd, 3rd, and 4th bending mode shape resulted in a strong increase of the eigenfrequency connected to the corresponding mode shape. Figure 8.9 shows exemplarily the first six eigenfrequencies of the beam pre-deformed according to the 3rd and 4th bending mode shape, while the results for the 1st and 2nd bending mode shape adaptation are attached in the appendix chapter A.1. Lower-order frequencies remained con-

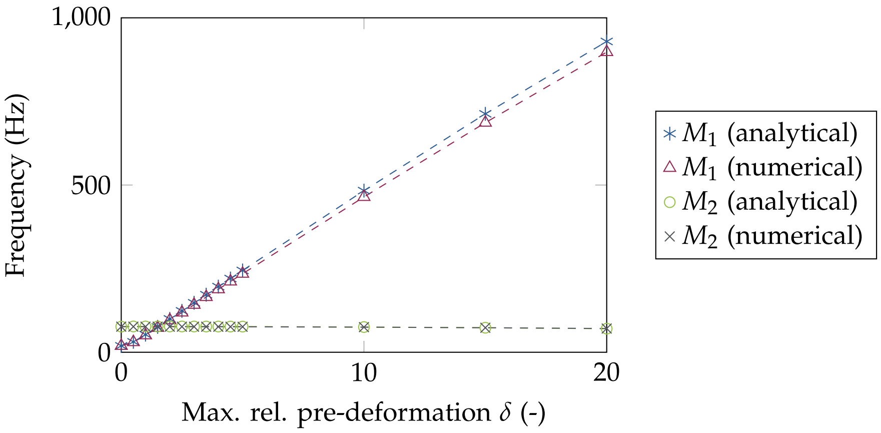

Figure 8.8: 1st and 2nd mode shape frequency of the beam pre-deformed according to the bending mode 1 for different maximum relative pre-deformations. The analytically obtained values are based on formulae for circular arches published by Den Hartog [38].

stant, also for higher maximum relative pre-deformations. However, higher-order frequencies mostly decreased slightly with increasing maximum relative pre-deformation. Especially the frequency of the 5th mode shape (i.e., 1st bending mode in the *xy* plane) strongly decreased with increasing maximum relative pre-deformation for all beam pre-deformations.

It may be reminded that the beam width was decreased with raising maximum relative pre-deformation to have a constant beam mass. Thus, the 5th mode shape frequency was certainly affected by the beam width adaptation. In addition, the boundary conditions varied for the 5th mode shape in comparison to the first four bending mode shapes in the *xz* plane (cf., figure 8.1).

Regarding the 5th mode adaptation, however, the corresponding eigenfrequency first increased and later decreased with increasing maximum relative pre-deformation (figure 8.10). The other recorded eigenfrequencies remained constant or decreased slightly.

In summary, a maximum relative pre-deformation of 5.0 already resulted in a frequency increase of a specific mode shape of more than 1,000% for a shape adaptation of the beam according to the 1st, 2nd, 3rd, and 4th bending mode shape. Maximum relative pre-deformation of 20.0 generated frequency increases of more than 4,000% for pre-deformations according to mode 1 and 2 and of more than 2,000% for mode 3 and 4. However, shaping the beam according to the 5th mode shape increased the corresponding eigenfrequency only by 164% for a maximum relative pre-deformation of 5.0.

The investigated methods to increase specific eigenfrequencies raised the targeted eigenfrequencies in almost all analyses, as shown in table 8.2. Only by shaping the beam according to the 4th mode

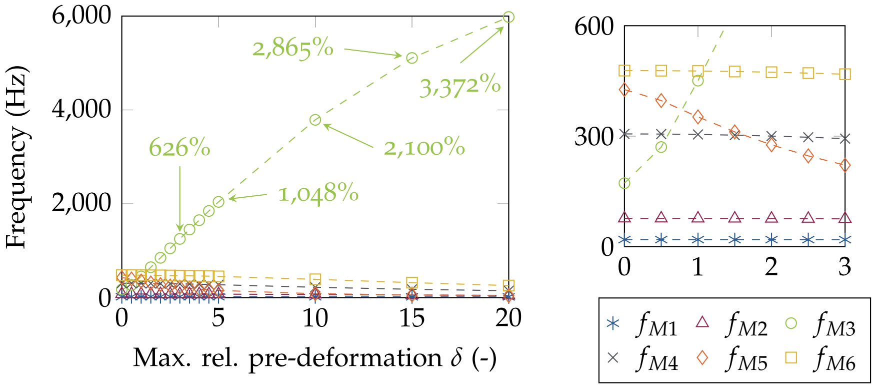

(a) Beam pre-deformation according to mode 3

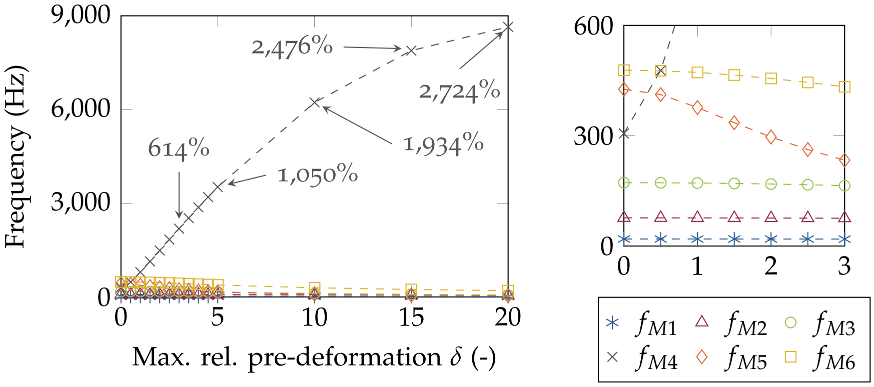

(b) Beam pre-deformation according to mode 4

Figure 8.9: Frequencies of the first six bending mode shapes of the slender beam depending on the maximum relative pre-deformation according to mode 3 (a) and mode 4 (b). For some data points, the frequency increase of the 3rd and 4th bending mode shape compared to the reference beam is given. A magnified view of the lower right corner of both diagrams involving small pre-deformations δ of 0 - 5 and low frequencies of 0 - 600 Hz is given on the right-hand side of the figure.

shape, a decrease of all six eigenfrequencies with strongest decrease for the 4th eigenfrequency was present. In addition, the eigenfrequencies not targeted were also altered (i.e., decreased or increased) by 8% to 28% applying maximum relative pre-deformations of 3.0.

Comparing the obtained frequency changes corresponding to a specific mode, all results showed highest frequency increase for the targeted mode shape (table 8.2). The increase varied from 614% for the frequency of the 4th bending mode shape to 641% for the frequency of the 1st bending mode shape for the mode shape adaptation method considering a maximum relative pre-deformation of 3.0. The mode shape frequencies which were not targeted changed between 1% and 12% in average.

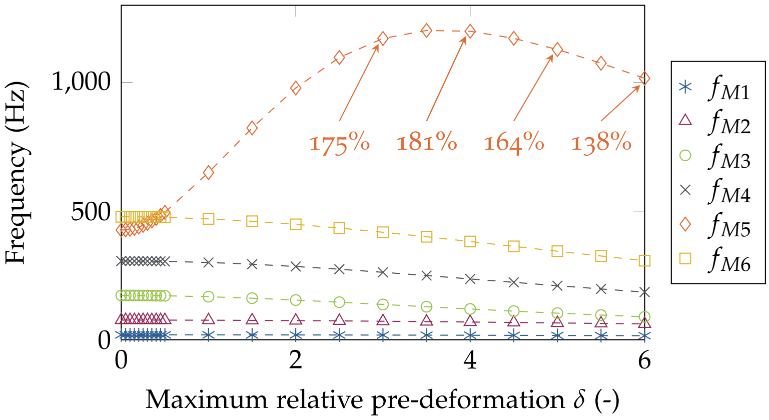

Figure 8.10: Frequencies of the first six bending mode shapes of the slender beam depending on the maximum relative pre-deformation according to mode 5 (1st bending mode shape in the xy plane). For some data points, the mode 5 frequency increase compared to the reference beam is given.

Table 8.2: Eigenfrequency changes compared to the reference beam due to the mode shape adaptation method, which was applied to the slender beam considering a maximum relative pre-deformation of 3.0, are displayed in (a). The alterations of the frequencies connected to specific mode shapes (M_n) are shown in (b). The average absolute values of the deviations of eigenfrequencies that were not targeted are given. All targeted eigenfrequencies or mode shapes are shown in bold numbers.

a)	Max. f_1	Max. f_2	Max. f_3	Max. f_4
f_1	**299%**	0%	-1%	-1%
f_2	85%	**122%**	-1%	-1%
f_3	0%	76%	**28%**	-5%
f_4	0%	36%	-4%	**-24%**
f_5	-5%	11%	10%	-23%
f_6	0%	15%	42%	-9%
Deviation	18%	28%	12%	8%

b)	Max. f_1	Max. f_2	Max. f_3	Max. f_4
M_1	**641%**	0%	-1%	-1%
M_2	0%	**636%**	-1%	-1%
M_3	0%	-1%	**626%**	-5%
M_4	0%	-1%	-4%	**614%**
M_5	-5%	-3%	-48%	-45%
M_6	0%	-1%	-2%	-9%
Deviation	1%	1%	11%	12%

8.2.1.2 *Maximisation of Multiple Eigenfrequencies*

Pre-deforming the reference beam according to a single mode shape led to high frequency increases of the considered mode shape, whereas the frequencies of the other mode shapes only differed slightly (table 8.3). This trend was also observed for combinations of the different mode shapes.

By shaping the reference beam according to a combination of the bending modes 1 and 2, only the frequencies of both considered mode shapes increased, while the frequencies of the other mode shapes remained almost constant. This also applied for the combinations of mode 1, 2, and 3 and of mode 1, 2, 3, and 4, however, the former also resulted in a raise of the 4th bending mode frequency for a maximum relative pre-deformation of 1.0. In all analysed mode combinations,

Table 8.3: Frequency deviations of the first four bending mode shapes compared to the reference beam for different maximum relative pre-deformations δ according to the 1st, 2nd, 3rd, and 4th single mode shapes and combinations of these four mode shapes.

	100% Mode 1				100% Mode 2			
δ	M_1	M_2	M_3	M_4	M_1	M_2	M_3	M_4
1.0	165%	0%	0%	0%	0%	164%	0%	0%
3.0	641%	0%	0%	0%	0%	636%	-1%	-1%
5.0	1,126%	0%	0%	0%	-1%	1,110%	-3%	-2%

	100% Mode 3				100% Mode 4			
δ	M_1	M_2	M_3	M_4	M_1	M_2	M_3	M_4
1.0	0%	0%	162%	0%	0%	0%	-1%	159%
3.0	-1%	-1%	626%	-4%	-1%	-1%	-5%	614%
5.0	-2%	-4%	1,084%	-10%	-3%	-4%	-12%	1,050%

	50% Mode 1, 50% Mode 2				33% Mode 1, 33% Mode 2, 33% Mode 3			
δ	M_1	M_2	M_3	M_4	M_1	M_2	M_3	M_4
1.0	27%	73%	0%	0%	16%	21%	55%	15%
3.0	36%	338%	0%	0%	21%	29%	277%	-1%
5.0	37%	616%	-1%	-1%	20%	29%	509%	-3%

	25% Mode 1, 25% Mode 2, 25% Mode 3, 25% Mode 4			
δ	M_1	M_2	M_3	M_4
1.0	10%	12%	15%	32%
3.0	14%	18%	23%	190%
5.0	14%	17%	24%	362%

the frequencies of the highest order mode shapes always increased most.

Pre-deforming the reference beam according to weighted combinations of the bending modes 1 and 2 led to different results for varying relative maximum pre-deformations (figure 8.11). For $\delta = 1.0$, the highest sum of the 1^{st} and 2^{nd} eigenfrequency was obtained by pre-deforming the beam according to 20% of bending mode 1 and 80% of bending mode 2, for $\delta = 3.0$ by 80% of bending mode 1, and 20% of bending mode 2, and for $\delta = 5.0$ by 100% of bending mode 1 and 0% of bending mode 2.

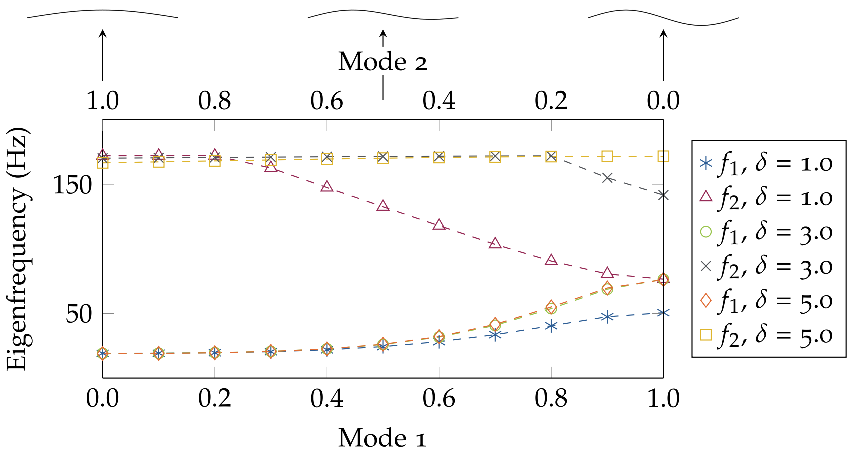

Figure 8.11: 1^{st} and 2^{nd} eigenfrequency of the beam shaped with a maximum relative pre-deformation δ of 1.0, 3.0, and 5.0 according to weighted combinations of the bending modes 1 and 2. Three beam shapes are exemplarily shown for $\delta = 10.0$. The trends of the 1^{st} eigenfrequencies for $\delta = 3.0$ and $\delta = 5.0$ almost coincided.

8.2.2 *Squared Plate*

The mesh size study indicated the sufficiency of an element edge size of 16.6 mm to obtain correct values for the 1^{st} and 6^{th} eigenfrequency (figure 8.12). However, a finer mesh with an element edge size of 1 mm and a total of 10.000 CQUAD4 elements was used to picture the mode shapes correctly. The bending mode shapes of the reference plate are shown in figure 8.13. The comparison between the numerical and analytical results for the plate shaped according to the 1^{st} bending mode shape showed good coincidence (figure 8.14).

8.2.2.1 *Maximisation of a Specific Eigenfrequency or Mode Shape Frequency*

The pre-deformations of the reference plate implied adaptations of the plate thickness to ensure a constant mass. Table 8.4 lists the decreased plate thicknesses dependent on the maximum pre-deforma-

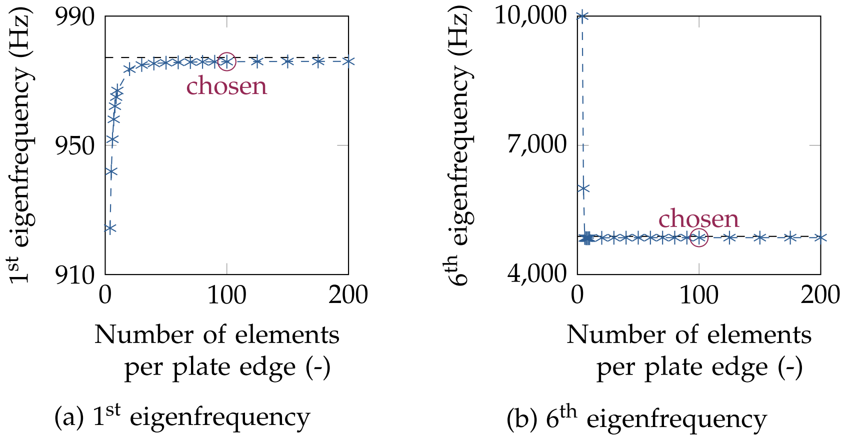

(a) 1st eigenfrequency (b) 6th eigenfrequency

Figure 8.12: Results of the plate mesh study involving the 1st (a) and the 6th (b) eigenfrequency depending on the number of elements per plate edge. The dashed black lines represent the analytically obtained results using the classic plate theory of Kirchhoff. The red circled data points indicate the chosen mesh properties.

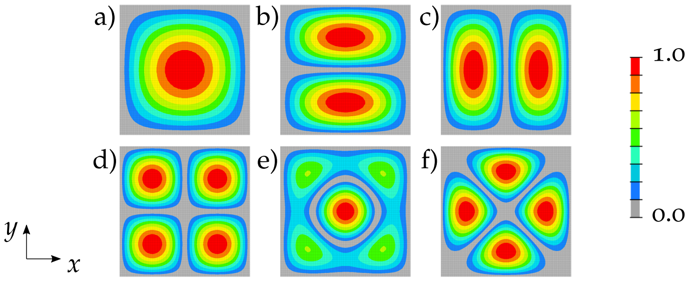

Figure 8.13: 1st (a), 2nd (b), 3rd (c), 4th (d), 5th (e), and 6th (f) bending mode shape of the reference plate. The colours represent the absolute normalised vibration amplitude.

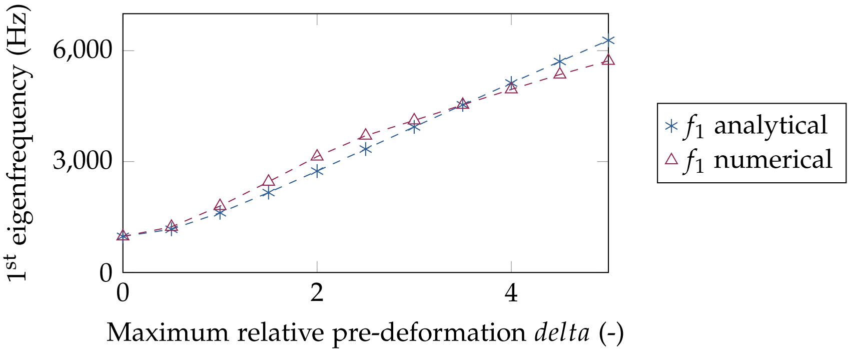

Figure 8.14: Analytically and numerically obtained 1st eigenfrequency of the reference plate shaped according to the 1st bending mode shape depending on different maximum relative pre-deformations. The analytical solutions were calculated using classic plate theory of Kirchhoff for $\delta = 0.0$ (equation 8.12) and shallow spherical shell theory for $\delta > 0.0$ (equation 8.15).

Table 8.4: Plate thickness h_p and maximum relative pre-deformations δ for the reference plate and the plates shaped according to the 1st, 2nd, 3rd, and 4th bending mode shape based on different maximum pre-deformations δ_{max}.

		Max. pre-deformation δ_{max} (mm)			
		0.0	6.0	10.0	40.0
Reference	h_p (mm)	2.0000	2.0000	2.0000	2.0000
	δ (-)	0.0	3.0	5.0	20.0
Max. f_1	h_p (mm)	2.0000	1.9843	1.9573	1.5392
	δ (-)	0.0	3.0	5.1	26.0
Max. f_2 / f_3	h_p (mm)	2.0000	1.9680	1.9154	1.3063
	δ (-)	0.0	3.0	5.2	30.6
Max. f_4	h_p (mm)	2.0000	1.9579	1.8897	1.1852
	δ (-)	0.0	3.1	5.3	33.7

tions δ_{max}. According to equation 8.10, the maximum relative pre-deformation depended on the plate thickness. Therefore, the plate thickness adaptations altered the maximum relative pre-deformation. As a result, a maximum pre-deformation of, for example, 40 mm according the 1st mode shape implied a maximum relative pre-deformation of 26.0, while the corresponding value for the 4th mode shape adaptation was 33.7 due to the reduced plate thickness (cf., table 8.4).

Pre-deforming the reference plate according to its 1st bending mode shape resulted at first in an increase of all considered eigenfrequencies (figure 8.15), which decreased after a maximum relative pre-deformation of 14.7 for the 1st and 6th eigenfrequency and 10.8 for the remaining eigenfrequencies. At its highest peak, the 1st eigenfrequency increased by 606% compared to the reference plate.

Figure 8.15 shows how the order of the first six bending mode shapes changed with increasing pre-deformation of the plate. The 1st bending mode shape frequency was increased by 488% at $\delta = 4.1$. In regard to higher maximum relative pre-deformations, this mode shape could not be found anymore within the first 50 mode shapes. For a maximum relative pre-deformation of 5.1, the 1st mode shape of the pre-deformed plate coincided with the 6th bending mode shape of the reference plate. The 2nd, 3rd, and 4th bending mode shapes were still present up to a maximum relative pre-deformation of 5.1.

Shaping the reference plate according to its 2nd or 3rd bending mode shape led to the same results (figure 8.16). Similar to the plate adaptation according to its 1st bending mode shape, all analysed eigenfrequencies first increased and then decreased with increasing maximum relative pre-deformation. At their highest peaks at a maximum relative pre-deformation of 11.6 for the 2nd and at 5.2 for the

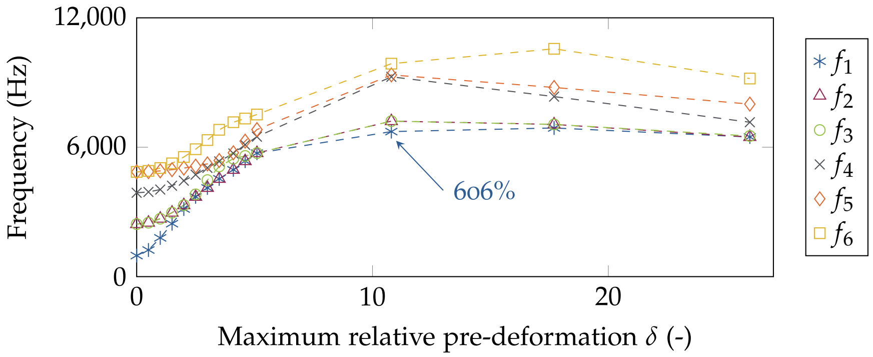

(a) Plate pre-deformation according to mode 1: Eigenfrequencies

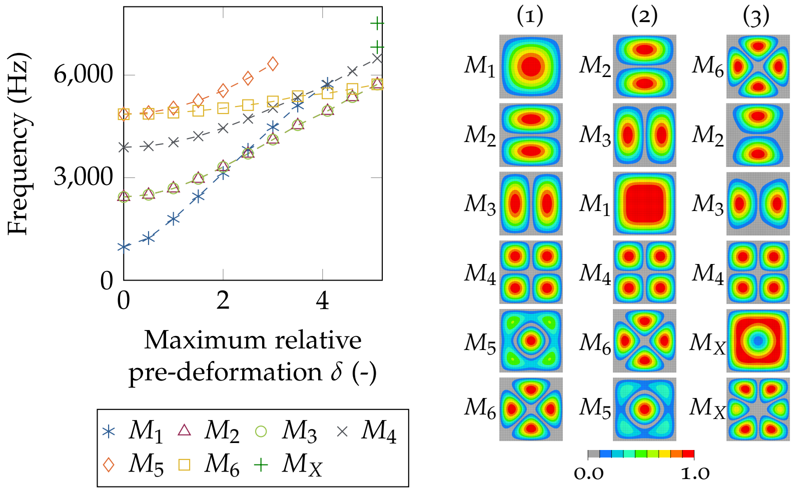

(b) Plate pre-deformation according to mode 1: Mode shape frequencies

(c) First six mode shapes for maximum relative pre-deformations of 0.0 (1), 3.0 (2), and 5.1 (3).

Figure 8.15: Eigenfrequencies (a) and frequencies of the different mode shapes (b) of the squared plate pre-deformed according to its 1st bending mode shape depending on different maximum relative pre-deformations. The highest 1st eigenfrequency increase is given. In b), mode shapes, which are not among the first six bending mode shapes of the reference plate, are named 'Mode X'. For δ = 0.0, 3.0, and 5.1, the mode shapes plotted in b) are displayed in c) (top view). They are ordered in ascending frequency values. The colours represent the absolute normalised vibration amplitude.

3rd eigenfrequency, the eigenfrequencies increased by 159% and 233%, respectively. Regarding the mode shapes, only the 1st bending mode shape did not change order until a maximum relative pre-deformation of 5.2, while the frequencies of the other studied mode shapes exceeded each other and thus led to alterations in the mode shape order. The 2nd bending mode shape was found among the first 50 mode shapes up to a maximum relative pre-deformation of 3.1 with 12,237 Hz, whereas the 3rd bending mode shape could be identified

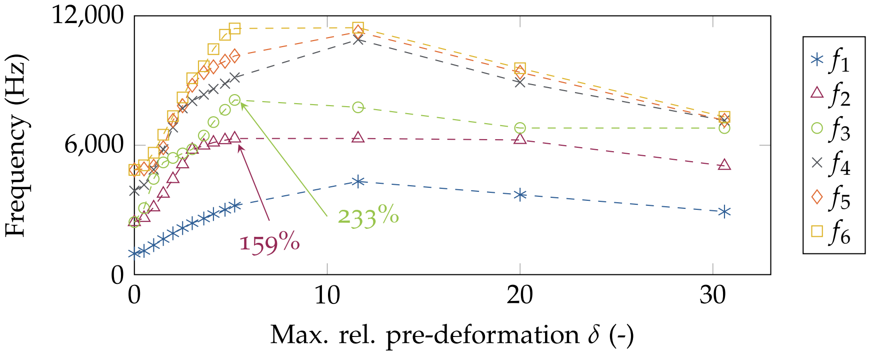

(a) Plate pre-deformation according to mode 2/3: Eigenfrequencies

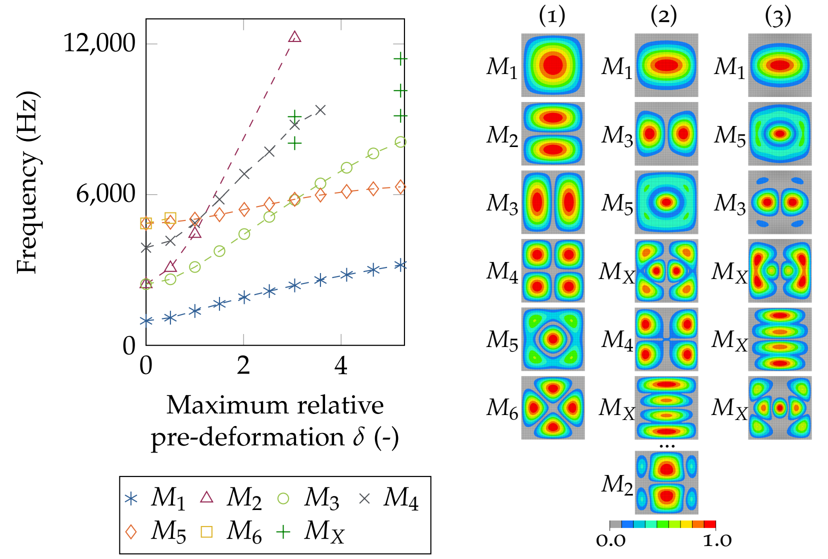

(b) Plate pre-deformation according to mode 2/3: Mode shape frequencies

(c) First six mode shapes for maximum relative pre-deformations of 0.0 (1), 3.1 (2), and 5.2 (3).

Figure 8.16: Eigenfrequencies (a) and frequencies of the different mode shapes (b) of the squared plate pre-deformed according to its 2nd or 3rd bending mode shape depending on different maximum relative pre-deformations. For both the 2nd and the 3rd eigenfrequency, the highest increases are given. In b), mode shapes, which are not among the first six bending mode shapes of the reference plate, are named 'Mode X'. For δ = 0.0, 3.1, and 5.2, the mode shapes plotted in b) are displayed in c) (top view). They are ordered in ascending frequency values. The colours represent the absolute normalised vibration amplitude.

up to a maximum relative pre-deformation of 5.2 showing only minor shape changes. Thus, the frequency of the 2nd bending mode shape increased by 402% at δ = 3.1 and the frequency of the 3rd bending mode shape by 233% at δ = 5.2.

A plate shape adaptation according to the 4th bending mode shape (figure 8.17) resulted in eigenfrequency plots similar to those obtained with the pevious shape adaptations in regard to the initial eigen-

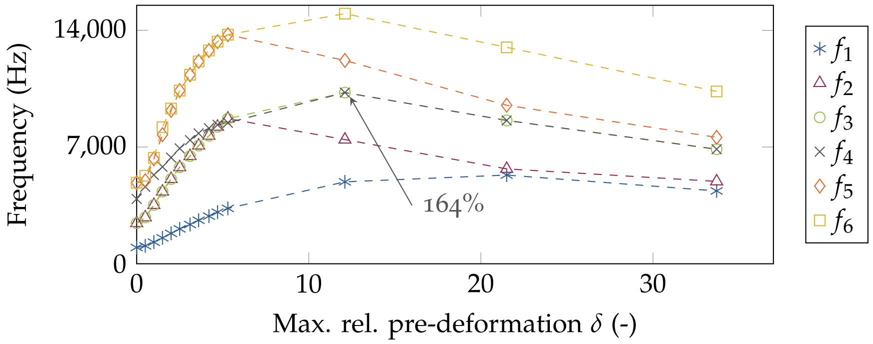

(a) Plate pre-deformation according to mode 4: Eigenfrequencies

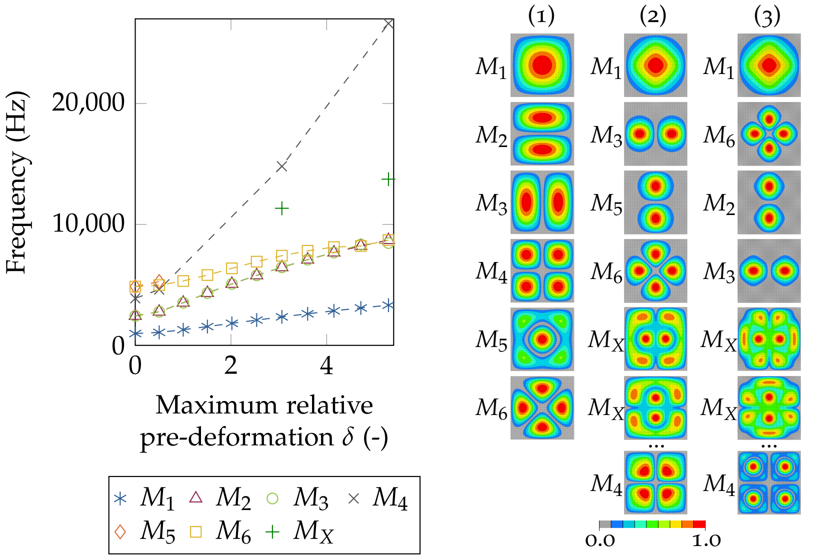

(b) Plate pre-deformation according to mode 4: Mode shape frequencies

(c) First six mode shapes for maximum relative pre-deformations of 0.0 (1), 3.1 (2), and 5.3 (3).

Figure 8.17: Eigenfrequencies (a) and frequencies of the different mode shapes (b) of the squared plate pre-deformed according to its 4th bending mode shape depending on different maximum relative pre-deformations. The highest 4th eigenfrequency increase is given. In b), mode shapes, which are not among the first six bending mode shapes of the reference plate, are named 'Mode X'. For δ = 0.0, 3.1, and 5.3, the mode shapes plotted in b) are displayed in c) (top view). They are ordered in ascending frequency values. The colours represent the absolute normalised vibration amplitude.

frequency increase and the decrease in all eigenfrequencies with increasing maximum relative pre-deformations. The 4th eigenfrequency reached its highest peak at a maximum relative pre-deformation of 12.1 showing an eigenfrequency increase of 164% compared to the reference plate. The 4th bending mode shape was found within the first 50 mode shapes up to a maximum relative pre-deformation of 5.3

and its frequency reached 26,612 Hz resulting in a frequency increase of 584% compared to the reference plate.

In summary, the mode shape adaptation method resulted in high eigenfrequency increases by pre-deforming a plate vertically by a maximum of 10% of the plate edge length (table 8.5). The applied plate pre-deformations led not only to an increase of the targeted eigenfrequency, but also to an increase of all other eigenfrequencies by 87% to 224% on average. An exclusive increase of the targeted eigenfrequency was not possible. While the objective to maximise the 1st and 3rd eigenfrequency resulted in the highest increase of the targeted eigenfrequency, pre-deforming the plate according to the 2nd or 4th bending mode shape resulted in highest raise of an eigenfrequency that was not targeted. However, the targeted eigenfrequencies also increased significantly.

Table 8.5: Eigenfrequency deviations compared to the reference plate for the eigenvector approach to increase the 1st, 2nd, 3rd, and 4th eigenfrequency for a maximum pre-deformation δ_{max} of 10.0 mm. The frequency which increased most is shown in bold numbers.

	Max. f_1	Max. f_2	Max. f_3	Max. f_4
f_1	**487%**	228%	228%	240%
f_2	135%	159%	159%	**257%**
f_3	135%	**233%**	**233%**	**257%**
f_4	67%	135%	135%	118%
f_5	40%	109%	109%	183%
f_6	55%	135%	135%	183%
Deviation	87%	168%	153%	224%

8.2.2.2 *Maximisation of Multiple Eigenfrequencies*

The plate pre-deformation according to linear combinations of the 1st, 2nd, and 3rd bending mode shape resulted in frequency raises for all analysed eigenfrequencies (table 8.6). However, while a plate adaptation according to the bending mode 1 caused highest increase for the 1st eigenfrequency, the plate pre-deformations according to higher-order mode shapes did not always raise the targeted eigenfrequencies most. Both the linear combination of the bending modes 1 and 2 and of the bending modes 1, 2, and 3 resulted in high eigenfrequency increases for the 1st, 2nd, and 3rd eigenfrequency, while the 4th eigenfrequency rose less. It has to be noted that due to symmetry, a linear combination of the bending modes 1 and 3 caused the same results as the linear combination of the bending modes 1 and 2.

Next to the linear combinations, the weighted combinations of the bending modes 1 and 2 were also considered. The results of figure 8.18 indicated that the highest eigenfrequency increase for the 1st eigenfrequency appeared at a full plate adaptation according to

Table 8.6: Frequency deviations of the first four eigenfrequencies compared to the reference plate for different maximum relative pre-deformations δ according to the 1st, 2nd, and 3rd single bending mode shapes and combinations of these mode shapes. The highest increase is shown in bold numbers.

	100% Mode 1				100% Mode 2			
δ	f_1	f_2	f_3	f_4	f_1	f_2	f_3	f_4
1.0	**84%**	10%	10%	4%	40%	28%	**82%**	25%
3.0	**322%**	69%	84%	30%	**145%**	138%	139%	107%
5.0	**487%**	135%	135%	67%	228%	159%	**233%**	135%

	100% Mode 3				50% Mode 1, 50% Mode 2			
δ	f_1	f_2	f_3	f_4	f_1	f_2	f_3	f_4
1.0	40%	28%	**82%**	25%	31%	13%	**40%**	11%
3.0	**145%**	138%	139%	107%	103%	68%	**125%**	66%
5.0	228%	159%	**223%**	135%	**181%**	132%	141%	96%

	33% Mode 1, 33% Mode 2, 33% Mode 3			
δ	f_1	f_2	f_3	f_4
1.0	28%	14%	**46%**	13%
3.0	99%	76%	**120%**	69%
5.0	**169%**	137%	141%	115%

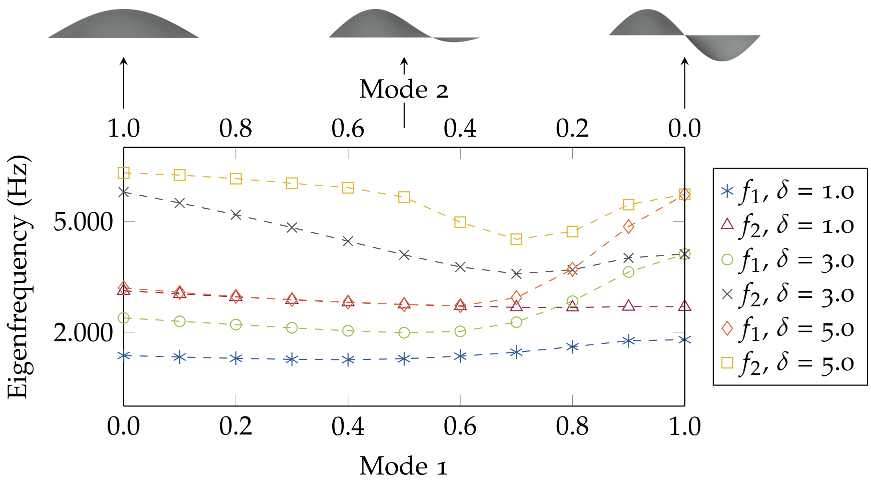

Figure 8.18: 1st and 2nd eigenfrequency of the plate pre-deformed with a maximum relative pre-deformation δ of 1.0, 3.0, and 5.0 according to weighted combinations of the bending modes 1 and 2. Three plate shapes are exemplarily shown for δ = 10.0.

the bending mode 1 for all considered maximum pre-deformations. With increasing influence of the 2nd bending mode, the 1st eigenfrequency decreased, but rose again after a certain ratio. A similar trend could also be observed for the bending mode 2, where highest values of the 2nd eigenfrequency appeared at the complete plate adaptation according to the bending mode 2. The eigenfrequency minima appeared for the 1st eigenfrequency at c values of 0.4, 0.5, and 0.6 for maximum relative pre-deformations of 1.0, 3.0, and 5.0, respectively. The 2nd eigenfrequency was minimised at c values of 0.8, 0.7, and 0.7 for maximum relative pre-deformations of 1.0, 3.0, and 5.0. The factor c symbolises the ratio of mode 1 as described in the corresponding sub-chapter about the slender beam.

8.3 DISCUSSION

8.3.1 *Slender Beam*

The numerical results obtained by using the defined sufficient mesh fineness coincided very well with the analytical results and are thus plausible.

8.3.1.1 *Maximisation of a Specific Eigenfrequency or Mode Shape Frequency*

The investigated method to increase specific eigenfrequencies by shaping the beam according to the corresponding mode shape led to high increases of the targeted 1st, 2nd, 3rd, and 4th eigenfrequencies. The results for small maximum relative pre-deformations according to the 1st, 2nd, and 3rd bending mode shape coincided very well with the results obtained by Da Silva and Nicoletti [34] indicating an exclusive increase of the targeted mode shape frequency, while especially lower-order eigenfrequencies remained constant. Similar results were obtained by shaping the beam according to the 4th bending mode shape. Among all investigated mode shape adaptations, highest frequency increase of up to 4,589% compared to the reference beam was achieved for the 1st bending mode by shaping the beam according to the targeted mode shape ($\delta = 20.0$). The pre-deformed beam corresponded to an arch, in which uniformly distributed transversal compressive forces lead exclusively to normal forces, as shear forces and bending moments disappear. This causes a high stiffness and thus high eigenfrequencies. However, this was only possible due to the axial (horizontal) constraint of the beam. In addition, Nicoletti [117] stated that the beam eigenfrequency increases are due to an energy transfer from longitudinal waves to transverse waves. This energy transfer only occurs when axial strain is defined at the boundaries, which is why the axial constraints are essential for the mode shape adaptation method to significantly raise the eigenfrequencies.

It has been stated that as soon as a beam receives a curved shape, the 1st mode shape becomes extensional implying high tangential displacement [38]. The 2nd mode shape, however, remains as a non-extensional mode characterised by a radial displacement. For small angles α, which imply small maximum relative pre-deformations, the extensional 1st mode shape has a lower frequency than the non-extensional 2nd mode shape [38]. However, the 1st mode shape frequency rises fast with increasing pre-deformation, so that relatively small pre-deformations caused already a mode order switch between the 1st and the 2nd mode, which could also be observed in the here analysed beam. The extensional energy is larger than the flexural energy, which is why the 1st mode shape frequency increases strongly with increasing maximum relative pre-deformation.

Regarding maximum relative pre-deformations larger than 5.0, variations (especially decreases) of not targeted eigenfrequencies were registered, which was not shown by Da Silva and Nicoletti [34]. At the same time, higher pre-deformations allowed an additional, very high frequency increase of the targeted mode shape.

A special role played the 5th mode shape, i.e., the 1st out-of-plane bending mode (1st bending mode in the xy plane). For all mode shape pre-deformations applied to the beam, the 5th mode shape frequency decreased strongly with increasing maximum relative pre-deformation. Since conservation of the beam mass was obtained by adapting, i.e., reducing the beam width, the out-of-plane bending stiffness $Eb^3h_b/12$ was continuously reduced with higher pre-deformations. Thus, the beam became weaker in the xy plane and the corresponding frequency was reduced strongly independent of the applied pre-deformation of the in-plane bending mode. Also the defined boundary conditions had a strong impact on the 5th mode shape frequency. As rotations around the z axis were prevented, the 5th mode shape was similar to a 1st in-plane bending mode shape of a clamped-clamped beam. It has been shown that this boundary condition results only in a small increase of the targeted eigenfrequency compared to a beam simply supported at both ends [34]. Consequently, regarding the 5th mode adaptation, the corresponding frequency first increased (arch effect) slightly (boundary condition) and later decreased (stiffness reduction) with increasing maximum relative pre-deformation.

Recently, an extension of the work from Da Silva and Nicoletti [34] has been published analysing the impact of applying linearised mode shapes instead of the complex, curved mode shapes. Nicoletti [116] showed that the pre-deformation of a slender beam according to a linearised (simplified) mode shape, which does not show any curvatures, still raised the corresponding eigenfrequency. However, the eigenfrequency increase was less strong and other beam eigenfrequencies were also significantly affected, even for small maximum relative pre-deformations.

In summary, shaping the beam according to its mode shapes is an efficient way to strongly increase the frequency of a specific mode shape, while the frequencies of the other mode shapes only differ slightly. It has to be noted, however, that the occurrence of mode order switching and multiple (repeated) eigenfrequencies due to the applied pre-deformations is possible.

8.3.1.2 *Maximisation of Multiple Eigenfrequencies*

Beam pre-deformations according to linear combinations of mode shapes are an efficient method to increase the frequencies of various mode shapes simultaneously. Shaping the beam according to its 3rd bending mode shape, for example, increased the corresponding frequency strongly, while the frequencies of the other analysed mode shapes remained constant or decreased insignificantly. Pre-deformations according to a linear combination of the 1st, 2nd, and 3rd bending mode shape, however, increased all three corresponding frequencies, while the frequency of the 4th bending mode shape changed only slightly. The weighted combinations of the bending modes 1 and 2 showed that the highest sum of the 1st and the 2nd eigenfrequency was obtained by shaping the beam according to either only the 1st or only the 2nd bending mode shape depending on the maximum relative pre-deformation.

8.3.2 *Squared Plate*

As for the analysed beam, the chosen mesh properties led to numerical results that corresponded to the analytical results for maximum relative pre-deformations up to 5.0. Higher pre-deformations were not calculated analytically, as the shell theory only applies for shallow shells.

8.3.2.1 *Maximisation of a Specific Eigenfrequency or Mode Shape Frequency*

By adapting the shape of a simply supported squared plate according to a specific mode shape, an increase of all eigenfrequencies could be accomplished up to a certain pre-deformation.

It has been shown that by applying structural modifications, the mode shapes change, resulting in an increase of the corresponding eigenfrequency [6]. In the case of the 1st bending mode shape, the alterations of the maximum relative pre-deformations led to an increase of the 1st eigenfrequency. Alshabatat and Naghshineh [6] concluded that the highest eigenfrequency increase of dimpled plates can be achieved by placing the dimples at the plate centre, as it increases the local bending stiffness at the region of high modal strain energy. Modal strain energy was not taken into account in this study, so no statement can be made with regard to the results obtained. However, as the modal strain energy is defined as the product of the element stiffness matrix and the second power of the mode shape component [154], it can be assumed that the mode shape has a high influence, and that therefore areas showing a high modal deflection also obtain high modal strain energy. This would mean that published statements on dimpled plates can also be applied here to a certain extent [6].

The results of this study showed that by altering the shape of a plate, a change in the mode shape frequencies and order always occurred. In addition, a connection between the mode shape change and the eigenfrequency increase could be observed, which supports the statement of Alshabatat and Naghshineh [6]. Considering the results of the eigenfrequency increase connected to the mode shapes, high mode shape changes led to high increases of the corresponding frequencies, while frequencies connected to mode shapes similar to the reference plate resulted in low eigenfrequency increases. This can be exemplarily seen for the adaptation of the plate according to the 1^{st} bending mode shape, where the bending modes 4 and 6 showed minor mode shape alterations up to a maximum relative pre-deformation of 5.0 and therefore also low corresponding eigenfrequency increases. High increases were achieved for the frequencies connected to the first three bending modes, while the 1^{st} bending mode frequency showed the highest rise. Regarding relative maximum pre-deformations above 5.0, the 1^{st} bending mode shape was not present within the first 50 mode shapes leading to the conclusion that the corresponding frequency increased strongly. In analogy to the beam, the 1^{st} extensional mode shape is characterised by a higher energy than for instance the 2^{nd} flexural mode shape. Consequently, the 1^{st} bending mode frequency showed the highest increase. Next, the 2^{nd} and 3^{rd} bending mode frequencies rose most. In addition, the vault dimensions of both mode shapes decreased with rising maximum relative pre-deformation. The remaining analysed mode shapes did not change significantly.

Similar conclusions could be made for the plate pre-deformations according to the bending modes 2/3 and 4. It has to be noted that the shape adaptation according to the 2^{nd} and 3^{rd} mode shapes led to the same results since the analysed plate was characterised by a constant edge length. Consequently, the 2^{nd} and 3^{rd} eigenfrequency coincided and the 2^{nd} mode shape corresponded to the 3^{rd} mode shape rotated by 90°.

Regarding the eigenfrequency decrease obtained for high maximum relative pre-deformations, it has been shown that the 1^{st} plate eigenfrequency increased with rising dimple height up to an optimum height and later decreased with further increasing dimple height

[6]. It was argued that the eigenfrequency decrease was due to the dimple thickness decrease. Also in the present study, the eigenfrequency decreases for high pre-deformations might be due to the reduction of the bending stiffness because of the decreasing plate thickness, which was inevitable to have a constant mass. Moreover, it has to be noted that the formulae used for the eigenfrequency calculations are restricted to small pre-deformations and different dependencies can be expected for plates with high pre-deformations. Figure 8.19 shows exemplarily the 1st mode shapes of a plate pre-deformed according to the bending mode 1 with maximum relative pre-deformations of 5.0, 10.0, 15.0, and 20.0, where it can be seen that a flexural mode shape appeared for all pre-deformations. However, this mode shape was shifted from a mainly z movement to a movement in the y direction with increasing maximum relative pre-deformation due to the reduced bending stiffness because of the smaller plate thickness. As up to a relative pre-deformation of 15.0 an increase of the 1st eigenfrequency can be stated, a connection between the eigenfrequency increase and the change in mode shape direction is assumed. A comparison of the results from plates shaped according to the bending modes 2/3 and 4 and their mode shapes confirm this assumption. The proposed method to increase eigenfrequencies can therefore only be used successfully when the deflections of the mode shapes appear in the same direction as the pre-deformations.

In contrast to the results of the slender beam, for which the exclusive increase of a specific mode shape frequency was quite successful, the plate pre-deformation according to the selected mode shapes always led to an increase of all considered eigenfrequencies. Consequently, in the case of plates, the mode shapes cannot be seen as independent. It should rather be noted that all mode shapes deflected certain plate areas that were also influenced by other mode shapes. Thus, all eigenfrequencies changed when shaping the plate according to a certain mode shape. In the results obtained here, the frequency of the 1st bending mode showed the highest or second highest frequency increase for any plate adaptation. As the 1st bending mode shape elevates the whole plate area, it is expected that an influence on the corresponding frequency is always present when adapting the plate according to any other mode shape. Thus, the highest increase of the 1st eigenfrequency could be achieved when shaping the plate according to the bending mode 1.

8.3.2.2 *Maximisation of Multiple Eigenfrequencies*

Contrary to the investigated beam, the linear combination of several mode shapes cannot be seen as a useful method to simultaneously increase multiple eigenfrequencies, since none of the considered combinations led to eigenfrequency increases as high as the adaptation according to the corresponding single mode shape. While in the case of the slender beam it was possible to track the frequency changes of the different mode shapes, the mode shapes of the plate altered so strongly that tracking was not possible. Consequently, only the increase of the different eigenfrequencies was evaluated regardless of the changing mode shape order.

The weighted combinations of the bending modes 1 and 2 also indicated that an adaptation according to one mode shape can simultaneously cause a strong increase of the other eigenfrequencies. Thus, an adaptation according to one mode shape provided better results

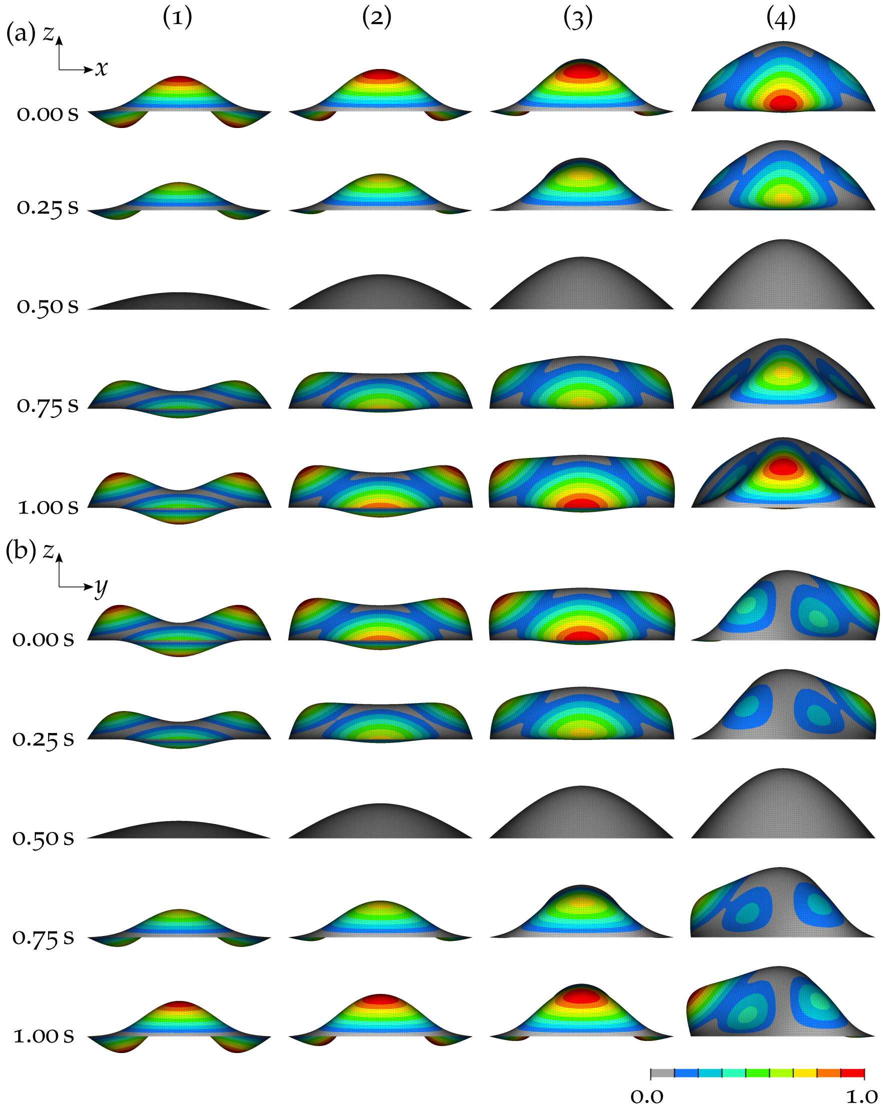

Figure 8.19: 1st mode shape and the normalised vibration amplitude of the squared plate pre-deformed according to the 1st mode shape at different time frames t. The maximum relative pre-deformations 5.0 (1), 10.0 (2), 15.0 (3), and 20.0 (4) are shown in the xz plane (front view; a) and in the yz plane (side view; b). The colours represent the absolute normalised vibration amplitude.

than a combination, concerning both eigenfrequencies, which had also been observed for the slender beam. The results are consistent with the findings of other already mentioned studies from Da Silva and Nicoletti [34] and Fredö and Hedlund [49].

8.3.3 *Outlook*

The mode shape adaptation is an efficient method to increase eigenfrequencies and mode shape frequencies of 1D and 2D structures.

In a first study that further extended the geometric complexity, the mode shape adaptation method has been successfully applied to a 3D beam structure (figure 8.20). The structure was meshed with Solid element (CTETRA) elements of 9 mm edge length based on a mesh study (figure 8.21), which resulted in 1,303,473 elements. The translations and rotations of all nodes at both ends were inhibited. Steel characterised by a Young's modulus of 210,000 MPa, a density of $7.85 \cdot 10^{-9}\,\mathrm{t\,mm^{-3}}$, and a Poisson's ratio of 0.3 was considered as material. A modal analysis revealed the first three eigenfrequencies and mode shapes (figure 8.22).

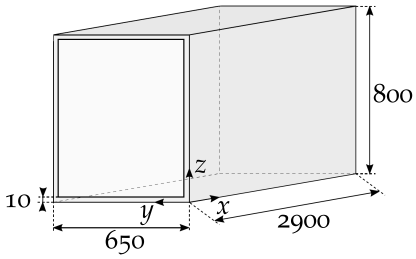

Figure 8.20: 3D beam structure with its dimensions (mm).

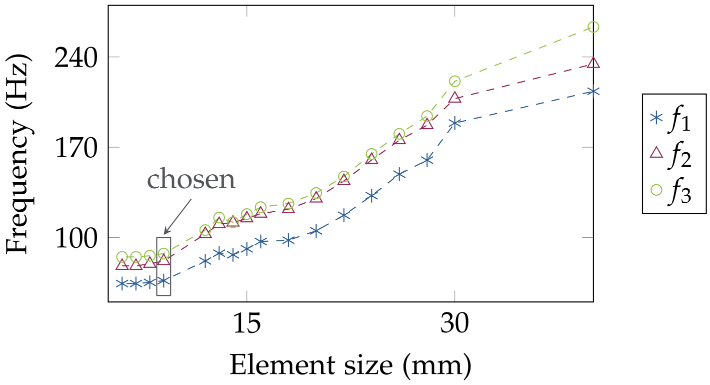

Figure 8.21: Mesh convergence study result for the 3D beam structure meshed with CTETRA elements. The chosen element size of 9 mm is framed.

Pre-deforming the structure according to its 1st mode shape resulted in an increase of the 1st, 2nd, and 3rd mode shape frequency (figure 8.23). The frequencies constantly rose with increasing normalised pre-deformation, which was equal to the maximum pre-deformation (mm) divided by the wall thickness of the structure (mm). A small normalised pre-deformation of 3.0 led already to frequency increases of 5%-11%, while a normalised pre-deformation of 15.0 resulted in frequency increase of up to 60%.

It has to be noted, though, that the obtained frequency increases were significantly lower than those of the 1D beam or the 2D plate studied here. In addition, since 3D structures are certainly more complex than 1D and 2D structures, the mode shape adaptation method should be applied to a variety of different 3D structures in order to generally state the effectiveness of this method to increase eigenfrequencies and mode shape frequencies of 3D structures.

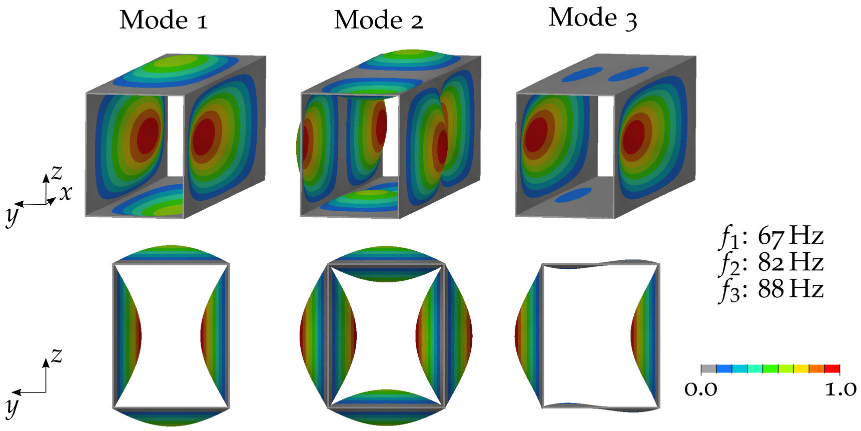

Figure 8.22: First three mode shapes and the corresponding eigenfrequencies of the 3D beam structure in a 3D view and a side view. The colours represent the absolute vibration amplitude.

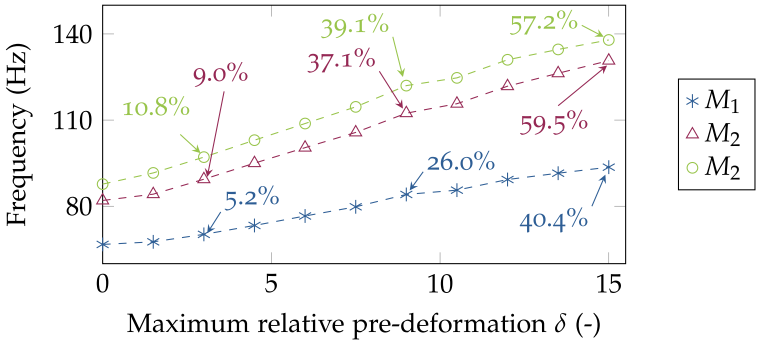

Figure 8.23: Frequencies of the 1st, 2nd, and 3rd mode shape of a 3D beam structure pre-deformed according to the 1st mode shape considering different relative pre-deformations. For several normalised pre-deformations, the frequency deviation compared to the undeformed structure is given.

8.4 CONCLUSION

Shaping axially constrained beams and squared plates according to their mode shapes led to strong eigenfrequency increases. This method allowed the almost exclusive increase of the n-th mode shape frequency (n = 1-5) of the beam, while the increase of the n-th plate mode shape frequency (n = 1-4) simultaneously altered significantly other eigenfrequencies. Overall, strong eigenfrequency increases were obtained by applying only small structural pre-deformations without weight increase.

9

SHAPE ADAPTATION BASED ON EVOLUTIONARY STRATEGIC OPTIMISATIONS

In the 1960s, I. Rechenberg and his colleagues applied the principles of biological evolution to technological optimisations involving accidents (mutation, cross over) and the proximate election strategies (selection) [136].

Evolutionary strategic optimisations are stochastic optimisation methods. In contrast to traditional optimisation methods, the genetic algorithms work over a set of candidate structures (individuals) that cover a large search space instead of a single individual at each iteration. They can be applied to multi-objective design problems and show a relatively high probability to reach the global optimum of a (unknown) fitness landscape that shows several local optima (figure 9.1) [4].

Definition of the mentioned biological terms:

Mutation *creates new individuals by randomly changing parameters of the individuals of the current generation.*

The **cross over** *method generates new individuals by exchanging the parameter values of two individuals from the current generation.*

Selection *implies the survival and reproduction of individuals based on their phenotype, i.e., the expression of their genes.*

The **fitness** *describes the reproductive success of an individual, i.e., its contribution to the genes of the next generation.*

Elitism *means that individuals with high fitness values are preferred.*

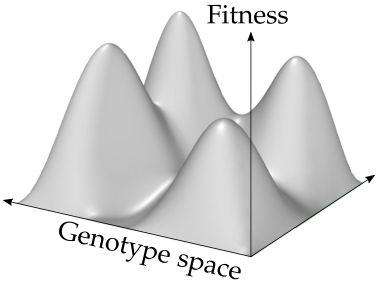

Figure 9.1: Arbitrary fitness landscape.

Evolutionary structural optimisations have already been used to solve vibration issues regarding beams and plates, e.g., by Xie and Steven [195], Zhao et al. [207], and Zhu et al. [212] (cf., chapter 4).

The optimisation process applied here is illustrated in figure 9.2. The genetic algorithm chooses randomly P candidate structures (individuals) from a large search space (gene pool) that form the starting population. The gene pool consists of twice as many individuals as the population, which are generated randomly. The chosen population forms the parental population, which is evaluated regarding the overall objective function (fitness). The best individuals are selected and form together with a certain number of randomly chosen individuals from the gene pool the reproducing population. The allowance of randomly chosen individuals in the reproducing population prevents a local optimisation, i.e., elitism is smaller than 1, which is important since the fitness landscape is unknown. Cross over and mutation affect the reproducing population leading to the offspring population, which then forms again the parental population. This process runs until reaching the stopping criterion, which, in the present work, is defined by the maximum number of generations N_G.

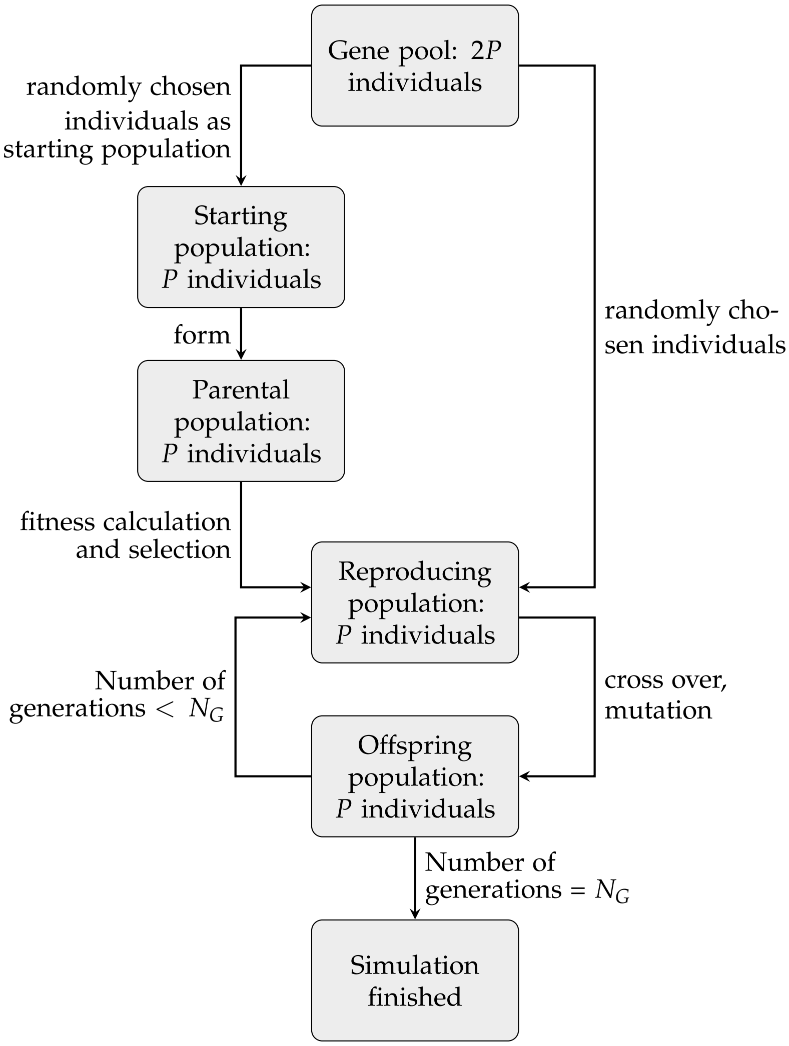
Gene pool: 2P individuals
randomly chosen individuals as starting population
Starting population: P individuals
form
Parental population: P individuals
randomly chosen individuals
fitness calculation and selection
Reproducing population: P individuals
Number of generations < N_G
cross over, mutation
Offspring population: P individuals
Number of generations = N_G
Simulation finished

Figure 9.2: Evolutionary strategic optimisation process, in which P denotes the population size and N_G the number of generations.

In this study, evolutionary strategic optimisations were applied to the beam (1D) and the plate (2D) investigated in chapter 8 to compare both eigenfrequency maximisation techniques. Also here, not only single eigenfrequencies, but also multiple eigenfrequencies were optimised.

In order to compare the evolutionary strategic optimisations and the mode shape adaptation method to a common optimisation procedure, topography optimisations of the plate were performed. As already mentioned in chapter 4, topography optimisations are a type of shape optimisations, in which the nodes of a structure are moved perpendicular to the structure's surface with the objective to generate an optimum structure. Here, the topography optimisations aimed at the maximisation of single eigenfrequencies.

9.1 MATERIAL AND METHODS

The analysed beam and plate geometries as well as the mesh properties and the boundary conditions were set analogous to those in chapter 8.

9.1.1 *Slender Beam*

The parametric studies on the shape adaptation of the slender beam were compared to evolutionary strategic optimisations. The used optimiser Octopus implemented in Grasshopper was developed for multi-objective evolutionary optimisations that allow to consider multiple objective functions simultaneously. The basic optimisation problem can be stated as the optimisation of a single-objective function vector [192]:

$$\min\{G_{arb}(x) = [g_{arb,1}(x), g_{arb,2}(x), ..., g_{arb,n}(x)]\} \;\; ; \;\; n = 1, 2, 3, ... \quad (9.1)$$

with $G_{arb}(x)$ representing an arbitrary function (i.e., fitness function) depending on the variable x and $g_{arb,n}(x)$ arbitrary functions depending on the variable x.

The Octopus settings that were taken into account are listed in table 9.1 and are based on the default and recommended settings. The elitism was set to 50%, as this value in combination with a mutation rate of also 50% is expected to lead to a successful optimisation [85].

Table 9.1: Octopus settings involving the Hypervolume Estimation Algorithm (HypE).

Algorithm setting	Value
Elitism	0.5
Mutation probability	0.1
Mutation rate	0.5
Cross over rate	0.8
Population size	80
Maximum generations	40 (stopping criterion)
HypE reduction	yes
HypE mutation	yes

The z values of the 25 beam nodes were varied in the range of -9.0 to 9.0 mm representing a vertical maximum relative pre-deformation of 3.0. At the beginning, all parameter values were set to 0.0 mm.

Six optimisations were conducted with the objectives summarised in table 9.2. Analogous to the shape adaptation according to the mode shapes, the beam width was adjusted to ensure a constant mass of 145 g.

Note:
The **maximum relative pre-deformation** *δ is defined as the quotient of the maximum pre-deformation (mm) and the beam/plate height (mm) (cf., equation 8.10).*

Table 9.2: Evolutionary strategic optimisation objectives specified for the slender beam and the squared plate.

Optimisation	Objective 1	Objective 2	Objective 3
1	$\max f_1$	$\min \lvert m - m_{ref} \rvert$	-
2	$\max f_2$	$\min \lvert m - m_{ref} \rvert$	-
3	$\max f_3$	$\min \lvert m - m_{ref} \rvert$	-
4	$\max f_4$	$\min \lvert m - m_{ref} \rvert$	-
5	$\max f_1$	$\max f_2$	-
6	$\max f_1$	$\max f_2$	$\max f_3$

Optimisation convergence was reached as soon as the highest eigenfrequency of the last generation differed less than 2% from the highest eigenfrequencies of the three previous generations. Regarding the first four optimisations, the beam structure with the highest eigenfrequency of the last generation was declared as the best structure. For the last two optimisations, the beam characterised by the highest sum of the 1^{st} and 2^{nd} or the 1^{st}, 2^{nd}, and 3^{rd} eigenfrequency of the last generation was declared as the best result. The optimisation results were compared among each other as well as to the reference beam and the parametric study results of the mode shape adaptation (chapter 8) using equation 8.11.

9.1.2 *Squared Plate*

The evolutionary strategic optimisations were also applied to the squared plate (chapter 8), which was based on 49 regularly distributed points in the parametric study (cf., figure 8.4). Since this large number of parameters would require very high computational effort, only 25 points were considered here (figure 9.3), in between which the plate surface was interpolated.

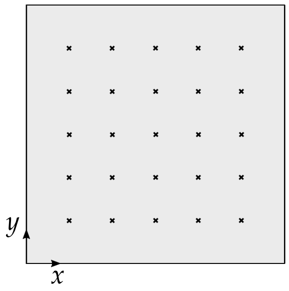

Figure 9.3: Regular distribution of 25 points on the plate that were used as parameters for the evolutionary strategic optimisations.

The z values of the 25 points were manipulated during the optimisation in a range of -10.0 to 10.0 mm representing a maximum relative pre-deformation of -5.0 to 5.0. The same optimisation settings as set for the slender beam were chosen (table 9.1), only differing in the population size, which was increased to 100. As for the shape adaptation according to mode shapes (chapter 8), the plate thickness was adapted to ensure a constant mass. The optimisation objectives corresponded to those for the slender beam (table 9.2). Also the convergence criterion and result evaluation were set according to those of the slender beam.

Regarding the topography optimisations, the same shell mesh was used as for the previous studies and the plate thickness was decreased to reach a total mass equal to the reference plate. The reduced plate thicknesses are listed in table 9.3 and corresponded to the plate thicknesses obtained by applying the mode shape adaptation method with a maximum relative pre-deformation of 5.0 (chapter 8). Four topography optimisations were performed with the objectives to (1) maximise the 1st, 2nd, 3rd, and 4th eigenfrequency and to (2) keep a constant mass compared to the reference plate. All elements not connected to a boundary condition were considered as design space. The set optimisation properties are summarised in table 9.4. The chosen pre-deformation height represented a maximum relative pre-deformation of 5.0.

Note that in the used software HyperMesh, the **pre-deformation height and pre-deformation angle** *are called 'draw height' and 'draw angle', respectively. The value of the pre-deformation angle controls the angle at the sides of the elevation of the plate, i.e., the pre-deformation.*

Table 9.3: Plate thickness h_p defined for the topography optimisations.

Objective	h_p (mm)
$\max f_1$	1.9573
$\max f_2$	1.9154
$\max f_3$	1.9154
$\max f_4$	1.8897

Table 9.4: Topography optimisation settings.

Setting	Value
Minimum width	1.5 mm
Pre-deformation angle	60°
Pre-deformation height	10.0 mm
Upper bounds	1.0
Lower bounds	1.0

9.2 RESULTS

For both the slender beam and the squared plate it was possible to increase the eigenfrequencies by applying evolutionary strategic and topography optimisations. Convergence was shown for all optimisations (cf., convergence plots in appendix chapter A.2).

9.2.1 *Slender Beam*

The evolutionary strategic optimisations aiming at the maximisation of single beam eigenfrequencies resulted in a strong increase of the targeted eigenfrequencies (figure 9.4). While the targeted eigenfrequency in all optimisations increased the most, the remaining analysed eigenfrequencies only changed slightly (maximum 6% to 10% in average) aside from the 5th eigenfrequency, which always decreased (table 9.5). The optimisation targeting a 1st eigenfrequency increase raised the 1st eigenfrequency by 297%, while the optimisation aiming at a 4th eigenfrequency increase only raised the 4th eigenfrequency by 35%. The results also show that the targeted eigenfrequency was in all cases maximised until it approximately coincided with the next higher-order eigenfrequency. As the mode shape orders switched only partly, the frequency increases of the 1st to 4th mode shapes were similar to the corresponding eigenfrequency increases. In summary, the obtained eigenfrequency increases were very similar to those reached by the mode shape adaptation approach as shown in chapter 8. However, shaping the beam according to a specific mode shape strongly raised the corresponding frequency, which was not reached by the optimisations.

The optimised beam shapes obtained by the maximisation of the 1st, 2nd, and 3rd eigenfrequency looked very similar to the corresponding mode shapes (figure 9.5). The maximum relative pre-deformations were slightly lower than the maximum permitted value of 3.0 (table 9.6). Regarding the beam shape for increasing the 4th eigenfrequency, the beam shape differed from the 4th mode shape of the reference beam. In addition, a relatively low pre-deformation of 1.3 was present and the eigenfrequency increase was the lowest among the four optimisations.

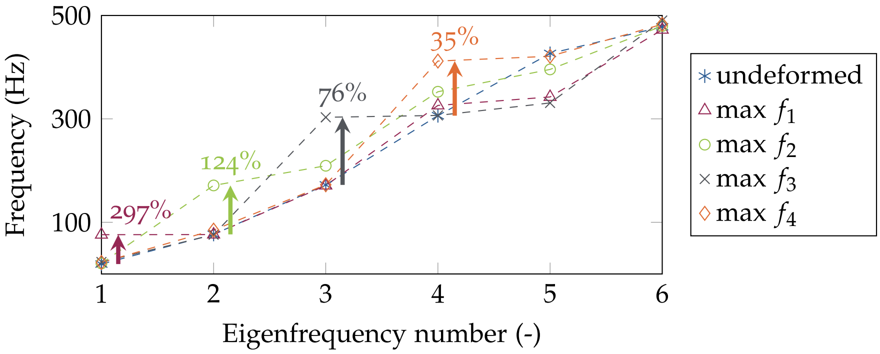

Figure 9.4: First six eigenfrequencies of the reference beam and the optimised beams targeting a maximisation of the 1st, 2nd, 3rd and 4th eigenfrequency. The increase of the targeted eigenfrequencies compared to the undeformed (reference) beam are given and symbolised by arrows.

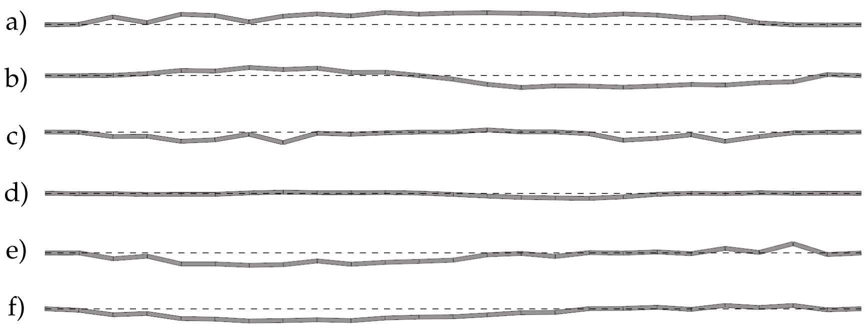

Figure 9.5: Side view (xz plane) of the optimised beam with the objectives to maximise the a) 1^{st}, b) 2^{nd}, c) 3^{rd}, d) 4^{th} eigenfrequency, e) 1^{st} and 2^{nd} eigenfrequency, and f) 1^{st}, 2^{nd}, and 3^{rd} eigenfrequency. The black dashed lines represent the horizontal line at $z = 0.0$ mm.

Table 9.5: Eigenfrequency increase (a) and increase of the frequencies connected to specific mode shapes (M_n) (b) compared to the reference beam due to the evolutionary strategic optimisation (Opti) and the mode shape adaptation method (Mode) for the slender beam deformed with a maximum relative pre-deformation of 3.0. The average absolute values of the deviations of eigenfrequencies that were not targeted are given. The targeted eigenfrequencies or mode shapes are shown in bold numbers.

a)		Eigenfrequency						Deviation
		f_1	f_2	f_3	f_4	f_5	f_6	
max f_1	Opti	**297%**	0%	-1%	6%	-20%	-1%	6%
	Mode	**299%**	85%	0%	0%	-5%	0%	18%
max f_2	Opti	6%	**124%**	22%	15%	-7%	0%	10%
	Mode	0%	**122%**	76%	36%	11%	15%	28%
max f_3	Opti	20%	-1%	**76%**	0%	-22%	3%	9%
	Mode	-1%	-1%	**28%**	-4%	10%	42%	12%
max f_4	Opti	16%	11%	0%	**35%**	-1%	1%	6%
	Mode	-1%	-1%	-5%	**-24%**	-23%	-9%	8%

b)		Frequency of mode shape						Deviation
		M_1	M_2	M_3	M_4	M_5	M_6	
max f_1	Opti	**297%**	0%	-1%	6%	-20%	-1%	6%
	Mode	**641%**	0%	0%	0%	-5%	0%	1%
max f_2	Opti	6%	**173%**	-1%	29%	-17%	17%	14%
	Mode	0%	**636%**	-1%	-1%	-3%	-1%	1%
max f_3	Opti	20%	-1%	**78%**	-1%	-22%	3%	9%
	Mode	-1%	-1%	**626%**	-4%	-48%	-2%	11%
max f_4	Opti	16%	11%	0%	**38%**	-3%	1%	6%
	Mode	-1%	-1%	-5%	**614%**	-45%	-9%	12%

Table 9.6: Maximum relative pre-deformation of the four optimised beams and the reference beam.

Objective	z values of beam nodes min (mm)	max (mm)	Maximum relative pre-deformation δ (-)
max f_1	-0.1	8.8	2.9
max f_2	-8.7	5.5	2.9
max f_3	-7.8	1.6	2.6
max f_4	-3.8	0.8	1.3
Reference	0.0	0.0	0.0

The beam structures resulting from the optimisations targeting at an increase of the 1st and 2nd and of the 1st, 2nd, and 3rd eigenfrequency looked similar and reminded of a linear combination of mode 1 and mode 2 (figure 9.5). Both beam shapes corresponded to a maximum relative pre-deformation of 3.0. The optimisations led to an increase of all targeted eigenfrequencies, however, the increases varied between 30% and 123% (table 9.7). The higher order eigenfrequencies changed only slightly with the exception of the decreasing 5th eigenfrequency. Regarding the frequencies of the different mode shapes, the 2nd and 3rd mode shape changed order resulting in a high increase of the mode 2 frequency, while the frequency of the 3rd mode shape slightly decreased during the second optimisation.

Table 9.7: Increase of the eigenfrequencies (a) and mode shape frequencies (b) compared to the reference beam due to the evolutionary strategic optimisations aiming at the maximisation of multiple eigenfrequencies. The targeted eigenfrequencies are shown in bold numbers.

a) Objective	Eigenfrequencies f_1	f_2	f_3	f_4	f_5	f_6
max f_1 & f_2	**30%**	**122%**	1%	-1%	-28%	5%
max f_1, f_2 & f_3	**46%**	**123%**	**48%**	0%	-11%	0%

b) Objective	Frequencies of mode shapes M_1	M_2	M_3	M_4	M_5	M_6
max f_1 & f_2	**30%**	**128%**	-1%	-1%	-28%	5%
max f_1, f_2 & f_3	**46%**	**232%**	**-1%**	0%	-11%	0%

Compared to the mode shape adaptation results for a maximum relative pre-deformation of 3.0 (cf., table 8.3), the optimisations aiming at raising the 1st and 2nd mode shape frequencies led to lower frequency increases (30% vs. 36% for the 1st mode shape frequency and 128% vs. 338% for the 2nd mode shape frequency). However, the optimisation targeting at a simultaneous increase of the 1st, 2nd, and 3rd mode shape frequency reached for the first two mode shape frequencies higher values than the mode shape adaptation, yet the 3rd mode shape frequency was decreased.

9.2.2 *Squared Plate*

The optimisation led to pre-deformed plates with increases in all analysed eigenfrequencies (figure 9.6). Similar to the beam results, the targeted eigenfrequency showed in nearly all cases the highest increase and almost coincided with the next higher-order eigenfrequency. However, the maximisation of the 2nd eigenfrequency raised the 3rd eigenfrequency slightly more (table 9.8).

The eigenfrequency increase varied from 372% for the maximisation of the 1st eigenfrequency to 178% for the maximisation of the 4th eigenfrequency. The maximisation of the 1st eigenfrequency led to a plate shape similar to the 1st mode shape of the reference plate. However, the maximisations of both the 2nd and the 3rd eigenfrequency generated plate shapes comparable to the 4th mode shape of the reference plate, while the maximisation of the 4th eigenfrequency resulted in a plate shape similar to the 5th mode shape of the reference plate. The maximum relative pre-deformations of the plate shapes showed values between 5.1 and 5.3.

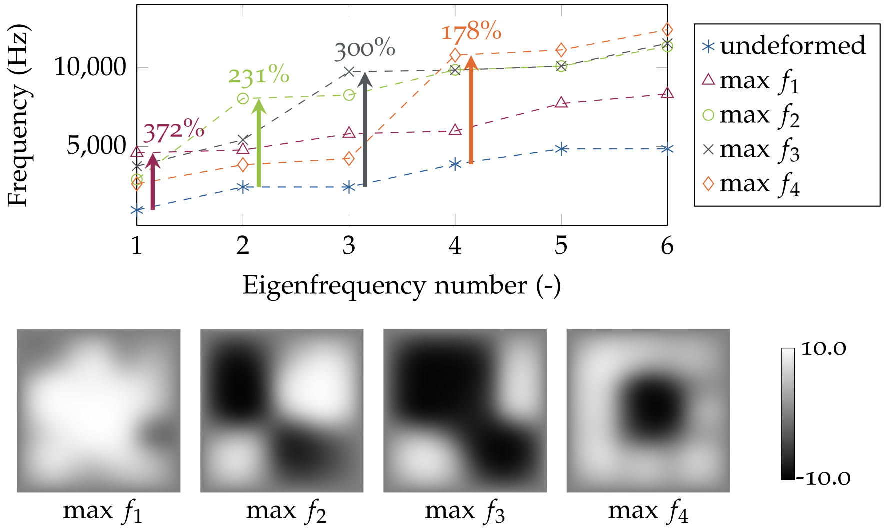

max f_1 max f_2 max f_3 max f_4

Figure 9.6: First six eigenfrequencies of the reference plate and the four plate shapes obtained by evolutionary strategic optimisations aiming to maximise the 1st, 2nd, 3rd, and 4th eigenfrequency. The increase of the targeted eigenfrequencies compared to the undeformed plate is given. Below, a top view (xy plane) of the four optimised plates is displayed. The grey scale represents the pre-deformation (mm).

Table 9.8: Eigenfrequency deviations compared to the reference plate for the three methods, the evolutionary strategic optimisation (Opti), topography optimisation (Topo), and the mode shape adaptation method (Mode), to increase the 1st, 2nd, 3rd, and 4th eigenfrequency for a maximum pre-deformation δ_{max} of 10.0 mm. For each study, the frequency which increased most shown in bold numbers. The highest increase for each eigenfrequency among all studies is underlined.

		Eigenfrequency						Deviation
Obj.		f_1	f_2	f_3	f_4	f_5	f_6	
max f_1	Opti	**372%**	96%	139%	54%	59%	72%	84%
	Topo	**294%**	59%	59%	31%	14%	28%	38%
	Mode	**487%**	135%	135%	67%	40%	55%	87%
max f_2	Opti	199%	231%	**240%**	154%	108%	134%	167%
	Topo	**158%**	114%	117%	90%	59%	67%	98%
	Mode	228%	159%	**233%**	135%	109%	135%	168%
max f_3	Opti	285%	123%	**300%**	153%	108%	138%	161%
	Topo	**231%**	42%	177%	83%	68%	72%	99%
	Mode	228%	159%	**233%**	135%	109%	135%	153%
max f_4	Opti	170%	58%	74%	**178%**	129%	156%	117%
	Topo	**216%**	74%	76%	159%	110%	111%	117%
	Mode	240%	**257%**	**257%**	118%	183%	183%	224%

Similar to the evolutionary strategic optimisations, the topography optimisations resulted in plate shapes with highest eigenfrequency increase obtained for the targeted eigenfrequencies (figure 9.7). All considered eigenfrequencies were higher than those of the reference plate. The eigenfrequency increases varied from 295% for the 1st eigenfrequency to 114% for the 2nd eigenfrequency and were thus lower than those resulting from the evolutionary strategic optimisations. While the plate shapes for maximising the 1st and 4th eigenfrequency were similar to those of the evolutionary strategic optimisations, the plate shapes of the 2nd and 3rd eigenfrequency maximisation looked similar to the 2nd and 3rd mode shapes of the reference plate. Regarding the topography optimised plates, the mode shapes were similar to those of the reference plate (cf., figure 8.13). It has to be noted that in contrast to the evolutionary strategic optimisations, the plates used for the topography optimisations were only deformed in positive z direction. Moreover, the maximum deformations of 7 mm were lower than the maximum absolute value of 10 mm reached by the evolutionary strategic optimisations.

Table 9.8 also lists the obtained eigenfrequency increases for the mode shape adaptation method. While the highest increase for the 1st eigenfrequency was reached by the mode shape adaptation ap-

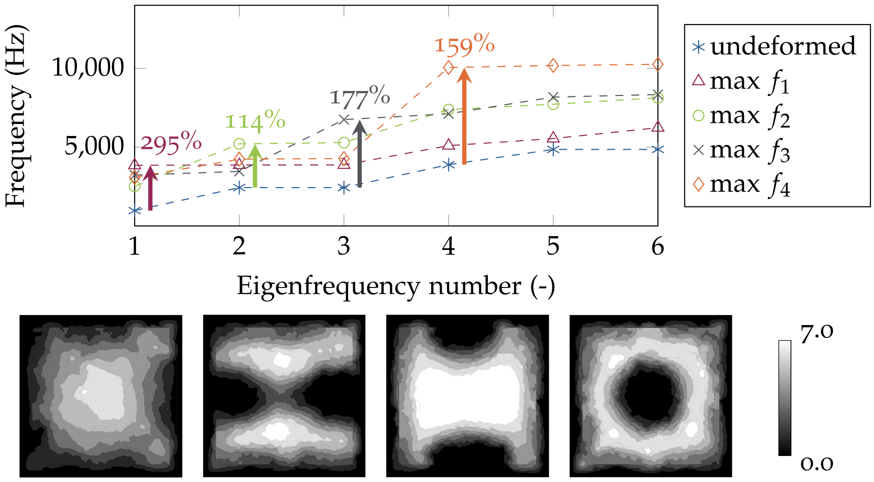

max f_1 max f_2 max f_3 max f_4

Figure 9.7: First six eigenfrequencies of the reference plate and the four plate shapes obtained by topography optimisations aiming to maximise the 1st, 2nd, 3rd, and 4th eigenfrequency. The increase of the targeted eigenfrequencies compared to the undeformed plate is given. Below, a top view (xy plane) of the four optimised plates is displayed. The grey scale represents the pre-deformation (mm).

proach, the evolutionary strategic optimisation led to highest increases of the 2nd, 3rd, and 4th eigenfrequency. The resulting eigenfrequencies of the topography optimisations were for the maximisation of the 1st, 2nd, and 3rd eigenfrequency lower than the other two methods and for the 4th eigenfrequency maximisation in the middle between the other two results. Generally, all three methods with the aim to maximise the 1st plate eigenfrequency resulted in highest increase of the targeted eigenfrequency. Regarding the maximisation of the 2nd to 4th eigenfrequency, however, the targeted eigenfrequencies rose, but in most of the simulations another analysed eigenfrequency exhibited a stonger increase.

Regarding the maximisation of multiple eigenfrequencies, both the maximisation of the 1st and 2nd eigenfrequency and the maximisation of the 1st, 2nd, and 3rd eigenfrequency caused similar results (Table 9.9). Highest increase was seen for the 1st, 2nd, and 3rd eigenfrequency compared to the reference plate. The remaining considered eigenfrequencies increased between 84% and 113%. The optimised plate shapes were very similar, but seemed to be mirrored at the xz and xy plane (figure 9.8). Compared to the mode shape adaptation (chapter 8), all targeted eigenfrequency increases were higher.

In comparison to the mode shape adaptation based on multiple mode shapes (table 8.6), the evolutionary strategic optimisation led in all cases to higher eigenfrequency increases (maximisation of the 1st and 2nd eigenfrequency: 246% vs. 181% for the 1st and 216% vs. 132% for 2nd eigenfrequency; 1st, 2nd, and 3rd eigenfrequency: 266% vs. 169% for the 1st, 204% vs. 137% for the 2nd, and 286% vs. 141% for the 3rd eigenfrequency).

Table 9.9: Eigenfrequency increase due to evolutionary strategic optimisations for the squared plate. The targeted eigenfrequencies are shown in bold numbers.

	Eigenfrequencies					
Objective	f_1	f_2	f_3	f_4	f_5	f_6
max f_1 & f_2	**246%**	**216%**	220%	112%	84%	113%
max f_1, f_2 & f_3	**266%**	**204%**	**286%**	149%	117%	153%

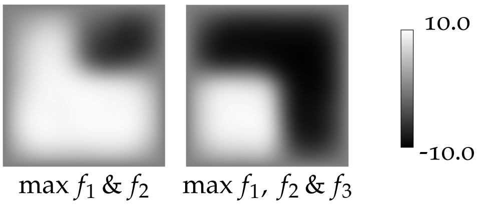

Figure 9.8: Top view (xy plane) of the plates obtained by evolutionary strategic optimisations aiming at a simultaneous maximisation of the 1st and 2nd eigenfrequency and the 1st, 2nd, and 3rd eigenfrequency. The grey scale represents the pre-deformation (mm).

9.3 DISCUSSION

9.3.1 *Slender Beam*

The evolutionary strategic optimisations with the aim to maximise single eigenfrequencies of the first four orders resulted in strongest increases of all targeted eigenfrequencies, while the eigenfrequencies not targeted, aside from the 5th eigenfrequency, were only slightly affected. Overall, the 1st eigenfrequency was the most increased, while the smallest eigenfrequency increase was reached for the 4th eigenfrequency. The resulting beam shapes of the optimisations aiming at the maximisation of the 1st, 2nd, and 3rd eigenfrequency looked similar to the 1st, 2nd, and 3rd mode shape of the reference beam. The maximisation of the 4th eigenfrequency led to a beam shape, which differed from the 4th mode shape of the reference beam, and the obtained eigenfrequency increase of 35% was comparably small. All reached eigenfrequency increases were comparable to the eigenfrequency increases obtained by the mode shape adaptation method and the 3rd and 4th eigenfrequency were even raised to higher values.

Since the optimisations were not combined with a mode tracking algorithm, the targeted eigenfrequency only increased until it coincided with the higher-order eigenfrequency. Consequently, the maximisation of the 1st eigenfrequency, for example, led to a beam structure, whose 1st and 2nd eigenfrequency almost coincided (multiple or repeated eigenfrequencies). These findings correspond to the 1st eigenfrequency maximisation of a simply supported 2D beam conducted by Du and Olhoff [44], where the 1st and the 2nd eigenfrequency of the optimised beam were similar. Also Krog and Olhoff [84] stated that the occurrence of multiple (repeated) eigenfrequencies during structural optimisations aiming at eigenfrequency increases is likely. In the present study, the 1st mode shape then switched order with the 2nd mode shape, but its frequency could not be increased further. Also the other targeted eigenfrequencies were only maximised until reaching the value of the next higher-order eigenfrequencies due to the absence of a mode tracking algorithm. Since almost no mode switch occurred, the frequencies of specific mode shapes were increased by almost the same amount as that of the corresponding eigenfrequencies. Thus, compared to the mode shape adaptation approach, the mode shape frequencies were increased less strongly.

The optimisations aiming at the increase of multiple eigenfrequencies were also successful, as all targeted eigenfrequencies increased. Interestingly, both optimised beams looked similar, although only one showed a 3rd eigenfrequency increase compared to the reference beam.

Regarding the increase of the 1st, 2nd, and 3rd mode shape frequencies, the optimisation did not lead to a 3rd mode shape frequency increase, while increases in the other two mode shape frequencies were higher than those resulting from the mode shape adaptation method. Thus, the evolutionary strategic optimisation is apparently not the best method to simultaneously increase multiple mode shape frequencies, which might be due to the missing mode tracking algorithm.

9.3.2 *Squared Plate*

All optimisations succeeded as they all increased the targeted eigenfrequencies. Regarding the evolutionary strategic optimisations, the targeted eigenfrequencies always rose most. However, the optimisation aiming at a 2nd eigenfrequency maximisation increased the 3rd eigenfrequency slightly more. This might be due to the fact that both the 2nd and the 3rd mode shapes were very similar and also the corresponding eigenfrequencies almost coincided.

In contrast to the evolutionary strategic optimisations, the topography optimisations always resulted in highest increases for the 1st eigenfrequency, regardless which eigenfrequency was targeted. But the targeted eigenfrequencies reached in any case the second highest increase.

In both optimisation approaches to increase eigenfrequencies, the 4th eigenfrequency maximisation generated a plate shape similar to the 5th mode shape of the reference plate. It can be assumed that due to the similar shapes of mode 4 and mode 5, which both showed maxima at the edges, a 4th eigenfrequency increase was still achieved.

As for the slender beam, the absence of mode tracking only allowed the frequency increase of a specific mode shape up to the frequency of the next higher-order mode shape, which can also be the reason for the resulting plate shape similar to the 5th mode shape of the undeformed plate.

The optimisation objective to maximise the 1st and 2nd or the 1st, 2nd, and 3rd eigenfrequency increased all targeted eigenfrequencies. Also the maximisation of single eigenfrequencies always led to an increase of all analysed eigenfrequencies. But, regarding the multiple eigenfrequency optimisations, the two (three) targeted eigenfrequencies rose by a similar amount (i.e., 246% and 216% for the maximisation of the 1st and the 2nd eigenfrequency, respectively, and 166%, 204%, and 286% for the maximisation of the 1st, 2nd, and 3rd eigenfrequency, respectively). In contrast to that, the optimisation aiming at a maximisation of the 1st eigenfrequency led to increases of 372%, 96%, and 139% for the 1st, 2nd and 3rd eigenfrequency, respectively.

Comparing the optimisation results to the mode shape adaptation method to increase single eigenfrequencies, it is not possible to state which used approach generated highest eigenfrequencies. Regarding the increase of multiple eigenfrequencies, the evolutionary strategic optimisations led to higher increases of the targeted frequencies.

9.3.3 *Methodology*

The evolutionary strategic optimisation required high computing capacity. Due to the large number of parameters, many generations had to be calculated to reach an optimisation convergence. The population and generation number were chosen according to the standard settings and can be seen as a good compromise concerning computational time and variability. Nevertheless, it might be possible to improve the obtained results further by varying the optimisation settings and – with regard to the plate – also the number of variables. It is also advised to alter the mutation probability in further studies in order to enable a more diverse variety of shapes. In addition, it has to be noted that even though all optimisations are within the set convergence criterion, it can be expected that, in particular regarding the plate, higher eigenfrequencies can be developed investing more computational time (i.e., considering more interpolation points and/or increasing the population size and/or the number of generations).

In general, optimisations based on evolutionary algorithms do not always provide the optimum results for the defined objectives and boundary conditions. Genetic algorithms do not have a well-defined solution as the set of interesting solutions have an almost infinite size and are therefore difficult to represent. Regarding the analysed plate, for example, the obtained eigenfrequency increases for the maximisation of the 3rd eigenfrequency and the maximisation of the 1st, 2nd, and 3rd eigenfrequency were – aside from the 2nd eigenfrequency increase – very similar. However, the corresponding plate shapes differed strongly, showing a disadvantage of this optimisation algorithm. During the optimisation, only one shape was followed, while many different shapes may have led to the same results. No statement can therefore be made regarding the global maximum, since the optimisation could also be converged towards a local maximum, although an elitism of 50% was specified to avoid local optimisation. In addition, Octopus is a multi-objective optimiser. It is therefore impossible for a non-dominated solution to improve one objective without negatively affecting other objective values [192]. As the mass difference, whose minimisation was set as one objective, can only be seen as a constraint in order to assure a constant mass and thus comparability with the other optimisation methods, not the Pareto front, but all individuals of the last generation were considered for evaluation in the present work.

The **Pareto front** *implies the set of all Pareto optimum solutions, for which no objective function can be improved further without degrading another objective function.*

The topography optimisation of the plate generally showed minor eigenfrequency increases. However, none of the results obtained the maximum allowed pre-deformation height, which could be due to meeting the convergence criteria prematurely. Further investigations varying the convergence criteria and the optimisation settings should be carried out in order to increase the performance of this shape optimisation approach. Nevertheless, similar plate shapes are expected. In addition, it has to be noted that the optimisation results need to be smoothed in order to enable easier manufacturing. By applying smoothing, similar shapes as for the eigenvalue approach appeared for the maximisation of the first two eigenfrequencies. Thus, it cannot be concluded from the comparison of the different optimisation results that the topography optimisation caused poorer results, but rather that more computational and post-processing work is needed to achieve similar results.

Regarding the mode shapes of the topography optimised plates, high similarity to the reference plate mode shapes were obtained, especially for the first three eigenfrequencies. This could not be observed for the two other approaches applied to the plate. Many optimisation algorithms are set to keep the corresponding mode shapes, which might apply in this case also, providing an additional possible explanation of why not the full allowed pre-deformation was used. Consequently, the topography optimisation results led to lower eigenfrequency increases, but kept the mode shapes similar to the reference plate, which might also be interesting for technical applications.

9.4 CONCLUSION

Evolutionary strategic optimisations of a slender beam and a squared plate to maximise single eigenfrequencies (n = 1-4) resulted in strong eigenfrequency increases at constant mass. While the targeted beam eigenfrequency raise hardly involved alteration in the remaining analysed eigenfrequency values, the plate shape optimisations always changed all analysed eigenfrequencies. Due to the absence of a mode tracking algorithm, the targeted eigenfrequencies were maximised until reaching the value of the next higher-order eigenfrequency. Regarding the analysed plate, the evolutionary strategic optimisations generally led to higher eigenfrequency increases than the additionally performed topography optimisations.

10

REGULAR AND IRREGULAR HONEYCOMB PLATES

Sandwich panels are widely-used lightweight structures because of their high density-specific stiffness and strength. Especially in the aerospace industry, sandwich panels are extensively applied. They commonly consist of two thin and stiff face layers that are separated by a thick lightweight core structure (figure 10.1). The resulting high second moment of inertia leads to a high bending stiffness [70]. This large bending stiffness per mass generally leads to high eigenfrequencies [46]. The eigenfrequencies of sandwich panels depend on the shear modulus of the core and the contribution of the face plates to the bending stiffness – aside from the impact of the panel's length, width, height, and the material properties [113].

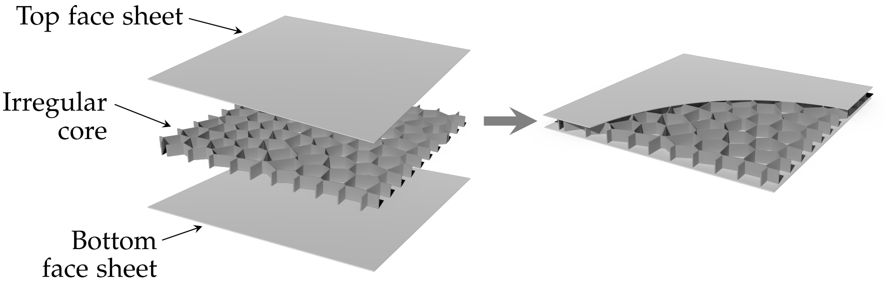

Figure 10.1: Sandwich panel composed of a top face sheet, an irregular core structure, and a bottom face sheet.

The impact of structural irregularities present in cellular structures on the mechanical properties have already been studied (cf., chapter 2), but the results have hardly been applied to sandwich panels. However, some studies investigated the impact of undesired irregularities in an overall regular sandwich panel core on the mechanical properties, because such irregularities can occur due to, for example, structural defects, variation in the manufacturing process, or prestressing [113]. Mukhopadhyay and Adhikari [113] performed free vibration analyses of sandwich panels with these unintentionally irregular honeycomb cores and stated an eigenfrequency increase with an increasing degree of irregularities. Another study published by Heimbs [70] investigated several core structures (hexagonal, over-expanded honeycomb, and folded cores of different geometries and materials) under compression and shear loads and compared the numerical results to experiments.

Regarding more complex sandwich structures, functional grading is one type of irregularity, which has been focused on in different studies (e.g., Zenkour [203] or Xiang et al. [194]). However, in these studies, the intentionally irregular sandwich cores were based on graded material properties, whereas the structure remained regular. Summing up, sandwich panels with irregular core structures to improve the mechanical properties have hardly been investigated.

Voronoi *cells are polygons that are defined by the intersection of contact lines built midway between points distributed on a plane (2D Voronoi) or in a space (3D Voronoi) (cf., figure 10.3)*

In the present study, the 1st eigenfrequency of a solid plate was compared to plates composed of regular rectangular cells and honeycombs as well as irregular Voronoi cells, which can be implemented as core structures in sandwich panels. The irregular Voronoi combs are inspired by nature, as they are very frequently present in diatom shells (figure 10.2). The impact of the structural irregularities on the 1st eigenfrequency was compared to the eigenfrequency increase obtained by pre-deforming the plates according to the 1st mode shape. Detailed studies on this method to raise eigenfrequencies are documented in chapter 8.

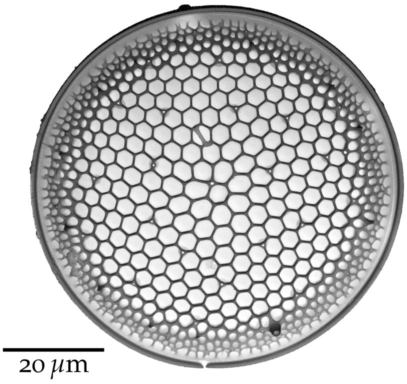

Figure 10.2: Scanning electron microscopic image of the diatom *Thalassiosira* sp. (reprinted from Andresen [12] with permission from Springer Nature). The characters and the scale bar are replaced to improve the resolution.

10.1 MATERIAL AND METHODS

The analysed plates had the geometric properties of the squared plate described in chapter 8.1.2 and the material properties listed in table 8.1. As the application of a cellular structure led to a reduced mass, the thickness of the solid plate was adapted to generate a solid reference plate of the same mass. All plates were meshed with Shell elements (PSHELLs) characterised by an element size in the range of 0.6 mm to 1.0 mm depending on the geometry. All plate edges were simply supported. The definition of a modal load case allowed the calculation of the plates' 1st eigenfrequencies. Table 10.1 lists the plates that were analysed:

The 1st eigenfrequency of the solid reference plate (plate 1) was calculated analytically considering Kirchhoff classic plate theory (equation 8.12) to demonstrate the plausibility of the numerical results. Sub-

Table 10.1: Six squared plates that were analysed.

	Name	a (mm)	h_p (mm)	m (g)
(1)	Solid plate (reference)	100	0.74	20.0
(2)	Regular rectangular plate	100	2.00	20.0
(3)	Regular hexagonal plate	100	2.00	20.0
(4)	Quasi-regular Voronoi plate	100	2.00	20.0
(5)	Irregular Voronoi plate (manually)	100	2.00	20.0
(6)	Irregular Voronoi plate (optimised)	100	2.00	20.0

sequently, the plates based on regular rectangular cells and honeycombs (plates 2 and 3), each having a cell/comb width of about 25 mm width, were generated. For both plates, the constant cell wall thickness was adapted to reach the defined plate mass of 20.0 g.

The irregular plates were composed of Voronoi cells, which are characterised as polygons defined by the intersection of contact lines built midway between points (figure 10.3). Hence, for a given distribution of points, the Voronoi cell distribution is unique and there is no empty space between cells [202]. As for the regular cellular plates, the Voronoi wall thickness was adapted to ensure the targeted plate mass of 20.0 g.

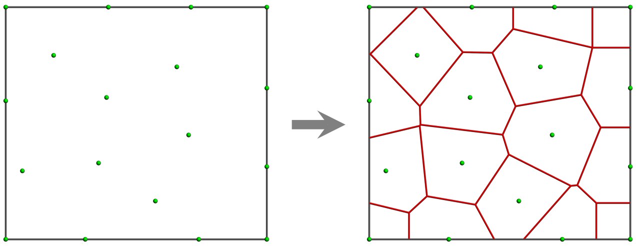

Figure 10.3: Based on an irregular point distribution (left-hand side), Voronoi cells are generated (right-hand side).

First, the constant Voronoi cell size was increased from 1 mm to 40 mm with a step size of 1 mm to study the impact of the cell size forming the quasi-regular Voronoi plates on the 1st eigenfrequency. A Voronoi plate with a constant cell size of 25 mm, which corresponded to the cell size of both regular plates, was chosen as the quasi-regular Voronoi plate (plate 4) to compare it to the other studied plates.

The two irregular Voronoi plates were based on a cell size interpolation algorithm, which consisted of an attractor value, a global value, and a transition area, which depended on an attractor area radius r and a decay factor β (figure 10.4). The outer edges of the plates were considered as attractors to increase the stiffness close to the simply supported edges. An irregular plate was constructed manually mimicking the shell geometry of the diatom *Thalassiosira* sp. displayed in figure 10.2 (plate 5). This smooth transition from smaller cells close to the edges to larger cells in the middle was realised by defining a global cell size of 18 mm, a cell size close to the attractor of 5.0 mm, an attractor radius of 6.0 mm, and a decay factor of the attractor cell size β of 5.5.

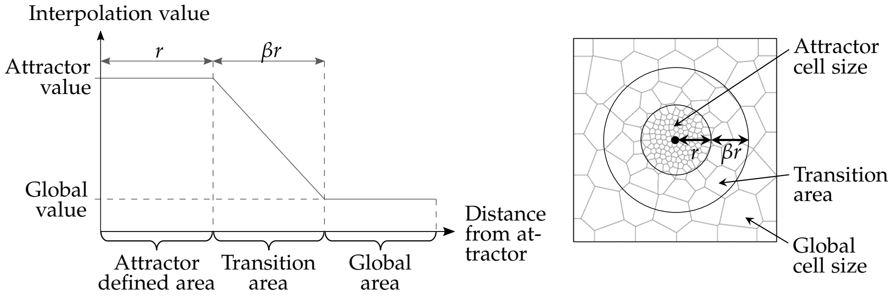

Figure 10.4: The interpolation function displayed on the left-hand side is based on an attractor value and a global value with a linear interpolation between them using the decay factor β. On the right-hand side, the described interpolation function is exemplarily applied to a 2D Voronoi structure. The cell size gradient depends on an attractor (here: black middle point), an attractor radius r defining the attractor cell size area, a transition area, whose area radius is the product of the attractor radius and the decay factor, and a global cell size.

The described parametric algorithm-based construction of the irregular plates allowed the generation of numerous different geometries by varying the parameter values. An evolutionary strategic optimisation (cf., introduction of chapter 9) using the optimiser Octopus implemented in Grasshopper was conducted considering the Octopus settings listed in Table 9.1 to design an optimised irregular Voronoi plate. The considered objective functions involved (1) the maximisation of the 1st eigenfrequency and (2) the minimisation of the mass difference compared to the targeted plate mass of 20.0 g. The population size was set to 50 and 20 generations were calculated, which was the stopping criterion of the optimisation. The attractor decay factor had a constant value of 1.1. The parameter definition covered different ranges and start values listed in table 10.2.

Table 10.2: Parameter definition ranges and start values for the evolutionary strategic optimisation applied to Voronoi plates.

	Global diameter	Attractor radius	Attractor area radius
Range	13.00-26.00 mm	1.00-10.00	4.00-8.00 mm
Start value	19.50 mm	2.50 mm	6.00 mm

Regarding the result evaluation, the plate with the highest 1st eigenfrequency of the last generation was declared as optimum irregular Voronoi plate (plate 6).

Afterwards, the solid reference plate and the five cellular plates were pre-deformed according to their 1st mode shapes as described in chapter 8 adapting the plate thickness to have a constant mass of 20.0 g. Different intensities of plate pre-deformations were studied involving maximum pre-deformations of 1-5 mm in step sizes of 1 mm (δ = 0.5 - 2.5) and of 5-20 mm in step sizes of 5 mm (δ = 2.5 - 10.0). The impact of the plate pre-deformation on the 1st eigenfrequency was analysed.

Note that the **maximum relative pre-deformation** δ *is defined as the quotient of the maximum pre-deformation* δ_{max} *(mm) and the plate thickness* h_p *(mm) (cf., equation 8.10).*

The 1st eigenfrequency results of the plates were compared to that of the solid plate using equation 8.11.

10.2 RESULTS

The analytical 1st eigenfrequency solution of 363.5 Hz of the here analysed, solid plate coincided well with the numerical value of 363.4 Hz.

Regarding the quasi-regular Voronoi plate, the 1st plate eigenfrequency depended on the Voronoi cell size as shown in figure 10.5. All 1st eigenfrequency values were between 631 Hz (Voronoi cell size: 2 mm) and 806 Hz (Voronoi cell size: 40 mm). The trend line fitted to the data had a slope of 4.1 Hz mm^{-1}.

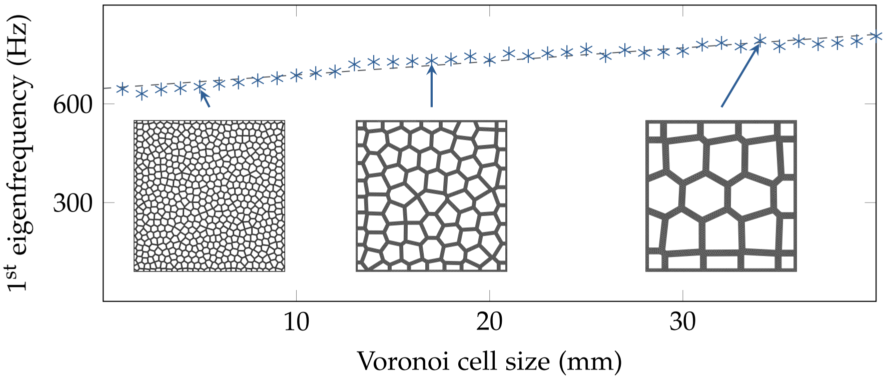

Figure 10.5: 1st eigenfrequencies of 2D Voronoi plates with different cell sizes. All plates exhibit a mass of 20.0 g. The grey dashed trend line has a slope of 4.1 Hz mm^{-1}

The evolutionary strategic optimisation of the irregular Voronoi plate converged as shown in the appendix chapter A.3. The plates of the last optimisation generation exhibiting a mass of 20.00 ± 0.15 g are displayed in figure 10.6. The 1st eigenfrequencies were in the range of 810 Hz to 962 Hz. All six exemplary displayed plates showed large cells in the plate middle and small cells close to the plate edges. The Voronoi plate with the highest 1st eigenfrequency of 962 Hz (plate 6) is displayed in figure 10.6 (6).

Figure 10.7 illustrates the six studied plates and the overall 1st eigenfrequency increase with increasing plate complexity. The plates composed of regular rectangular and honeycomb cells, and the quasi-

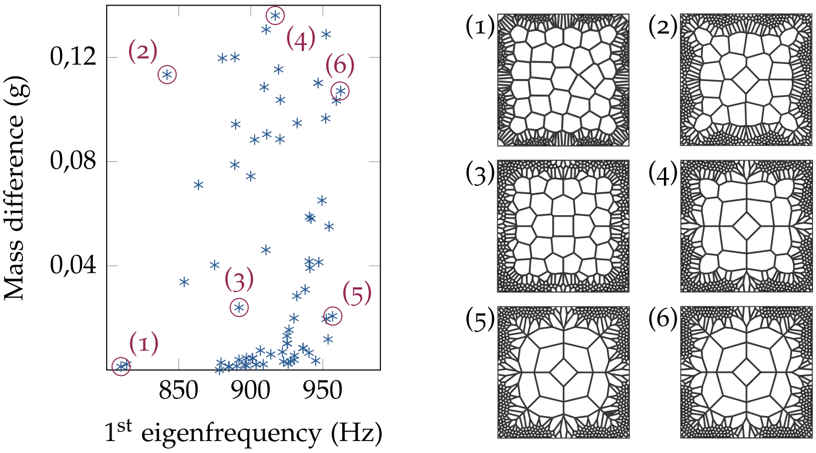

Figure 10.6: For the irregular Voronoi plates of the last optimisation generation, the 1st eigenfrequency and the absolute mass difference compared to the reference plate are displayed. All plates with a maximum absolute mass differences of 0.15 g compared to the reference mass of 20.00 g are considered. Six Voronoi cell configurations circled in red are displayed on the left hand side.

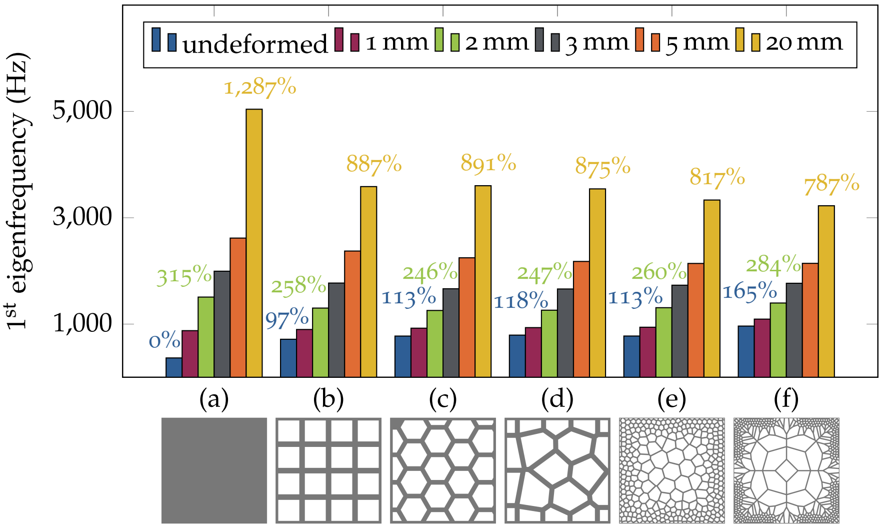

Figure 10.7: 1st eigenfrequency depending on the maximum pre-deformations of 0 mm (undeformed), 1 mm, 2 mm, 3 mm, 5 mm, and 20 mm according to the 1st mode shape for different plates (constant mass of 20 g, varying plate thickness) including a solid plate (a), regular rectangular plate (b), regular hexagonal plate (c), quasi-regular Voronoi plate (d), irregular Voronoi plate (manually) (e), and irregular Voronoi plate (optimised) (e). The deviation compared to the undeformed solid plate's 1st eigenfrequency is given for maximum pre-deformations of 0 mm, 2 mm, and 20 mm.

regular Voronoi plate had similar cell sizes. Regarding the undeformed plates, their 1^{st} eigenfrequencies showed similar values of 715 Hz, 775 Hz, and 792 Hz, respectively. The manually constructed irregular Voronoi plate, which showed a cell size interpolation similar to the diatom *Thalassiosira* sp., had the same 1^{st} eigenfrequency like the honeycomb plate. Optimising the irregular Voronoi cell configuration, however, led to a maximum 1^{st} eigenfrequency of 962 Hz. Thus, without applying pre-deformations, the 1^{st} eigenfrequency was increased by 165% compared to the solid plate of the same mass.

Pre-deforming the plates according to the 1^{st} mode shape, however, led to a significantly higher 1^{st} eigenfrequency increase for all plates than the application of irregular cellular structures. The solid plate already reached a 1^{st} eigenfrequency increase of 141% by applying a pre-deformation of only 1 mm height ($\delta = 0.5$). From a pre-deformation of 2 mm on, the 1^{st} eigenfrequency increase of the solid plate was always the highest compared to all lightweight plates. Overall, the 1^{st} eigenfrequency rose most for the solid plate (up to 5,041 Hz for $\delta_{max} = 20$ mm), while the cellular plates with a maximum pre-deformation of 20 mm showed similar increases (between 3,226 Hz for the irregular optimised Voronoi plate and 3,602 Hz for the regular hexagonal plate).

Figure 10.8 shows all six plates pre-deformed by a maximum value of 20 mm according to the 1^{st} mode shape. It has to be noted that all pre-deformed plates exhibited plate thicknesses lower than 2 mm to meet the constant mass of 20 g. Regarding the pre-deformation of 20 mm, for example, the solid plate's thickness was only 0.68 mm and the thickness of the optimised irregular Voronoi was 1.87 mm.

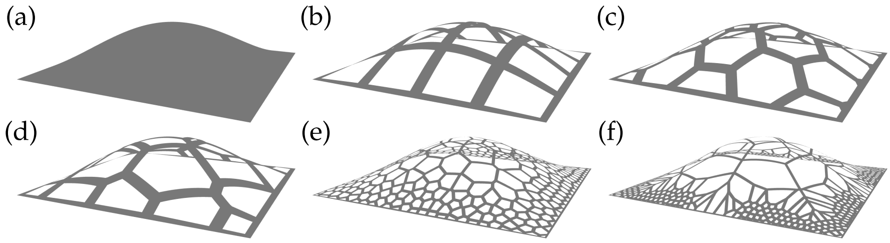

Figure 10.8: A solid plate (a), regular rectangular plate (b), regular hexagonal plate (c), quasi-regular Voronoi plate (d), irregular Voronoi plate (manually) (e), and irregular Voronoi plate (optimised) (e) pre-deformed according to the corresponding 1^{st} mode shape ($\delta_{max} = 20$ mm).

10.3 DISCUSSION

Both an increasing cell complexity and a rising plate pre-deformation according to the 1^{st} mode shape led to a 1^{st} eigenfrequency increase.

Regarding the Voronoi plate, the results showed a 1^{st} eigenfrequency increase with rising Voronoi cell size. As the material properties and the overall plate geometry remained constant, the eigenfrequency increase was mainly based on the stiffness increase due to an improved material distribution. Similar results were obtained by Tekoğlu et al. [168], who presented a Young's modulus increase with increasing foam cell size.

The last generation of an evolutionary strategic optimisation contained the individuals with the highest fitness, thus the irregular Voronoi plates with the highest 1^{st} eigenfrequencies. All optimised plates were characterised by small Voronoi cells close to the simply supported plate edges, which led to an increased stiffness. At the same time, material was removed from the plate middle, which showed the highest amplitude of the 1^{st} bending plate mode. A similar gradient in Voronoi cell size can be observed in some diatoms (cf., figure 10.2). Regarding the irregular Voronoi plates displayed in figure 10.6, the 1^{st} eigenfrequencies varied in a range of approximately 150 Hz although the plate geometries looked similar. This indicates the high potential of small geometrical changes to influence the eigenfrequencies significantly. It has to be noted, though, that the conducted evolutionary strategic optimisations possibly did not reveal best possible irregular Voronoi plates and that further optimisations with altered settings might lead to higher 1^{st} eigenfrequencies (cf., chapter 9.3.3).

The comparison of all plates revealed a progressive 1^{st} eigenfrequency increase from the solid plate to the regular and up to the irregular plate. Also Mukhopadhyay and Adhikari [113] have stated a 1^{st} eigenfrequency increase with rising structural irregularities.

It is known that sandwich panels show high eigenfrequencies due to their high bending stiffness per mass [46]. Replacing a regular with an irregular core structure is expected to even raise the eigenfrequencies further, which might prevent resonance phenomena by shifting the eigenfrequencies out of the range of external exciting frequencies.

The plate pre-deformation resulted in extremely high eigenfrequency increases. Small pre-deformations of the solid plate led already to a 1^{st} eigenfrequency that was higher than that of the irregular plates. Compared to these exceedingly high 1^{st} eigenfrequency increases of the solid plate, the application of irregular cellular structure raised the 1^{st} eigenfrequency less strongly. A combination of both methods, the application of irregular structures and the mode shape adaptation, is not a promising design approach, as it even led to poorer results than using only the mode shape adaptation.

Although the reached eigenfrequency increases due to the structural irregularities seem to be small compared to those achieved with the mode shape adapation method, eigenfrequency increases of more than 100% are still high values. Since given technical specifications do not always allow a global deformation of the structure, the application of irregular core structures might be easier to realise. Moreover, additional functions of a cellular core, e.g., a good heat dissipation performance, are still possible. Regarding the realisation of sandwich plates with the here studied, irregular Voronoi structures as cores, the manufacturing process is certainly more complex than for core structures composed of a foam structure or regular honeycombs, which has to be taken into account when complex core structures are implemented.

In this study, only the core structures have been simulated. In future investigations, the top and lower layer of the sandwich panel should be included in the simulation, as they will have a strong impact on the mechanical properties. Dai et al. [35] studied the eigenfrequencies and mode shapes of different sandwich structures with a honeycomb core varying the top and bottom layer thickness. Since the thickness increase involved a nonlinear increase of mass and stiffness, the resulting 1^{st} eigenfrequency raise was accompanied by mode order switching (note: resulting mode shapes are always ordered depending on their frequency). Thus, the inclusion of top and bottom layers in this study would probably also lead to alterations in mode shape orders, which should be analysed in further investigations.

10.4 CONCLUSION

The investigations showed the high potential of biologically inspired, irregular Voronoi plates not only for lightweight design structures, but also for structures with improved vibration properties, i.e., increased eigenfrequencies. The 1^{st} eigenfrequency was significantly raised by using irregular cellular structures. In addition, the mode shape adaptation led to even higher frequency increases.

11

REGULAR AND IRREGULAR LATTICE STRUCTURES

Irregular lattice structures show improved mechanical properties compared to regular lattice structures, as already mentioned in chapter 2. However, the impact of structural irregularities in lattice structures on the eigenfrequencies has hardly been investigated. Thus, in this study, a regular strut-based lattice structure was compared to irregular strut-based lattice structures characterised by different degrees of structural irregularities. The procedure of this study displayed in figure 11.1 is divided intro three parts including the lattice design and optimisation, vibration measurements, and further lattice optimisations.

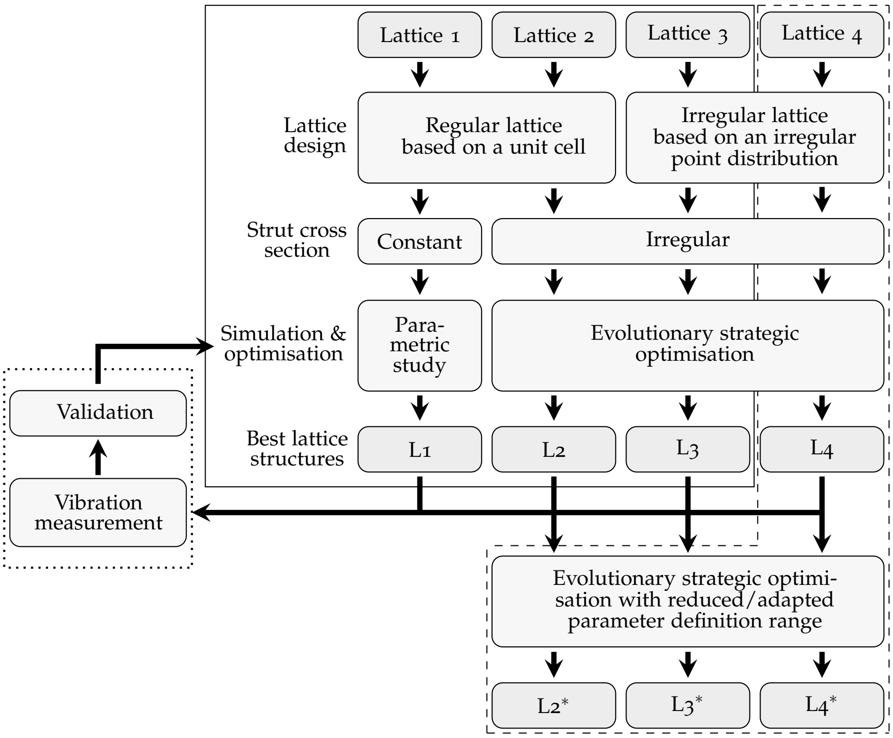
Lattice 1
Lattice 2
Lattice 3
Lattice 4
Lattice design
Regular lattice based on a unit cell
Irregular lattice based on an irregular point distribution
Strut cross section
Constant
Irregular
Simulation & optimisation
Para-metric study
Evolutionary strategic optimisation
Best lattice structures
L1
L2
L3
L4
Validation
Vibration measurement
Evolutionary strategic optimisation with reduced/adapted parameter definition range
L2*
L3*
L4*

Figure 11.1: Overview of the study on regular and irregular lattice structures containing the lattice design and optimisation (solid line), vibration measurements (dotted line), and further lattice optimisations (dashed line).

11.1 MATERIAL AND METHODS

11.1.1 *Lattice Design and Optimisation*

To evaluate the impact of structural irregularities in lattices on the vibration characteristics, three lattice structures were designed and simulated: (a) a regular lattice with constant strut cross sections, (b) a regular lattice with irregular strut cross sections, and (c) an irregular lattice with irregular strut cross sections. Each lattice was constructed inside a defined design space (figure 11.2), which was connected to four blocks with bore holes to screw the lattice onto an adapter plate during the subsequent vibration measurements. While the four blocks were meshed with solid elements (CTETRA), the lattice struts were incorporated as beams (CBEAM) connected to the blocks via Rigid Body Elements (RBE3s). The blocks' lower surfaces were mounted. The aluminium alloy AlSi10Mg (Young's modulus: 75,000 MPa, density: $2.7\,10^{-9}\,\mathrm{t\,mm^{-3}}$, Poisson's ratio: 0.33) was defined as a lattice material. A modal load case was specified to obtain the structure's eigenfrequencies. The three types of lattices were designed as follows:

a. *Regular lattice with constant strut cross sections (Lattice 1)*:
   This lattice was based on a simple unit cell composed of four diagonal struts (figure 11.3a). A parametric study varying the number of unit cell repetitions in each axis from 2 to 8 for axes x and y and from 1.5 to 7.5 for axis z was conducted. The circular strut cross section with a diameter of 2.08 mm remained constant. Regarding the evaluation, only lattice structures with angles between the strut and the horizontal axis of more than 35° were considered, as demanded by the subsequent additive manufacturing process. The lattice structure with the lowest mass at a 1st eigenfrequency of 1,500 Hz (value given by the later-used test facility operating sphere) was chosen as test body L1.

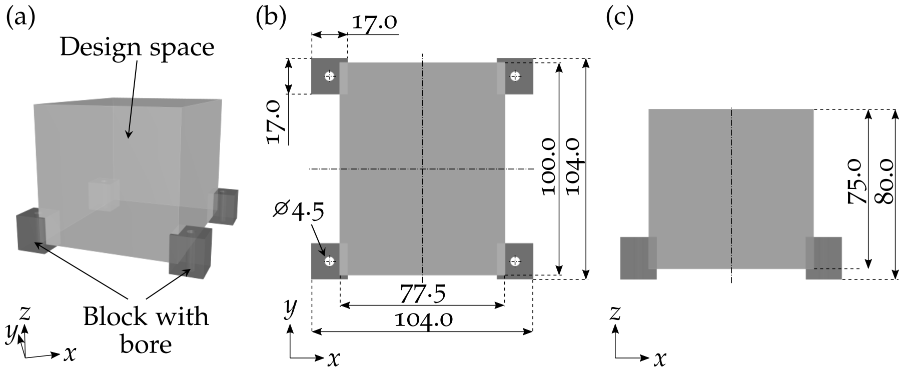

Figure 11.2: 3D view (a), top view (b), and side view (c) of the lattice design space. The dimensions are given in mm.

b. *Regular lattice with irregular strut cross sections (Lattice 2)*:

This lattice configuration corresponded to the chosen L1 structure. To provide varying diameters of the circular cross sections along one strut, each strut was divided into three to five sections, depending on the strut length. The parametric strut diameters were interpolated as shown in figure 10.4 considering the lower design space-surface as the attractor. The parameter definition ranges and start values are summarised in table 11.3.

The strut cross section optimisation was conducted utilising the optimiser Octopus implemented in Grasshopper to perform evolutionary strategic optimisations (c.f., introduction of chapter 9) considering different objective functions. The objectives were (1) the maximisation of the 1^{st} eigenfrequency and (2) the minimisation of the mass difference compared to the structural mass of the chosen L1 structure (m_{L1}), which both formed the fitness in equal parts. The optimisation settings are summarised in Table 9.1. The gene pool contained 100 structures, and the population size P was 50. The optimisation stopped after calculating the 20^{th} generation. Evaluating the last generation lattice structures, the lattice structure with the highest 1^{st} eigenfrequency at a maximal mass difference of 0.5% compared to m_{L1} was selected as the test body.

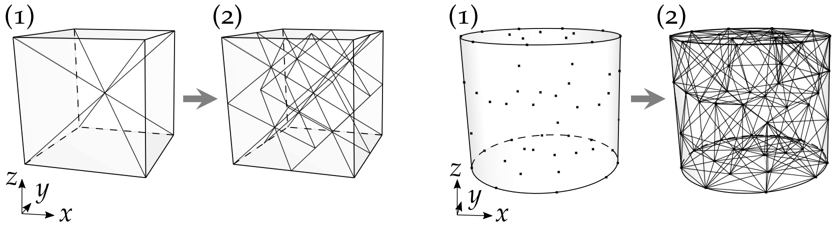

(a) A unit cell (1) multiplied by 2 in the three directions leads to a regular lattice structure (2).

(b) Connecting irregularly distributed points (1) generates an irregular lattice structure (2).

Figure 11.3: Design of a regular lattice structure based on a unit cell (a) and of an irregular lattice structure generated by connecting points distributed in a body (b).

c. *Irregular lattice with irregular strut cross sections (Lattice 3)*:

The irregular lattice design was based on a point distribution inside the design space. The point distribution density was interpolated as previously illustrated in figure 10.4 with the design space centre point as the attractor. Similar to the irregular lattice construction performed by Nourbakhsh et al. [119], the lattice structures were constructed by connecting each point to a varying number of neighbouring points (figure 11.3b). In the case of two struts forming an angle smaller than 20°, the larger strut was discarded in order to avoid disorder. The irregular strut cross section diameters were interpolated analogous to Lattice 2. All parameter definition ranges and starting values (i.e., middle value of each range) are listed in table 11.2.

The optimisation process was conducted in the same way as that of Lattice 2. However, the gene pool contained 200 structures, and the population size was augmented to 100 because of the higher number of parameters. To conform with Lattice 2, all lattice structures of the last generation were evaluated. The chosen test body corresponded to the lattice with the highest 1st eigenfrequency at a maximal mass difference of 0.5% compared to m_{L1}.

The three lattice test bodies chosen were transformed into 3D models and meshed with CTETRA elements (element size 0.5 mm). Modal analyses with boundary conditions in analogy to the beam models led to structural eigenfrequency values of the solid models. Both the beam and solid models were also calculated considering three ac-

Table 11.1: Parameter definition ranges and start values for the lattice strut cross section interpolation.

	Global diameter	Attractor radius	Attractor area radius	Attractor decay factor
Range	2.00-3.00 mm	1.50-2.30	30-50 mm	1.0-2.0
Start value	2.50 mm	1.90 mm	40 mm	1.1

Table 11.2: Parameter definition ranges and start values for the Lattice 3 optimisation.

Point distribution density				
	Global distance	Attractor distance	Attractor area radius	Attractor decay factor
Range	10.0-40.0 mm	5.0-40.0 mm	2.0-4.0 mm	5-20
Start value	25.0 mm	22.5 mm	3.0 mm	13
Connecting neighbouring points				
	Number of neighbours	Min. angle between strut & horizontal	Min. angle between two struts	
Range	5-30	35°-60°	20°-60°	
Start value	18	48°	40°	
Strut cross section diameter				
	Global diameter	Attractor diameter	Attractor area height	Attractor decay factor
Range	1.5-5.0 mm	1.5-5.0 mm	10-40 mm	2.0-4.0
Start value	3.3 mm	3.3 mm	25 mm	3.0

celerometers, each as a point mass of 0.6 g, which were implemented in the subsequent vibration measurements. To compare the 1st eigenfrequencies obtained by the beam model and the solid model, the differences were calculated using equation 8.11.

The three lattice test bodies were manufactured with AlSi10Mg using the selective laser melting additive manufacturing system EOS M 290.

11.1.2 *Lattice Vibration Measurements*

The vibration measurements were performed at the Deutsches Zentrum für Luft- und Raumfahrt (German Aerospace Centre) (DLR) vibration laboratory in Bremen, Germany. During measurements, the cleanroom (class ISO 8) had a constant temperature of 20.5 ± 0.5°C at ambient pressure and a constant humidity of 57.5 ± 1.5% rF. The test facility TIRAvib 51010 / LS (TIRA GmbH) was used.

The test bodies were screwed to an aluminum adapter plate as shown in figure 11.4. Two uniaxial accelerometers (Delta Shear, Type 4371, Brüel & Kjær) controlling the vertical movement of the shaker, and one triaxial accelerometer (Triax-ICP, Type 356A33, PCB Piezotronics, Inc.) were fixed with resin to the adapter plate. Each test body was equipped with three uniaxial accelerometers (Delta Shear, Type 4517-C, Brüel & Kjær) at three different positions connected to a charge amplifier (Type 2692 Nexus, Brüel & Kjær).

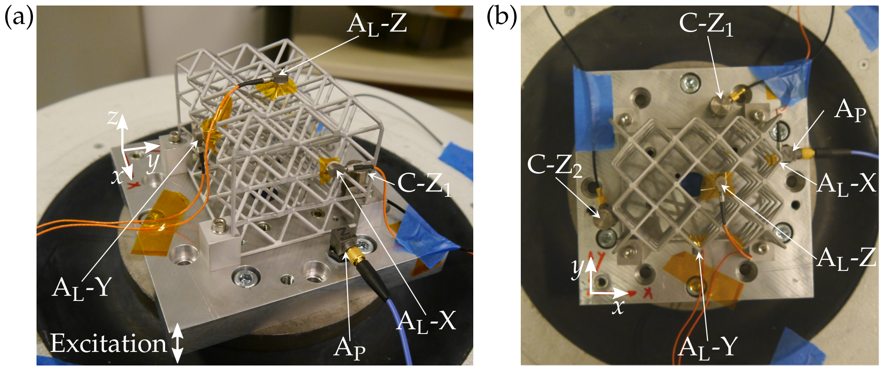

Figure 11.4: 3D (a) and top view (b) of the vibration test setup for L1 lattice structure including uniaxial control accelerometers C-Z_1 and C-Z_2, a triaxial accelerometer on the adapter plate A_P, and three uniaxial accelerometers on the lattice structure A_L-X, A_L-Y, and A_L-Z.

Vertical acceleration considering sinusoidal and random vibration was applied to each of the three test bodies. Random vibration was employed for 4min per test body with a frequency resolution of 0.5 Hz. Sine-up and sine-down sweeps were then conducted with a sweep rate of $1\,\mathrm{Hz\,s^{-1}}$. The vibration test levels are summarised in table 11.3. For each test body, the first three eigenfrequencies and the vibration amplitude were calculated. Differences between the solid model and the measurement results were obtained by equation 8.11. The half-power bandwidth method demonstrated in figure 11.5 was used to estimate the damping ratio for the 1^{st} eigenfrequency in excitation direction z of each test body. This method assumes a symmetrical response curve, light damping, and no effect of neighbouring modes on the analysed mode [24]. The damping ratio ζ was defined as

$$\zeta = \frac{1}{2}\frac{f_{max} - f_{min}}{f} \tag{11.1}$$

Here, f denotes the resonance frequency (eigenfrequency) and f_{min} and f_{max} the frequencies at the half-power amplitude $\left(\hat{x}/\sqrt{2}\right)$ with $\hat{x}$ symbolising the vibration amplitude. The calculated damping ratios for the 1^{st} eigenfrequency were applied to the frequency response analysis of each structure to assess the consistency between simulations and measurements.

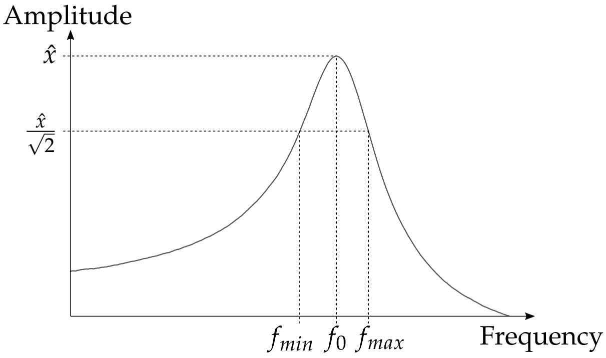

Figure 11.5: Application of the half power bandwidth method to the vibration amplitude plot.

Table 11.3: Sinusoidal (a) and random (b) vibration test levels.

	Test body	Frequency range	Level	Overall level
a)	Lattice 1 (L1)	600-2,500 Hz	1.0g	-
	Lattice 2 (L2)	1,400-3,000 Hz	1.0g	-
	Lattice 3 (L3)	2,000-4,000 Hz	1.0g	-
b)	Lattice 1 (L1)	500-2,500 Hz	$5.0 \cdot 10^{-4}\, g^2\, \mathrm{Hz}^{-1}$	$1.000\, g_{RMS}$
	Lattice 2 (L2)	500-2,500 Hz	$5.0 \cdot 10^{-4}\, g^2\, \mathrm{Hz}^{-1}$	$1.000\, g_{RMS}$
	Lattice 3 (L3)	500-4,000 Hz	$3.0 \cdot 10^{-4}\, g^2\, \mathrm{Hz}^{-1}$	$1.025\, g_{RMS}$

11.1.3 *Further Lattice Optimisation*

The initial optimisation round comprised 1^{st} eigenfrequency maximisations of different lattice structures, including the structure fabrication and the execution of experiments. Additional optimisations were then conducted to investigate the possible development of further-improved lattice structures. Based on the optimised lattice structures for Lattices 2 and 3, the parameter definition ranges were confined so that the parameter values of the printed structures remained inside the newly defined ranges. For both Lattices 2 and 3, optimisations configured as previously were conducted, and the results were evaluated likewise, leading to the best structures $L2^*$ and $L3^*$.

To analyse whether the acceptance of struts oriented less than 35° to the horizontal leads to structures with higher eigenfrequencies, another optimisation was conducted. Here, the lattice generation and the optimisation approach were based on those of Lattice 3, but the minimum angle between the struts and the horizontal plane was set to 0° permitting the development of horizontal struts. After obtaining the best lattice structure based on the specified evaluation method (Lattice L4), the parameter definition ranges were reduced around the parameter values of the obtained best lattice structure as before. Furthermore, the maximum number of generations was changed from 20 to 40 to provide a longer optimisation process. The evaluation method led to the best lattice structure $L4^*$.

11.2 RESULTS

11.2.1 *Lattice Design and Optimisation*

Figure 11.6 shows the parametric study results filtered by a minimum angle between the strut and the horizontal of 35°. The lattice structure revealing the lowest mass of 127.7 g at a 1^{st} eigenfrequency of 1,500 Hz was chosen as lattice L1. It was built by three, four, and three and a half unit cell repetitions in the x, y, and z axes, respectively.

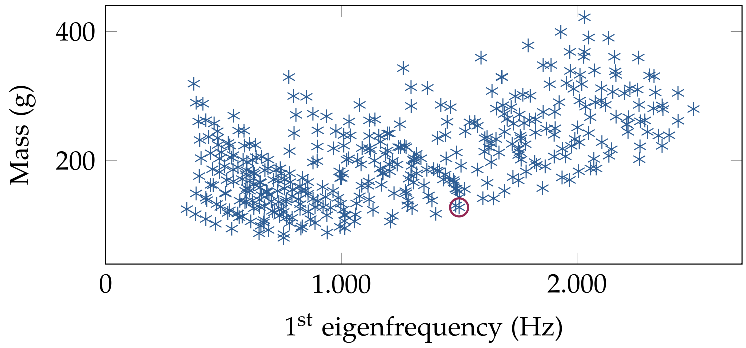

Figure 11.6: Parametric study results for lattice 1. The red circled data point indicate the chosen lattice L1.

Figure 11.7a displays the structures forming part of the last generation developed during the optimisation process for lattice 2. The structure with the lowest mass difference compared to Lattice 1 of 0.03 g and a 1st eigenfrequency of 1,615 Hz was selected as the test body L2. The global strut cross section diameter was 2.41 mm, the diameter at the attractor was 1.79 mm, the attractor space height was 40 mm, and the attractor decay factor was 1.1. Thus, the application of the strut diameter grading from larger diameters at the lower part of the structure to smaller diameters at the top led to an 1st eigenfrequency increase of 7.7% compared to that of lattice L1.

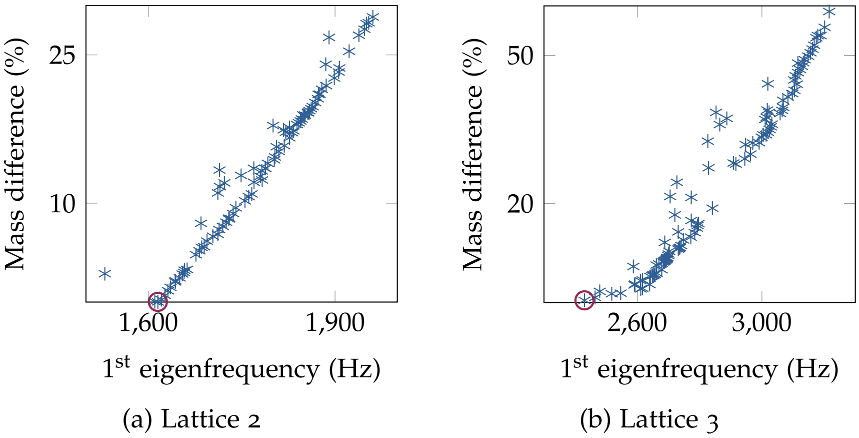

(a) Lattice 2

(b) Lattice 3

Figure 11.7: Optimisation results for lattice 2 (a) and lattice 3 (b). The red circled data point indicate the chosen lattices L2 and L3, respectively.

Figure 11.7b shows the last generation structures for Lattice 3. The structure with the lowest mass difference compared to structure L1 of 0.55 g and a 1st eigenfrequency of 2,430 Hz was chosen as the test body. Table 11.4 summarises the defined parameter values for reaching the chosen lattice design. The obtained lattice structure's 1st eigenfrequency was increased by 62% compared to the L1 structure. The three chosen lattice structures L1, L2, and L3 are illustrated in figure 11.8. L2 differs from L1 by showing graded stut cross section diameters from smaller values at the bottom to higher values at the top. The irregular lattice structure L3 has two symmetry axes parallel to the *xz* and the *yz* plane.

Table 11.5 summarises the 1st eigenfrequencies for the three test bodies obtained by the beam and the solid model, as well as by neglecting or including the accelerometers. The inclusion of the accelerometers resulted in slightly lower frequency values for both models. The eigenfrequencies obtained by the beam models including the attached accelerometers were about 7%–22% lower than that of the solid models. The masses of L1, L2, and L3 showed only small differences for both models. However, the conversion of the beam models into solid models led to a slight decrease in mass up to 7%. The structural masses of the manufactured lattice structures L1, L2, and L3 were 124.9 g, 124.6 g, and 123.4 g, respectively, and differed less than 5% from the solid model masses (table 11.5).

Table 11.4: Defined parameter values for the chosen L3 lattice structure.

Point distribution density	Global distance	Attractor distance	Attractor area radius	Attractor decay factor
Value	36.5 mm	16.0 mm	2.5 mm	12
Connecting neighbouring points	Number of neighbours	Min. angle between strut and horizontal	Min. angle between two struts	
Value	18	59°	33°	
Strut cross section diameter	Global diameter	Attractor diameter	Attractor area height	Attractor decay factor
Value	2.5 mm	2.1 mm	22 mm	2.5

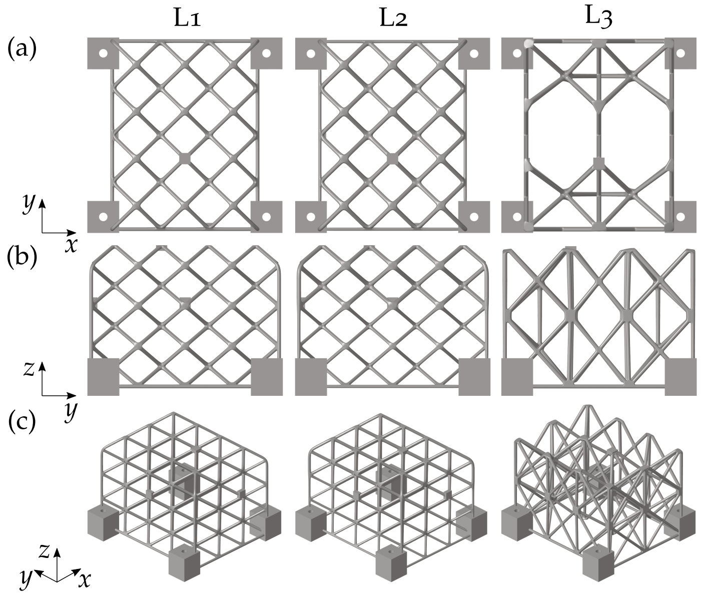

Figure 11.8: Top view (a), side view (b), and 3D view (c) of the lattice structures L1, L2, and L3.

Table 11.5: 1st eigenfrequencies of the three test bodies L1, L2, and L3 obtained by the beam model and solid model, both with accelerometers (acc.) neglected (negl.) and included (incl.), as well as the model masses and the eigenfrequency deviation of the beam models to the solid models with accelerometers included.

	Beam model			Solid model			Dev.
	negl. acc.	incl. acc.	mass	acc. negl.	acc. incl.	mass	acc. incl.
L1	1,500 Hz	1,471 Hz	127.7 g	1,925 Hz	1,895 Hz	119.3 g	-22.4%
L2	1,615 Hz	1,586 Hz	127.7 g	2,073 Hz	2,028 Hz	119.1 g	-21.8%
L3	2,430 Hz	2,404 Hz	127.2 g	2,619 Hz	2,581 Hz	121.4 g	-6.9%

11.2.2 *Lattice Vibration Measurements*

The obtained 1st eigenfrequencies of the three lattice structures by applying random vibration and by performing sine-up and sine-down sweeps are shown in table 11.6. The random and sine sweep eigenfrequency values coincided very well. For L1 and L2, the three accelerometers measured the same eigenfrequency values. However, the 1st eigenfrequency in the z direction of L3 was significantly higher than that in the x and y direction. Table 11.6 also lists the calculated damping ratios for the three structures using the half-power bandwidth method. Lattice L3 showed the lowest damping ratio of 0.0026 for the 1st eigenfrequency in excitation direction z followed by L1 with 0.0044. The highest damping ratio of 0.01 was calculated for L2. Applying the averaged damping ratios to the frequency response analysis showed response curves similar to the measured values as exemplarily shown in figure 11.9 for L3. The peak position values of 3,725 Hz for the simulation and 3,877 Hz for the experiment differed by 3.9%, whereas the peak height of 17.3 for the experiment was 23.7% higher than the simulation peak height of 13.2. For the lattices L1 and L2, the frequency response analysis plots compared to the experimental results are displayed in appendix chapter A.4.

Comparing the measured eigenfrequencies with the numerically obtained eigenfrequencies of the solid model with attached accelerometers showed a deviation of less than 5% (table 11.7). For all structures, the numerically obtained values were slightly higher.

Table 11.6: Measured 1^{st} eigenfrequencies obtained by the application of random and sinusoidal-up and -down excitation and calculated damping ratios ζ in z direction for the 1^{st} eigenfrequency.

		Random	Sine up	Sine down
L1	x	1,812 Hz	1,809 Hz	1,807 Hz
	y	1,811 Hz	1,814 Hz	1,815 Hz
	z	1,810 Hz	1,809 Hz	1,807 Hz
	ζ in z direction	0.0044	0.0043	0.0044
L2	x	1,995 Hz	2,009 Hz	2,010 Hz
	y	1,995 Hz	2,007 Hz	2,008 Hz
	z	1,995 Hz	2,003 Hz	2,005 Hz
	ζ in z direction	0.0104	0.0096	0.0100
L3	x	2,565 Hz	2,568 Hz	2,570 Hz
	y	2,565 Hz	2,568 Hz	2,570 Hz
	z	3,877 Hz	3,877 Hz	3,879 Hz
	ζ in z direction	0.0026	0.0026	0.0026

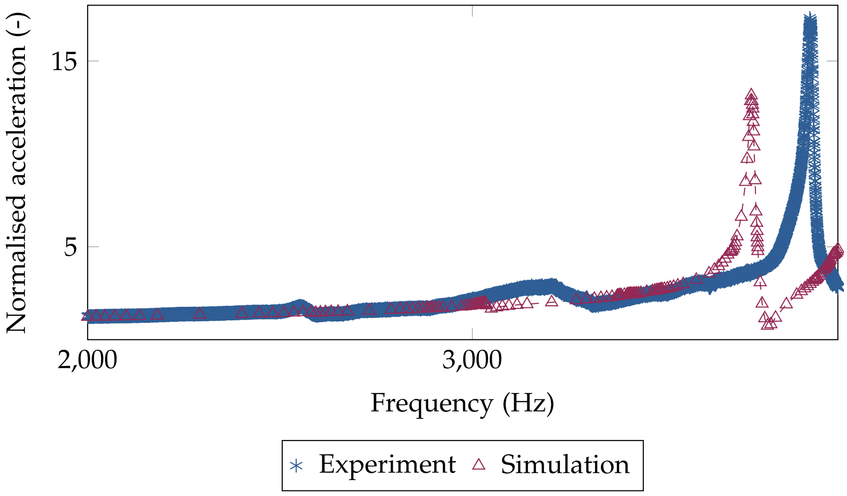

Figure 11.9: Frequency response curves for L3 obtained by experiment and simulation using a solid model including accelerometers with a damping ratio of 0.0026.

11.2.3 *Further Lattice Optimisation*

The measured data coincided well with the numerical data of the solid models, therefore, the solid model results were also considered in the further lattice optimisations. Figure 11.10 shows the 1^{st} eigenfrequency of the four lattice structures and the further-optimised lattice structures L2*, L3*, and L4*. Although there was only a slight difference in the eigenfrequency values of L2 and L2*, further optimisations led to significantly higher 1st eigenfrequencies for L3* and L4* compared to the lattice structures of the first optimisation. Altogether, the 1st eigenfrequency was increased by 58% comparing L4* to L1. All lattice masses differed by less than 3% from the L1 solid mass (figure 11.11).

The chosen lattice structures of each model are displayed in figure 11.12. While L2* was very similar to L2, the struts and their cross sections of L3* differed from L3. The lattice structure L4* showed a higher structural complexity than L4.

Table 11.7: 1st eigenfrequency obtained by simulation using a solid model including accelerometers and by measurements based on sinusoidal-up excitation. The deviation between the measured and the simulated 1st eigenfrequency is also given.

	Simulation	Measurement	Deviation
L1	1,895 Hz	1,809 Hz	-4.5%
L2	2,028 Hz	2,003 Hz	-1.2%
L3	2,581 Hz	2,568 Hz	-0.5%

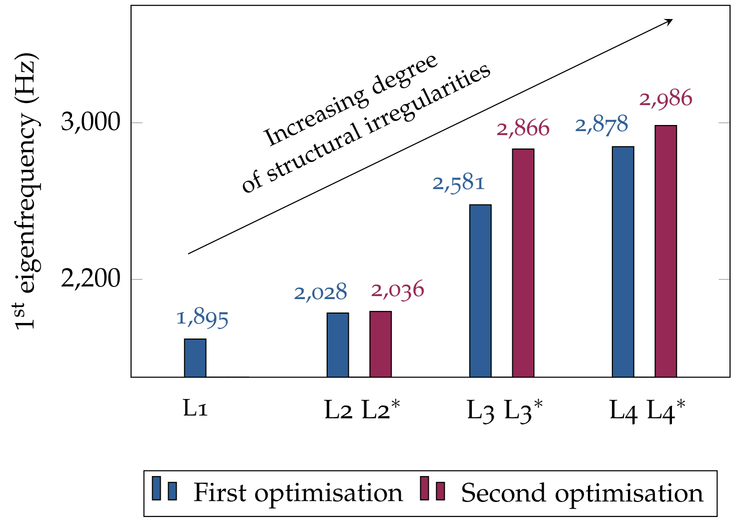

Figure 11.10: 1st eigenfrequency obtained numerically using solid models including accelerometers for different lattices. The eigenfrequency values are given above each bar.

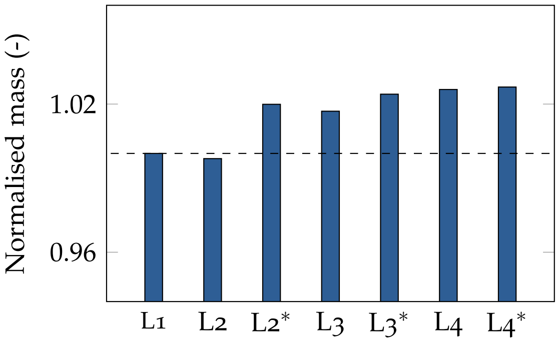

Figure 11.11: For all optimum lattice structures, the mass values obtained numerically using solid models normalised with the L1 mass of 119.3 g are given. The dashed black line at a normalised mass value of 1.0 represents the L1 mass.

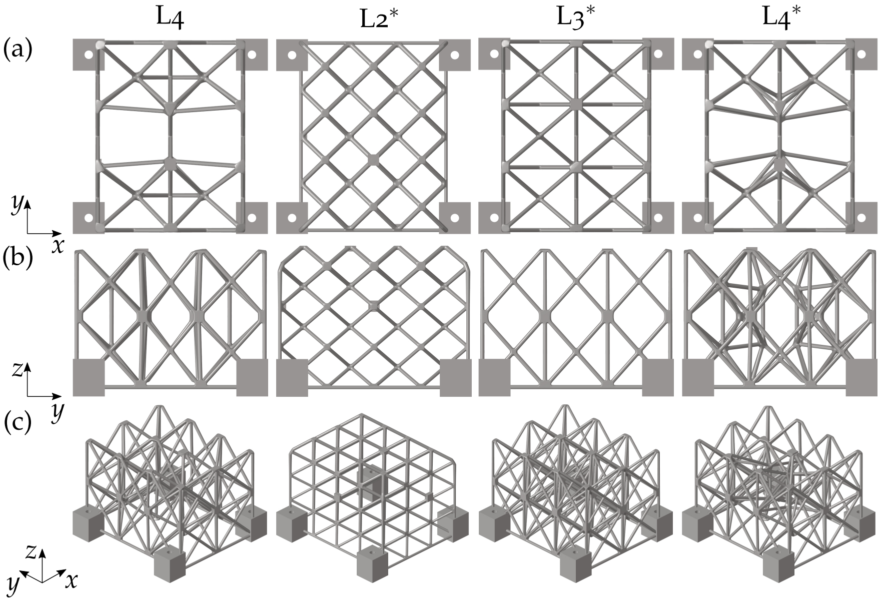

Figure 11.12: Top view (a), side view (b), and 3D view (c) of the lattice structures L4, L2*, L3*, and L4*.

11.3 DISCUSSION

11.3.1 *Lattice Design and Optimisation*

The lattice design method used allowed the development of lattice structures with increasing degrees of structural irregularity involving an enhancement of the structural eigenfrequencies. It was possible to increase the 1st eigenfrequency by 7% from L1 to L2 and by 36% from L1 to L3. Using beam models facilitated the optimisation procedure because far less computational time was required in comparison to that of the solid models.

The regular lattice with a constant stut cross sections L1 was based on a simple unit cell with diagonal struts. Considering the vibration analyses of different regular lattice structures conducted by Syam et al. [166], it is likely that the inclusion of horizontal struts into the unit cell forming the structure L1 leads to a higher 1^{st} eigenfrequency. Also Zhao et al. [208] showed in their studies that the 1^{st} eigenfrequency of a uniform lattice depends on the unit cell shape. However, as our aim was to meet the fabrication requirements of the angles between the struts and the horizontal of more than 35°, the horizontal struts were neglected.

The optimisation results for Lattice 2 and 3 showed an increase in the 1^{st} eigenfrequency with an increase in the mass difference compared to the structural mass of L1. Regarding a SDOF system, the eigenfrequency f depends on the root of the stiffness divided by the mass (cf., equation 6.21). Thus, a larger lattice mass can lead to a lower eigenfrequency. However, in this study, the increasing mass owing to changes in the lattice structures results in a higher stiffness and thus to enhanced eigenfrequencies.

The defined optimisation objectives led to structures with high eigenfrequencies and low mass differences. However, most of the last-generation structures showed masses exceeding the aimed 0.5% mass difference compared to the mass of L1, and were therefore neglected. The 1^{st} eigenfrequencies of the chosen L2 and L3 structures were among the lowest 1^{st} eigenfrequencies of all structures forming the last generation while complying with the weight limit. It is likely that improving the definition of the optimisation objectives will result in more structures with acceptable (e.g. lower) mass differences, e.g., by implementing the mass difference constraint directly into the evolutionary algorithm.

The stut cross sections of the structure L2 were graded from a thinner cross section diameter at the bottom to a higher diameter at the top. The results showed that the applied small-scale grading led already to an eigenfrequency increase of almost 8%. Maskery et al. [105], Cheng et al. [32], and Plocher and Panesar [135] also showed that the implementation of grading to regular lattice structures leads to improved properties.

The conversion of the beam models into solid models led to a slight decrease in mass, because the strut intersection points were combined to form one solid connection. This connection was stiffer than the connection simulated in the beam model. Therefore, the overall 1^{st} eigenfrequency was also higher. As L1 and L2 were quite similar, the differences between the beam and solid model results coincided. However, for L3, the differences between the beam and solid model were far less because of the lower number of strut intersection points compared to that of L1 and L2. Accordingly, there was a smaller increase in stiffness in the solid model compared to the beam model for structure L3 and consequently a smaller increase in the 1st eigenfrequency.

11.3.2 *Lattice Vibration Measurements*

The measured 1st eigenfrequency based on the random and the sine-up and -down excitation coincided very well indicating a successful experiment. Moreover, the numerical results of the solid models corresponded to the measurement results by more than 95%. The slightly higher simulation results might result from the high stiffness of the fixed support in comparison to the fixation of the lattice structures with four screws to the adapter plate during measurements. Thus, the higher stiffness led to slightly higher eigenfrequencies in the simulation.

The masses of the additive manufactured structures hardly differed from those of the solid model masses indicating a successful manufacturing process. However, the manufactured lattice structures were not analysed in detail to check for the existence of cracks or microstructural imperfections.

Previous studies comparing numerical results with measurements on additive manufactured lattice structures revealed differences between simulation and measurement results of less than 4% for the 1st eigenfrequency [32], of 4%-14% for the 1st eigenfrequency and the stiffness [166], and of 4%-18% for elastic moduli [106]. In the two latter studies, the differences were justified with imperfections in the material properties and, in the last case, with a high surface roughness of the additive manufactured structures, which can lead to a reduction in stiffness. However, the differences between measurements and simulations were quite low in the present study. Because of this successful validation, the numerical results of the further lattice optimisations can be seen as a realistic prediction for future realised lattice structures.

The calculated damping ratios were the highest for L2, followed by L1 and L3. For all three lattice structures, the damping ratios of the sine-up and -down excitation coincided very well, although the values were rather low. Considering the analysis of Wang et al. [185] on estimating the possible error by using the half-power bandwidth method for calculating damping ratios, the obtained damping ratios have to be treated with caution, because the method is originally based on the frequency response of a single degree of freedom system and might thus overestimate the damping ratios. However, the numerically obtained frequency response curve showed good conformity with the measurements, especially regarding the peak positions. The existing differences in the amplitude values might indicate an overestimation of the damping ratio in the simulation, because the consideration of the calculated damping ratios in the simulation led to lower amplitudes than in the experiments.

Separate systematic investigations to analyse the damping properties of lattice structures with different degrees of structural irregularities would be highly promising for potential applications, because eigenfrequencies apparently do not correlate with damping properties.

It was not possible to verify the calculated eigenmodes of the lattice structures experimentally, because the three uniaxial accelerometers were placed at different locations. In continuative studies, the lattice structures should be equipped with more triaxial accelerometers to measure not only the eigenfrequency, but also the mode shape. This also allows a more precise characterisation of the damping ratios of each lattice structure. In this study, however, the intention of the vibration measurements was to obtain the eigenfrequencies to validate the simulation results.

11.3.3 *Further Lattice Optimisation*

The evolutionary strategic optimisation was used to generate optimised lattice structures, because it allowed the generation of multiple optimised structures that represent a compromise of various defined objectives. Moreover, the evolutionary strategic optimisation can be applied to optimisation problems including many parameters and large parameter definition ranges, whereas the conduction of a parametric study involving the analysis of all parameter combinations would not have been possible. However, although elitism of 50% was specified to avoid local optimisation, the optimisation results of this approach might still not include the best possible lattice structures (c.f., discussion of methodology in chapter 9.3.3). Therefore, further lattice optimisations were conducted based on the results of the first optimisations. The aim was to develop lattice structures with even higher 1^{st} eigenfrequencies. The results showed only a slight eigenfrequency improvement of 0.4% for Lattice 2 indicating that the first optimisation had already generated an almost optimal lattice structure under the defined constraints. Regarding Lattice 3 and 4, however, further optimisations led to significantly improved lattice structures. This shows that conducting lattice optimisation in two steps is a valid approach to exploit the full potential of the respective lattice design concepts. It is important to point out that the structure L4 clearly showed a higher 1^{st} eigenfrequency than that of the structure L3. Thus, the implementation of nearly horizontally oriented struts into an irregular lattice seemed to enhance the eigenfrequency. Similar results have been published by Syam et al. [166]. Although they solely studied regular lattice structures based on different unit cells, some of the unit cells contained horizontal struts. The lattice structures with the lowest eigenfrequencies were lacking horizontal struts. However, the additive manufacturing process of lattice structures including horizontal struts involves the use of support structures that must be subsequently removed. Here, the 1^{st} eigenfrequency of the further-optimised structure $L3^{*}$ was already quite close to the 1^{st} eigenfrequency of the structure $L4^{*}$, although the latter contained nearly horizontal struts. This shows the possibility of designing lattice structures with high 1^{st} eigenfrequencies that meet the additive manufacturing requirements to reduce the amount of support structures. However, it is likely that the implementation of higher degrees of irregularities and more delicate structures would lead to even higher 1^{st} eigenfrequencies. This should be demonstrated in further studies focusing on eigenfrequency maximisation without manufacturing restrictions.

11.4 CONCLUSION

The design and optimisation of irregular lattice structures can be used to raise eigenfrequencies of technical lightweight structures. The eigenfrequency increase is a function of the degree of structural irregularities allowed. Low degrees of structural irregularities meeting additive manufacturing restrictions already increase significantly the eigenfrequencies.

12

COMPARISON OF DIFFERENT METHODS TO INCREASE EIGENFREQUENCIES

Different methods to increase eigenfrequencies have been published as summarised in chapter 4. Regarding the methods studied here, the advantages and disadvantages of evolutionary strategic optimisations have already been discussed in chapter 9.3.3. Therefore, the following paragraphs focus mainly on the mode shape adaptation method. Finally, all investigated methods to increase eigenfrequencies are compared among each other.

The main advantage of the mode shape adaptation method to increase eigenfrequencies over other types of stiffening techniques and optimisations is that stiffening and thus high eigenfrequency increase is already achieved with small computational effort. In addition, no mass increase or reduction is needed and the method is already efficient for small pre-deformations: a 1^{st} eigenfrequency increase of 300% for the beam and 221% for the plate was generated by a maximum relative pre-deformation δ of 2.0 according to the 1^{st} bending mode shape. The 1^{st} bending mode frequency of the beam was even increased by 400%. Maximum relative pre-deformations of 3.0 led to 1^{st} eigenfrequency raises of 300% for the beam and 322% for the plate. The 1^{st} bending mode frequency of the beam increased by 641%. Regarding the plate, both mentioned eigenfrequency increases corresponded to the 1^{st} bending mode shape, because no mode switching occurred.

The eigenfrequency increase of simply supported 2D beams due to the application of topology optimisations has been studied by Du and Olhoff [44]. Huang et al. [73] applied their proposed modifications of the SIMP model to avoid artificial modes also on the same 2D beam. In both studies, the 1^{st} eigenfrequency rose by about 154% including a mass reduction of 50%, which is a significantly lower eigenfrequency increase compared to shaping the beam according to its 1^{st} mode shape. The increase of the 1^{st} eigenfrequency of a squared plate with similar boundary conditions has also been investigated by using topology optimisation, where an eigenfrequency increase of 101% with a mass reduction of 50% occurred [44].

While comparing these published studies to the results obtained within this work, it has to be noted that the published studies proposed an eigenfrequency raise combined with a mass reduction. Here, the mass was contant. Considering equation **??** valid for a SDOF system, the eigenfrequency depends on the root of the stiffness divided by the mass. Thus, a mass reduction tends to increase the eigenfrequency. However, although the mass was strongly reduced in the mentioned published studies, the eigenfrequency increases obtained by the mentioned studies were still significantly lower than those received in the present work for structures having a constant mass.

A study on the optimum distribution of dimples and beads using a genetic algorithm to maximise the 1st eigenfrequency of simply supported rectangular plates was performed by Alshabatat and Naghshineh [6]. They obtained a 1st eigenfrequency increase of 25.4% considering four 9.8 mm high dimples, each in one plate corner, which corresponded to a maximum relative pre-deformation δ of 9.8, as the plate thickness was 1 mm. Their beading technique increased the 1st eigenfrequency by 160.5% based on four 8 mm high beads, i.e., a maximum relative pre-deformation δ of 8.0. Comparing these values with the plate eigenfrequency increases that were achieved using the mode shape adaptation approach, higher values occurred at all times taking similar pre-deformations into account: a plate pre-deformation according to the 1st bending mode considering a maximum relative pre-deformation of only 5.1 raised the 1st eigenfrequency by 487%. Also the evolutionary strategic and the topography optimisations resulted in significantly higher 1st eigenfrequency increases.

Another study dealt with the 1st eigenfrequency of a 2D plate by inserting a hole in the plate's middle [131]. The results showed only small eigenfrequency increases of about 4% for a simply supported plate, although the hole's shape and size was optimised. The method, however, strongly increased the 1st eigenfrequency of a clamped plate by about 44%.

As the mode shape adaptation is most similar to beading, the following text focuses on a comparison between these two techniques. The following advantages and disadvantages apply in both cases: Stiffening is achieved without any additional weight increase and without adding any joints. However, the method is limited to the material capacity to deform plastically without cracking [6]. Beading causes a higher computational effort than the shape adaptation according to mode shapes, but smaller or similar expenses in the manufacturing are expected, since the beads have to be applied only in some parts of the plate. In contrast to that, the overall plate shape needs to be adapted for the mode shape adaptation. On the one hand, this can be seen as an advantage, because the not beaded area of beaded plates should be kept as small as possible, as otherwise high stress peaks appear [150]. On the other hand, the bulging must also be possible, without restraining attached parts or the installation space. Finally, it has to be noted that the mode shape adaptation approach is highly dependent on the boundary conditions and is not applicable to structures that are not axially constrained. Moreover, the applied pre-deformations certainly lead to more complex geometries compared to the un-deformed structures, yet, the complexity of the here investigated pre-deformed structures is small in comparison to the irregular plate or lattice structures. In addition, other mentioned structural adaptation methods to raise eigenfrequencies also involve an increase of structural complexity. But the present results showed that even small pre-deformations according to mode shapes, which are supposed to be applied more easily, increased the eigenfrequencies strongly.

Figure 12.1 displays the obtained 1^{st} eigenfrequency increases based on the here investigated methods and four published studies, which aimed at a 1^{st} eigenfrequency maximisation of simply supported 2D structures. The dashed lines represent the average 1^{st} eigenfrequency increase obtained by the mode shape adaptation, the evolutionary strategic optimisations, and the remaining displayed studies including the topography optimisation and other published methods to increase eigenfrequencies. Note that the presented structures partly vary in the maximum relative pre-deformation. In addition, the structural mass is not always kept constant.

Highest 1^{st} eigenfrequency increases were obtained for the mode shape adaptation approach. The 1^{st} beam eigenfrequency did not rise as strongly as the 1^{st} eigenfrequency of the plate, because it then coincided with the 2^{nd} beam eigenfrequency. Regarding the plate, however, higher-order eigenfrequencies were also increased, which is why the 1^{st} eigenfrequency could also be raised further. Applying the mode shape adaptation method to the cellular plates also led to strong 1^{st} eigenfrequency increases that were, however, lower than the increase of the solid plate.

The evolutionary strategic optimisations resulted in average in the second largest 1^{st} eigenfrequency increase. Also here, multiple (repeated) eigenfrequencies ($f_1 = f_2$) appeared for the 1D beam. While the solid 2D plate's 1^{st} eigenfrequency was raised strongly, the increase of the cellular plate's 1^{st} eigenfrequency was less intense. The lowest 1^{st} eigenfrequency increase of 58% was obtained for the irregular lattice structure. However, this lattice was compared to a regular lattice structure, which was already a quite stiff lightweight structure. If the irregular lattice eigenfrequency would have been compared to that of a hollow solid structure, for instance, the eigenfrequency increase might have been higher.

Among the remaining studies aiming at an eigenfrequency increase including the topography optimisation and other published methods, the topography optimisation led to the highest 1^{st} eigenfrequency raise, which was comparable to the eigenfrequency increase obtained for the 1D beam based on both the mode shape adaptation and the evolutionary strategic optimisations. The published studies considered here raised the 1^{st} eigenfrequencies by 4%-161%, which are a smaller eigenfrequency increases than those obtained by the here

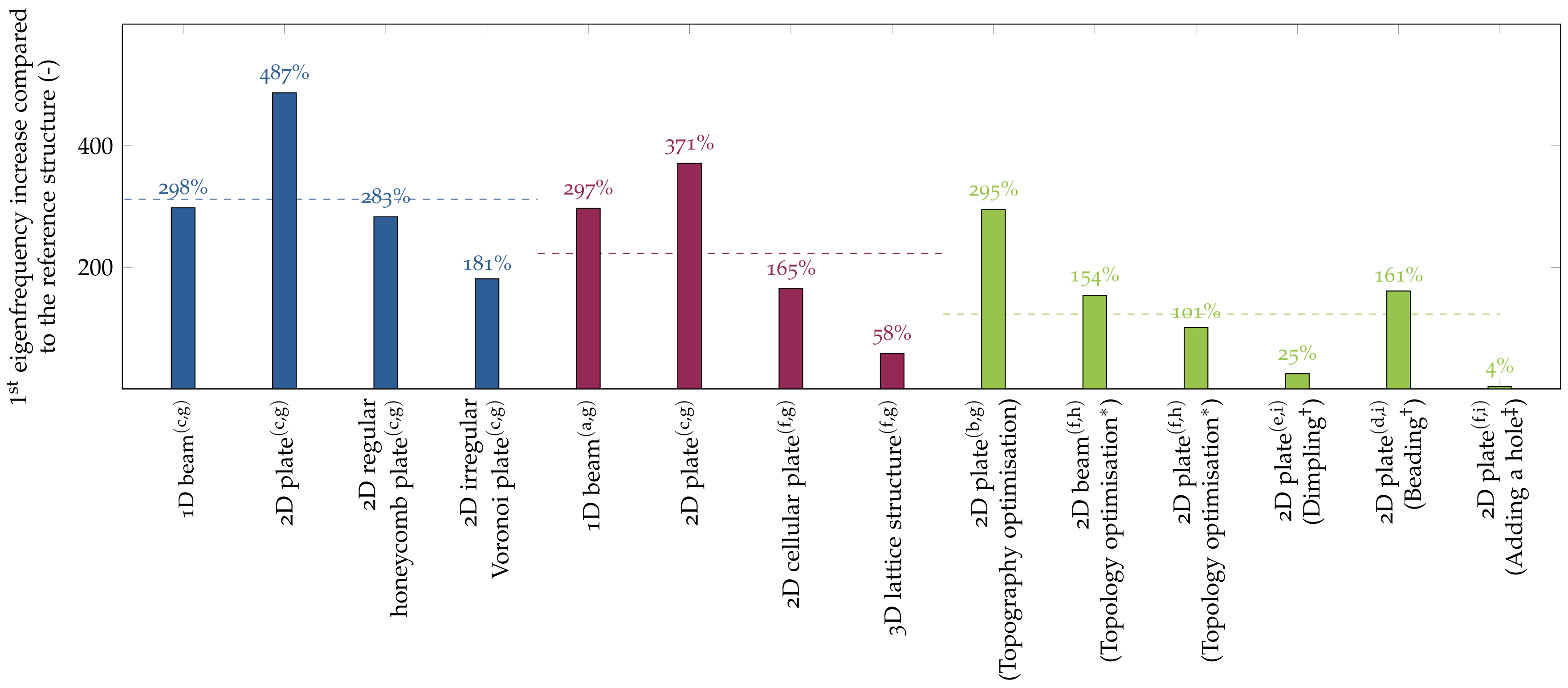

Figure 12.1: 1st eigenfrequency increases compared to the corresponding reference structures obtained by the mode shape adaptation method (blue), the evolutionary strategic optimisations (red), the topography optimisation (green), and other published methods (green) based on (*): Du and Olhoff [44], (†): Alshabatat and Naghshineh [6], and (‡): Pedersen [131]. The increases are shown above each bar. For each coloured group, the average increase is marked as a horizontal dashed line. Note that the displayed results vary in the applied maximum relative pre-deformation δ and the mass deviation as marked with the following letters: (a) $\delta = 3.0$, (b) $\delta = 3.5$, (c) $\delta = 5.0$, (d) $\delta = 8.0$, (e) $\delta = 9.8$, (f) $\delta =$ n/a, (g) mass = constant, (h) 50% mass reduction, and (i) mass = n/a.

investigated methods. It may be noted that many other, published studies aiming at 1st eigenfrequency increases considered alternative boundary conditions (e.g., cantilevers or fully clamped plates, cf., literature review in chapter 4), which is why they are not mentioned here.

Figure 12.2 shows that both investigated methods to increase multiple (1st and 2nd eigenfrequency or 1st, 2nd, and 3rd eigenfrequency) eigenfrequencies were successful. However, in almost all studies, all three eigenfrequencies were raised. Regarding the mode shape adaptation approach applied to the 1D beam, for example, the maximisation of the 1st and 2nd eigenfrequency increased both targeted eigenfrequencies and also the 3rd eigenfrequency more strongly than the maximisation aiming at an increase of all three eigenfrequencies. In regard to the squared plate, both analysed methods led to stronger eigenfrequency raises than for the beam. This can be explained by the maximum relative pre-deformation of 5.0 considered for the plate, while the beam was only pre-deformed by $\delta = 3.0$. The present investigations are not compared to other studies, because there are no published studies on this topic that use comparable boundary conditions. Also the obtained frequency increase of specific mode shapes is not compared here among the different methods, because even small structural adaptation resulted in strong mode shape variations for the plate. Thus, mode tracking was not successful. However, especially the results for the mode shape adaptation method indicated a high frequency increase of the targeted mode shape due to the structural modification.

To sum up, the following bullet points characterise each method:

– *Mode shape adaptation*
  - Easy and fast application
  - Low computational effort required
  - Significant eigenfrequency increase at constant mass
    → Small pre-deformations have already strong impacts on eigenfrequencies
  - Frequencies of specific mode shapes can be shifted
  - Increase of multiple eigenfrequencies possible
  - ! Effective application to 3D structures has to be further investigated

– *Evolutionary strategic optimisations*
  - Effective solutions for multi-objective optimisations
  - Significant eigenfrequency increase at constant mass
  - Many solutions are created, out of which the best compromise between the objectives can be chosen

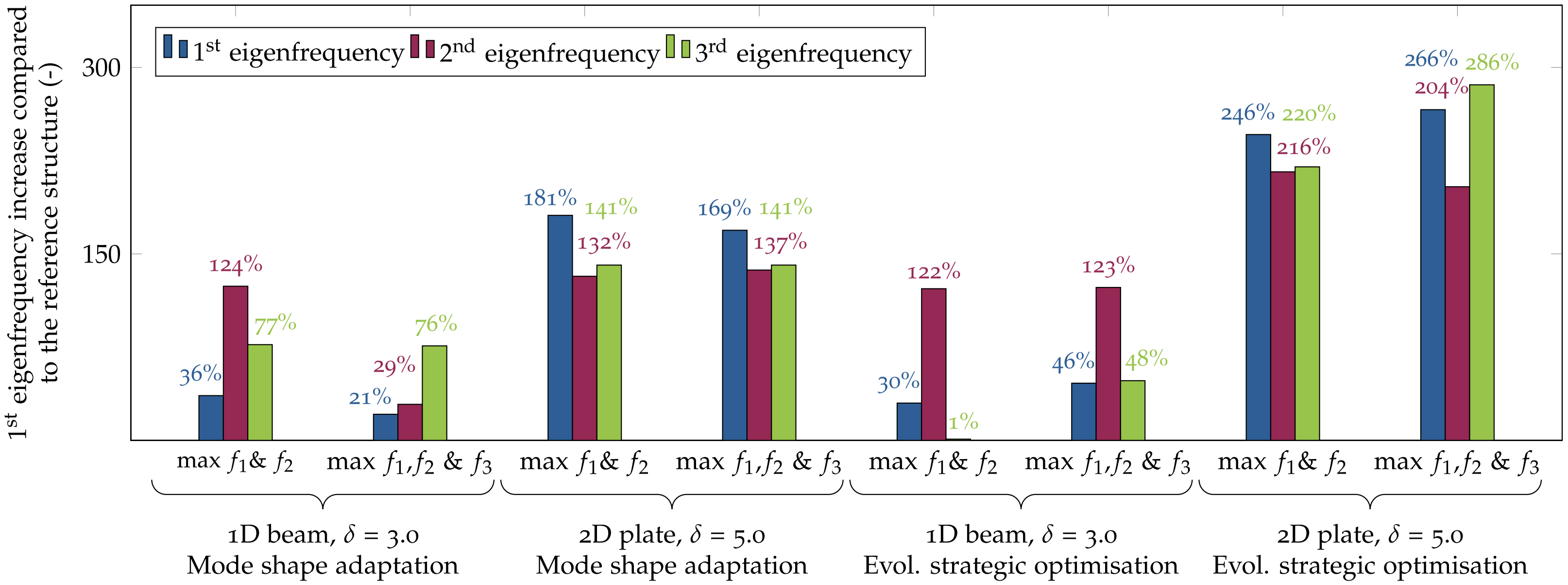

Figure 12.2: Multiple eigenfrequency (i.e., 1st and 2nd or 1st, 2nd, and 3rd eigenfrequency) increase compared to the reference structure for the mode shape adaptation method and the evolutionary strategic optimisations applied to a 1D beam and a 2D squared plate for maximum relative pre-deformations δ of 3.0 and 5.0. The eigenfrequency increase is displayed above each bar.

  - High increase of multiple eigenfrequencies possible
  - ! Multiple eigenfrequencies possible due to lacking of mode tracking
  - ! High computational effort due to the iterative process

- *Application of irregular cellular and lattice structures*
  - Significant eigenfrequency increase at constant or reduced mass
  - Lightweight structures that allow an optimum material distribution
  - Parametric constructions permit a high variety of different structures
  - High potential for the integration of additional functions like damping, which has to be studied in detail
  - ! High computational effort, if combined with evolutionary strategic optimisations or parametric studies

Part IV

GIRDER DESIGN FOR PETRA IV

The previous part dealt with the impact of biologically inspired structures and optimisation techniques on the vibration properties. In this part, biologically inspired vibration optimisation is applied to a technical component, more precisely, to a magnet supporting structure (girder) of the synchrotron radiation facility PETRA IV that is currently planned at the DESY and expected to start operation in January 2027.

After a detailed problem definition, a study on the impact of different components and boundary conditions on the eigenfrequencies of the magnet-girder assembly is presented. Based on the results, the boundary conditions for the subsequent girder development process are defined. The generated girder development process is composed of different steps including a topology optimisation, the result abstraction, the implementation of biologically inspired structures (e.g., irregular Voronoi combs studied in chapter 10), and the conduction of cross section optimisations using the evolutionary strategy studied in chapter 9. The designed biologically inspired girder structure is then manufacturing from grey cast iron, before vibration measurements are performed ultimately.

13

HIGHLY BRILLIANT PETRA IV SYNCHROTRON RADIATION SOURCE

In the framework of various challenges human society is currently facing, e.g., the climate change, the extinction of species, or the rapidly increasing population on earth, it is crucial to deeply understand complex biological, physical, and chemical processes in nature to find solutions for the challenges. As synchrotron radiation sources allow the investigation of structures, materials, and processes in different time and length scales *in situ*/*in vivo*, they are essential to create a deeper understanding of nature [149]. With the help of synchrotrons, for example, large membrane protein complexes have been investigated [55], the novel coronavirus SARS-CoV-2 has been studied [43], and the rhizosphere chemistry was analysed [176]. But also the detailed investigation of technical structures, materials, and fabrication processes is fundamental to improve technology. The synchrotron radiation technology plays a key role in engineering science, permitting, for example, a detailed analysis of the structure solidification process of alloys [187] or the *in situ* analyses of metal additive manufacturing [165]. Altogether, synchrotron radiation facilities are used in many different disciplines and are very important to find solutions for today's challenges.

Brilliance *describes how the number of photons per second per unit bandwidth, i.e., the spectral flux, is distributed in space and angular range.[191] A highly brilliant synchrotron light source creates a bright X-ray beam, i.e., an X-ray beam that is small, intense, and nearly parallel.*

As a considerable part of this work is dealing with the development of an innovative biologically inspired girder design for the synchrotron radiation facility PETRA IV at DESY, this chapter introduces the field of synchrotron radiation facilities and the current situation of the PETRA IV project. The third sub-chapter is dedicated to the general structure and the importance of magnet-girder assemblies, before the last sub-chapter summarises the specifications considered for the development of an optimised girder design.

13.1 SYNCHROTRON RADIATION FACILITY

The heart of a synchrotron radiation facility is a storage ring, in which electrons circle at a constant energy. Deflecting their trajectory using magnetic fields generates electromagnetic waves, i.e., synchrotron radiation [191].

Today's synchrotron light sources are able to produce tuneable particle beams covering the electromagnetic radiation from far infrared to the hard X-ray regime. There are more than 70 synchrotron facility in operation or under construction worldwide. Users from different disciplines of natural sciences use their services, highlighting the importance of synchrotrons for multidisciplinary research [191].

A synchrotron is composed of five main components displayed in figure 13.1 [191]:

- Electron source: the electrons generated by a heated filament inside an electron gun are accelerated using a Linear Accelerator (LINAC).
- Booster ring: the electrons are injected from the LINAC into an evacuated booster ring to be further accelerated to reach the energy of the electrons in the main storage ring, into which they are then injected.
- Main storage ring: the ring is composed of arced sections with dipole, quadrupole, and sextupole magnets (i.e., the magnet lattice) and straight sections, in which Insertion Devices (IDs), like for example undulators, generate the synchrotron radiation. The electrons are maintained on a defined path. Dipole (bending) magnets deflect the electrons around the arced sections, quadrupoles focus the electron beam, and the sextupole magnets control the chromatic aberrations.
- Radio Frequency (RF) cavity: due to the emission of synchrotron radiation, the electrons loose energy, which is restored by a RF cavity supplying the electrons with energy.
- Beamlines: the beamlines come off tangentially to the storage ring. The particle beam is normally focussed and/or monochromatised in the optics hutch before entering the experimental hutch.

The **magnet lattice** *is the positioning of the magnet along the X-ray beam path in the synchrotron radiation facility.*

13.2 PETRA IV PROJECT

All synchrotron radiation sources worldwide are limited in spectral brightness [149]. However, a new (fourth) generation of synchrotron sources has been developed based on stronger focusing lattices ('Multi-Bend Achromats'), which generate highly parallel and narrow particle beams characterised by high-intensity X-rays [191]: highly brilliant light sources.

Several synchrotron radiation facilities are already working with new or upgraded machines, e.g., MAX IV (Lund, Sweden), SIRIUS (Campinas, Sao Paolo, Brazil) or European Synchrotron Radiation Facility's Extremely Brilliant Source (ESRF-EBS) (Grenoble, France). Many other facilities like Diamond (Oxfordshire, England), SOLEIL (Saint-Aubin, France), Super Photon ring-8 GeV (SPring-8) (Sayo Town, Hyōgo Prefecture, Japan) or DESY (Hamburg, Germany) are discussing upgrades [66]. At DESY (figure 13.2), the current PETRA IV project aims

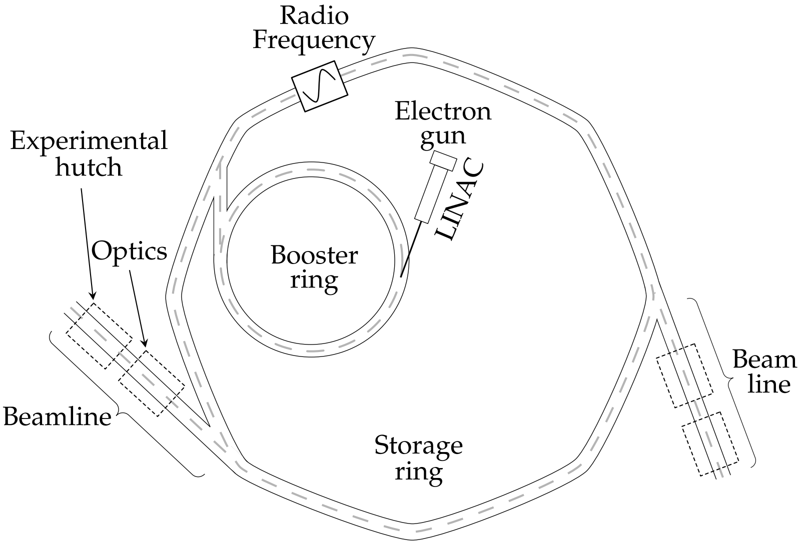

Figure 13.1: Main components of today's synchrotron radiation facilities.

at upgrading the present synchrotron radiation source PETRA III to PETRA IV, which will be an ultralow-emittance source and diffraction limited up to X-rays of 10 keV. Thus, its X-rays will be used for 3D microscopy of biological, chemical, and physical structures and processes under realistic conditions considering time scales down to the sub-nanosecond regime. The analysed length scales will vary from atomic dimensions to millimetres [149].

The PETRA IV project started in spring 2016. After finishing the conceptual design phase by publishing the conceptual design report in November 2019, the technical design phase will probably last until December 2022. The construction work is planned to be initiated at the beginning of 2025, involving certainly a shut-down of PETRA III. PETRA IV is expected to start operation in January 2027. For more information about the PETRA IV project and its current status it is referred to Agapov et al. [2], Röhlsberger et al. [141], Schroer et al. [148], and Wanzenberg et al. [188].

The currently operating PETRA III synchrotron is installed in a tunnel built in 1976, which has a large circumference of 2.304 km [148, 149]. This tunnel will also be used for the upgraded machine. The layout of PETRA IV consists of eight arcs of 201.6 m length each and eight straight sections, of which four are 108 m long and the remaining four 64.5 m (figure 13.3). One arc is composed of eight identical cells, each of 26.2 m length. In each cell, five girders of 1 m, 3 m, and 6 m length are planned to support the magnets (figure 13.4) [148], which would lead to 320 girders supporting the magnets. The magnet lattice is not yet fully defined. Generally, a seven bend acomatic lattice as used for ESRF-EBS is also earmarked for PETRA IV, but it will be supplemented by stronger sextupole magnets due to the larger cir-

Emittance *is the product of the linear particle source size and the x-ray beam divergence in the same plane [191]. A large emittance states a high movement of the particles relative to particle bunch, which is why synchrotron radiation facilities strive for a low emittance.*

The **diffraction limit** *is the theoretical limit of the resolution of an optical system, i.e., the limit of the achievable focus. In a diffraction limited storage ring, the horizontal emittance of the X-ray beam is smaller than the diffraction limit of the X-ray beam leading to highly coherent laser-like X-ray beams.*

cumference [2]. First magnets have been designed and several prototype magnets based on different materials will be studied soon [188].

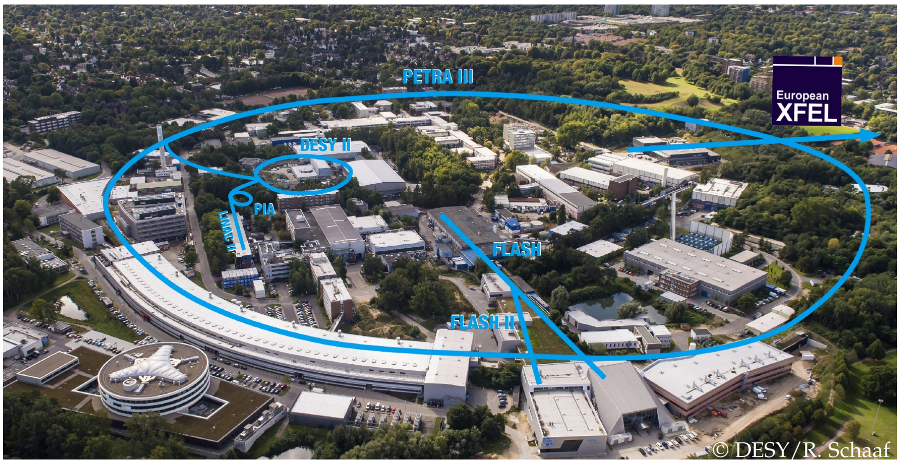
PETRA III
DESY II
PIA
LINAC II
FLASH
FLASH II
European XFEL
© DESY/R. Schaaf

Figure 13.2: View on the DESY ground with the different accelerators (printed with permission from DESY).

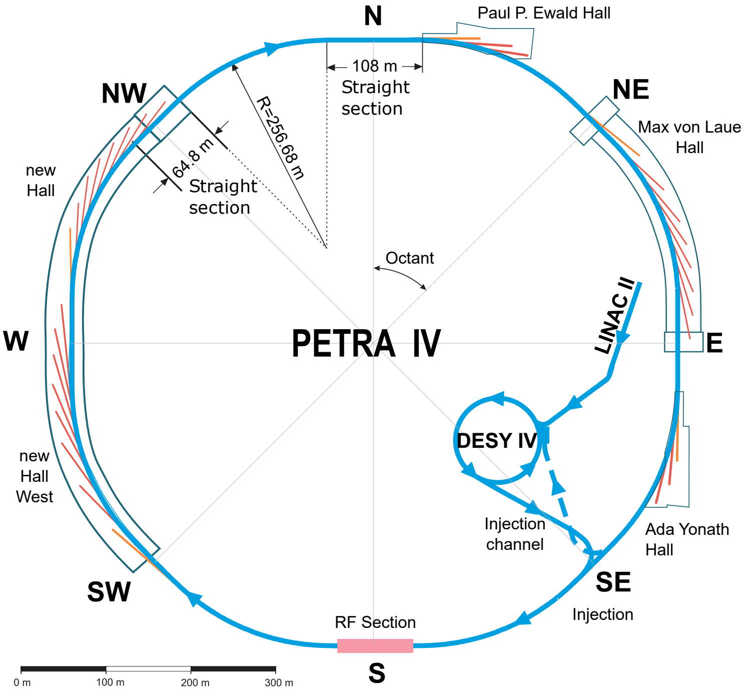
N
Paul P. Ewald Hall
108 m
Straight section
NE
Max von Laue Hall
NW
new Hall
64.8 m
Straight section
R=256.68 m
Octant
LINAC II
W
PETRA IV
E
DESY IV
new Hall West
Injection channel
Ada Yonath Hall
SE
Injection
SW
RF Section
S
0 m
100 m
200 m
300 m

Figure 13.3: PETRA IV layout including the linear accelerator LINAC II, the booster ring DESY IV, and different experimental halls (reprinted from Schroer et al. [148] with permission from DESY).

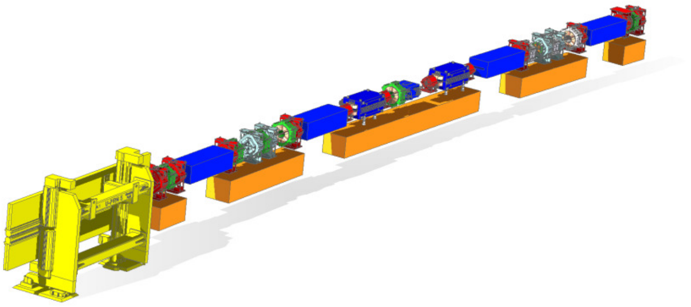

Figure 13.4: Planned support using girders for the magnets and other components in a 26.2 m lattice cell of PETRA IV. The girders (orange) are 1 m, 3 m, and 6 m long. The displayed magnet models are artificial (modified according to Andresen et al. [14], printed with permission from DESY).

13.3 MAGNET-GIRDER ASSEMBLIES

A high particle beam stability is essential to obtain a low-emittance and diffraction limited storage ring [204]. For this, the magnet-girder assembly plays an important role.

A girder acts like a beam to which different components are fixed [143]. The girder studied here supports magnets of a particle accelerator. For girders used in particle accelerators, the following advantages can be summarised [143, 153]:

- Girders lift all components (magnets) up to the particle beam height.
- All components can be mounted and aligned outside the tunnel, which permits a faster installation and alignment of the whole particle accelerator.
- Neighbouring components that require a very precise positioning against each other (i.e., very low tolerances) can be placed on one girder. Thus, the individual components are isolated from ground movements.
- Girders allow at all time an easy re-alignment of all components together, e.g., in the case of ground settling.

Aside from these advantages, it has to be noted that girders are another part of the accelerator machine. Each part can reduce the particle beam stability due to amplification of the ground vibrations or thermal deformations [153]. However, because of the considerable advantages of using girders, they are widely utilised in particle accelerators.

Girder structures installed in accelerator machines generally have to meet the following requirements:

- Because of the heavy components mounted to the girder, a high stiffness is essential for low static deflections due to gravity.
- All eigenfrequencies shall be above 30 Hz [153], because ground vibrations strongly drop with increasing frequency (cf., figure 13.7). As the numerically obtained eigenfrequencies are often higher than the actual ones, the objective is to reach a 1^{st} eigenfrequency of about 50 Hz in the numerical models.
- High temperature stability is required, because possible thermal deformations (e.g., studied for ESRF-EBS by Tampigny et al. [167]) strongly influence the particle beam stability.
- An easy transportation has to be possible, during which structural deformations of the equipped girder have to be as low as possible.
- The girder should be light to keep the total weight of a fully equipped girder assembly as low as possible to allow a transportation of the equipped girder.
- The girder structure must be easy to align.
- Often, an adjustability of the girder (and the magnets) positioned in the tunnel is required to allow a re-alignment of all components.
- The manufacturing of the girder structure has to be cost effective.

It is therefore of high interest to design a girder structure with high eigenfrequencies, a high stiffness, and a low mass. A systematic investigation of how theses aspects can be combined to design an optimised girder structure was the aim of this work. Other mentioned requirements regarding the girder structure are not considered here.

The stability of the particle beam depends, aside from the thermal issues, on the transfer function of the ground vibration to the particle beam. This vibration transmission path is illustrated in figure 13.5. Ground motions are inevitable. However, the vibrations reaching the particle beam $\Delta\, x_{beam}$ should be less than 10% of the particle beam size $\sigma_{x,beam}$ to obtain the required particle beam stability and can be calculated as follows [204]:

$$\begin{aligned}\Delta\, x_{beam} = x_{gr} \cdot TF_{gr-sl} \cdot \left[TF_{sl-gir} \cdot TF_{gir-mag}\right] \cdot\ q_d \\ \cdot TF_{mag-beam} \cdot q_{fofb} < 0.1\ \sigma_{x,beam}\end{aligned} \tag{13.1}$$

Thus, $\Delta\, x_{beam}$ depends on the ground vibrations x_{gr} and on the transfer functions from the ground to the slab TF_{gr-sl}, from the slab to the girder TF_{sl-gir}, from the girder to the magnet $TF_{gir-mag}$, and on the transfer function amplification due to the lattice design $TF_{mag-beam}$.

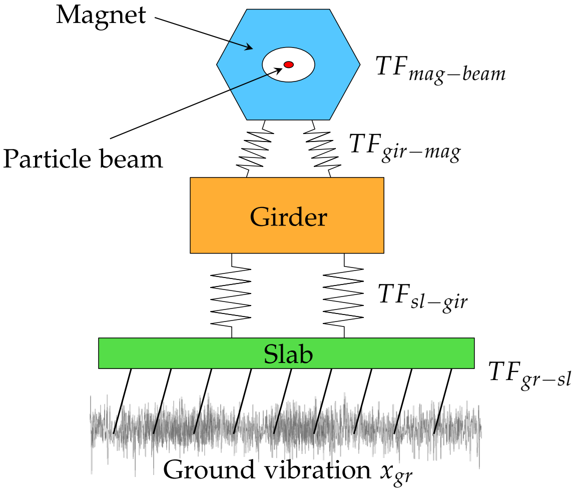

Figure 13.5: Vibration transmission path from the ground vibration to the particle beam including the differen transfer functions TF (based on Zhang [204]).

The latter can be positively influenced by a fast orbit feedback factor q_{fofb}. In addition, in the case of low magnet-girder assembly eigenfrequencies, passive damping mechanisms (damping pads or materials) can reduce high vibration amplifications by a factor q_d as applied to the Advanced Photon Source (APS) (Argonne National Laboratory, Lemont, Illinois, USA) [102] or to the European Synchrotron Radiation Facility (ESRF) (Grenoble, France) [205].

In regard to damping, the dynamic amplification factor H is defined as the ratio of the dynamic amplitude and the static displacement due to a constant force (cf., chapter 6.2.3). Figure 6.5 shows the dependency of the dynamic amplification factor on the ratio of the excitatory frequency Ω and the eigenfrequency of the system ω: $\eta = \Omega/\omega$. Thus, soft magnet-girder assemblies lead to a ratio η larger than $\sqrt{2}$ due to the low magnet-girder assembly eigenfrequency. Consequently, the vibration transmissibility from the ground to the particle beam is very low and the structure is isolated from the ground motion. Nevertheless, soft supports cannot be implemented in the accelerator machine because of the low tolerances between neighbouring girders.

Damping mechanisms can be effectively applied to intermediate-stiffness supports that show η values around 1 (resonance). As visible in figure 6.5, the dynamic amplification factor decreases with raising damping ratio ζ. However, if the structural eigenfrequency is significantly larger than the excitation frequency ($\eta << 1$), a high structural stiffness is present and damping mechanisms are not necessary because of the already low transmissibility [153]. Therefore, stiff magnet-girder assemblies are inevitable to reach a high particle beam stability.

Zhang [204] gave an overview on magnet-girder assemblies of different accelerator machines worldwide. The 1st eigenfrequencies of the magnet-girder assemblies vary from about 10 Hz of the 3rd generation machines (ESRF, APS) and about 20 Hz for SPring-8 or Shanghai Synchrotron Radiation Facility (SSRF) (Shanghai, People's Republic of China) to above 40 Hz for the new-generation light sources (SOLEIL, ESRF-EBS). Meyners [109] measured a 1st eigenfrequency of the currently installed PETRA III girder of about 35 Hz and a 1st magnet mode at 25 Hz. A PETRA III girder installed in the PETRA tunnel is displayed in figure 13.6.

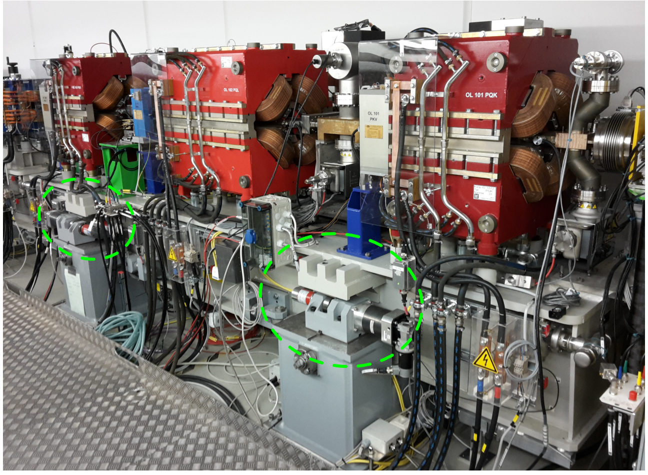

Figure 13.6: 4.2 m long PETRA III girder (light grey) inside the PETRA tunnel that is positioned on bases (dark grey) and equipped with several components including three large magnets (red). The girder alignment system (cam movers) placed between the girder and the bases is circled in a dashed light green line.

So far, most girders have box-like structures. However, new design approaches have been made, e.g., at the Argonne National Laboratory, where topology optimisations of the Advanced Photon Source Upgrade (APS-U) girder combined with thickness optimisations of the upper solid girder plate allowed a 1st eigenfrequency increase towards 39 Hz for a 6.5 m long ductile cast iron (GR-60/40/18) girder considering three support points [91, 120].

Generally, a compromise between stability (vibration, temperature) and adjustability (alignment) has to be made. On the one hand, a large number of girder support points increases the stiffness and thus the 1st eigenfrequency [8]. Moreover, the support points should be placed as close as possible to the upper girder surface and thus to the magnets, because low support points reduce the eigenfrequencies. The National Synchrotron Light Source (NSLS)-II (Brookhaven National Laboratory, Long Island, New York, USA) girder, for example, is supported by eight support points, but still shows a 1st eigenfrequency of only 30 Hz, since the support points are located close to the ground [139]. On the other hand, an over-determined system of more than three support points is difficult to align, especially considering the small tolerances. In addition, a three point support allows a free horizontal expansion and thus a smooth thermal deformation [204].

While motorised jacks and cam movers (e.g., applied to the PETRA III girder) have been used as girder alignment systems, manual adjustments are more present in the latest magnet-girder assemblies, e.g., wedge jacks (APS, SSRF [204]) or precision levellers made by AirLoc AG (`www.airloc.com`) (e.g., SOLEIL [103] or ESRF-EBS [33]). Nevertheless, a support system allowing a girder adjustment at any time generally shows a lower stiffness than a non-adjustable support.

Summing up, there are different specifications and demands that have to be taken into account to develop a new girder design. Some specifications are studied in chapter 14. The main objective of the later girder design process (chapter 15) is the development of an biologically inspired girder characterised by high eigenfrequencies, a high stiffness, and a low mass.

13.4 PROBLEM DEFINITION, SPECIFICATIONS, AND MODEL ASSEMBLY

One of the big challenges in the PETRA IV project is to design an upgraded machine that allows a horizontal emittance of less than 30 pm rad, which is almost two orders of magnitude smaller than the emittance of the currently operated PETRA III storage ring [148]. At the same time, the estimated alignment and field tolerance of one girder to the neighbouring girders is 50 μm [148]. Therefore, a high stability of the storage ring is essential.

As mentioned in the previous chapter 13.3, the stability of the synchrotron facility, and thus of the particle beam, strongly depends on the temperature and the ground stability. Regarding the first, the temperature inside the PETRA tunnel will be stabilised to ± 1 K [148] to avoid strong movements or deformations of tunnel segments or machine components like girders.

In addition, the parts of the tunnel utilised for PETRA IV will be reinforced by massive concrete rings to increase the stability [148]. However, the ground vibration also influences the synchrotron facility stability. Measurements show that the ground vibration amplitudes at the DESY campus strongly drops with increasing frequency (figure 13.7) [26, 108]. High amplitudes result from ocean waves at about 0.2 Hz, traffic noise at about 2-8 Hz, and strong in-house noise between 20 Hz and 50 Hz [148]. Above 50 Hz, the ground vibration amplitudes are small, which is why all eigenfrequencies of the magnet-girder assembly shall be higher than 50 Hz. Thus, the targeted 1^{st} eigenfrequency of the PETRA IV girder is significantly higher than the eigenfrequency value of 30 Hz proposed by Sharma et al. [153].

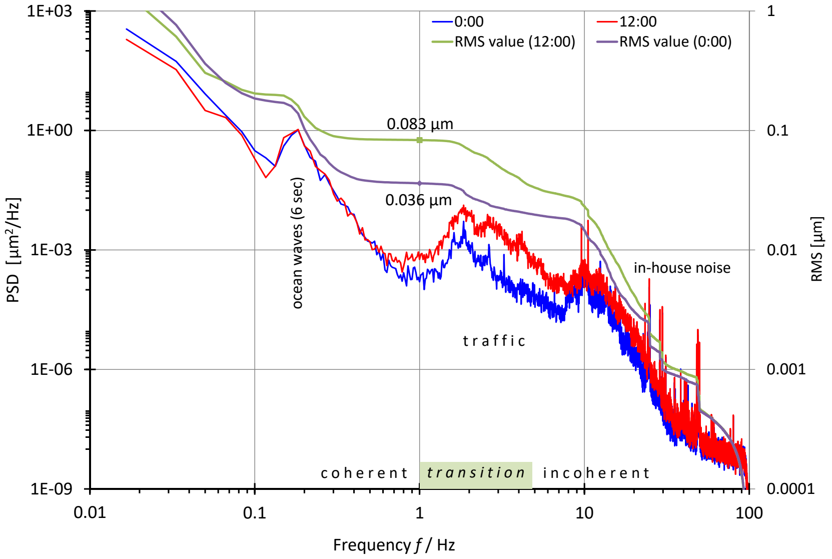

Figure 13.7: Vertical Power Spectral Density (PSD) and the Root Mean Square (RMS) of the ground vibration at the DESY campus during midday and night. The figure is reprinted from Schroer et al. [148] with permission from DESY. Minor modifications include the correction of the axis labels.

Besides the high eigenfrequencies, the girder is expected to show a high stiffness, since it has to carry the heavy magnets. Static deflections below 0.5 mm are allowed. In addition, the girder structure should be as light as possible owing to the transport of the magnet-girder assembly from the assembly area, where the girder is equipped with magnets and the magnet alignment takes place, into the long and small tunnel. In order to fulfill these requirements, complex biologically inspired geometries are considered in this work, which enable a higher performance. The designed girder will be manufactured using the casting technology. During this process, a mould representing the negative structure of the desired part is filled with high temperature, liquid metal (figure 13.8). Cooling leads to the solidification of the metal, which forms the designed structure [196]. Traditional casting constraints would limit the design freedom and consequently lead to structures with less-improved mechanical properties, which has been studied by Xu et al. [196]. However, the implementation of 3D printed sand moulds (cores) into the casting process allows the manufacturing of a complex, optimised structure [184]. The fabrication of the sand moulds is similar to other powder-based processes. A thin layer of sand mixed with an activator is distributed on the job box surface. According to each cross section (slice) of the manufactured part, a binder is sprayed on the area. During the subsequent bonding reaction, the sand particles stick together forming the cross section. In other regions, which were not provided by the binder, the sand remains loose. The job box surface moves then downward by a

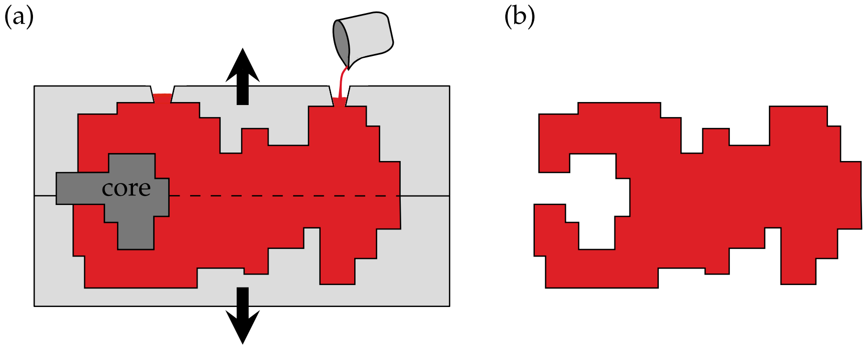

Figure 13.8: Casting process with additively manufactured cores: The fused metal (red) fills the voids of the mould (light grey) that is composed of two parts (a). The complex structure is realised by using a core (dark grey). The black arrows show the parting direction of the mould to obtain the final casted part (b).

defined layer thickness and the next slice of the part is made. This process continues until the part is completely printed [174]. Consequently, aside from the inevitable avoidance of small cross section values and voids inside the structure, the girder development process was not constrained by demands of the subsequent manufacturing technology.

In the following, the general FEM model of the here studied PETRA IV magnet-girder assembly is described.

As already mentioned, the PETRA IV machine will be installed in the already available PETRA tunnel. Therefore, the design space for the girders followed the dimensions of the currently installed PETRA III girders (cf., figure 13.6). All following studies were exemplarily applied to the 2nd (4th) girder of figure 13.4 that is equipped with eight magnets. Figure 13.9 shows the girder design space, which was connected to three bases at three points with the x coordinates $0.05\,l_G$, $0.50\,l_G$, and $0.95\,l_G$ ($l_G = 2{,}900$ mm, the girder length). The connection was realised using Beam elements (CBEAMs) with a diameter of 50 mm and a length of 20 mm, which were connected to the girder and the bases via RBE3s. The lower surface of the bases was considered as mounted.

For the girder, the bases, and the three connection beams, Structural Steel with a minimum yield strength of 235 MPa (S235) was specified as material characterised by a Young's modulus of 210,000 $\mathrm{N\,mm^{-2}}$, a density of $7.83\,10^{-9}\,\mathrm{t\,mm^{-3}}$, and a Poisson's ratio of 0.3.

The girder was equipped with eight magnets varying in width (cf., figure 13.9) and mass (table 13.1), which were fixed to the upper girder surface. As the volume of each magnet V_{mag} was fixed, its targeted mass m_{mag} was obtained by defining an artificial density ρ_{mag} for each magnet. At the same time, a factor q of 1.15 was included to conservatively assume a slightly higher mass, as the heavy magnets have a strong impact on the overall eigenfrequencies:

$$\rho_{mag} = q\frac{m_{mag}}{V_{mag}} \tag{13.2}$$

Hereinafter, the impact of different components and boundary conditions of the magnet-girder assembly on the eigenfrequencies was analysed.

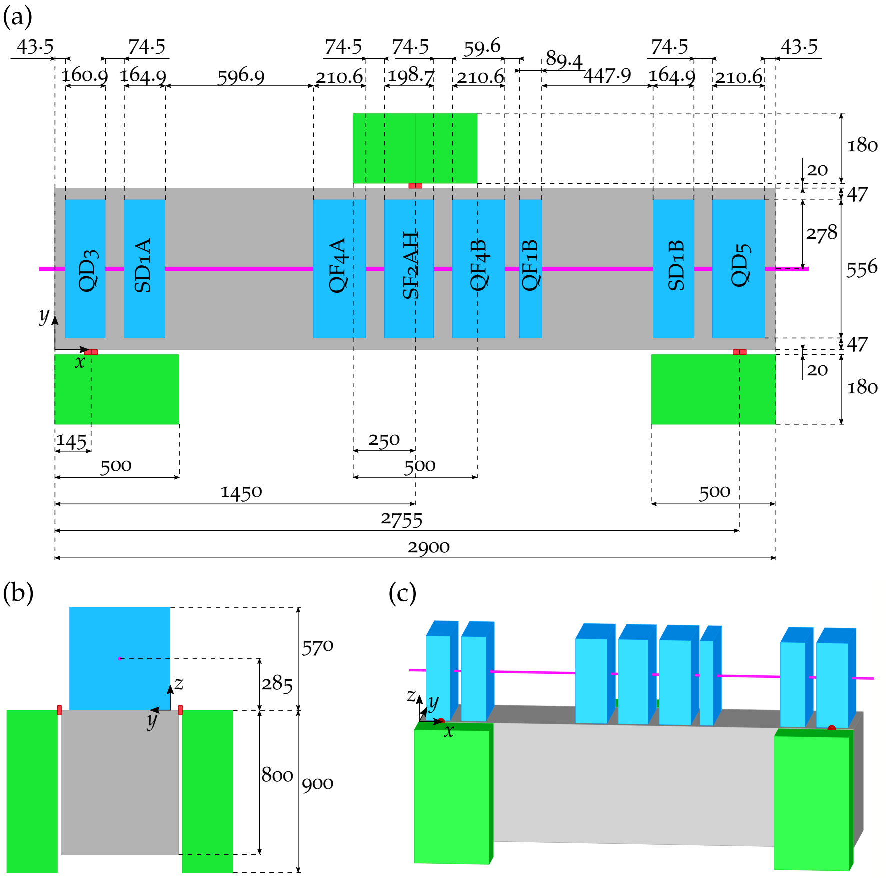
(a)
43.5
74.5
74.5
74.5
59.6
89.4
74.5
43.5
160.9
164.9
596.9
210.6
198.7
210.6
447.9
164.9
210.6
180
20
47
278
556
47
20
180
QD3
SD1A
QF4A
SF2AH
QF4B
QF1B
SD1B
QD5
y
x
145
500
250
500
1450
500
2755
2900
(b)
570
285
z
y
800
900
(c)
z
y
x

Figure 13.9: Top view (a), side view (b), and 3D view (c) of the general model of the 3 m PETRA IV magnet-girder assembly including the girder design space (grey), the three bases (green), the eight magnets (blue), and the three beams connecting the girder to the bases (red). The location of the particle beam is shown in magenta. All given dimensions are in mm.

Table 13.1: Magnet properties including the mass m_{mag}, the volume V_{mag}, and the artificial density ρ_{mag}.

Magnet	Mass	Volume	Artificial density
QD3	0.155 t	$5.099\,10^7\,\mathrm{mm}^3$	$3.496\,10^{-9}\,\mathrm{t\,mm}^{-3}$
SD1A	0.540 t	$5.226\,10^7\,\mathrm{mm}^3$	$1.188\,10^{-8}\,\mathrm{t\,mm}^{-3}$
QF4A	0.280 t	$6.674\,10^7\,\mathrm{mm}^3$	$4.825\,10^{-9}\,\mathrm{t\,mm}^{-3}$
SF2AH	0.650 t	$6.297\,10^7\,\mathrm{mm}^3$	$1.187\,10^{-8}\,\mathrm{t\,mm}^{-3}$
QF4B	0.280 t	$6.674\,10^7\,\mathrm{mm}^3$	$4.825\,10^{-9}\,\mathrm{t\,mm}^{-3}$
QF1B	0.385 t	$2.833\,10^7\,\mathrm{mm}^3$	$1.563\,10^{-8}\,\mathrm{t\,mm}^{-3}$
SD1B	0.540 t	$5.226\,10^7\,\mathrm{mm}^3$	$1.188\,10^{-8}\,\mathrm{t\,mm}^{-3}$
QD5	0.385 t	$6.674\,10^7\,\mathrm{mm}^3$	$6.634\,10^{-9}\,\mathrm{t\,mm}^{-3}$

14

PARAMETRIC STUDY ON COMPONENTS AND BOUNDARY CONDITIONS

In this study, different structural components and boundary conditions of the magnet-girder assembly were altered to investigate their impact on the eigenfrequencies.

14.1 MATERIAL AND METHODS

Two different girder geometries were taken into account to assess the influence of the girder design on the analysed parameters (figure 14.1): (1) a box girder that corresponded to the defined girder design space and possessed a wall thickness of 50 mm and (2) a 4,200 mm long PETRA III girder currently installed in the PETRA III machine, which has seven inner vertical ribs. The PETRA III girder geometry was adapted to obtain a girder length of 2,900 mm.

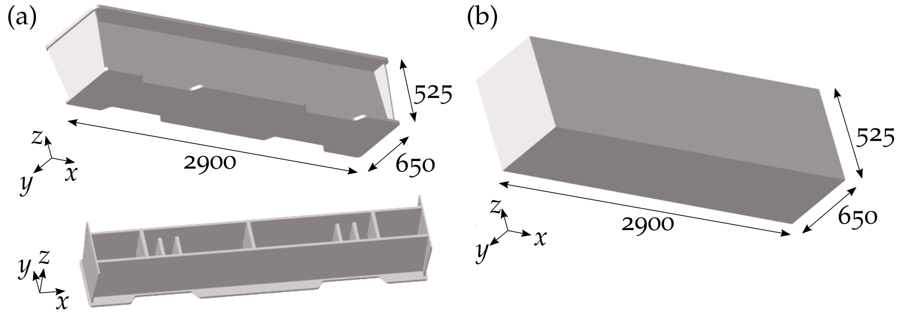

Figure 14.1: The PETRA III girder scaled in y-direction to 2,900 mm length (a) and a box girder (b) that were both analysed in a parametric study. In (a), the lower figure shows the adapted PETRA III girder with hidden top surface to visualise the inner rib structure.

A mesh study of the FEM model varying the CTETRA element size from 10 mm to 45 mm in step sizes of 2.5 mm identified a sufficient element size applied to both the girder structures and the magnets. Regarding the mesh study, only the girder structure equipped with magnets was considered. Thus, as the bases were neglected, a fixed support was defined at the three support point locations, i.e., all translations and rotations were inhibited. The element size, which showed result differences compared to the three previous element size steps of maximum 5%, was declared as sufficient.

During the parametric study, the following components and boundary conditions were altered and their impact on the first six eigenfrequencies of the magnet-girder assembly was investigated:

1. Magnet position height and connection
2. Stiffness of the magnet-girder connection
3. Magnet mass
4. Girder support point position
5. Stiffness of the girder support
6. Material properties of the girder and the bases

Table 14.1 lists the model components that were considered for each analysis.

14.1.1 *Magnets*

14.1.1.1 *Magnet Position Height and Connection*

The distance between the lower magnet surface and the girder was altered from 15 mm to 215 mm with a step size of 25 mm. In addition, the distances 0 mm – magnets fixed to the girder – and 290 mm were analysed. Similar to the magnet-girder assembly currently installed in the PETRA III accelerator (cf., figure 13.6), in which each magnet is connected to the girder via four screws imbedded in resin, the magnets were positioned on the girder using four beams of 50 mm diameter each. The analyses were conducted for both the magnets positioned individually and the magnets connected to each other. The latter was realised using beams of 50 mm diameter that were fixed to the middle node of the front and back side of each magnet. All beams were connected to the magnets and the girder via RBE3s. Figure 14.2 shows exemplarily the model assembly for the position height study of the connected magnets.

14.1.1.2 *Stiffness of the Connection between Girder and Magnet*

The diameter of the beams connecting the magnets to the girder was varied from 5 mm to 100 mm with a step size of 5 mm to investigate the impact of the connection stiffness on the magnet-girder assembly eigenfrequencies. A distance between magnets and girder of 215 mm was assumed following the magnet position height of the PETRA III girder.

The fixation of a magnet on the girder can be abstracted as a frame composed of four elastic posts (height h_{post}, bending stiffness EI) and

Table 14.1: Parametric study components and properties defined for the models 1a: Magnet position height, 1b: Magnet position height and connection, 2: Stiffness of the magnet-girder connection, 3: Magnet mass, 4: Girder support point position, 5: Stiffness of the girder support, and 6: Material properties.

	Magnets				Girder support		Material
	1a	1b	2	3	4	5	6
Magnets	✓	✓	✓	✓	✓	✓	✓
Girder	✓	✓	✓	✓	✓	✓	✓
Bases	✓	✓	✓	✓	✗	✓	✓
Beams girder-magnets incl. RBEs	✓	✓	✓	✗	✗	✗	✗
Beams girder-bases incl. RBE3	✓	✓	✓	✓	✗	✓	✓
Beams connecting magnets incl. RBE3	✗	✓	✗	✗	✗	✗	✗
x value of the three SPs	1,645, 4,255, 2,950 mm	1,645, 4,255, 2,950 mm	1,645, 4,255, 2,950 mm	1,645, 4,255, 2,950 mm	var var	1,645, 4,255, 2,950 mm	1,645, 4,255, 2,950 mm
Distance girder-magnets	var	var	215 mm	0 mm	0 mm	0 mm	0 mm
Beam diameter girder-magnets	50 mm	50 mm	var	✗	✗	✗	✗
Beam diameter girder-bases	50 mm	50 mm	50 mm	50 mm	✗	var	50 mm
Beam diameter connecting magnets	✗	50 mm	✗	✗	✗	✗	✗
Girder material	S235	S235	S235	S235	S235	S235	var
Bases material	S235	S235	S235	S235	S235	S235	var
Model view	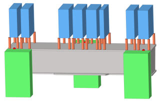	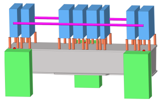	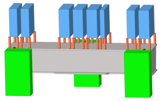	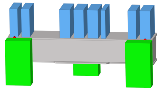	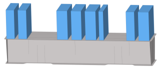	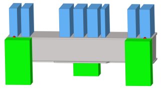	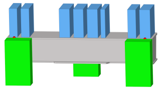

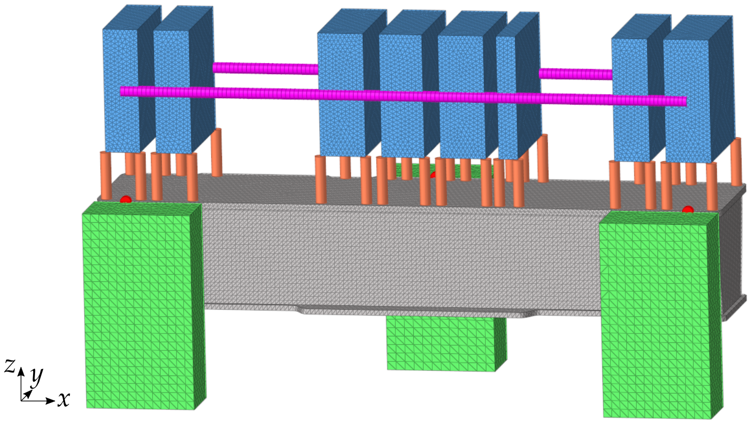

Figure 14.2: Parametric study model for the magnet position height study with connected magnets exemplarily displayed for the PETRA III girder. The model includes the girder (grey), the magnets (blue), and the bases (green) as well as the beams connecting the girder to the bases (red), the magnets to the girder (orange), and the magnets among each other (magenta).

a rigid bar, on which a mass m is fixed that can only move horizontally (figure 14.3). According to Gross et al. [58], the stiffness k_{post} of one post depends on the applied force F and the deflection w:

$$k_{post} = \frac{F}{w} = \frac{12\ EI}{{h_{post}}^3} \quad ; \quad \text{with :} \quad w = \frac{F\ {h_{post}}^3}{12\ EI} \tag{14.1}$$

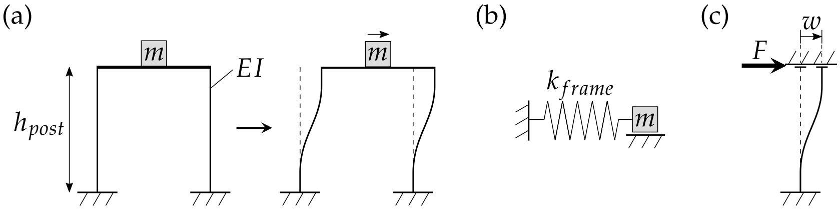

Figure 14.3: A frame composed of four elastic posts with the height h_{post} and the bending stiffness EI and a rigid bar with a mass m that can only move horizontally is displayed in (a). It is abstracted as a SDOF spring-mass system with the spring k_{frame} (b). The applied force F leads to the deflection w (c). The sketches are based on Gross et al. [58].

As the four posts are connected side-by-side (i.e., parallel), the resulting stiffness of the frame k_{frame} is the sum of the four single stiffnesses:

$$k_{frame} = 4\ k_{post} \tag{14.2}$$

Thus, the 1st eigenfrequency of the frame $f_{1,frame}$ is

$$f_{1,frame} = \frac{1}{2\pi}\sqrt{\frac{k_{frame}}{m}} = \frac{1}{2\pi}\sqrt{\frac{48\ EI}{m\ {h_{post}}^3}} \tag{14.3}$$

Based on these equations, the horizontal stiffness of the connection between girder and magnet was estimated using equation 14.2, in which the stiffness is multiplied by 4, since one magnet is supported by four parallel beams. The lowest frequency of a horizontal rigid magnet mode was estimated using equation 14.3 considering the mass of the heaviest magnet SF2AH (cf., table 13.1). Regarding both equations, the magnets were abstracted as point masses on top of the beam neglecting the beam masses and the connection stiffness of the beam to the girder was assumed as infinitely stiff.

To estimate the vertical stiffness of the magnet support, the support was abstracted as four parallel massless rods, each of a length l_{rod} and an extensional stiffness EA provided with a mass m at its end. Figure 14.4 shows one of these rods. A movement of the mass leads to an equal extension Δl of the rods. Thus, a restoring force acts on the mass. The total stiffness of the four rods is four times the rod stiffness k_{rod} defined as [58]:

$$k_{rod} = \frac{EA}{l_{rod}} \tag{14.4}$$

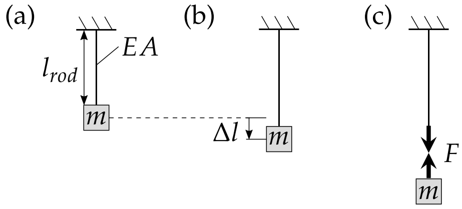

Figure 14.4: A massless rod of an extensional stiffness EA that is provided with a mass m at its end (a) is extended by Δl owing to a movement of the mass (b). A restoring force acts on the mass (c). The sketches are based on Gross et al. [58].

14.1.1.3 *Magnet Mass*

To investigate the impact of the magnet mass on the magnet-girder assembly, the factor q (cf., equation 13.2) was varied from 0.10 to 2.05 with a step size of 0.15. The magnets were considered as fixed to the upper girder surface.

14.1.2 *Girder Support*

14.1.2.1 *Support Point Position*

In first studies, the impact of the number and location of the girder support points on the eigenfrequencies were studied (figure 14.5). For more details it is refered to Andresen [10].

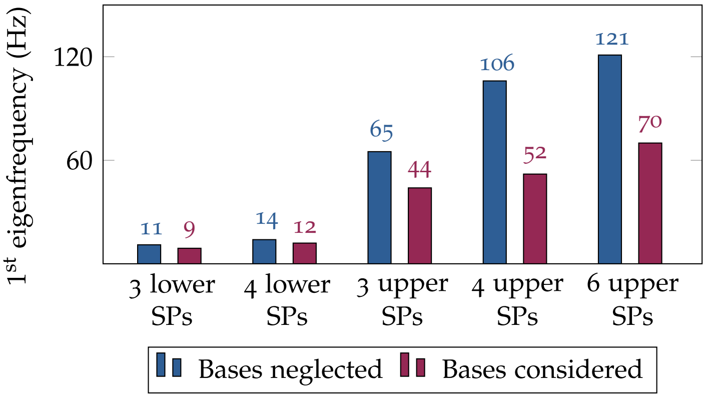

Figure 14.5: 1^{st} eigenfrequency of the magnet-girder assembly depending on the number and the position height (i.e., at the lower or higher part of the girder) of the support points (SPs) and on the implementation of the bases. The study was performed on a 4.2 m long box-shaped girder equipped with magnets. The eigenfrequency values are given above each bar.

The results showed a significant 1^{st} eigenfrequency increase with a rising support point number. However, assuming more than three support points would result in an over-determined system, which makes an accurate adjustment of the equipped girder in the tunnel difficult or even impossible. Thus, different positions of only three support points were analysed.

Since both investigated girder geometries showed a thin wall compared to the girder length, a consideration of the girder as a shell body with the same element size that was obtained in the mesh study was possible. Due to the high number of analysed combinations of support point positions, a solid girder would have involved very time-consuming computational effort. In contrast, the magnets were still considered as solids to consider not only their masses, but also their moments of inertia.

The x values of the support points were varied during the parametric study from $0.05\,l_G$ to $0.35\,l_G$ for point 1, from $0.65\,l_G$ to $0.95\,l_G$ for point 2, and from $0.3\,l_G$ to $0.7\,l_G$ for point 3 in step sizes of $0.1\,l_G$, whereby l_G symbolises the girder length. In addition, the study was conducted three times with different z values of the support points considering 900 mm, 700 mm, and 500 mm, which resulted in a total of 243 analysed support point position combinations.

Figure 14.6 shows all support points that were considered. The front and back wall of the PETRA III girder were positioned at $y = 185.5$ mm and $y = 462.5$ mm, i.e., closer to the girder centre (cf., figure 14.1a). Consequently, the support points at heights of 500 mm and 700 mm were moved by 185.5 mm in the y direction (support points 1 and 2) and in the negative y direction (support point 3) to be defined on the girder wall.

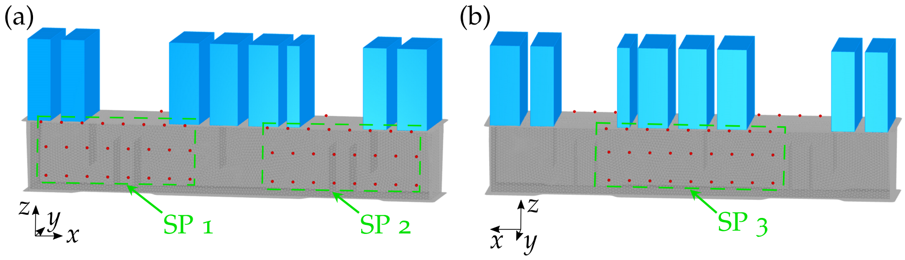

Figure 14.6: All positions of the three support points (SP, small red circles) that were considered in the parametric study are displayed exemplarily for the PETRA III girder in a 3D front view (a) and back view (b). The girder (grey) is slighly transparent making the inner ribs visible. All positions that the support points 1, 2, and 3 are assigned to during the parametric study are framed in light green. The magnets supported by the girder are shown in blue.

The support point combination which led to the highest 1^{st} eigenfrequency was chosen. Subsequently, the model was calculated with the girder considered as a solid body to estimate the deviation of the shell model from the volume model.

14.1.2.2 *Stiffness of the Girder Support*

To study how the girder support stiffness affects the overall magnet-girder assembly eigenfrequencies, the diameter of the beams connecting girder and bases was varied from 5 mm to 100 mm in 5 mm steps.

Since only shear forces were relevant owing to the shortness of the beams, the shear stiffness k_{shear} of the connection between girder and bases was estimated based on a cantilever beam with a point load (figure 14.7). The maximum deflection w_{max} at $x = l$ is [57]:

$$w_{max} = \frac{F\ l}{G\ A\ \kappa} \tag{14.5}$$

As the stiffness depends on the force and the deflection (cf., equation 14.1), it is defined as:

$$k_{shear} = \frac{G\ A\ \kappa}{l} \tag{14.6}$$

where G symbolises the shear modulus and κ is defined as $3/4$ for the here present circular cross section [162].

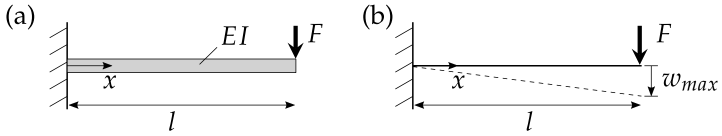

Figure 14.7: A point load F is applied to a cantilever beam of a length l and a bending stiffness EI (a). The beam deflects as shown with a dashed line in (b) leading to a maximum deflection w_{max}. The sketches are based on Gross et al. [57].

14.1.3 *Material Properties*

In the previous studies, S235 was considered as material for the girder and the bases. Here, the impact of the material properties on the eigenfrequencies was analysed by considering the materials aluminium, grey cast iron, spheroidal cast iron, and mineral cast for the girder and the bases (table 14.2). The results were compared to those obtained for the girder and bases made out of S235. Additionally, the ratio $\sqrt{E/\rho}$ was considered as it can be seen as a parameter of how the Young's modulus and the density, which are significant material properties, affect the eigenfrequency.

Table 14.2: Material properties of aluminium AlSi10Mg, grey cast iron (EN-GJL-350), spheroidal cast iron (EN-GJS-700-2), and mineral cast (EPUMENT® 140/5 [138]) considered for the girder and the bases involving the Young's modulus E, the material density ρ, and the Poisson's ratio ν. In the last row, the ratio $\sqrt{E/\rho}$ was normalised with the corresponding value for S235 of $5.2 \cdot 10^6$.

	Aluminium	Grey cast iron	Spheroidal cast iron	Mineral cast
E (N mm^{-2})	75,000	130,000	176,000	30,000
ρ (t mm^{-3})	$2.7 \cdot 10^{-9}$	$7.3 \cdot 10^{-9}$	$7.2 \cdot 10^{-9}$	$2.3 \cdot 10^{-9}$
ν (-)	0.33	0.26	0.28	0.30
$\sqrt{E/\rho}$ (N mm^{-1})	$5.3 \cdot 10^6$	$4.2 \cdot 10^6$	$4.9 \cdot 10^6$	$3.6 \cdot 10^6$
$\sqrt{E/\rho}$ (-)	1.02	0.81	0.95	0.70

14.2 RESULTS

This sub-chapter contains the parametric study results. The mesh study revealed a sufficient element size of 20 mm for both girder geometries considering the first six eigenfrequencies (figure 14.8). The total number of elements was 76,600 for the PETRA III girder and 67,799 for the box girder.

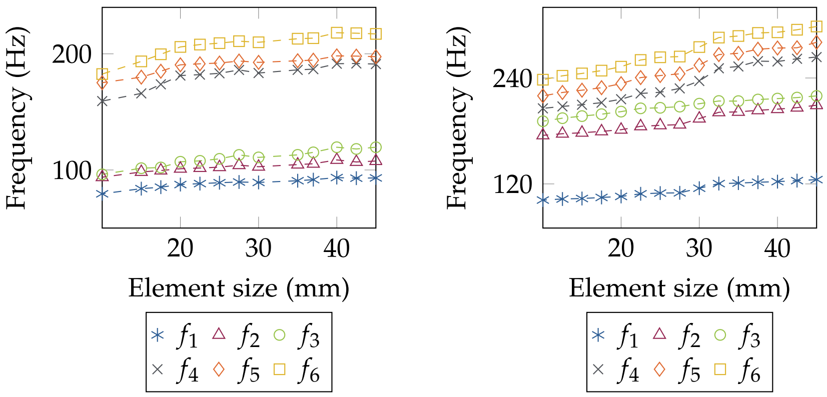

(a) PETRA III girder

(b) Box girder

Figure 14.8: First six eigenfrequencies depending on the element size for the PETRA III girder (a) and the box girder (b). A element size of 20 mm was chosen.

14.2.1 *Magnets*

14.2.1.1 *Magnet Position Height and Connection*

Eigenfrequency decreases with rising distance between the magnets and the girder were obtained for both girder geometries (figure 14.9). Regarding the PETRA III girder with individually positioned magnets, a strong eigenfrequency decrease from 0 mm to 15 mm distance was followed by a slight continuous decrease of all eigenfrequencies with further increasing distance. Figure 14.10 shows the 1st mode shape for 15 mm distance between the magnets and the girder. Girder deformations at the connection to the magnet-beams occurred and indicated a lower connection stiffness, which did not appear at a distance of 0 mm, i.e., for the magnets fixed to the upper girder surface.

Apparently, including a magnet connection did not prevent the general trend of decreasing eigenfrequencies with increasing distance between girder and magnets. However, the eigenfrequencies decreased less strongly. The strongest impact of the magnet connection on the eigenfrequencies was obtained for large distances between girder and magnets and for the higher-order eigenfrequencies. In addition, the magnet connection led to higher eigenfrequency increases for the PETRA III girder than for the girder box.

Comparing exemplarily the 5th mode shape for the distances 0 mm, 115 mm, and 215 mm between the magnets and the box girder shows the impact of the magnet connection (figure 14.11). With regard to the magnets fixed to the girder, the magnet connection did not alter the eigenfrequencies nor the mode shape. At a distance of 115 mm, the magnet connection prevented the local magnet modes and the overall mode shape was still similar to the 5th mode shape for the magnets fixed to the girder. However, at a high distance of 215 mm, the local

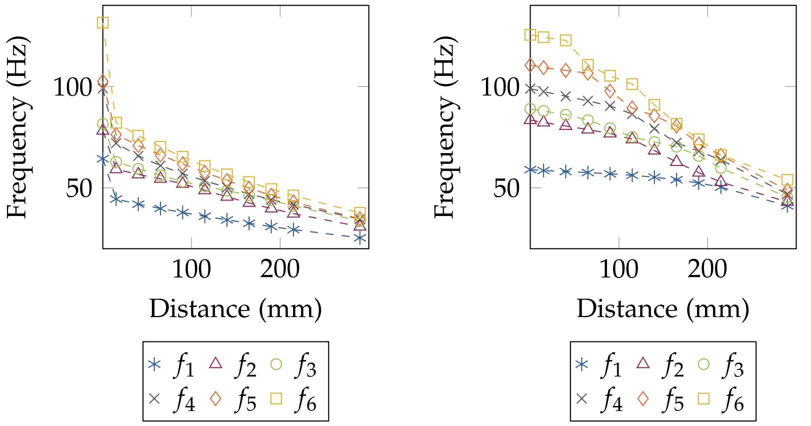

(a) PETRA III girder with individually positioned magnets

(b) Box girder with individually positioned magnets

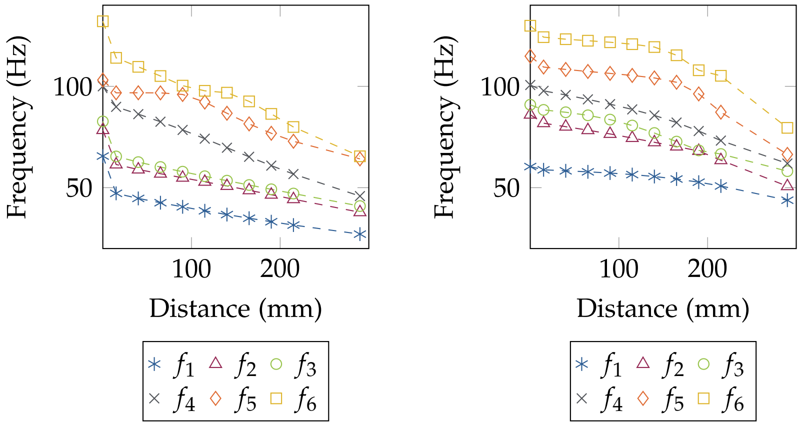

(c) PETRA III girder with connected magnets

(d) Box girder with connected magnets

Figure 14.9: First six eigenfrequencies depending on the distance between girder and magnets for the PETRA III girder (a) and the box girder (b) with individually positioned magnets as well as for the PETRA III girder (c) and the box girder (d) with connected magnets.

magnet modes appeared despite the magnet connection that was also oscillating. Thus, the corresponding frequency decreased strongly.

14.2.1.2 *Stiffness of the Connection between Girder and Magnet*

For both girder geometries, all analysed eigenfrequencies rose with increasing connection stiffness between girder and magnets up to a certain stiffness value, after which the frequencies almost remained constant (figure 14.12). Although the box girder eigenfrequencies showed higher values than the PETRA III girder and the trends of the curves also varied, the 1st eigenfrequency of both girder geometries remained almost constant from a beam cross section diameter of about 50 mm on. Higher-order eigenfrequencies reached constant

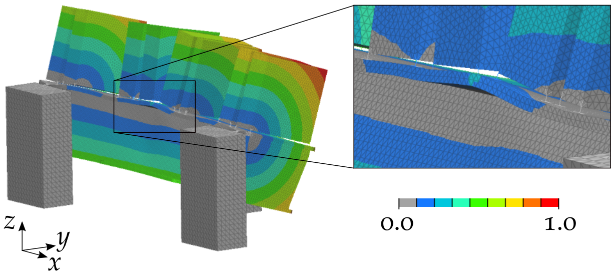

Figure 14.10: 1st mode shape of the PETRA III girder with magnets positioned individually 15 mm above the upper girder surface. The detailed view shows local deformations of the upper girder surface. The colors represent the normalised vibration amplitude.

values at higher beam diameters. Regarding the mode shapes, the 1st mode shape was characterised by local magnet modes for small beam diameters (figure 14.13). As soon as the mode shape changed into a global tilting mode (beam cross section diameter of 30 mm for the PETRA III girder and 50 mm for the box girder), the corresponding 1st eigenfrequency remained almost constant. For a beam cross section diameter of 50 mm, the horizontal stiffness can be estimated as 311 N μm^{-1} (equation 14.2) and the vertical stiffness as $7.7 \cdot 10^3$ N μm^{-1} (equation 14.4).

Regarding the model based on a beam cross section diameter of 5 mm, the frequency of this mode shape characterised by a horizontal movement of the heaviest magnet SF2AH (cf., table 13.1) can be compared to an analytically calculated eigenfrequency. Applying equation 14.3 to the PETRA III girder model, the analytically obtained

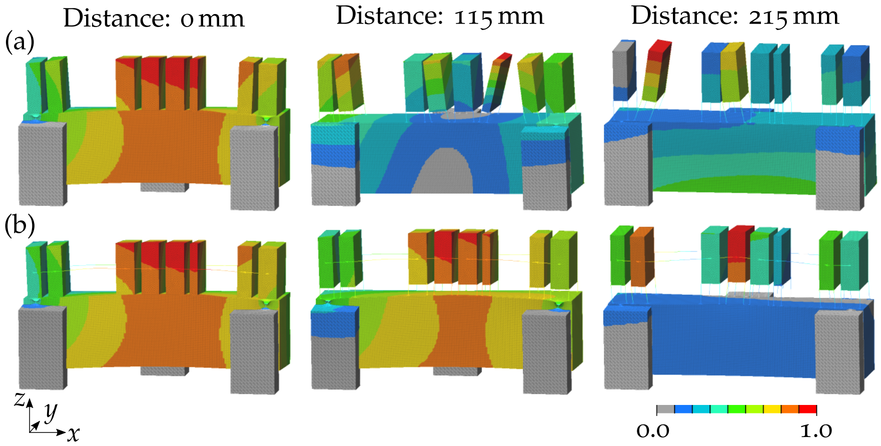

Figure 14.11: 5th mode shape of the box girder for individually positioned (a) and connected (b) magnets for distances between the magnets and the girder of 0 mm (magnets fixed to the upper girder surface), 115 mm, and 215 mm. The colours represent the normalised vibration amplitude.

1st eigenfrequency value of 5.7 Hz was higher than the numerical value of 1.1 Hz.

14.2.1.3 *Magnet Mass*

Almost all eigenfrequencies decreased with increasing magnet mass for both girder geometries (figure 14.14). However, the 1st eigenfrequency of the box girder remained unaffected by the changing magnet mass. The corresponding mode shape showed a global rotation around an axis parallel and almost equal to the magnet axis (figure 14.15). The rotation axis of the 1st mode shape of the PETRA III girder was farther away from the magnet axis, thus, the 1st eigenfrequency decreased with the rising magnet mass.

14.2.2 *Girder Support*

14.2.2.1 *Support Point Position*

The support point position strongly affected the 1st magnet-girder assembly eigenfrequency for both girder geometries (figure 14.16). The higher the support points were located, the higher was the obtained 1st eigenfrequency. As exemplarily shown for the PETRA III girder in figure 14.17, lowering the support points led to a lower rotation axis of the 1st rotational mode shape, which caused a 1st eigenfrequency decrease and larger vibration amplitudes of the magnets.

In addition, the 1st eigenfrequency generally increased with rising distance in x direction between the support points. Regarding the box girder, the 1st eigenfrequency reached its highest value for a maximum distance between the support points 1 and 2 and an equal distance of about 1,300 mm between the support points 2 and 3 and the

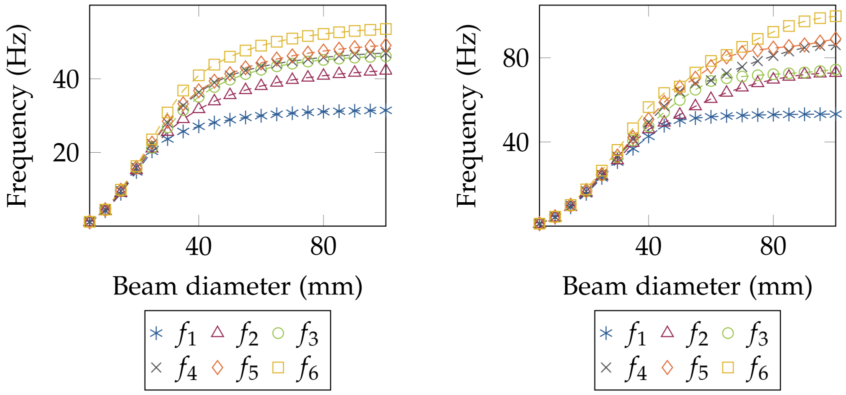

(a) PETRA III girder (b) Box girder

Figure 14.12: First six eigenfrequencies depending on the cross section diameter of the beams connecting the magnets to the PETRA III girder (a) and the box girder (b).

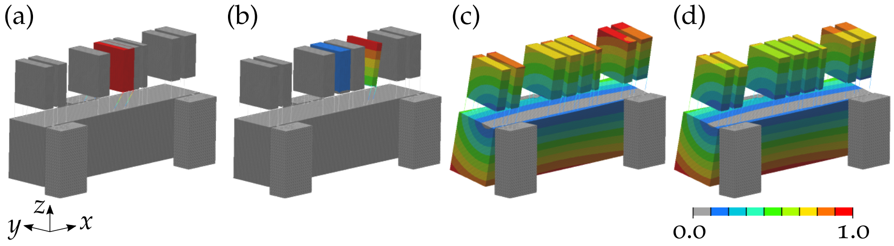

Figure 14.13: 1st mode shape of the magnet-girder assembly with the box girder depending on the connection stiffness between the magnets and the girder, i.e., different cross section diameters of the beams connecting the magnets to the girder involving 5 mm (a), 30 mm (b), 60 mm (c), and 100 mm (d). The colours represent the normalised vibration amplitude.

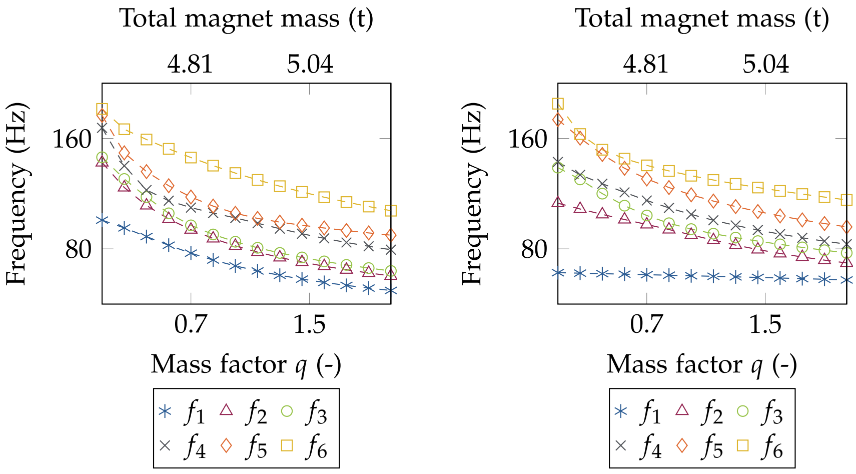

(a) PETRA III girder (b) Box girder

Figure 14.14: First six eigenfrequencies of the magnet girder assembly with the PETRA III girder (a) and the box girder (b) depending on the magnet mass factor q, which was multiplied with the given magnet masses and led to the total mass of all eight magnets displayed on the top horizontal axis.

support points 1 and 3 (table 14.3). For the PETRA III girder, the support point 1 position slightly differed to reach the maximum 1st eigenfrequency. Nevertheless, for both girder geometries, highest eigenfrequencies were obtained defining the three support points to form a large (isosceles) triangle in the xy plane.

The obtained results based on a shell model were finally compared to those of a volume model. While the shell model resulted in a 1st eigenfrequency of 90 Hz for the box girder and 69 Hz for the PETRA III girder, the volume model revealed 1st eigenfrequencies of 98 Hz for the box girder and 76 Hz for the PETRA III girder. Thus, the results of both models coincided by 91% for the box girder and by 90% for the PETRA III girder.

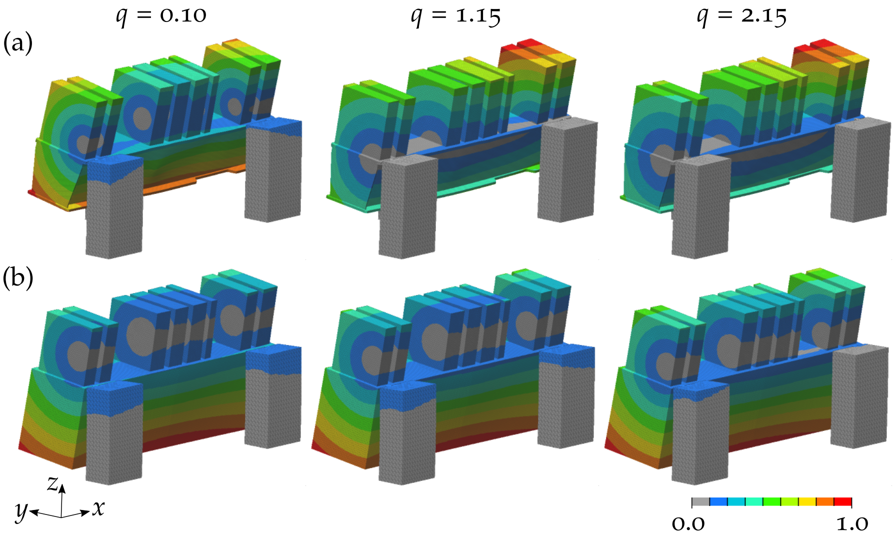

Figure 14.15: 1^{st} mode shape of the magnet-girder assembly with the PETRA III girder (a) and the box girder (b) depending on different magnet masses that were generated by multiplying the mass of each magnet with the factor q. The colours represent the normalised vibration amplitude.

Table 14.3: Position of the three support points (SPs) at a height of 900 mm that led to the highest 1^{st} eigenfrequency of the magnet-girder assembly.

	x value of the SP (mm)			distance x of SPs (mm)		
	SP 1	SP 2	SP 3	SP 1-2	SP 1-3	SP 3-2
Box girder	1,645	4,255	2,950	2,610	1,305	1,305
PETRA III girder	1,935	4,255	2,950	2,320	1,015	1,305

14.2.2.2 *Stiffness of the Girder Support*

Similar to the results for the varying stiffness of the magnet-girder connection, an increasing girder support stiffness resulted in an eigenfrequency raise for both girder geometries until an almost constant value was reached for a specific beam cross section diameter of about 50 mm for the 1^{st} eigenfrequency (figure 14.18). For small beam diameters, the 1^{st} mode shape was characterised by a tilting rigid body mode of the girder as shown exemplarily for the PETRA III girder in figure 14.19. With increasing beam cross section diameter, the rigid body mode transformed into a girder twist mode. A similar behaviour of a rigid body mode being transformed into a girder deflection mode with increasing beam cross section diameter was also observed for the higher-order mode shapes.

For the analysed girder mode shapes, primarily shear forces were acting on the short support beams. Regarding a beam cross section

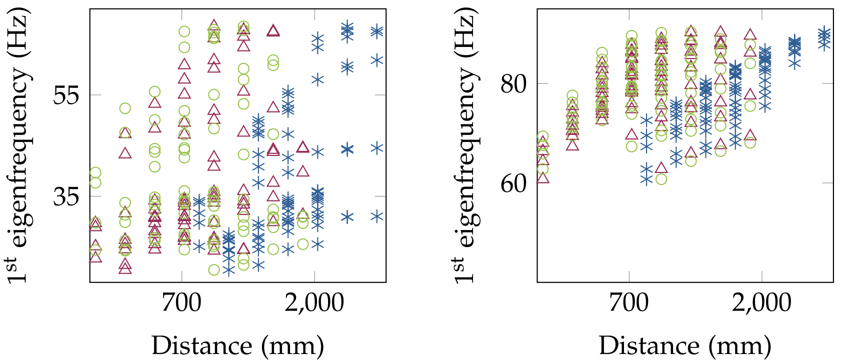

(a) PETRA III girder: 900 mm (b) Box girder: 900 mm

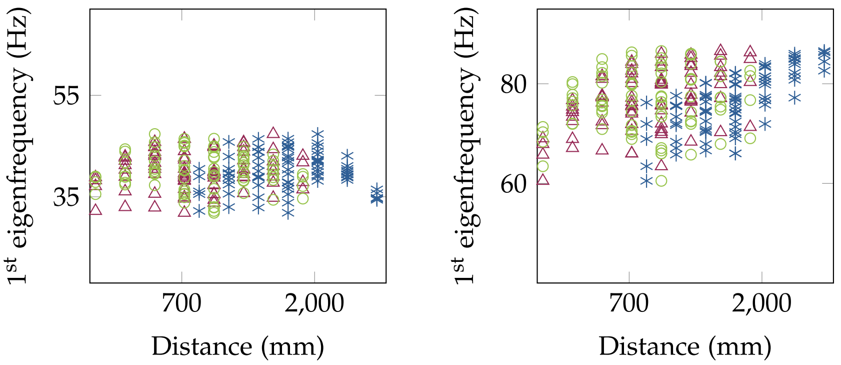

(c) PETRA III girder: 700 mm (d) Box girder: 700 mm

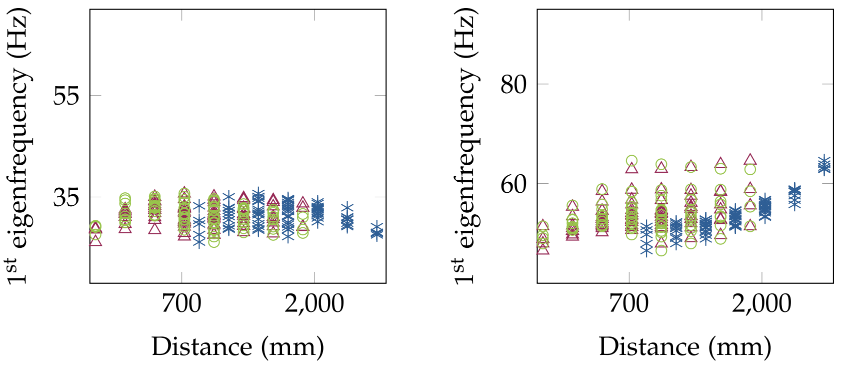

(e) PETRA III girder: 500 mm (f) Box girder: 500

Figure 14.16: 1st eigenfrequency of the magnet-girder assembly depending on the position height and the distance between the three support points located at the front left (SP 1), the front right (SP 2), and the back (SP 3) of the girder. The support points are positioned at different heights (i.e., z values) of 900 mm (a), 700 mm (c), and 500 mm (e) for the PETRA III girder and of 900 mm (b), 700 mm (d), and 500 mm (f) for the box girder. The distances in x direction between SP 1 and SP 2, between SP 1 and SP 3, and between SP 2 and SP 3 are symbolised by blue asteriks, red triangles, and green circles, respectively.

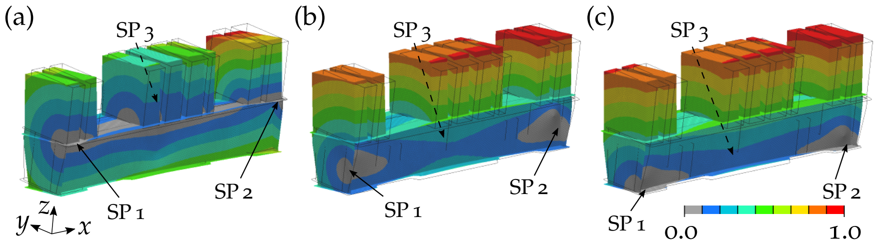

Figure 14.17: 1^{st} mode shape of the loaded PETRA III girder considering the support point positions at $x = 1{,}645$ mm (SP 1), $x = 4{,}255$ mm (SP 2), and $x = 2{,}950$ mm (SP 3, at the rear side of the girder) leading to the highest 1^{st} eigenfrequency. The support points were located at heights of 900 mm (a), 700 mm (b), and 500 mm (c). The colours represent the normalised vibration amplitude and the undeformed loaded girder structures are sketched with grey lines.

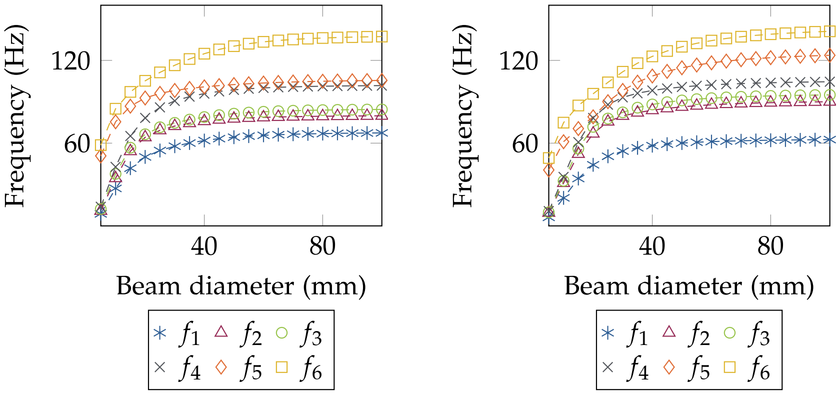

(a) PETRA III girder

(b) Box girder

Figure 14.18: First six eigenfrequencies of the magnet-girder assembly depending on the cross section diameter of the three beams connecting the PETRA III girder (a) and the box girder (b) to the three bases.

diameter of 50 mm, the support stiffness for each support point can be estimated as $5.95 \cdot 10^3\,\mathrm{N}\,\mu\mathrm{m}^{-1}$ considering equation 14.6.

14.2.3 *Material Properties*

The eigenfrequency strongly depended on the material properties. Regarding the box girder, the 1^{st} eigenfrequency differences compared to the S235 girder coincided well with the $\sqrt{E/\rho}$ ratio (cf., table 14.2) indicating that a high $\sqrt{E/\rho}$ ratio led to a high 1^{st} eigenfrequency (figure 14.20). However, for the PETRA III girder, this relation only partly applied, as the normalised 1^{st} eigenfrequency values of the aluminium and the mineral cast girder were lower than those of the box girder.

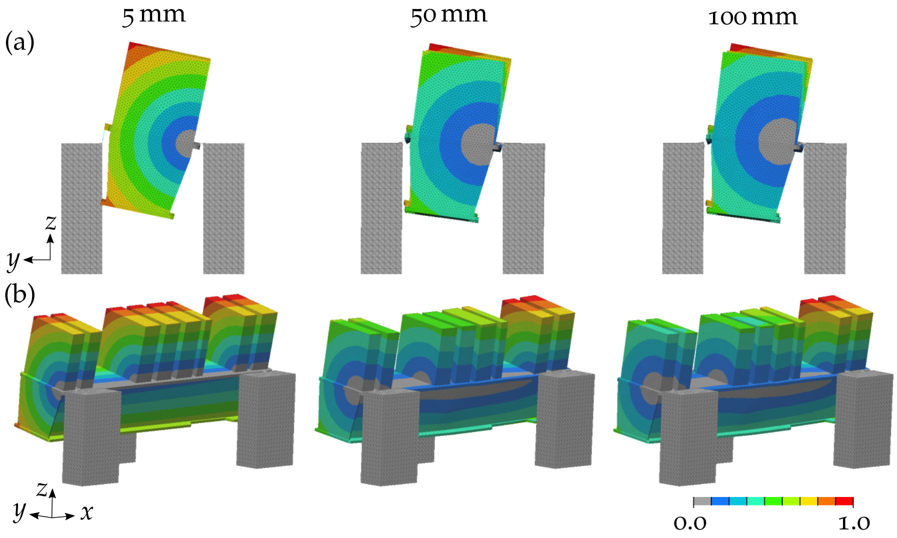

Figure 14.19: Side view (a) and 3D view (b) of the 1st mode shape of the magnet-girder assembly based on the PETRA III girder. The three different cross section diameters 5 mm, 50 mm, and 100 mm of the beams connecting the girder to the bases are considered. The colours represent the normalised vibration amplitude.

14.3 DISCUSSION

The parametric study revealed a strong impact of all analysed components/boundary conditions on the eigenfrequencies of the magnet-girder assembly. Generally, the majority of the analysed relationships between the components/boundary conditions and the overall eigenfrequencies were independent of the studied girder geometries. In the following, the obtained results are discussed.

14.3.1 *Magnets*

The impact of the magnet position height and connection, the magnet connection stiffness, and the magnet mass on the magnet-girder assembly eigenfrequencies was studied. In the following, some comments on the obtained results are given.

Concerning the magnet position height and connection study, the strong eigenfrequency decrease from 0 mm to 15 mm height for the PETRA III girder resulted from the girder geometry. The beams connecting the magnets to the girder were fixed to the girder at the outer part of the upper surface that was not directly supported by the vertical girder walls, since those were slightly moved towards the girder centre (cf., figure 14.1a). Consequently, already a slight lift of the magnets above the girder surface resulted in high stresses – and thus high deformations – in these areas. The connection stiffness of the magnets was reduced and so were the eigenfrequencies. This was not the case

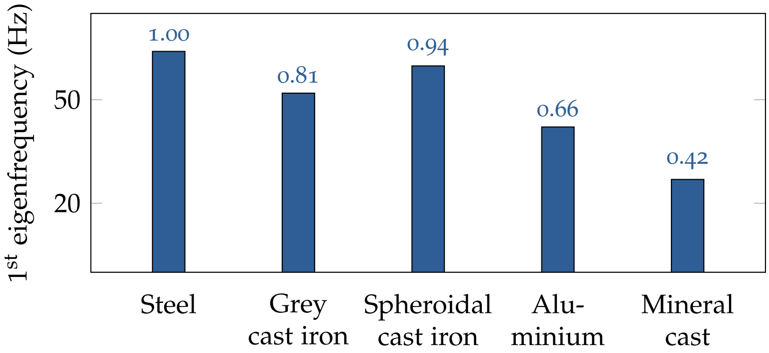

(a) PETRA III girder

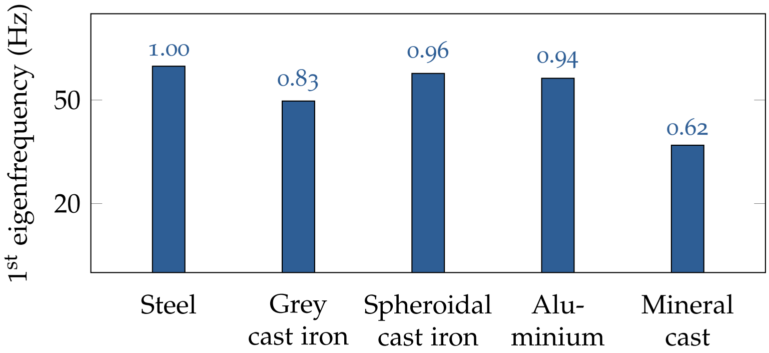

(b) Box girder

Figure 14.20: 1st eigenfrequency of the magnet-girder assembly depending on the material properties of the bases and the PETRA III girder (a) and the box girder (b). Above each bar, the 1st eigenfrequency value normalised with the 1st eigenfrequency for S235 is given.

for the box girder, because the vertical girder walls were at the very ends of the upper girder surface, which is why the connection area to the beams was directly supported.

Regarding the study on the magnet connection stiffness, the analytical calculation of the magnet mode shape frequency was in the same order of the numerically obtained value, but still differed (5.7 Hz vs. 1.1 Hz). The differences can be explained by the simplification of the analytical model, in which the magnet volume was not considered. Consequently, the centre of mass was assumed to be lower than that in the numerical model and the magnet mass inertia was also neglected. In addition, the girder had a certain stiffness, which was abstracted to be infinite in the analytical model. However, since both obtained frequency values were still in the same order, the numerical value can be seen as plausible.

The analyses of the magnet mass impact on the eigenfrequencies showed that the 1st box girder eigenfrequency did not vary with increasing magnet mass. This highlights that the girder eigenfrequency can be independent of the magnet mass, if the corresponding mode shape is characterised by a global rotation around an axis as close as possible to the magnet axis (i.e., to the particle beam).

In summary, the study indicated that the following aspects positively influence (i.e., increase) the magnet-girder assembly eigenfrequencies:

- a low position of the magnets (i.e., as close as possible to the upper girder surface),
- connecting the magnets to each other,
- a high stiffness of the connection between girder and magnets (i.e., a high stiffness of the magnet alignment system),
- a low magnet mass, and
- mode shapes that show a global rotation around an axis close to the particle beam.

The currently installed PETRA III girder is equipped with magnets positioned high above the upper girder surface using an alignment system for each magnet (cf., figure 13.6), which leads to a decrease of the overall eigenfrequencies as shown in the parametric study. For PETRA IV, a different magnet alignment system is planned to increase the magnet support stiffness and to avoid low frequency magnet eigenmodes.

Recently, the alignment system Easy Alignment System (EASy) has been invented at DESY [134]. The EASy type A3 is discussed to be placed between the PETRA IV magnets and the girder. The alignment component is 234 mm high [134], which implies a distance between magnets and girder similar to the maximum value of 215 mm that was analysed in the present parametric study. First experiments on the EASy A3 revealed a minimum horizontal stiffness of $50\,\mathrm{N}\,\mu\mathrm{m}^{-1}$ and a vertical stiffness of slightly more than $1.0{\cdot}10^{3}\,\mathrm{N}\,\mu\mathrm{m}^{-1}$ [145].

In contrast, the parametric study model, in which each magnet was connected to the girder using four beams with a cross section diameter of 50 mm, showed a magnet support stiffness of $311\,\mathrm{N}\,\mu\mathrm{m}^{-1}$ horizontally and $7.7{\cdot}10^{3}\,\mathrm{N}\,\mu\mathrm{m}^{-1}$ vertically. These values are significantly higher than the measured stiffness for the EASy A3. Moreover, considering the analytical calculations based on equation 14.4, a vertical stiffness of $1{,}000\,\mathrm{N}\,\mu\mathrm{m}^{-1}$ would correspond to a beam diameter of about 18.1 mm. Following the relation between the beam cross section diameter and the 1st eigenfrequency displayed in figure 14.12, a cross section diameter of 18.1 mm would result in a 1st eigenfrequency of the magnet-girder assembly of about 13 Hz. However, it shall be noted again that this calculation is based on a simplified analytical model, which is why the estimated eigenfrequency value, as well as the calculated stiffness value of the magnet support have to be interpreted with caution. In further studies, the connection stiffness of the magnets positioned on the girder should be measured to ensure that reliable values are discussed.

At the MAX IV synchrotron radiation facility laboratory, all magnets positioned on one girder are linked in one large box to avoid low frequency magnet bending modes [76]. The parametric study results also indicated that connecting the magnets raises the overall eigefrequencies, because rigid magnet modes at low frequencies are prevented. However, the implementation of a magnet connection is probably not possible for PETRA IV, because an easy and individual adjustment of all magnet installed in the tunnel is required. Consequently, the low frequency magnet bending modes have to be avoided by a very high stiffness of the alignment system.

In the following girder development process (chapter 15), the magnets will be considered as fixed to the upper girder surface, since otherwise an optimisation to increase the girder modes would hardly be possible due to the various low frequency magnet modes.

14.3.2 *Girder Support*

The study of the girder support position and stiffness indicated that the following aspects increase the eigenfrequencies:

- a high position of the support points,
- a horizontal support point positioning in form of a large (isosceles) triangle, and
- a high girder support stiffness.

In different synchrotron machines worldwide, girders are fixed by using more than three support points (e.g., SOLEIL [103] or NSLS-II [139]). However, as already mentioned in chapter 13.3, more than three support points result in an over-determined system, which makes the girder alignment in the tunnel almost impossible. In addition, due to a possible ground settlement during the accelerator operation for many years, a girder alignment might be necessary. Therefore, only three support points were considered here.

Based on the results, the support points should be positioned in a large triangle involving an increased support span to obtain a higher stability and thus higher eigenfrequencies. This was also stated by Liu et al. [91] working on an APS-U girder design. Moreover, the support points should be placed as high as possible, which was also obtained by Amirikas et al. [8] and in previous studies (cf., figure 14.5). Low support point locations would decrease the eigenfrequencies and increase the vibration amplitudes of the magnets in the case of resonance, which should be avoided to guarantee a high functionality of the particle accelerator.

In addition to the support point position, a high stiffness of the girder support system is essential, which is why an appropriate girder alignment system should be chosen. Apparently, wedge jacks and AirLoc AG's precision levellers allow a high girder support stiffness, because they have been used in the latest magnet-girder assemblies (cf., chapter 13.3). Regarding the APS-U girder, the implementation of stiff lateral pushers also rose the eigenfrequencies significantly [120]. Once a girder is aligned, an additional clamping system can further increase the support stiffness and the magnet-girder assembly eigenfrequencies, as applied to the SOLEIL girder [54, 103]. However, considering the targeted alignment tolerance of one girder to the neighbouring girders of 50 μm [148], clamping an aligned girder might lead to small structural deformations and thus to a misalignment of the magnets.

It is also important to note that a high stiffness of the bases, on which the girder is positioned, is necessary to obtain high eigenfrequencies. As shown in previous studies, a low base stiffness can strongly reduce eigenfrequencies (cf., figure 14.5). For this reason, the here considered bases were heavy and stable solid blocks, which can also be utilised for PETRA IV.

14.3.3 *Material Properties*

The material properties strongly influence the eigenfrequencies of the magnet-girder assembly. As eigenfrequencies are known to be proportional to the Young's modulus and anti-proportional to the mass (cf., equation 8.1 or equation 8.12), the observed high dependency of the 1st eigenfrequency on the $\sqrt{E/\rho}$ ratio was expectable. However, this effect seems to only fully apply to the simple box girder. The PETRA IV girder shows a more complex geometry involving an irregular material (mass) distribution. Consequently, not only the $\sqrt{E/\rho}$ ratio, but also the irregular mass distribution has a significant effect on the eigenfrequencies. Thus, it can be concluded that the consideration of the $\sqrt{E/\rho}$ ratio is very useful as a first approach to evaluate the effectiveness of a girder (bases) material, especially for simple girder structures, before further detailed analyses shall be carried out.

Aside from the $\sqrt{E/\rho}$ ratio, further material properties have to be taken into account for the decision on the girder/bases material: Girders placed next to an undulator should have a very low magnetisability to avoid an undesired impact on the undulator magnetic field. Also the temperature stability and corrodibility of a girder and bases material are important characteristics, because variations in the tunnel air temperature and humidity can cause corrosion and structural deformations. Although the PETRA IV tunnel temperature will be stabilised to ± 1 K (cf., chapter 13.4), an outage is always possible, which is why the girder (and bases) material should show a high temperature stability. However, the temperature stability will not be analysed in this work.

As the desired material properties for the girder and bases have not been specified yet, the following girder design process (chapter 15) will consider S235 as material for both girder and bases. Girders of other synchrotron facilities are made of similar materials such as carbon steel (ESRF-EBS [**Cianciosi2016a**]) or ductile cast iron (APS-U [120]). The PETRA IV girder or bases might also be made of grey or spheroidal cast iron. Both materials showed a $\sqrt{E/\rho}$ ratio similar to S235 (cf., table 14.2) and the small deviations in the ratio correlate with the 1st eigenfrequency deviations. Consequently, based on the eigenfrequency results using a steel girder, the eigenfrequency values for a cast iron girder can be estimated.

Since this work focuses on the 3 m PETRA IV girder, which is not located directly next to an undulatur, the magnetisability is not a relevant factor here. However, the parametric study results indicate that the design process of a girder located close to an undulator should consider alternative material properties (e.g., aluminium) from the beginning, as the optimisation outcome can presumably not be applied directly to a girder with a different $\sqrt{E/\rho}$ ratio.

14.4 CONCLUSION

The impact of different boundary conditions and material properties on the magnet-girder assembly was studied. The loading conditions (magnet position height and stiffness, and the magnet mass), the girder support (location of the support points and the support stiffness), and the material properties of the girder and bases strongly influence the eigenfrequencies of the magnet-girder assembly.

Based on the results of the parametric study and the specifications defined by DESY, the following boundary conditions were considered for the subsequent development of a biologically inspired girder design (chapter 15):

- The magnets will be placed directly on the girder surface to have a maximum stiffness and to be able to optimise the girder without the appearance of magnet bending modes in the range of low-order frequencies.

- The magnet mass will be multiplied by a factor q of 1.15 to calculate conservatively with a slightly higher magnet load.

- The girder will be supported at three locations characterised by the x values 1,935 mm (0.05 l_G), 4,255 mm (0.95 l_G), and 2,950 mm (0.5 l_G), which allowed an optimum stability. The girder will be connected to the bases via beams each showing a cross section diameter of 50 mm.

- S235 will be defined as material for the girder and the bases. The latter will be considered in the models as solid blocks.

15

DEVELOPMENT OF A BIOLOGICALLY INSPIRED GIRDER DESIGN

An innovative girder structure is required to achieve the particle beam stability that is essential for an optimum functionality of the PETRA IV machine. In this chapter, the development of a design process for a new 3 m PETRA IV girder is described. The design process is based on biologically inspired structures and optimisation techniques.

15.1 MATERIAL AND METHODS

The development of a new girder design involved different steps, which are summarised in figure 15.1. At first, a topology optimisation was performed to disclose an optimum material distribution (cf., figure 4.1) based on the given specifications that are presented in chapter 13.4. However, a topology optimisation only indicates where material should be placed or removed and does not present an optimum dimensioned structure.

Figure 15.2 shows exemplarily the development process of an optimised 2D structure with the objective to increase the stiffness at reduced mass. Based on the defined boundary conditions and load cases, the topology optimisation identifies an optimum material distribution. The abstraction of the topology optimisation result allows the creation of a beam model with an initial constant cross section diameter. Subsequently, a cross section optimisation shows the optimum dimension of each strut. The result clearly varies from the cross section dimensions obtained by the topology optimisation. Finally, the structure was partly adapted, e.g., replacing sharp corners by smooth connections and thickening critical intersection points to allow a successful manufacturing process.

Thus, also here, the topology optimisation served as an inspiration for an optimum material distribution within the defined design space. The topology optimisation result was interpreted and abstracted, before, in combination with the implementation of biologically inspired structures, a parametric beam-shell model of the girder was created. The subsequent cross section optimisation using the evolutionary strategy led to numerous structures that were evaluated. After transforming the best structure into a volume model, the results of both the beam-shell and the volume model were compared to identify a possible deviation of the results using a comparably fast calculating beam-shell model. The volume model was then improved implementing further biologically inspired structures. Last structural adaptations demanded by changes in the specifications and by special requirements regarding the manufacturing process led to the final girder structure. After the manufacturing process, the eigenfrequencies and mode shapes were measured performing impact tests and compared to the numerical results obtained for the volume model.

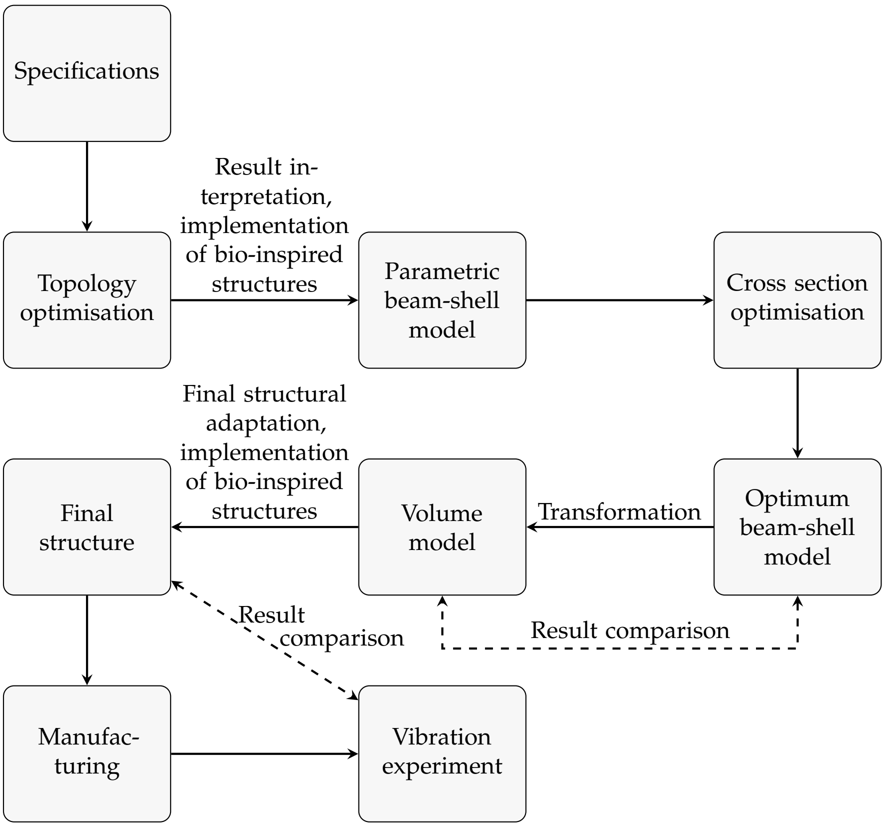
Specifications
Result interpretation, implementation of bio-inspired structures
Topology optimisation
Parametric beam-shell model
Cross section optimisation
Final structural adaptation, implementation of bio-inspired structures
Final structure
Volume model
Transformation
Optimum beam-shell model
Result comparison
Result comparison
Manufacturing
Vibration experiment

Figure 15.1: Overview of the girder design procedure including nine steps.

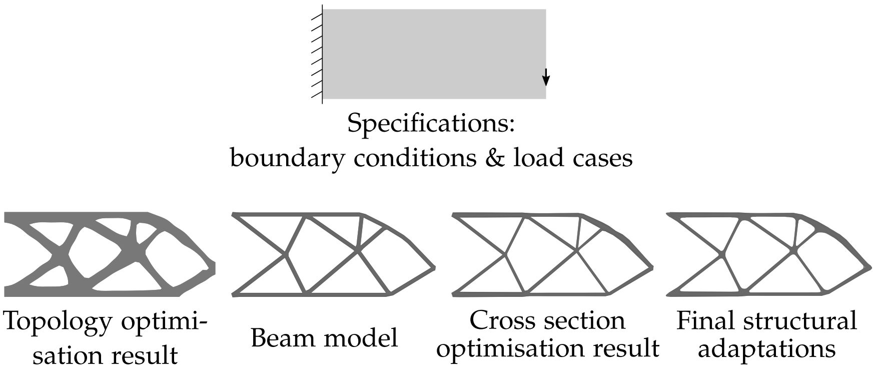
Specifications: boundary conditions & load cases

Topology optimisation result

Beam model

Cross section optimisation result

Final structural adaptations

Figure 15.2: Development of an optimised 2D structure based on the given specifications. The process comprised a topology optimisation, the development of a beam model, a cross section optimisation, and the finalisation of the structure implementing small structural adaptations, e.g., rounding of sharp edges and corners.

15.1.1 *Topology Optimisation*

A topology optimisation was conducted to reveal an optimum material distribution. The model was built up following the specifications in chapter 13.4 and the model assembly shown in figure 13.9. Thus, the design space, from which material was removed during the optimisation, was shaped like a box. However, the upper surface with a thickness of 20 mm was defined as non-design space, because a continuous upper girder surface was required for the later fixation of different components in the tunnel. The box girder was equipped with magnets and connected via beams to the bases. Consequently, the non-design space comprised, aside from the upper girder surface, the magnets, the bases, the connection beams, and the RBE3s defined between the connection beams and both the girder and the bases.

The box girder, the magnets, and the bases were meshed with constant element sizes of 20 mm, 50 mm, and 100 mm, respectively, leading to a very fine mesh of the design space to allow the development of clear load paths during the optimisation. Table 15.1 lists the total number of nodes and elements.

Table 15.1: Number of volume mesh nodes and elements of the topology optimisation for the 3 m PETRA IV girder.

	Number of nodes	Number of elements
Girder design space	279,541	1,574,726
Girder non-design space	17,150	50,181
Magnets	7,066	25,725
Bases	2,609	9,132
Total	306,366	1,659,764

All nodes of the lower bases' surfaces were considered as fixed (all translations = all rotations = 0). A modal load case to calculate the 1st eigenfrequency and a linear static load case to obtain the maximum static deformation due to gravity ($g = 9.81\,\mathrm{m\,s^{-2}}$ in -z direction) were defined.

The optimisation objective was to maximise the 1st eigenfrequency considering two constraints: a maximum volume fraction of 20% for material removal from the solid design space and a maximum static deformation due to gravity of 0.05 mm.

The topology optimisation result assigns to each element of the design space an artificial element density value. While a value of 1 indicates that the corresponding element is essential to reach the defined objectives, elements with low artificial density values are removed. Here, the threshold value of the artificial element density was chosen as low as possible to obtain a connected structure.

15.1.2 *Abstraction and Cross Section Optimisation*

The structure obtained from the topology optimisation was abstracted into a beam-shell model. For this, strut- and beam-like parts were replaced by lines (beams) and surface-like parts by surfaces (shells). Thick, surface-like parts were abstracted as surfaces stiffened by additional rectangular ribs or as sandwich structures with an inner core based on ribs oriented in 45° angles with respect to the horizontal.

All lines were divided into sections of about 50 mm length and considered as CBEAMs that were connected to the upper solid plate via RBE3s. The surfaces were meshed with an element size of 30 mm using Shell elements (CTRIAs) and connected to the corresponding beams by sharing nodes. The top surface that had been defined as non-design space, the magnets, and the bases were considered as solids. Also the beams connecting the girder and the bases were included in the model.

Subsequently, an evolutionary strategic optimisation of the shell thicknesses and the beam cross section diameters was performed using the optimiser Octopus implemented in Grasshopper that permitted a multi-objective optimisation considering various parameters (for more information related to Octopus, it is referred to chapter 9). The optimisation objectives were (1) the maximisation of the 1^{st} eigenfrequency, (2) the minimisation of the maximum deformation due to gravity, and (3) the minimisation of the girder mass. The 21 parameters involved 11 shell thicknesses (definition range for each thickness: 5.0-30.0 mm) and 10 beam cross section diameters each varying in the range 20.0-70.0 mm. The population size was set to 100 and the stopping criterion was a maximum number of 20 generations. Regarding the optimisation settings, the default Octopus values were chosen (cf., table 9.1).

All structures forming the last generation were considered for evaluation choosing the structure with the highest 1^{st} eigenfrequency as the girder structure with an optimum parameter combination. With the help of different algorithms implemented in the Grasshopper-based module ELISE, the beam-shell model was transferred into a volume model that was also evaluated regarding its eigenfrequencies, mode shapes, and maximum static displacement due to gravity ($g = 9.81\,\mathrm{m\,s^{-2}}$ in -z direction). A comparison of the results obtained by the volume model to those based on the beam-shell model indicated whether the fast calculating beam-shell model had already revealed plausible results.

15.1.3 *Biologically Inspired Structures and Further Structural Adaptation*

Based on the numerical results of the previous section, structural adaptations of the girder were performed. The 1^{st} mode shape of the optimised girder structure showed a bending of the large lower strut. In order to avoid this deformation and to raise the corresponding eigenfrequency, a vertical strut was implemented in the middle front of the structure connecting the large lower strut to the upper girder surface.

Subsequently, the structure was provided with different biologically inspired structural elements to further improve both the mechanical properties and the design. Table 15.2 summarises all biologically inspired structures implemented in the girder design.

Due to posterior changes in the specifications by DESY, further structural changes have been applied to the designed girder. These changes involved a small reduction of the girder design space, which led to the removal of a small amount of material at the left girder side close to the base. In addition, the girder structure was slightly adapted to create space for a middle, inner screw. In the areas of the support point positions, material was added horizontally to fix the girder on machine shoes that allow a later vertical adjustment and connect the girder to the bases. At DESY, it was decided to use the machine shoe type UMS5-KDSA (isoloc Schwingungstechnik GmbH, `www.isoloc.de`).

In the final vibration experiments, the eigenfrequencies and the mode shapes of the unloaded girder positioned on soft springs were measured. In order to compare the numerical results to those obtained by the experiments, the eigenfrequencies and the mode shapes of the free and unloaded bio-inspired girder were calculated specifying grey cast iron (EN-GJL-350) as girder material (cf., material properties in table 14.2). In addition, the 1^{st} eigenfrequency of the free and unloaded PETRA III girder of 4.2 m length currently installed in the tunnel (figure 13.6) was also calculated considering grey cast iron as girder material and compared to that of the bio-inspired girder.

After that, the magnets, the bases provided by DESY, and the machine shoes were included into the model to obtain the eigenfrequencies, the mode shapes, and the maximum deformation due to gravity of the magnet-girder assembly. For the bases, spheroidal cast iron (EN-GJS-700-2) was defined as material (cf., material properties in table 14.2). The machine shoes were abstracted as solid cylinders made of S235 following the dimensions of the already mentioned machine shoe type UMS5-KDSA. For all model components, a fine volume mesh was used as characterised in table 15.3.

Table 15.2: Five biologically inspired design principles implemented in the PETRA IV girder design. The figures show the branches of a tree (1), a shell structure detail of the diatom *Thalassiosira* sp. (© AWI, the scale bar represents 10 μm) (2), a detail of a Scanning Electron Microscopic (SEM) image of the diatom *Roperia tesselata* (reprinted from Lee and Lee [87] with permission from Taylor & Francis, the scale bar represents 1 μm) (3), a SEM image of *Stephanopyxis nipponica* (reprinted from Ferrario et al. [48] with permission from Schweizerbart science publishers, the scale bar represents 10 μm) (4), and a SEM image of *Hemiaulus* sp. (reprinted from Friedrichs [51] with permission from the author) (5).

(1) *Hierarchical structures:* Tree branches are hierarchical structures allowing a smooth load distribution and high stiffness. A hierarchical structure was implemented in the lower part of the girder structure replacing the cross-struts and the small surface in between that were obtained from the topology optimisation.	
(2) *Voronoi combs:* Voronoi combs present in many diatom shells, e.g., *Thalassiosira* sp., lead to high surface stiffening, high eigenfrequencies, and increased energy absorption. Here, Voronoi combs replaced the initially regular rectangular ribs of four surfaces.	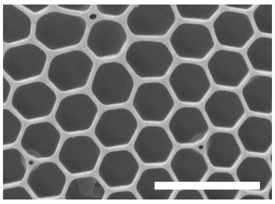
(3) 45° *oriented ribs:* Many diatom shell structure show structures oriented in 45°, e.g., *Roperia* sp., which increase the torsional stiffness. These ribs were implemented in the girder structure to increase the torsional stiffness, as the lower order mode shapes were likely to be characterised by a global girder torsion.	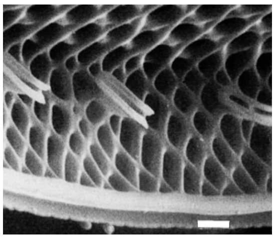
(4) *Round / oval holes:* Round/oval structures result in a reduction of peak stresses and are present in numerous diatom shell structures, e.g., in *Stephanopyxis* sp. Additionally, these holes reduce weight. They were implemented in the back surface of the girder structure. Besides the weight reduction, these structures are also essential for the subsequent casting process, because they allow the removal of material inside.	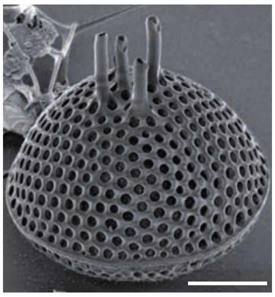
(5) *Smooth connections:* In almost all diatom shells, smooth connections and transitions to reduce peak stresses can be observed. Smooth connections were also adopted to the girder structure. Besides the reduction of peak stresses, it is also necessary for a successful casting process.	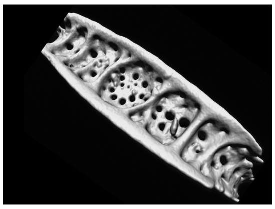

Table 15.3: Number of volume mesh nodes and elements of the final magnet-girder assembly for the 3 m PETRA IV girder.

	Number of nodes	Number of elements
Girder	499,552	2,815,203
Magnets	197,111	920,933
Mashine shoes	1,164	4,202
Bases	35,472	162,810
Total	733,299	3,903,148

15.1.4 *Manufacturing and Impact Testing*

The designed girder structure was manufactured by the foundry Wurzen GmbH using the casting technology in connection with 3D printed sand moulds. Grey cast iron (EN-GJL-250) was used due to its low ductility [184], which supported the filling of the complex mould. Wurzen GmbH also took care of additional adaptations of the manufactured part requested by DESY, including bore holes, notches, and a high surface evenness.

Impact testing was conducted at DESY to measure the eigenfrequencies of the free and unloaded girder. The girder was positioned on three springs to abstract the free positioning (cf., figure 15.15). Eight uniaxial accelerometers (Type 4507 B 005, Brüel & Kjær) were fixed with resin to the upper girder surface at the different positions shown in figure 15.3. Using a recoilless hammer (Halder Supercraft 3377.050, 1.15 kg), the girder was hit through a rubber mat at the positions 4 and 8. Subsequently, the accelerometers were fixed to one pedestal and to the floor next to the set up in order to measure the vibrations of the pedestal and the floor. After converting the analog signals into digital signals using the ADC Data Translator DT9857E-08, the custom-made software VSI DataServer (Mark Lomperski, DESY) was utilised to store the data and perform the Fourier transformation to obtain the Power Spectral Density PSD of the girder.

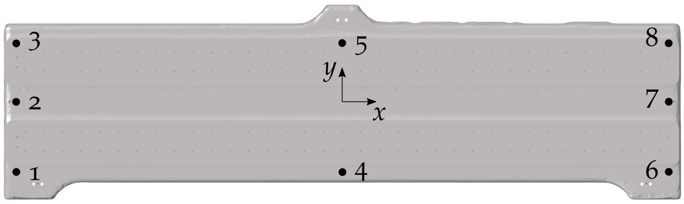

Figure 15.3: Top view of the bio-inspired girder, in which the positions 1 to 8 of the eight accelerometers are shown in black circles. The considered coordinate system differs from that used in the simulations.

The measured first five eigenfrequencies of the girder corresponded to the average of the eigenfrequency values detected by the eight accelerometers. Deviations between the simulation results and the measured eigenfrequencies were calculated using equation 8.11.

As the impact testing did not involve a force measuring modal hammer, a custom-made MATLAB (The MathWorks, Inc.) script (Daniel Thoden, DESY) was used to obtain the measured mode shapes (i.e., the displacement of the upper girder surface) from the acceleration data. The first step of the procedure included in the MATLAB script was the double integration of the measured data using the Newton-Cotes formulas (quadrature). Then, the eigenfrequencies were separated applying a 6th order Infinite Impulse Response (IIR) bandbass filter. After applying a frequency bandpass filter with the range 90%f_n to 110%f_n (f_n denotes the n-th eigenfrequency) to the data, the resulting displacement was plotted for each accelerometer in a 3D plot matching the actual accelerometer positions. A movie was created for each mode shape visualising the vibration of the upper girder surface, which was compared to the numerically obtained mode shapes.

The **Newton-Cotes formulas** *are used for numerical integration. They are helpful for integrand data given at equidistant points.*

IIR filters *produce filters with sharp frequency cutoff characteristics and only require a small number of coefficients and thus comparably little memory capacity. They are often applied to obtain the amplitude response.[126]*

15.2 RESULTS

This sub-chapter presents the results of the girder development process aiming at a biologically inspired PETRA IV girder design.

15.2.1 *Topology Optimisation*

The topology optimisation resulted in a continuous structure involving all elements of an artificial element density larger than 0.55 (figure 15.4a). At a first glance, the structure reminded of a bridge. It consisted of two large arch-like structures connected to the upper girder surface, which were also interconnected at several positions. The rear arch-like structure was filled with matrial. At both ends of the front arch-like structure, material was accumulated forming surface-like structures. The convergence plots shown in appendix A.5 indicated a successfull maximisation of the defined optimisation objective considering the constraints on the maximum static displacement and the volume.

15.2.2 *Abstraction and Cross Section Optimisation*

The topology optimisation result was abstracted to a beam-shell model to perform a cross section optimisation. As illustrated in figure 15.4b, thin, beam-like structures were abstracted as curves/lines, whereas large, surface-like structures were considered as surfaces. The rear, thick arch-like structure was transformed into a biologically inspired sandwich structure with two outer surfaces and inner ribs oriented

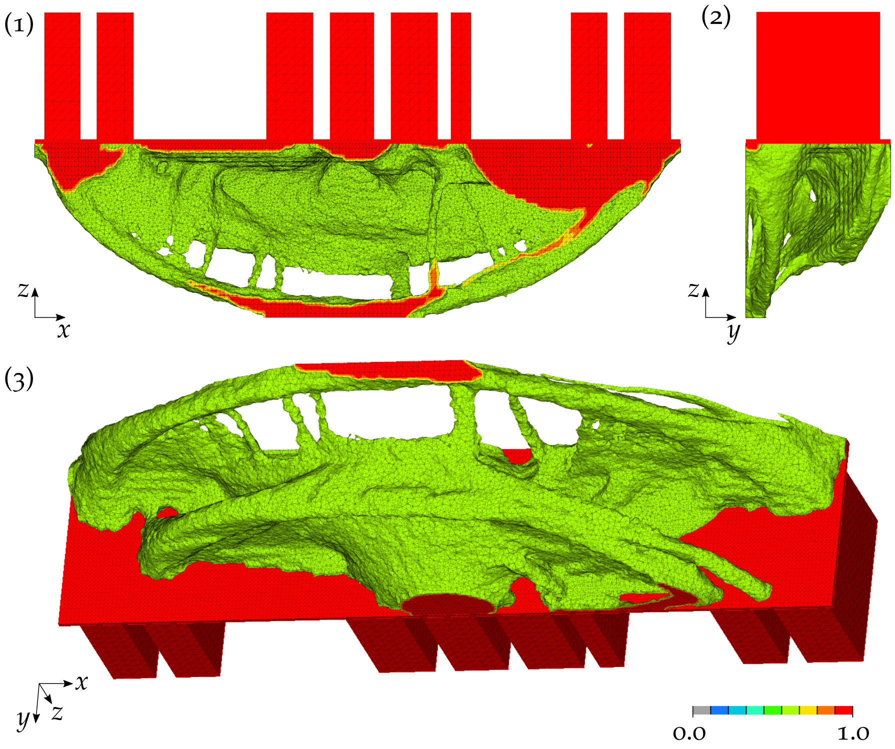

(a) Topology optimisation result

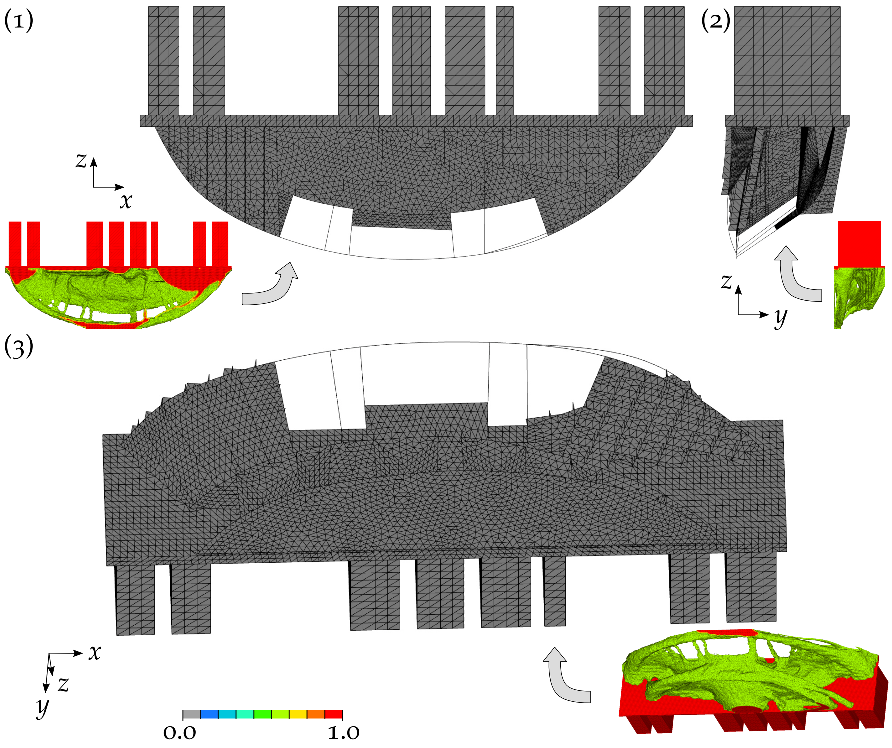

(b) Beam-shell model

Figure 15.4: Front view (1), side view (2), and 3D view (3) of the topology optimisation result for the loaded girder structure (a) and the abstracted beam-shell model (b). The topology optimisation result comprises all elements with an artificial element density larger than 0.55 represented by the colouring.

with an angle of 45° towards the horizontal. The two surfaces on the right and on the left side of the structure were stiffened by applying cellular structures as ribs. In a first step, regular rectangular ribs were applied.

The evolutionary strategic optimisation led to numerous girder structures varying in their parameter values. Figure 15.5 shows the highest 1^{st} eigenfrequency reached in each generation and the corresponding maximum static displacement and girder mass of that girder structure. All three objectives converged towards a maximised (1^{st} eigenfrequency) or minimised (maximum static deformation and girder mass) value. However, the differences between the objective values of the first and the last generation were only 1.3% (1^{st} eigenfrequency), -3.0% (maximum static deformation), and -2.9% (girder mass) considering equation 8.11. Comparing all structures of the first and the last generation (figure 15.6), a general improvement of the whole population can be seen. The structures were pushed towards a higher 1^{st} eigenfrequency, a lower girder mass, and a lower maximum static displacement as it has been defined in the optimisation

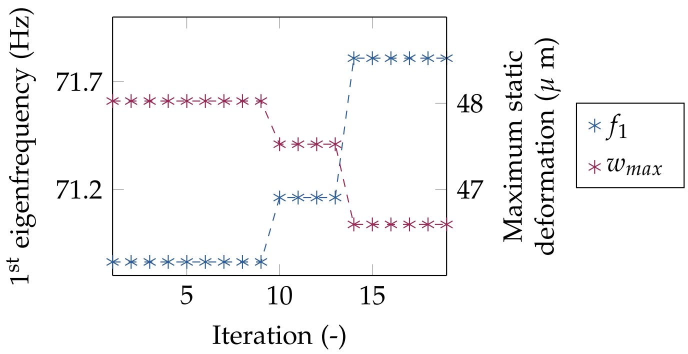

(a) 1^{st} eigenfrequency and maximum static deformation

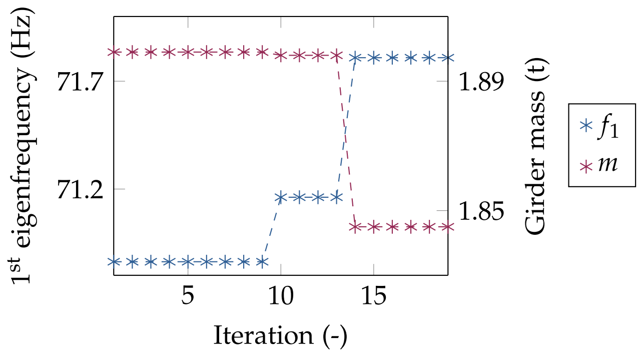

(b) 1^{st} eigenfrequency and girder mass

Figure 15.5: The cross section optimisation convergence plots for the beam-shell girder model are displayed. For each iteration (generation), the highest 1^{st} eigenfrequency f_1 and the corresponding maximum static deformation w_{max} (a) as well as the corresponding girder mass m (b) are given.

objectives. Four different parameter combinations were exemplarily highlighted. The structures 1 and 2 showed a very similar maximum static deformation, whereas their girder mass and 1st eigenfrequency varied strongly. In contrast to that, the structures 1 and 4 had a similar girder mass, but differed in their maximum static displacement and their 1st eigenfrequency. Also interesting is the comparison of the structures 2 and 3, which were characterised by the same 1st eigenfrequency and also a similar girder mass, but showed very different maximum static displacements.

The girder structure with the highest 1st eigenfrequency (highlighted with a square in figure 15.6) showed a 1st eigenfrequency of 71.8 Hz, a maximum static deformation of 0.047 mm, and a girder mass of 1.84 t. The beam cross section diameters and shell thicknesses leading to this structure are illustrated in figure 15.7. The beam cross section diameters varied from 39.6 mm to 68.8 mm and the shell thicknesses from 13.1 mm to 29.5 mm.

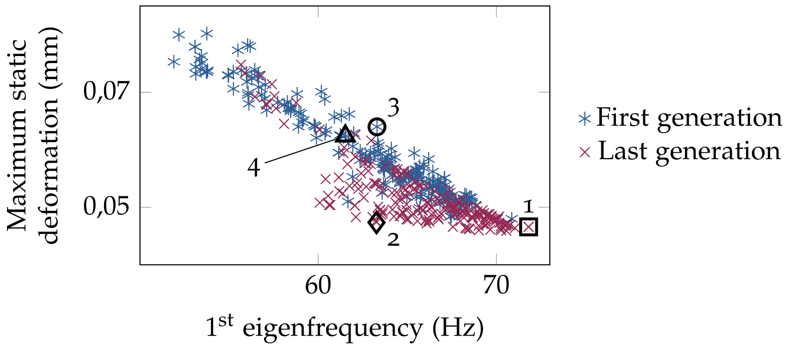

(a) 1st eigenfrequency and maximum static deformation

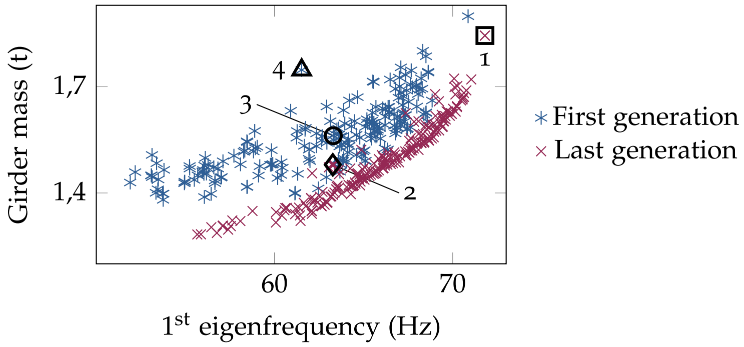

(b) 1st eigenfrequency and girder mass

Figure 15.6: For all structures of the first and the last generation obtained by the evolutionary strategic cross section optimisation, the 1st eigenfrequency and the corresponding maximum static deformation (a) as well as the 1st eigenfrequency and the corresponding girder mass (b) are displayed. Four structures are exemplarily bordered in shape of a square (structure 1), a diamond (structure 2), a circle (structure 3), and a triangle (structure 4).

Table 15.4 summarises the properties of the chosen girder structure with the highest 1st eigenfrequency based on a beam-shell model and a volume model. The results coincided very well showing deviations of maximum 9.2% for the first four eigenfrequencies, 2.0% for the maximum static deformation, and 0.0% for the girder mass. Figure 15.8 displays the first four mode shapes considering the volume model, which coincided with those of the beam-shell model. All mode shapes showed global girder deformations. Additionally, the first two mode shapes were characterised by a strong deformation of the large lower strut.

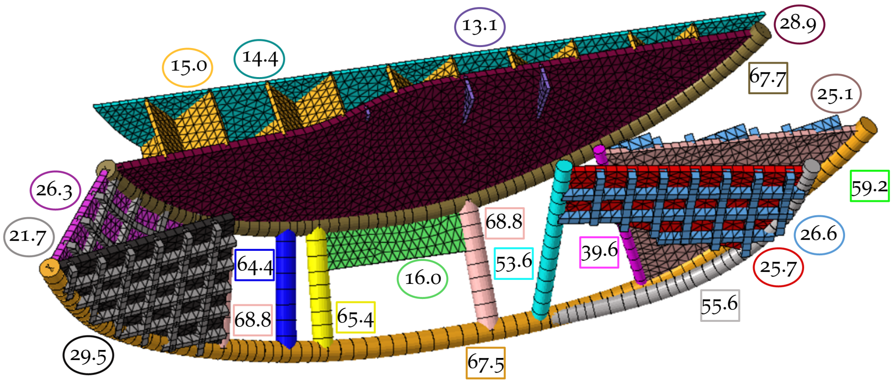

Figure 15.7: The structure with the highest 1st eigenfrequency among all structures of the last optimisation iteration was based on the displayed shell thicknesses (circled values) and beam cross section diameters (framed values). The border colours of the dimensions given in mm match the colours of the corresponding shell or beam. The upper girder surface is hidden.

Table 15.4: First four eigenfrequencies, maximum static deformation due to gravity, and the girder mass for the beam-shell model and the volume model. The deviation of the beam-shell model compared to the volume model is given. In all models, steel S235 was considered as material of the girder and the bases.

		Beam/shell model	Volume model	Deviation
Eigenfrequencies	f_1	67.3 Hz	69.3 Hz	-2.9
	f_2	73.2 Hz	72.8 Hz	0.5%
	f_3	87.4 Hz	96.3 Hz	-9.2%
	f_4	95.1 Hz	104.3 Hz	-8.8%
Maximum static deformation		0.051 mm	0.050 mm	2.0%
Girder mass		1.84 t	1.84 t	0.0%

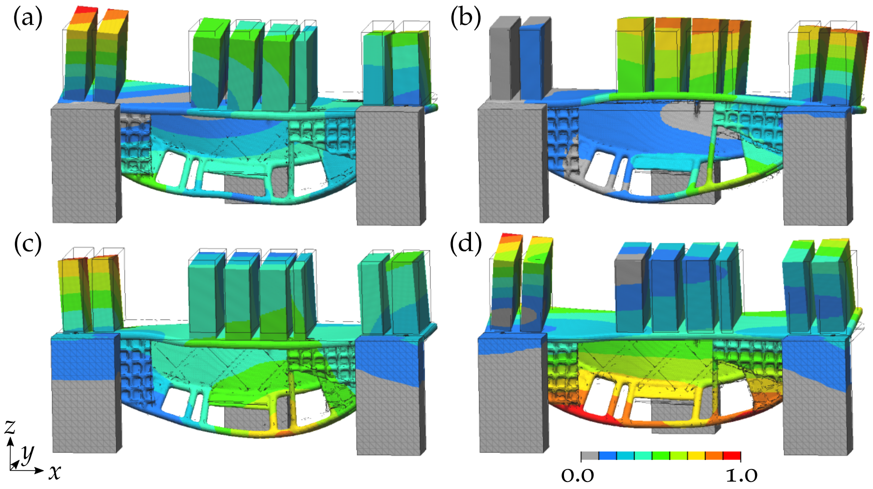

Figure 15.8: 1st (a), 2nd (b), 3rd (c), and 4th (b) mode shape of the volume model that resulted from the cross section optimisation. The colours represent the normalised vibration amplitude and the undeformed magnet-girder assemblies are sketched with grey lines. Steel S235 is specified as material of the girder and the bases.

15.2.3 *Biologically Inspired Structures and Further Structural Adaptation*

The final bio-inspired girder design is pictured in figure 15.9 including an illustration of the biologically inspired features implemented in the design. Moreover, the additional structural adaptations due to late changes in the specifications are marked. They include (1) the slight removal of material at the front-left side and at the rear middle creating space for the bases that were moved horizontally towards the beam axis, (2) the small material removal at the lower side of the upper thick surface to make space for the middle screw, and (3) the implementation of material in form of 'ears' at the three support point positions allowing a connection to the machine shoes.

The designed girder mad of grey cast iron had a volume of 2.76 m^3 and a mass of 2.01 t. The eigenfrequencies of the free, unloaded girder and of the magnet-girder assembly, considering the bases provided by DESY and the machine shoes abstracted as cylinders, are listed in table 15.5. The 1st eigenfrequency dropped by 54% comparing the magnet-girder assembly to the free girder. The 1st eigenfrequency of the free, 4.2 m long PETRA III girder was with 119.1 Hz very similar to that of the here designed girder.

Figure 15.10 shows the first four mode shapes of the free, unloaded girder. The 1st eigenmode is a twist around the centre of the upper girder surface. This corresponds to the 1st mode shape of the magnet-girder assembly (figure 15.11). The remaining displayed mode shapes of the magnet-girder assembly differed from those of the free unloaded girder. Nevertheless, they were were similar to those of the first volume model (figure 15.8). However, the 1st mode shape showed already a deformation of the bases, which has not been observed for the previously used box-shaped bases.

Regarding the maximum deformation due to gravity of the magnet-girder assembly, the highest value of 53 μm ocurred in the middle front of the girder far away from the support points (figure 15.12).

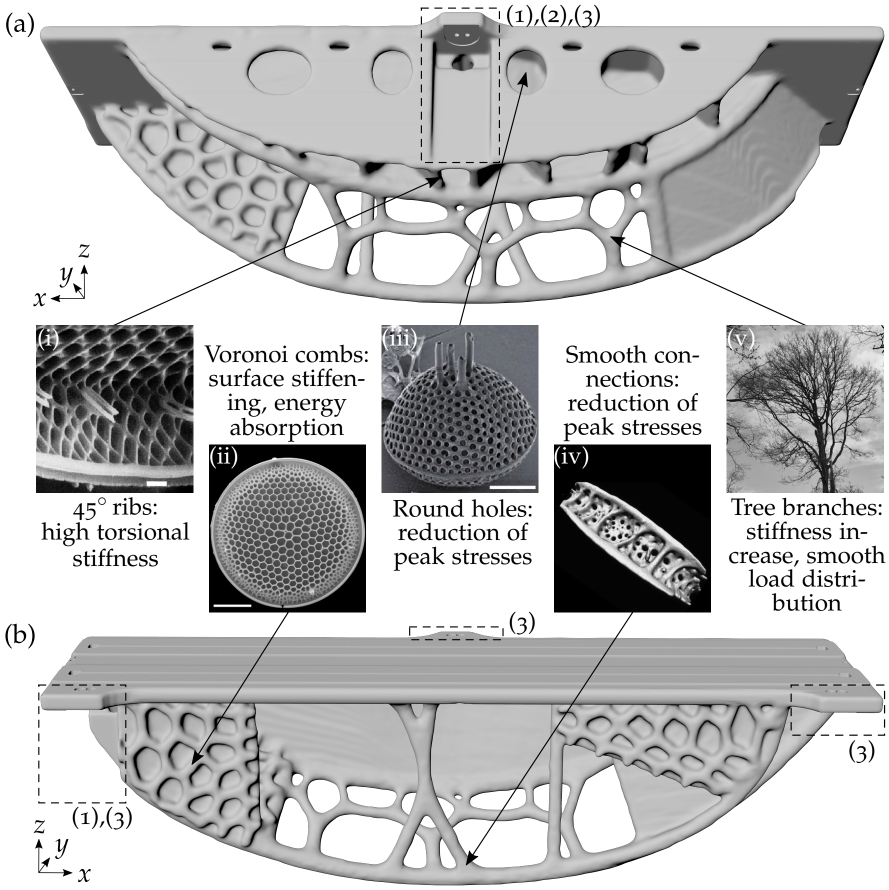
(a)
(1),(2),(3)
z
y
x
(i)
Voronoi combs: surface stiffening, energy absorption
(iii)
Smooth connections: reduction of peak stresses
(v)
(ii)
(iv)
45° ribs: high torsional stiffness
Round holes: reduction of peak stresses
Tree branches: stiffness increase, smooth load distribution
(b)
(3)
(3)
(1),(3)
z
y
x

Figure 15.9: Rear view (a) and front view (b) of the biologically inspired girder design. The figures of the biological role models are displayed: a detail of a Scanning Electron Microscopic (SEM) image of the diatom *Roperia tesselata* (reprinted from Lee and Lee [87] with permission from Taylor & Francis, the scale bar represents 1 μm) (i), the diatom *Thalassiosira* sp. (© AWI, the scale bar represents 10 μm) (ii), a SEM image of *Stephanopyxis nipponica* (reprinted from Ferrario et al. [48] with permission from Schweizerbart science publishers, the scale bar represents 10 μm) (iii), a SEM image of *Hemiaulus* sp. (reprinted from Friedrichs [51] with permission from the author) (iv), and the branches of a tree (v). The additional structural modifications are bordered with dashed black lines and include material removal due to position changes of the bases (1) and due to the location of a large middle screw (2) as well as the implementation of 'ears' (3).

Table 15.5: First five eigenfrequencies of the free unloaded bio-inspired girder and the magnet-girder assembly considering the bio-inspired girder. Grey cast iron is specified as girder material.

	free and unloaded girder	magnet-girder assembly
f_1	119.6 Hz	55.0 Hz
f_2	189.8 Hz	59.8 Hz
f_3	236.8 Hz	74.8 Hz
f_4	257.1 Hz	82.7 Hz
f_5	290.4 Hz	94.6 Hz

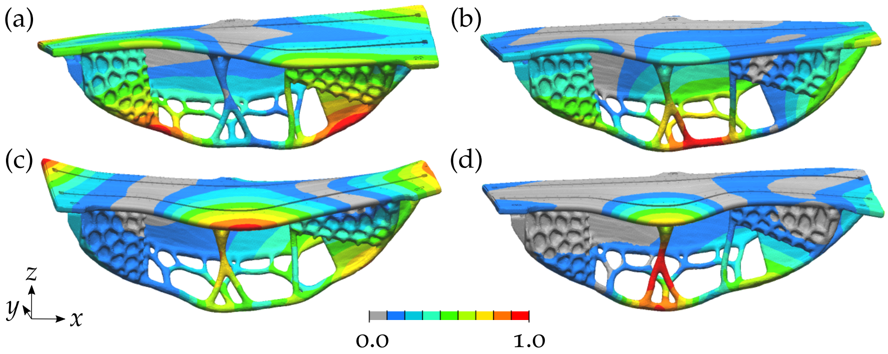

Figure 15.10: 1^{st} (a), 2^{nd} (b), 3^{rd} (c), and 4^{th} (d) mode shape of the free and unloaded final biologically inspired girder. The colours represent the normalised vibration amplitude. Grey cast iron is specified as girder material.

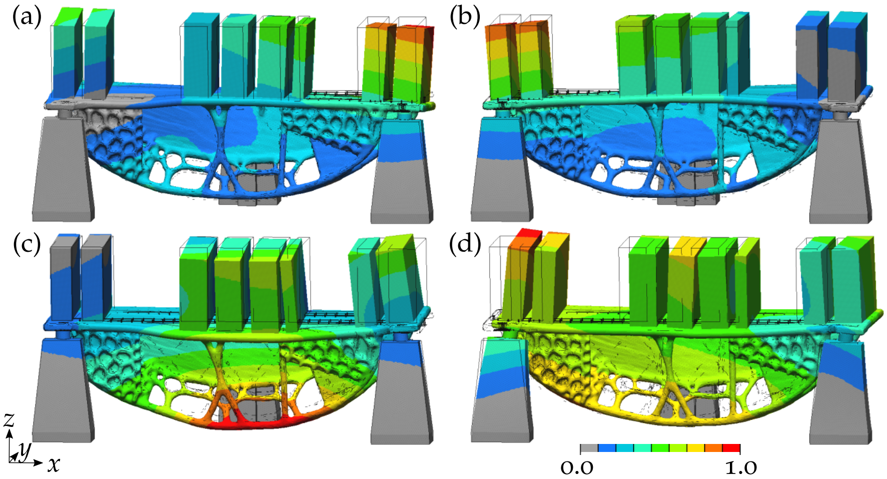

Figure 15.11: 1^{st} (a), 2^{nd} (b), 3^{rd} (c), and 4^{th} (d) mode shape of the final magnet-girder assembly. The colours represent the normalised vibration amplitude and the undeformed models are sketched with grey lines. Grey cast iron is specified as girder material, spheroidal cast iron as material of the bases.

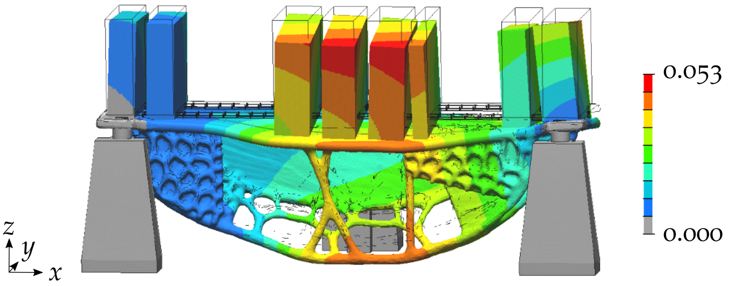

Figure 15.12: Deformation due to gravity of the final magnet-girder assembly. The colours represent the deformation in mm and the undeformed model is sketched with grey lines. Grey cast iron is specified as girder material, spheroidal cast iron as material of the bases.

15.2.4 *Manufacturing and Impact Testing*

The designed girder structure was manufactured using the casting technology. Bauch [23] documented the manufacturing process. The final mould is displayed in figure 15.13a. At a temperature of 1,340 °C, the liquid metal (grey cast iron EN-GJL-250) was filled into the mould's voids (figure 15.13b) leading to the cast component illustrated in figure 15.13c. Figure 15.13d shows the final cast component after removing sand leftovers, burrs, and feeders and after the cleaning procedure.

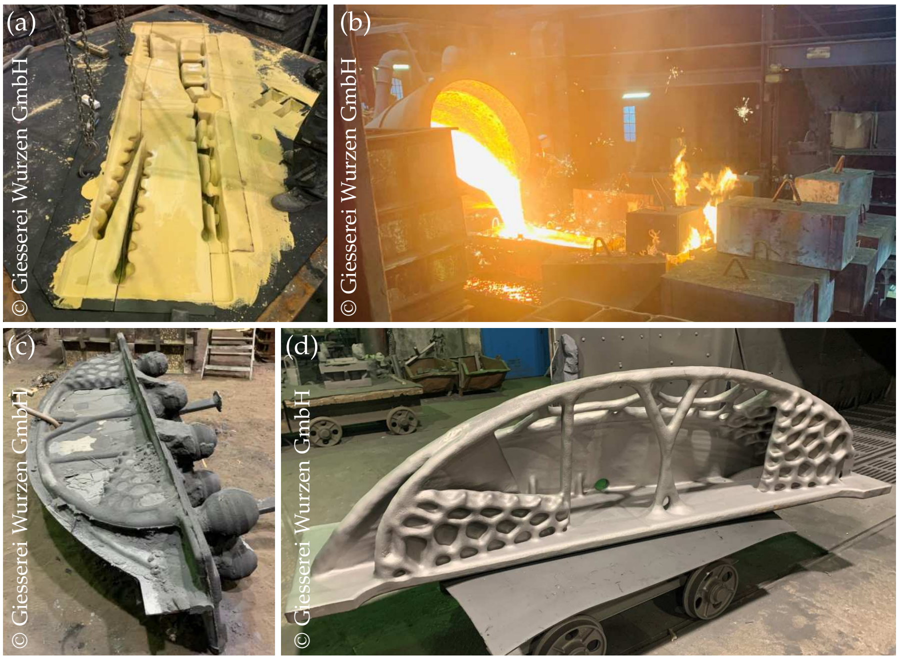

Figure 15.13: Casting process of the biologically inspired girder including the development of the final mould (a), the filling of the mould with liquid metal (b), the raw cast component (c), and the cleaned cast component (d). The photos are displayed with permission from Giesserei Wurzen GmbH.

In the end, further structural adaptations including bore notches, holes, and the requested surface evenness were applied to finalise the developed biologically inspired PETRA IV girder structure (figure 15.14).

The impact testing allowed the detection of the first five eigenfrequencies of the free and unloaded bio-inspired girder, which were visible as peaks in the Power Spectral Density (PSD) plot (figure 15.15) that additionally shows the numerically obtained eigenfrequencies. The measured peak at the 2nd eigenfrequency value was not as sharp as the peaks for the other four eigenfrequencies. Moreover, there were several smaller peaks at frequency values below 80 Hz. Likewise, the PSD plot of the floor and the pedestal (figure 15.16) showed various peaks between 20 Hz and 80 Hz. In addition, there was a peak at about 150 Hz in the PSD of the pedestal, which was not present in the floor movement.

In table 15.6, the measured eigenfrequencies are compared to the numerically obtained values. As it was already visible in the PSD plots, both eigenfrequency values corresponded very well, showing deviations of maximal 5.2%.

The visualisation of the vibration amplitude of the upper girder surface based on hitting the girder on position 8 is displayed in figure 15.17, exemplarily for the 1st eigenfrequency. The data obtained

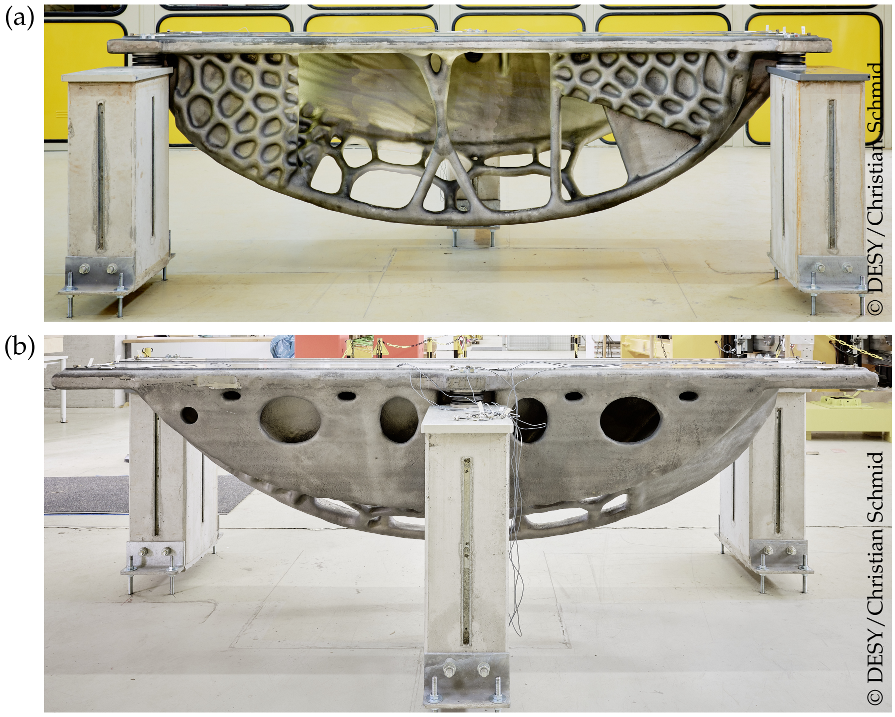

Figure 15.14: Photos of the manufactured bio-inspired girder in a front view (a) and back view (b). Springs are positioned between the bases and the girder. This setup was used for the impact testing. The photos are printed with permission from DESY.

by the eight accelerometers allowed the detection of a torsional 1st mode shape, which corresponds to the mode shape obtained by the modal analysis (cf., figure 15.10a). A comparably high displacement was detected at the position 8, where the girder had been hit for this impact testing.

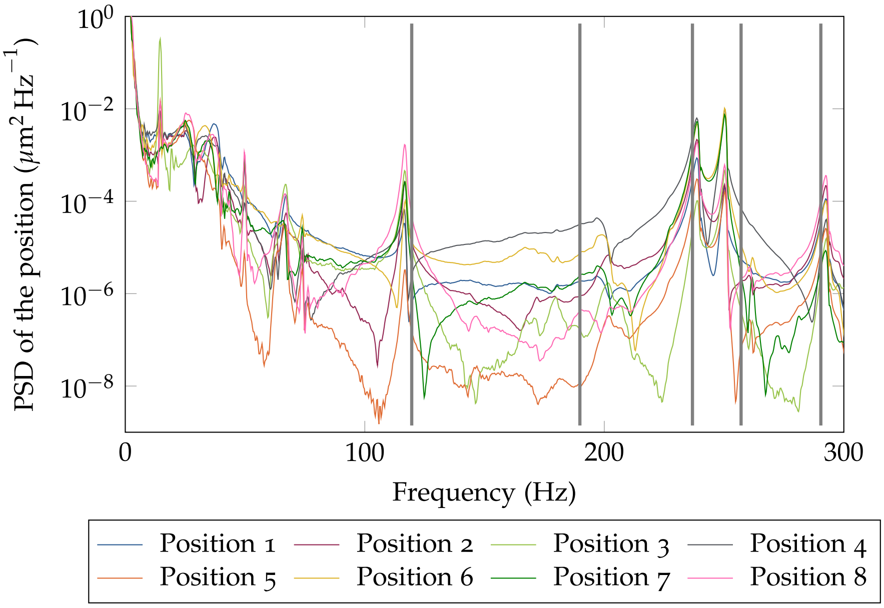

Figure 15.15: Power spectral density (logarithmic scale) depending on the frequency obtained by eight accelerometers fixed to the upper surface of the biologically inspired girder. The unloaded girder was positioned on springs and hit with an impact hammer on position 4. The grey vertical lines show the numerically obtained eigenfrequencies.

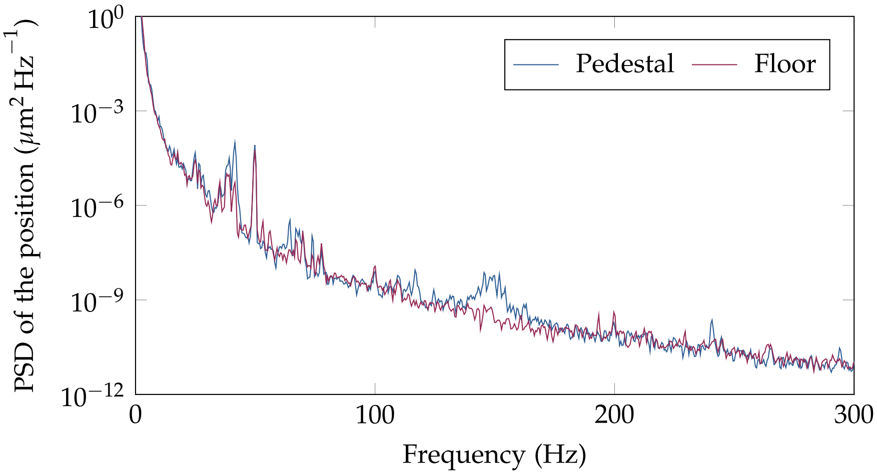

Figure 15.16: Power spectral density (logarithmic scale) depending on the frequency obtained by two accelerometers fixed to the floor and to the pedestal, on which is biologically inspired girder was placed.

Table 15.6: First five eigenfrequencies of the free unloaded bio-inspired girer obtained by simulation and by measurements based on impact testing. The measured eigenfrequencies are the mean values of the eight sensors positioned at different locations of the upper girder surface. The deviation between the measured and the simulated eigenfrequencies is also given.

	Simulation	Measurement	Deviation
f_1	119.6 Hz	116.6 Hz	-2.5%
f_2	189.8 Hz	199.7 Hz	5.2%
f_3	236.8 Hz	238.7 Hz	0.8%
f_4	257.1 Hz	250.2 Hz	-2.7%
f_5	290.4 Hz	292.5 Hz	0.7%

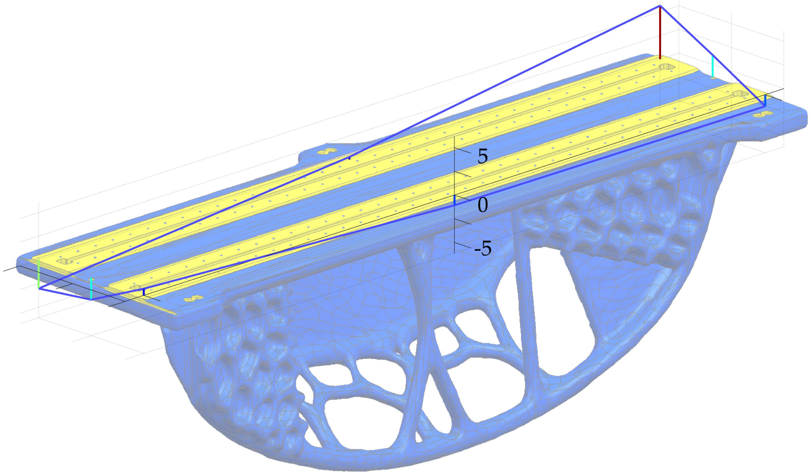

Figure 15.17: Visualisation of the measured 1st mode shape of the bio-inspired girder based on eight accelerometers placed on the upper girder surface. The vertical axis shows the displacement in μm. The figure is made by and printed with permission from Daniel Thoden, DESY.

15.3 DISCUSSION

In this chapter, the results of the girder development process are discussed.

15.3.1 *Topology Optimisation*

The topology optimisation converged successfully and the chosen mesh properties were appropriate, since the establishment of clearly defined load paths was possible.

The resulting unsymmetrical structure was comparable to a typical bridge structure. A girder encounters high loads due to the heavy magnets it has to carry. Thus, a bridge-like structure was expected to appear, since a maximum static deformation due to gravity was set as a constraint. The non-symmetry of the structure results from the similarly non-symmetrical loading. In addition, Warwick et al. [190] stated that topology optimisations with frequency objectives rarely result in symmetrical structures, because the mode shapes of complex geometries are often non-symmetrical. Regarding compliance minimisation objectives, however, topology optimisations often lead to symmetric structures allowing an equally distributed load path. Consequently, although the here generated structure is non-symmetrical, it still has the appearance of a symmetrical structure that was deformed afterwards.

15.3.2 *Abstraction and Cross Section Optimisation*

The structure resulting from the topology optimisation was successfully abstracted into a beam-shell model, because both the load paths and the surface-like structures were explicitly visible.

The subsequent cross section optimisation showed a clear convergence of the three optimisation objectives. A comparison of the structures forming the first and the last generation of the optimisation indicated a general improvement of the properties, i.e., the 1st eigenfrequency increased and the maximum static deformation and the mass decreased. Thus, it can be concluded that the algorithm worked successfully. However, the cross section optimisation improved the objectives only slightly: the maximum 1st eigenfrequency increase from the first to the last generation was only 1.3%, and the corresponding decrease in the maximum static deformation and the mass was -3.0% and -2.9%, respectively. The obtained optimum structure was based on cross section values that strongly varied, which possibly shows that the optimisation was yet successful.

On the one hand, the small improvement of the objectives might indicate that the topology optimisation result and the abstraction into a beam-shell model resulted already in a girder structure with very good properties, where the 1st eigenfrequency could almost not be increased further considering the defined boundary conditions. On the other hand, it is possible that the improvement of the optimisation objectives was limited due to the used optimisation method. As already discussed in chapter 9.3.3, evolutionary strategic optimisations do not always reveal the best solution, because the algorithm might have followed a local maximum of the fitness landscape instead of the global maximum. Thus, although all defined optimisation objectives converged, they possibly converged towards a local maximum. Also, the defined optimisation settings and the number of parameters could have influenced the only small improvement of the structures from the first to the last generation.

In general, raising the number of parameters in an evolutionary strategic optimisation certainly increases the computational effort. Thus, although the struts of the girder model were subdivided, the same cross section diameter values were assigned to all subdivisions, because otherwise the number of parameters would have been too large. The large strut in the front of the beam-shell model, for example, certainly plays an important role for the stability of the structure. Varying cross section diameters along the strut could have further improved the girder structure. To study the impact of many parameters on the analysed properties, a combination of the optimisation with a preceding Design of Experiments (DoE) is possible. The DoE identifies the impact of each parameter on the overall objectives. Thus, more parameters (i.e., varying cross-section diameters along one strut or different thicknesses applied to one shell) could have been considered. The outcome of the DoE would indicate the parameters strongly influencing the eigenfrequency and the maximum static deformation. Those parameters would have then been included in the subsequent evolutionary strategic optimisation, while less affecting parameters would have been given a constant cross section value. Thus, in continuative studies, the effectiveness of a DoE prior to the evolutionary strategic optimisation should be studied.

The eigenfrequencies and the maximum static deformation due to gravity of the beam-shell model conformed to the corresponding values of the volume model. The appearing deviations of 0.5% to 9.2% (absolute values) can be explained by the different mesh properties and also by small structural adaptations due to transforming the beam-shell model into a volume model. Since neither the structure, nor the mode shape were symmetrical, the small structural adaptations affected some mode shapes (and thus the corresponding eigenfrequencies) more strongly than others. While the 1st and 2nd eigenfrequency coincided by more than 97%, the 3rd and 4th eigenfrequency varied up to 9.2%. The 3rd and 4th mode shapes involved not only a girder deflection, but also deformations of the bases, which did not occur for the 1st and 2nd mode shape. A detailed view on the connection between girder and bases shows that the transformation of the beam-shell model into the volume model made the corners of the upper girder surface round (figure 15.18). This involved the removal of material at the connection point to the beam that connected the girder and the bases. Thus, more RBE3 were necessary to connect the beam to the girder, which presumably increased the connection stiffness and thus the eigenfrequencies of the volume model compared to the beam-shell model. However, both models can be seen as plausible, because the mode shapes coincided and the eigenfrequency deviations were small taking the size and the complexity of the structure into account.

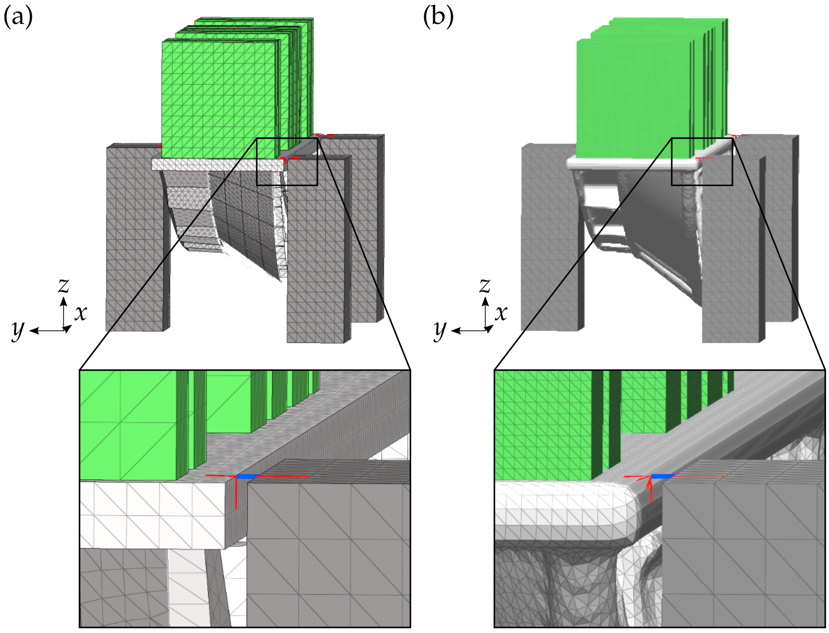

Figure 15.18: Beam-shell model with displayed cross sections (a) and volume model (b) of the best magnet-girder assembly that resulted from the cross section optimisation. For both models, a detailed view on a beam connecting the girder to the bases is given. The models are composed of the girder (light grey), the bases (dark grey), the magnets (green), the beams connecting the girder to the bases (blue), and the RBE3 elements (red).

15.3.3 *Biologically Inspired Structures and Further Structural Adaptation*

The successful implementation of biologically inspired structures into the girder design led to a complex girder structure with an attractive design.

The comparison of the 1st eigenfrequency of the free and unloaded bio-inspired girder to the 1st eigenfrequency of the free and unloaded PETRA III girder (figure 13.6) reveals the same 1st eigenfrequency value (120 Hz vs. 119 Hz) specifying grey cast iron as girder material. Note though, that the PETRA III girder was 4.2 m long, while the length of the here developed girder was 2.9 m. Yet, this comparison is only partly meaningful for the application in the synchrotron facility, because the properties of the loaded girder positioned on the bases inside the tunnel are relevant and do certainly vary from the properties of the free and unloaded girder.

Comparing the 1st eigenfrequency of the bio-inspired magnet-girder assembly of 55 Hz to the 1st eigenfrequency of 69 Hz of the magnet-girder assembly obtained after the cross section optimisation (volume model) gives a 21% lower 1st eigenfrequency value of the first model. It has to be noted, though, that a comparison of both models is hardly possible, because – aside from the different mesh properties - they varied in the geometry and the material properties of the girder (S235 vs. grey cast iron) and the bases (S235 vs. spheroidal cast iron). The study on the impact of the material properties on the magnet-girder assembly had already shown that grey cast iron reduces the 1st eigenfrequency by almost 20% compared to S235 (cf., figure 14.19). Also the mounting stiffness of the girder has a strong impact on the eigenfrequencies, which has also been investigated in the parametric study (cf., figure 14.17). The mounting stiffness of the final bio-inspired magnet-girder assembly was reduced due to the smaller bases, which is presumably why the 1st mode shape at 55 Hz showed already deformations of the bases. Regarding the initial, cross section optimisation based magnet-girder assembly, the first deformations of the bases were obtained for the 3rd mode shape at 75 Hz. Also previous studies have pointed out that the stiffness of the bases strongly influences the magnet-girder assembly (cf., figure 14.4). Thus, future studies should include an optimisation of the bases' geometry to maximise the stiffness.

While measurements have revealed a 1st eigenfrequency of the magnet-girder assembly used in the PETRA III synchrotron facility of about 35 Hz [109], the numerically obtained 1st eigenfrequency of the here studied magnet-girder assembly was with 55 Hz considerably higher. However, the latter value has to be dealt with caution, because the abstraction of the machine shoes as cylinders might have led to a girder support stiffness varying from the actual one. Therefore, in addition to the vibration measurements of the unloaded and free bio-inspired girder, the eigenfrequencies of the here studied magnet-girder assembly should also be measured to verify the numerical results.

In regard to the impact of the loading on the girder, Giorgetta [54] conducted eigenfrequency measurements of the loaded and the unloaded SOLEIL girder. The 1st eigenfrequency of the unloaded girder of 108 Hz dropped by 59% to 44 Hz with added magnets. Assuming that this value can be applied to the here developed PETRA IV girder, the 1st eigenfrequency of 120 Hz of the unloaded girder would decrease to 49 Hz, which is slightly lower than the 55 Hz that were numerically obtained for the magnet-girder assembly. In addition, Nudell et al. [120] stated a 1st eigenfrequency decrease of 10% by considering the floor compliance in the numerical model. Applying this value to the estimated 49 Hz for the 1st eigenfrequency would decrease the 1st eigenfrequency to 44 Hz. However, this 1st eigenfrequency value of the bio-inspired magnet-girder assembly is only hypothetical and based on two studies applied to different magnet-girder assemblies varying in geometry, loading, boundary conditions, and material properties. In addition, applying the 1st eigenfrequency decrease of 59% obtained by Giorgetta [54] and of 10% received by Nudell et al. [120] to the PETRA III girder would result in a 1st eigenfrequency of 44 Hz, which is slightly higher than the actually measured 1^{st} eigenfrequency of 35 Hz. Therefore, the mentioned 1^{st} eigenfrequency estimation has to be treated with caution. Yet, it can be concluded that the numerically obtained 1^{st} eigenfrequency value of the bio-inspired magnet-girder assembly might overestimate the real 1^{st} eigenfrequency, which is why the eigenfrequencies should be determined experimentally.

15.3.4 *Manufacturing and Impact Testing*

The today's achievements in the field of casting technologies allowed a successful fabrication of the bio-inspired girder structure. Despite the large dimensions and the complexity of the structure, a mould was manufactured and successfully filled with the liquid metal to built the casted part.

Regarding the financial expense, the manufacturing of the here designed girder structure was certainly more expensive than in the case of simple box-like girders. However, if the higher structural complexity increases the stability of the magnet-girder assembly, and thus of the particle beam, a higher financial expense might be justifiable. Regarding the casting process including 3D printed sand moulds, Upadhyay et al. [174] stated that the cost per part remains constant independent of the part complexity, while the costs for traditional manufacturing processes would rise strongly with increasing part complexity. Thus, in the case of manufacturing the PETRA IV girders using the casting technology with 3D printed sand moulds, a high structural complexity is possible, which might allow very stable magnet-girder assemblies.

The impact testing completed the girder development process. The high correspondence of the numerically obtained eigenfrequencies with the experimental data does not only show that the numerical models are reliable, but it also indicates a successful manufacturing process. Despite the already mentioned complexity of the designed girder, it was possible to produce a casted part without critical blowholes or a significant discrepancy from the modelled geometry.

Regarding the obtained PSD of the bio-inspired girder, the less distinct peak at the 2^{nd} eigenfrequency can be explained by the corresponding mode shape, which showed highest vibration amplitudes at the lower part of the girder, whereas the upper girder surface equipped with the accelerometers vibrated less strongly. Nevertheless, the detected 2^{nd} eigenfrequency corresponds to the numerically obtained eigenfrequency by about 95%.

Various peaks appeared at frequencies below 80 Hz. As the peaks were also present in the PSDs of the floor and the pedestal, it is concluded that those vibrations result from the in-house noise. In-house noise has also been detected in the ground vibration measurements at DESY displayed in figure 13.7. The additional peak at about 150 Hz appearing in the PSD of the pedestals might indicate a resonance frequency of the pedestal. Summing up, the impact testing clearly identified the eigenfrequencies of the unloaded girder, especially when considering the PSDs of the floor and the pedestal.

15.3.5 *Outlook*

The application of a parametric product development process based on a topology optimisation, the implementation of biologically inspired structures, and an evolutionary strategic cross section optimisation allowed the successful generation of an optimised biologically inspired girder structure for PETRA IV that has been manufactured. The coincidence of the structural eigenfrequencies and mode shapes measured in final experiments to the numerically obtained results validates the conducted methods and the simulation models. However, for the verification of the whole magnet-girder assembly, further experiments are necessary. Especially the stiffness of the machine shoes should be determined to include the correct stiffness values into the model. In addition, the stiffness of the ground and the PETRA tunnel should be considered in the model, as studies at different synchrotron radiation facilities noted a strong impact of the ground compliance on the magnet-girder assembly properties (e.g., at the APS-U [120] or at the ESRF-EBS [**Cianciosi2016a**]).

In future applications of the here studied girder design process, the process might be complemented by optimising the shape of the implemented bio-inspired structures, e.g., of the Voronoi combs, to further improve the mechanical properties of the girder. In addition, as already mentioned in chapter 15.3.2, the beam-shell model obtained from the topology optimisation result should be based on a higher number of parameters allowing a very precise dimensioning of all structural elements of the designed structure. To deal with the numerous parameters, a DoE could identify the parameters strongly affecting the analysed mechanical properties. Subsequently, the cross section optimisation would disclose the optimum diameters and shell thicknesses for those parameters.

Regarding the specifications defined at the beginning of the girder development process, several inputs changed. These changes imply, for example, the boundary conditions (size of the girder design space) and the loading (magnet properties and position). In addition, specifications relevant for the girder design, which have not been determined yet, should be specified prior to a reapplication of the design development process. These include the alignment system for the magnets and for the girder, because the connection stiffness strongly influences the properties of the magnet-girder assembly. Also the design of the bases and the material properties of both the bases and the girder should be defined before re-conducting the girder optimisation. The updated specifications for the PETRA IV girder can then be considered in the generated design development process to obtain an adapted girder geometry.

After generating a new girder design based on the adapted specifications, the girder structure should also be studied regarding the thermal deformation. As the PETRA tunnel temperature will be maintained at a constant value, the thermal deformation for the girder is likely not to be an issue, which is why a thermal load case should not be included in the girder design process. Nevertheless, the thermal behaviour of the structure should be analysed. In addition, studies on the transportation of the loaded girder into the PETRA tunnel have to be carried out, as the transportation could involve structural deformations and thus a misalignment of the components on the girder and/or the girder.

In summary, the generated girder development process has successfully been applied to a 2.9 m long PETRA IV girder. Changes in the specifications and input data can be implemented into the design process to receive adapted girder structures.

15.4 CONCLUSION

A development process for a girder structure installed in a synchrotron radiation facility has been generated. Based on a topology optimisation result, a parametric beam-shell model including biologically inspired structures was built up. The subsequent cross section optimisation using evolutionary strategic optimisation revealed an optimum girder structure, which was successfully manufactured using the casting technology. Eigenfrequency measurements validated the numerical models. Future changes in the specifications can be implemented in the development process to obtain adapted girder structures.

Part V

SUMMARY

16

SUMMARY

Finding the optimal structural design to avoid resonance has been a goal for decades as it is of high interest in many technical areas. Especially lightweight design structures show a high susceptibility to vibration. There are different ways to prevent high vibration amplitudes of an oscillating system involving the alteration of stiffness and/or mass to shift the eigenfrequencies above external, exciting frequencies ('detuning the system'), which is mainly studied here. As an increase in eigenfrequency can substantially reduce the dynamic response of a structure, an eigenfrequency maximisation is of great interest for numerous technical applications.

Diatoms face vibrational load cases, while being attacked by their predators. It is likely that the shape of their shells, which often shows irregular honeycomb and lattice structures, are optimised with regard to their vibration characteristics. A detailed literature review on technical lightweight structures reveals little findings on the vibration properties of irregular cellular and lattice structures. However, regarding structural optimisations with emphasis on vibration characteristics, a broad literature study shows the quantity of research related to vibrations highlighting the relevance of this topic. Aside from these common procedures to improve the vibration characteristics, the here studied methodologies to increase eigenfrequencies are inspired by nature. Thus, in the frame of biomimetics and biological inspiration, structures and phenomena present in nature, especially in diatoms, are investigated considering their vibration characteristics.

It has been observed that diatom shells are shaped according to their vibration mode shapes leading to the assumption that these shells have been vibration optimised during the process of evolution. Applying this idea of mode shape adaptation to axially constrained beams (1D) and plates (2D) results in strong eigenfrequency increases at a constant mass. A pre-deformation of maximum five times the beam height/plate thickness raises the 1st eigenfrequency by 298% for the beam and 487% for the plate. In addition, the increase of multiple eigenfrequencies combining various mode shapes is possible.

The mode shape adaptation results are compared to evolutionary strategic optimisations and, in the case of the plate, also to topography optimisations. The optimisations using commercially available optimisers successfully increase the targeted eigenfrequencies, e.g., the 1st eigenfrequency was raised by 297% for the beam and 371% for the plate. However, the single eigenfrequency increases are generally lower than that obtained through the mode shape adaptation method, while the evolutionary strategic optimisations lead to better results for the multiple eigenfrequency increase. In addition, the application of mode shapes on a structure is significantly faster than conducting optimisations.

In regard to complex honeycomb and lattice structures observed in aquatic plankton organisms, the impact of structural complexity on the eigenfrequencies is studied. The 1^{st} eigenfrequency of a 2D cellular plate is significantly raised by 165% using irregular structures. In addition, the application of the mode shape methodology to the studied cellular plates raised the 1^{st} eigenfrequency even further. Also concerning lattice structures, a strong 1^{st} eigenfrequency increase with rising structural complexity is obtained, including a maximum 1^{st} eigenfrequency raise of 58%. Additional constraints on the design allow the development of vibration optimised lattices that can be additively manufactured (3D printed) without using support structures.

As an example of a vibration-optimised structure, a girder used in synchrotron radiation facilities to support the magnets and to assure a stable particle beam is studied. It is focused on the girder design for the currently planned synchrotron radiation facility upgrade PETRA IV at DESY. In a parametric study, the impact of different boundary conditions on the magnet-girder assembly is studied, involving variations of the loading conditions (magnet mass, magnet position height, and connection stiffness between girder and magnets), the girder support definitions (location of support points, support stiffness), and the material properties of the girder and bases. Afterwards, a development process for a girder structure installed in a synchrotron radiation facility is generated. Based on a topology optimisation result, a parametric beam-shell model including biologically inspired structures is built up. The subsequent cross section optimisation using evolutionary strategic optimisation reveals an optimum girder structure. The biologically inspired girder design includes Voronoi combs, tree branches, smooth connections, round holes, and 45° oriented ribs. The girder structure was manufactured using the casting technology and vibration experiments (impact testing) showed a very good coincidence of the numerically obtained and measured eigenfrequencies. The 1^{st} eigenfrequency of the free unloaded girder was 120 Hz. Future changes in the specifications can be implemented in the development process to obtain adapted girder structures.

Part VI

APPENDIX

A

SUPPLEMENTAL MATERIAL

A.1 SHAPE ADAPTATION ACCORDING TO MODE SHAPES

Figure A.1.1 shows the first six eigenfrequencies of the studied beam pre-deformed according to mode 1 and to mode 2.

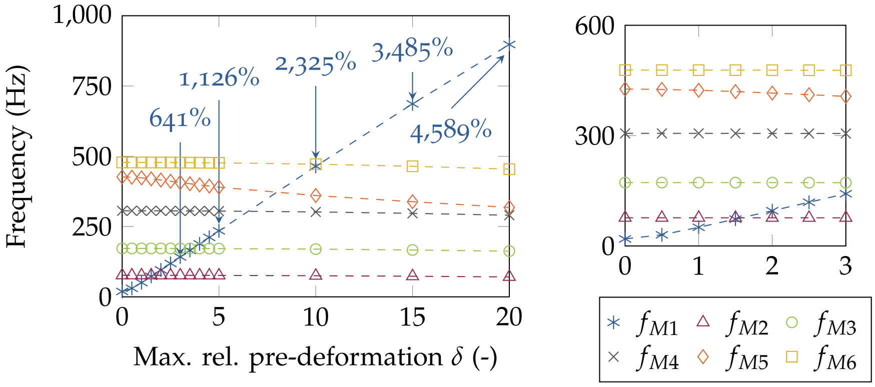

(a) Beam pre-deformation according to mode 1

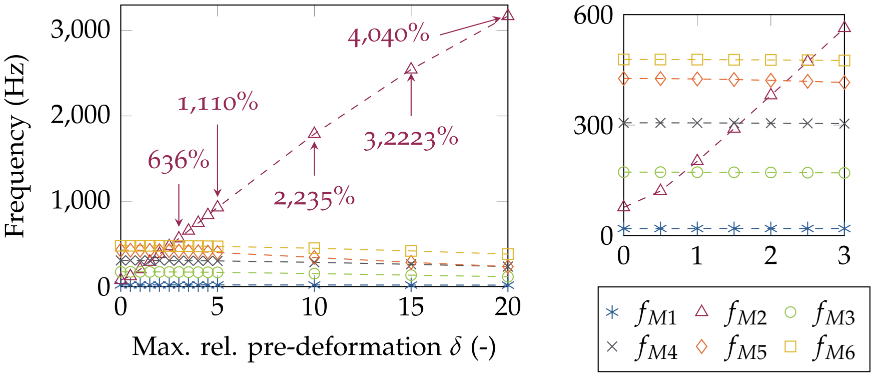

(b) Beam pre-deformation according to mode 2

Figure A.1.1: Frequencies of the first six bending mode shapes of the slender beam depending on the maximum relative pre-deformation according to mode 1 (a) and mode 2 (b). For some data points, the frequency increase of the 1^{st} and 2^{nd} bending mode shape compared to the reference beam is given. A magnified view of the lower right corner of both diagrams involving small pre-deformations δ of 0 - 5 and low frequencies of 0 - 600 Hz is given on the right-hand side of the figure.

A.2 SHAPE ADAPTATION BASED ON EVOLUTIONARY STRATEGIC OPTIMISATIONS

The following figures display the convergence plots for the evolutionary strategic optimisations of the slender beam aiming at (1) a minimisation of the mass difference compared to the mass of the reference beam and (2) a maximisation of the 1st (figure A.2.1), 2nd (figure A.2.2), 3rd (figure A.2.3), and 4th eigenfrequency (figure A.2.4). In addition, the convergence plots of the evolutionary strategic optimisations aiming at a maximisation of the 1st and 2nd eigenfrequency (figure A.2.5) and of the 1st, 2nd, and 3rd eigenfrequency (figure A.2.6) are shown.

Regarding the analysed squared plate, the convergence plots for the evolutionary strategic optimisations aiming at (1) a minimisation of the mass difference compared to the mass of the reference plate and (2) a maximisation of the 1st (figure A.2.7), 2nd (figure A.2.8), 3rd (figure A.2.9), and 4th eigenfrequency (figure A.2.10) are depicted. The evolutionary strategic optimisations of the plate to raise the 1st and 2nd eigenfrequency as well as the 1st, 2nd, and 3rd eigenfrequency are displayed in figures A.2.11 and A.2.12, respectively.

Additionally, topography optimisations of the plate were conducted. The corresponding convergence plots for the maximisation of the 1st, 2nd, 3rd, and 4th eigenfrequency are shown in figures A.2.13, A.2.14, A.2.15, and A.2.16, respectively.

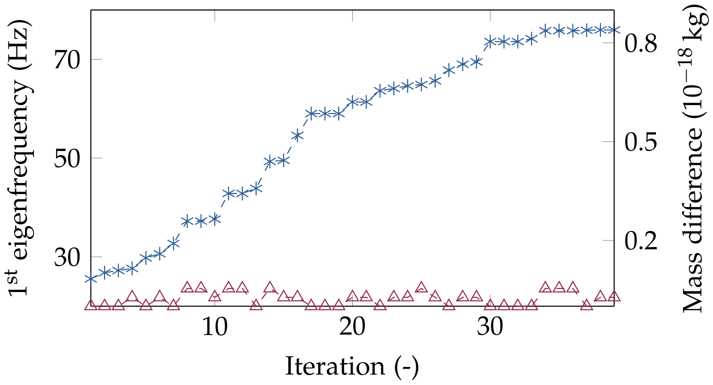

Figure A.2.1: Convergence plot of the evolutionary strategic optimisation of the beam aiming at a maximisation of the 1st eigenfrequency and a minimisation of the mass difference compared to the reference beam. Displayed are the 1st eigenfrequency (blue) and the corresponding mass difference (red) depending on the iteration number. The mass difference values are very small, because for each calculated structure the beam width was adapted to have a constant mass.

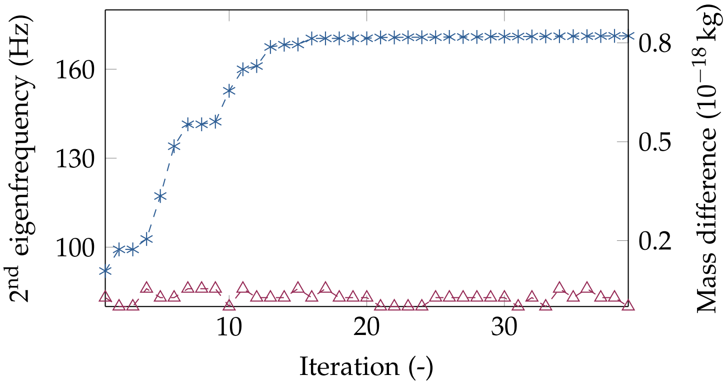

Figure A.2.2: Convergence plot of the evolutionary strategic optimisation of the beam aiming at a maximisation of the 2^{nd} eigenfrequency and a minimisation of the mass difference compared to the reference beam. Displayed are the 2^{nd} eigenfrequency (blue) and the corresponding mass difference (red) depending on the iteration number. The mass difference values are very small, because for each calculated structure the beam width was adapted to have a constant mass.

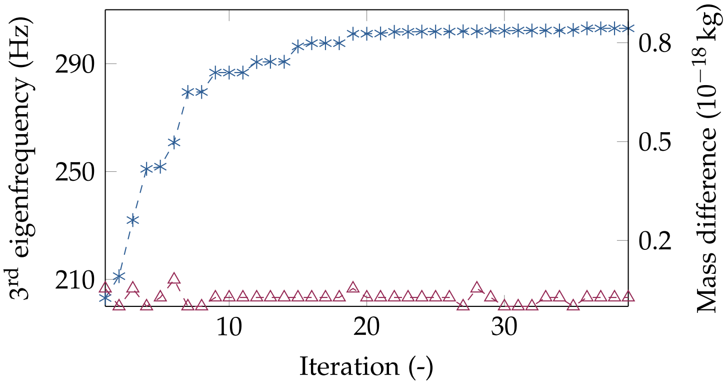

Figure A.2.3: Convergence plot of the evolutionary strategic optimisation of the beam aiming at a maximisation of the 3^{rd} eigenfrequency and a minimisation of the mass difference compared to the reference beam. Displayed are the 3^{rd} eigenfrequency (blue) and the corresponding mass difference (red) depending on the iteration number. The mass difference values are very small, because for each calculated structure the beam width was adapted to have a constant mass.

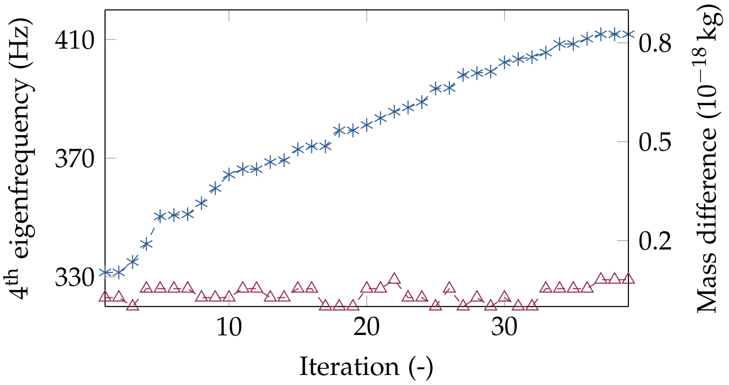

Figure A.2.4: Convergence plot of the evolutionary strategic optimisation of the beam aiming at a maximisation of the 4^{th} eigenfrequency and a minimisation of the mass difference compared to the reference beam. Displayed are the 4^{th} eigenfrequency (blue) and the corresponding mass difference (red) depending on the iteration number. The mass difference values are very small, because for each calculated structure the beam width was adapted to have a constant mass.

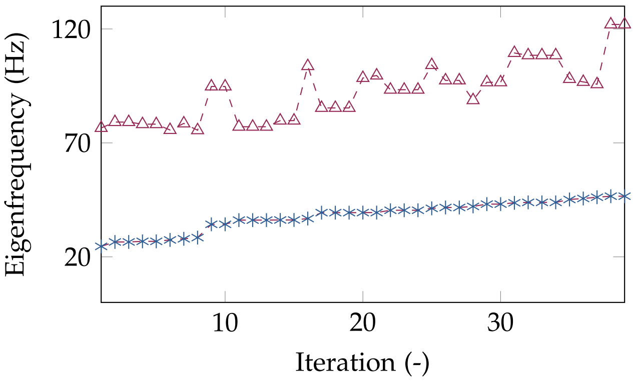

Figure A.2.5: Convergence plot of the evolutionary strategic optimisation of the beam aiming at a maximisation of the 1^{st} and the 2^{nd} eigenfrequency. Displayed are the 1^{st} (blue) and corresponding 2^{nd} eigenfrequency (red) depending on the iteration number.

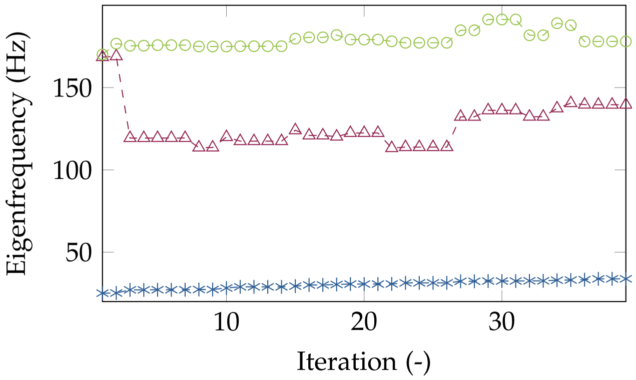

Figure A.2.6: Convergence plot of the evolutionary strategic optimisation of the beam aiming at a maximisation of the 1^{st}, 2^{nd}, and the 3^{rd} eigenfrequency. Displayed are the 1^{st} (blue) eigenfrequency and the corresponding 2^{nd} (red) and 3^{rd} eigenfrequency (green) depending on the iteration number.

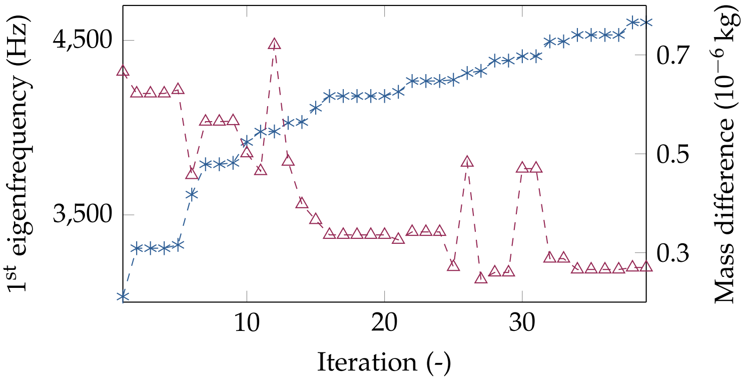

Figure A.2.7: Convergence plot of the evolutionary strategic optimisation of the plate aiming at a maximisation of the 1^{st} eigenfrequency and a minimisation of the mass difference compared to the reference plate. Displayed are the 1^{st} eigenfrequency (blue) and the corresponding mass difference (red) depending on the iteration number. The mass difference values are very small, because for each calculated structure the plate height was adapted to have a constant mass.

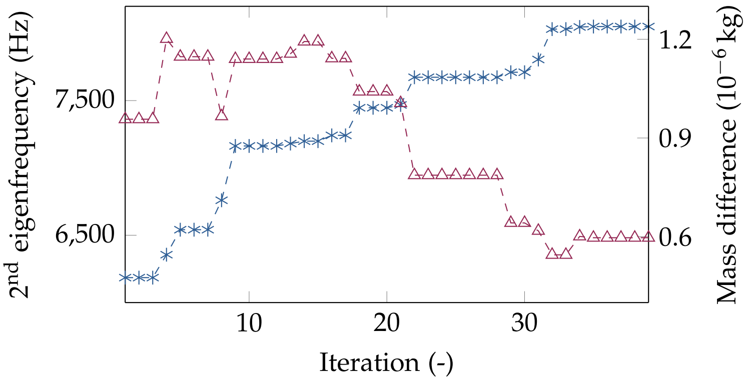

Figure A.2.8: Convergence plot of the evolutionary strategic optimisation of the plate aiming at a maximisation of the 2^{nd} eigenfrequency and a minimisation of the mass difference compared to the reference plate. Displayed are the 2^{nd} eigenfrequency (blue) and the corresponding mass difference (red) depending on the iteration number. The mass difference values are very small, because for each calculated structure the plate height was adapted to have a constant mass.

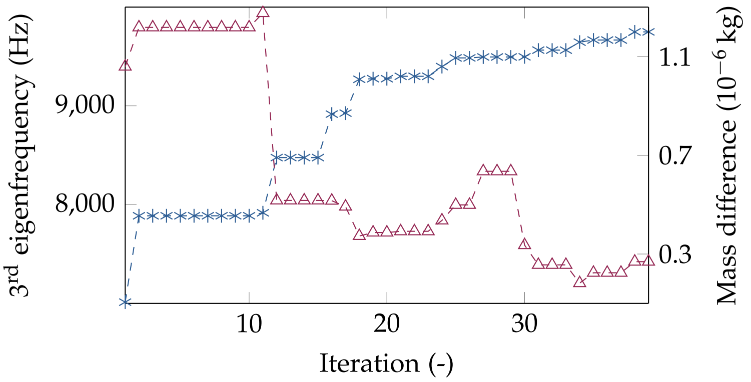

Figure A.2.9: Convergence plot of the evolutionary strategic optimisation of the plate aiming at a maximisation of the 3^{rd} eigenfrequency and a minimisation of the mass difference compared to the reference plate. Displayed are the 3^{rd} eigenfrequency (blue) and the corresponding mass difference (red) depending on the iteration number. The mass difference values are very small, because for each calculated structure the plate height was adapted to have a constant mass.

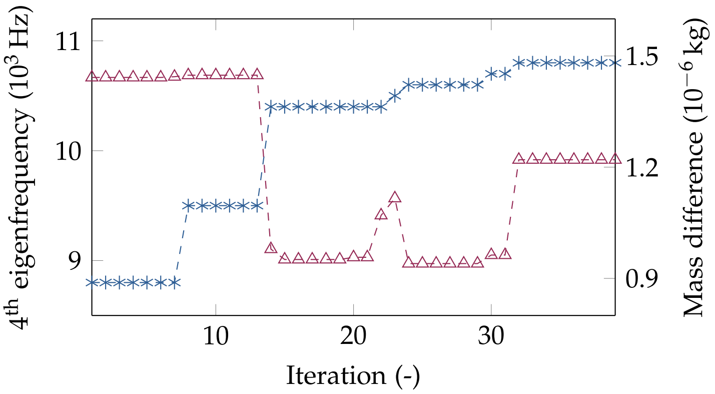

Figure A.2.10: Convergence plot of the evolutionary strategic optimisation of the plate aiming at a maximisation of the 4th eigenfrequency and a minimisation of the mass difference compared to the reference plate. Displayed are the 4th eigenfrequency (blue) and the corresponding mass difference (red) depending on the iteration number. The mass difference values are very small, because for each calculated structure the plate height was adapted to have a constant mass.

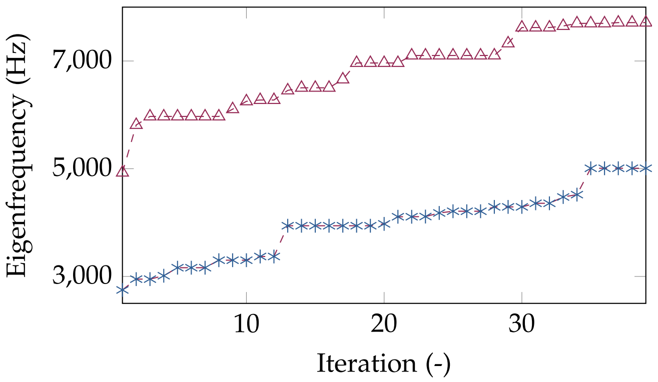

Figure A.2.11: Convergence plot of the evolutionary strategic optimisation of the plate aiming at a maximisation of the 1st and 2nd eigenfrequency. Displayed are the 1st eigenfrequency (blue) and the corresponding 2nd eigenfrequency (red) depending on the iteration number.

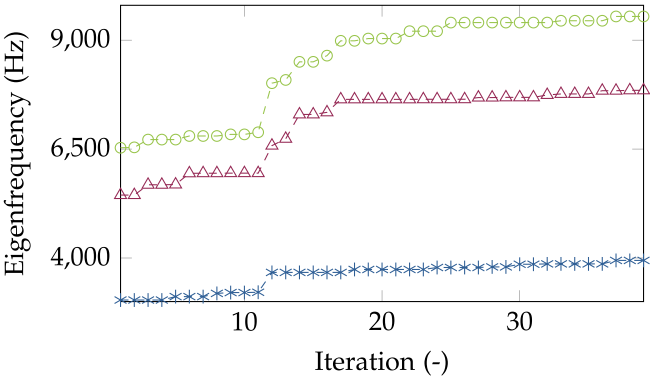

Figure A.2.12: Convergence plot of the evolutionary strategic optimisation of the plate aiming at a maximisation of the 1st, 2nd, and 3rd eigenfrequency. Displayed are the 1st eigenfrequency (blue) and the corresponding 2nd (red) and 3rd eigenfrequency (green) depending on the iteration number.

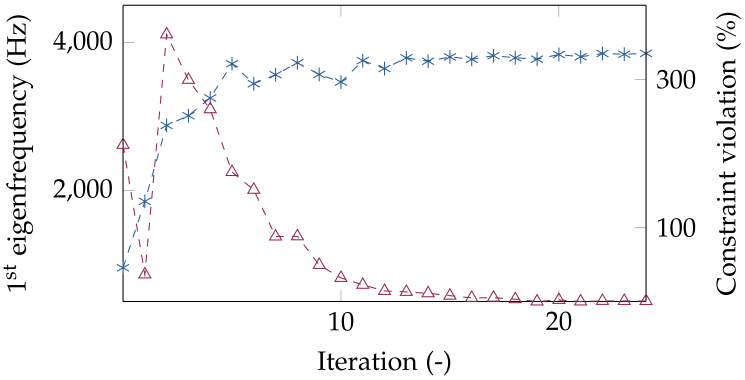

Figure A.2.13: Convergence plot of the topography optimisation of the plate aiming at a maximisation of the 1st eigenfrequency. Displayed are the 1st eigenfrequency (blue) and the corresponding constraint violation (red) depending on the iteration number.

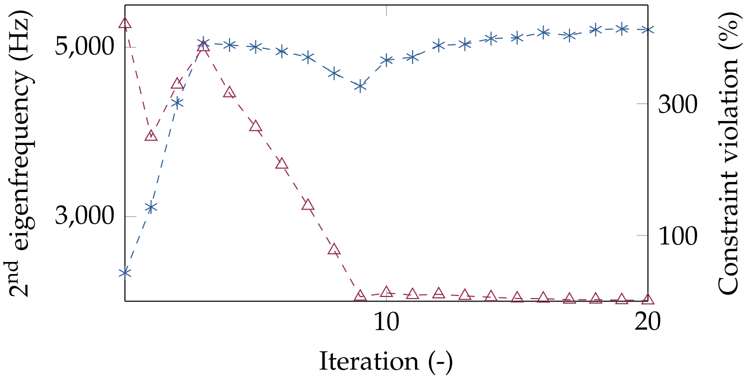

Figure A.2.14: Convergence plot of the topography optimisation of the plate aiming at a maximisation of the 2^{nd} eigenfrequency. Displayed are the 2^{nd} eigenfrequency (blue) and the corresponding constraint violation (red) depending on the iteration number.

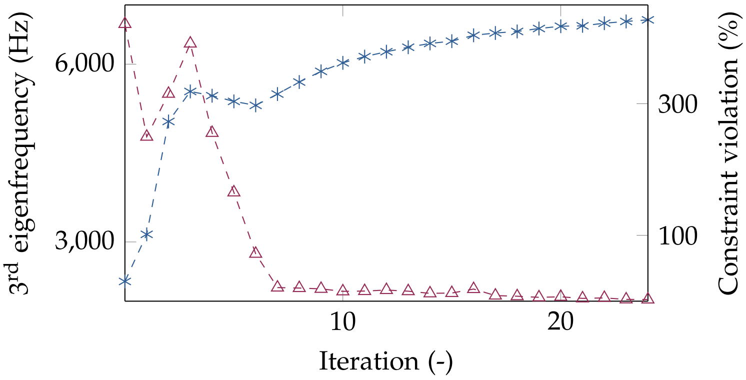

Figure A.2.15: Convergence plot of the topography optimisation of the plate aiming at a maximisation of the 3^{rd} eigenfrequency. Displayed are the 3^{rd} eigenfrequency (blue) and the corresponding constraint violation (red) depending on the iteration number.

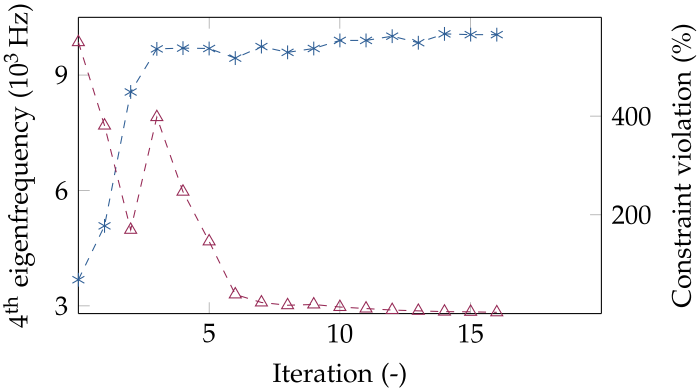

Figure A.2.16: Convergence plot of the topography optimisation of the plate aiming at a maximisation of the 4th eigenfrequency. Displayed are the 4th eigenfrequency (blue) and the corresponding constraint violation (red) depending on the iteration number.

A.3 REGULAR AND IRREGULAR HONEYCOMB PLATES

The convergence plot of the evolutionary strategic optimisation aiming at a 1st eigenfrequency maximisation of an irregular Voronoi plate is displayed in figure A.3.1.

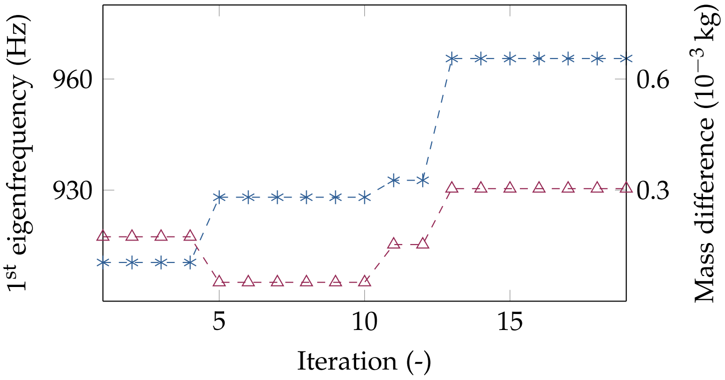

Figure A.3.1: Convergence plot of the evolutionary strategic optimisation of the irregular Voronoi plate aiming at a maximisation of the 1st eigenfrequency and a minimisation of the mass difference compared to the reference beam. Displayed are the 1st eigenfrequency (blue) and the corresponding mass difference (red) depending on the iteration number.

A.4 REGULAR AND IRREGULAR LATTICE STRUCTURES

The figures A.4.1 and A.4.2 show the frequency response curves of the lattices L1 and L2, respectively, obtained by experiment and simulation.

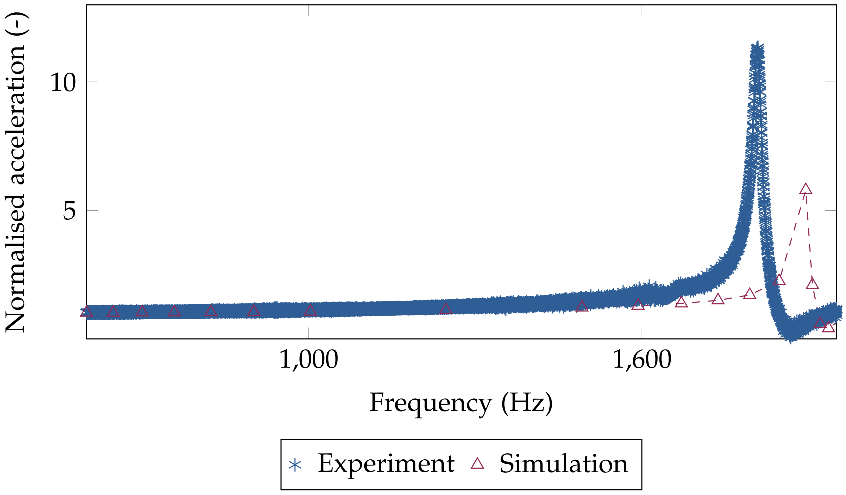

Figure A.4.1: Frequency response curves for L1 obtained by experiment and simulation using a solid model including accelerometers with a damping ratio of 0.0044.

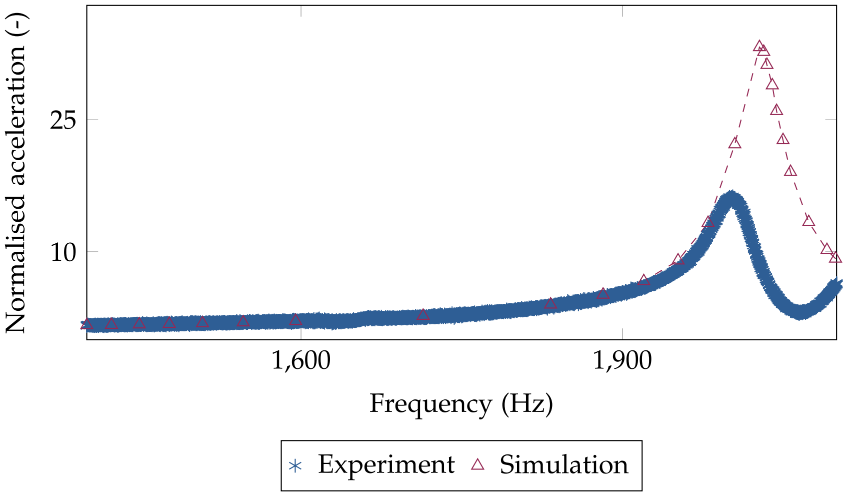

Figure A.4.2: Frequency response curves for L2 obtained by experiment and simulation using a solid model including accelerometers with a damping ratio of 0.01.

A.5 DEVELOPMENT OF A BIOLOGICALLY INSPIRED GIRDER DESIGN

Figure A.5.1 displays the convergence plots of the topology optimisation of the PETRA IV girder.

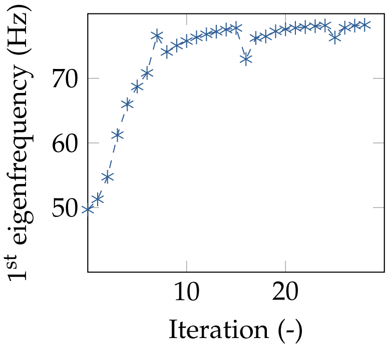

(a) 1^{st} eigenfrequency.

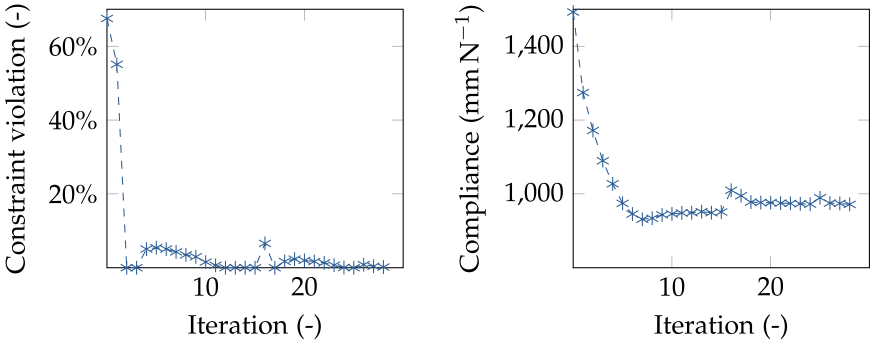

(b) Constraint violation.

(c) Compliance.

Figure A.5.1: Girder topology optimisation convergence plots of the 1^{st} eigenfrequency (a), the constraint violation (b), and the compliance (c) depending on the number of iteration.

BIBLIOGRAPHY

[1] S.M.B. Afonso and E. Hinton. "Free vibration analysis and shape optimization of variable thickness plates and shells - II. Sensitivity analysis and shape optimization." In: *Computing Systems in Engineering* 6.1 (1995), pp. 47–66. DOI: `10.1016/0956-0521(95)00012-O`.

[2] I. Agapov et al. "Status of the PETRA IV project." In: *10th International Particle Accelerator Conference (IPAC'19), Melbourne, Australia*. Ed. by M. Boland, H. Tanaka, D. Button, R. Dowd, V.R.W. Schaa, and E. Tan. Geneva (Switzerland): JACoW Publishing, 2019, pp. 1404–1407. DOI: `10.18429/JACoW-IPAC2019-TUPGW011`.

[3] B. Åkesson and N. Olhoff. "Minimum stiffness of optimally located supports for maximum value of beam eigenfrequencies." In: *Journal of Sound and Vibration* 120.3 (1988), pp. 457–463. DOI: `10.1016/s0022-460x(88)80218-9`.

[4] N. Alshabatat. "Design of corrugated plates for optimal fundamental frequency." In: *Advances in Acoustics and Vibration* 2016 (2016), pp. 1–9. DOI: `10.1155/2016/4290247`.

[5] N.T. Alshabatat, K. Myers, and K. Naghshineh. "Design of in-plane functionally graded material plates for optimal vibration performance." In: *Noise Control Engineering Journal* 64.2 (2016), pp. 268–278. DOI: `10.3397/1/376377`.

[6] N.T. Alshabatat and K. Naghshineh. "Optimization of the natural frequencies of plates via dimpling and beading techniques." In: *International Journal of Modelling and Simulation* 32.4 (2012), pp. 244–254. DOI: `10.2316/Journal.205.2012.4.205-5739`.

[7] G. Altıntas. "Effect of material properties on vibrations of nonsymmetrical axially loaded thin-walled Euler-Bernoulli beams." In: *Mathematical and Computational Applications* 15.1 (2010), pp. 96–107. DOI: `10.3390/mca15010096`.

[8] R. Amirikas, A. Bertolini, and W. Bialowons. *Measurement of vibration characteristics of a magnet prototype girder for ALBA*. DESY, EUROTeV-Report-2007-057, 2007. URL: `http://vibration.desy.de/sites2009/site_ground-vibrations/content/e1454/e3974/e3979/infoboxContent4512/EuroTeV-Report-2007-057.pdf` (visited on 08/02/2021).

[9] S. Andresen. "Ansätze zur Entwicklung von Tiefsee-Membranhalterungen nach Vorbild von diffusiven und druckfesten Porengeometrien unterschiedlicher Diatomeen." Bachelor's thesis. University of Bremen, 2015. URL: `https://epic.awi.de/id/eprint/41482/1/Simone_Andresen_BA_2015.pdf` (visited on 08/02/2021).

[10] S. Andresen. "Optimizing the PETRA IV girder by using bio-inspired structures." In: *Proceedings of the* 10^{th} *Mechanical Engineering Design of Synchrotron Radiation Equipment and Instrumentation Conference* (Paris, France). Ed. by V.R.W. Schaa, K. Tavakoli, and M. Tilmont. Geneva (Switzerland): JACoW Publishing, 2018, pp. 297–301. DOI: `10.18429/JACoW-MEDSI2018-THOAMA01`.

[11] S. Andresen. "Improving vibration characteristics by using bio-inspired structures." In: *Bionik: Patente aus der Natur, Innovationspotenziale für Technologieanwendungen, 9. Bremer Bionik--Kongress*. 9. Bionik-Kongress. Ed. by A.B. Kesel and D. Zehren. Bremen (Germany), 2019, pp. 30–42.

[12] S. Andresen. "Impact of Bio-inspired Structural Irregularities on Plate Eigenfrequencies." In: *Proceedings of the* 14^{th} *International Conference on Vibration Problems. Lecture Notes in Mechanical Engineering*. Ed. by Sapountzakis E.J., Banerjee M., Biswas P., and Inan E. Singapore: Springer, 2021, pp. 1117–1125. DOI: `10.1007/978-981-15-8049-9_71`.

[13] S. Andresen, A. Bäger, and C. Hamm. "Eigenfrequency maximisation by using irregular lattice structures." In: *Journal of Sound and Vibration* 465 (2020), p. 115027. DOI: `10.1016/j.jsv.2019.115027`.

[14] S. Andresen, M. Körfer, B. Krause, N. Meyners, A. Petrov, and M. Thede. *Research and developement PETRA IV. Magnets, girders and vibrations.* Poster at the 6th International Diffraction Limited Storage Ring (DLSR) Workshop. 2018. URL: `https://epic.awi.de/id/eprint/48567/` (visited on 08/02/2021).

[15] S. Andresen, L.M. Lottes, S.K. Linnemann, and R. Kienzler. "Shape adaptation of beams (1D) and plates (2D) to maximise eigenfrequencies." In: *Advances in Mechanical Engineering* 12 (2020), pp. 1–18. DOI: `10.1177/1687814020971903`.

[16] M. Ansari, A. Khajepour, and E. Esmailzadeh. "Application of level set method to optimal vibration control of plate structures." In: *Journal of Sound and Vibration* 332.4 (2013), pp. 687–700. DOI: `10.1016/j.jsv.2012.09.006`.

[17] D.K. Anthony, S.J. Elliott, and A.J. Keane. "Robustness of optimal design solutions to reduce vibration transmission in a lightweight 2-D structure, part i: Geometric design." In: *Jour-*

nal of Sound and Vibration 229.3 (2000), pp. 505–528. DOI: `10.1006/jsvi.1999.2493`.

[18] A.O. Aremu, J.P.J. Brennan-Craddock, A. Panesar, I.A. Ashcroft, R.J.M. Hague, R.D. Wildman, and C. Tuck. "A voxel-based method of constructing and skinning conformal and functionally graded lattice structures suitable for additive manufacturing." In: *Additive Manufacturing* 13 (2017), pp. 1–13. DOI: `10.1016/j.addma.2016.10.006`.

[19] M.F. Ashby. "The properties of foams and lattices." In: *Philosophical Transactions of the Royal Society A: Mathematical, Physical and Engineering Sciences* 364 (2006), pp. 15–30. DOI: `10.1098/rsta.2005.1678`.

[20] S. Banerjee and A. Bhaskar. "Free vibration of cellular structures using continuum modes." In: *Journal of Sound and Vibration* 287.1 (2005), pp. 77–100. DOI: `10.1016/j.jsv.2004.10.051`.

[21] S. Banerjee and A. Bhaskar. "The applicability of the effective medium theory to the dynamics of cellular beams." In: *International Journal of Mechanical Sciences* 51.8 (2009), pp. 598–608. DOI: `10.1016/j.ijmecsci.2009.06.001`.

[22] W. Barthlott et al. "The salvinia paradox: superhydrophobic surfaces with hydrophilic pins for air retention under water." In: *Advanced Materials* 22.21 (2010), pp. 2325–2328. DOI: `10.1002/adma.200904411`.

[23] M. Bauch. *Dokumentation Ablauf DESY Projekt*. Tech. rep. unpublished. Giesserei Wurzen GmbH, 2020.

[24] C.F. Beards. *Structural Vibration: Analysis and Damping*. New York (USA), Toronto (Canada): John Wiley & Sons Inc., 1996.

[25] M.P. Bendsøe and O. Sigmund. *Topology Optimization. Theory, Methods, and Applications*. 2nd ed. Berlin, Heidelberg (Germany), New York (USA): Springer-Verlag, 2004. DOI: `10.1007/978-3-662-05086-6`.

[26] W. Bialowons, R. Amirikas, A. Bertolini, and D. Kruecker. "Measurement of ground motion in various sites." In: *Proceedings of the European Particle Accelerator Conference 2006, Edinburgh, UK*. Ed. by C. Biscari, H. Owen, C.H. Petit-Jean-Genaz, J. Poole, and J. Thomason. Geneva (Switzerland): JACoW Publishing, 2006. URL: `http://accelconf.web.cern.ch/e06/PAPERS/MOPLS064.PDF` (visited on 08/02/2021).

[27] R.D. Blevins. *Formulas for natural frequency and mode shape*. New York (USA): Van Nostrand Reinhold Company, 1979.

[28] E. Brommundt and D. Sachau. *Schwingungslehre mit Maschinendynamik*. 2nd ed. Wiesbaden (Germany): Springer Vieweg, 2014. DOI: `10.1007/978-3-658-06548-5`.

[29] A.H. Brothers and D.C. Dunand. “Mechanical properties of a density-graded replicated aluminum foam.” In: *Materials Science and Engineering: A* 489.1-2 (2008), pp. 439–443. DOI: `10.1016/j.msea.2007.11.076`.

[30] L. Chen, J. Zhang, B. Du, H. Zhou, H. Liu, Y. Guo, W. Li, and D. Fang. “Dynamic crushing behavior and energy absorption of graded lattice cylindrical structure under axial impact load.” In: *Thin-Walled Structures* 127 (2018), pp. 333–343. DOI: `10.1016/j.tws.2017.10.048`.

[31] K.-T. Cheng and N. Olhoff. “Regularized formulation for optimal design of axisymmetric plates.” In: *International Journal of Solids and Structures* 18.2 (1982), pp. 153–169. DOI: `10.1016/0020-7683(82)90023-3`.

[32] L. Cheng, X. Liang, E. Belski, X. Wang, J.M. Sietins, S. Ludwick, and A. To. “Natural frequency optimization of variable-density additive manufactured lattice structure: theory and experimental validation.” In: *Journal of Manufacturing Science and Engineering* 140.10 (2018), p. 105002. DOI: `10.1115/1.4040622`.

[33] F. Cianciosi, L. Zhang, T. Brochard, P. Marion, L. Goirand, Y. Dabin, and M. Lesourd. “The girders system for the new ESRF storage ring.” In: *Proceedings of the 9^{th} Mechanical Engineering Design of Synchrotron Radiation Equipment and Instrumentation Conference* (Barcelona, Spain). Ed. by I. Costa, D. López, M. Prieto, and V.R.W. Schaa. Geneva (Switzerland): JACoW Publishing, 2016, pp. 147–151. DOI: `10.18429/JACoW-MEDSI2016-TUCA06`.

[34] G.A.L. Da Silva and R. Nicoletti. “Optimization of natural frequencies of a slender beam shaped in a linear combination of its mode shapes.” In: *Journal of Sound and Vibration* 397 (2017), pp. 92–107. DOI: `10.1016/j.jsv.2017.02.053`.

[35] X. Dai, X. Shao, C. Ma, H. Yun, F. Yang, and D. Zhang. “Experimental and numerical investigation on vibration of sandwich plates with honeycomb cores based on radial basis function.” In: *Experimental Techniques* 42.1 (2017), pp. 79–92. DOI: `10.1007/s40799-017-0220-3`.

[36] L. De Stefano, M. De Stefano, E. De Tommasi, I. Rea, and I. Rendina. “A natural source of porous biosilica for nanotech applications: the diatoms microalgae.” In: *Physica Status Solidi C* 8.6 (2011), pp. 1820–1825. DOI: `10.1002/pssc.201000328`.

[37] L. De Stefano, I. Rendina, M. De Stefano, A. Bismuto, and P. Maddalena. “Marine diatoms as optical chemical sensors.” In: *Applied Physics Letters* 87.23 (2005), p. 233902. DOI: `10.1063/1.2140087`.

[38] J.P. Den Hartog. "The lowest natural frequency of circular arcs." In: *The London, Edinburgh, and Dublin Philosophical Magazine and Journal of Science* 5.28 (1928), pp. 400–408. DOI: `10.1080/14786440208564480`.

[39] V.S. Deshpande, N.A. Fleck, and M.F. Ashby. "Effective properties of the octet-truss lattice material." In: *Journal of the Mechanics and Physics of Solids* 49.8 (2001), pp. 1747–1769. DOI: `10.1016/S0022-5096(01)00010-2`.

[40] A.R. Díaz and N. Kikuchi. "Solutions to shape and topology eigenvalue optimization problems using a homogenization method." In: *International Journal for Numerical Methods in Engineering* 35.7 (1992), pp. 1487–1502. DOI: `10.1002/nme.1620350707`.

[41] M. Diaz Moreno, K. Ma, J. Schoenung, and L.P. Dávila. "An integrated approach for probing the structure and mechanical properties of diatoms: toward engineered nanotemplates." In: *Acta Biomaterialia* 25 (2015), pp. 313–324. DOI: `10.1016/j.actbio.2015.07.028`.

[42] X. Ding and K. Yamazaki. "Stiffener layout design for plate structures by growing and branching tree model (application to vibration-proof design)." In: *Structural and Multidisciplinary Optimization* 26.1-2 (2004), pp. 99–110. DOI: `10.1007/s00158-003-0309-4`.

[43] A. Douangamath et al. "Crystallographic and electrophilic fragment screening of the SARS-CoV-2 main protease." In: *Nature Communications* 11 (2020), p. 5047. DOI: `10.1038/s41467-020-18709-w`.

[44] J. Du and N. Olhoff. "Topological design of freely vibrating continuum structures for maximum values of simple and multiple eigenfrequencies and frequency gaps." In: *Structural and Multidisciplinary Optimization* 34.2 (2007), pp. 91–110. DOI: `10.1007/s00158-007-0167-6`.

[45] A. Du Plessis, C. Broeckhoven, I. Yadroitsava, I. Yadroitsev, C.H. Hands, R. Kunju, and D. Bhate. "Beautiful and functional: a review of biomimetic design in additive manufacturing." In: *Additive Manufacturing* 27 (2019), pp. 408–427. DOI: `10.1016/j.addma.2019.03.033`.

[46] A.G. Evans, J.W. Hutchinson, N.A. Fleck, M.F. Ashby, and H.N.G. Wadley. "The topological design of multifunctional cellular metals." In: *Progress in Materials Science* 46.3 (2001), pp. 309–327. DOI: `10.1016/S0079-6425(00)00016-5`.

[47] F. Ferrari, B.S. Lazarov, and O. Sigmund. “Eigenvalue topology optimization via efficient multilevel solution of the frequency response.” In: *International Journal for Numerical Methods in Engineering* 115.7 (2018), pp. 872–892. DOI: `10.1002/nme.5829`.

[48] M.E. Ferrario, G.O. Almandoz, A.O. Cefarelli, E. Fabro, and M. Vernet. “Stephanopyxis species (bacillariophyceae) from shelf and slope waters of the argentinean sea: Ultrastructure and distribution.” In: *Nova Hedwigia* 96.1-2 (2012), pp. 249–263. DOI: `10.1127/0029-5035/2012/0077`.

[49] C.R. Fredö and A. Hedlund. “NVH optimization of truck cab floor panel embossing pattern.” In: *SAE Technical Paper* (2005). DOI: `10.4271/2005-01-2342`.

[50] R. Freymann. *Strukturdynamik. Ein anwendungsorientiertes Lehrbuch*. Berlin, Heidelberg (Germany): Springer-Verlag, 2011. DOI: `10.1007/978-3-642-19698-0`.

[51] L. Friedrichs. “Biomechanics of diatom frustules - techniques and ecological implications.” PhD thesis. University of Bremen, 2014. URL: `https://epic.awi.de/id/eprint/41548/` (visited on 07/30/2021).

[52] L.J. Gibson. “The mechanical behaviour of cancellous bone.” In: *Journal of Biomechanics* 18.5 (1985), pp. 317–328. DOI: `10.1016/0021-9290(85)90287-8`.

[53] L.J. Gibson and M.F. Ashby. *Cellular solids: structure and properties*. 2nd ed. Cambridge University Press, 1997. DOI: `10.1017/CBO9781139878326`.

[54] J.-L. Giorgetta. *Measurements on S.R girder prototype*. Presentation at the 8^{th} Machine Advisory Committee MAC meeting (unpublished). Mar. 31, 2004.

[55] C. Gisriel et al. “Membrane protein megahertz crystallography at the European XFEL.” In: *Nature communications* 10.1 (2019), pp. 1–11. DOI: `10.1038/s41467-019-12955-3`.

[56] R.V. Grandhi. “Structural optimization with frequency constraints - a review.” In: *4th AIAA/USAF/NASA/OAI Symposium on Multidisciplinary Analysis and Optimizations*. Cleveland, Ohio (USA), 1992. DOI: `10.2514/3.11928`.

[57] D. Gross, W. Hauger, J. Schröder, and W.A. Wall. *Technische Mechanik 2. Elastostatik*. 12th ed. Berlin, Heidelberg (Germany): Springer Vieweg, 2014. DOI: `10.1007/978-3-642-40966-0`.

[58] D. Gross, W. Hauger, J. Schröder, and W.A. Wall. *Technische Mechanik 3. Kinetik*. 13th ed. Wiesbaden (Germany): Springer Vieweg, 2015. DOI: `10.1007/978-3-642-53954-1`.

[59] A. Gutiérrez, R. Gordon, and L.P. Dávila. “Deformation modes and structural response of diatom frustules.” In: *Journal of Materials Science and Engineering with Advanced Technology* 15 (2017), pp. 105–134. DOI: `10.18642/jmseat_7100121810`.

[60] A. Gutiérrez, M.G. Guney, G.K. Fedder, and L.P. Dávila. “The role of hierarchical design and morphology in the mechanical response of diatom-inspired structures via simulation.” In: *Biomaterials Science* 6.1 (2018), pp. 146–153. DOI: `10.1039/C7BM00649G`.

[61] E. Haeckel. *Die Radiolarien (Rhizopoda Radiaria). Eine Monographie*. Berlin (Germany): Georg Reimer, 1862.

[62] C. Hamm and V. Smetacek. “Armor: why, when, and how.” In: *Evolution of primary producers in the sea*. Ed. by P.G. Falkowski and A.H. Knoll. Elsevier, 2007, pp. 311–332. DOI: `10.1016/B978-012370518-1/50015-1`.

[63] C.E. Hamm. “The evolution of advanced mechanical defenses and potential technological applications of diatom shells.” In: *Journal of Nanoscience and Nanotechnology* 5.1 (2005), pp. 108–119. DOI: `10.1166/jnn.2005.023`.

[64] C.E. Hamm, R. Merkel, O. Springer, P. Jurkojc, C. Maier, K. Prechtel, and V. Smetacek. “Architecture and material properties of diatom shells provide effective mechanical protection.” In: *Nature* 421.6925 (2003), pp. 841–843. DOI: `10.1038/nature01416`.

[65] C.H. Hands, A. du Plessis, N. Minnaar, B.A. Blakey-Milner, and E. Burger. “Can additive manufacturing help win the race.” In: *Preprints* (2018). DOI: `10.20944/preprints201811.0040.v1`.

[66] J.B. Hastings, L. Rivkin, and G. Aeppli. “Present and future accelerator-based x-ray sources: a perspective.” In: *Reviews of Accelerator Science and Technology* 10.1 (2019), pp. 33–48. DOI: `10.1142/S1793626819300044`.

[67] E.J. Haug, J.S. Arora, and K. Matsui. “A steepest-descent method for optimization of mechanical systems.” In: *Journal of Optimization Theory and Applications* 19.3 (1976), pp. 401–424. DOI: `10.1007/BF00941484`.

[68] E.J. Haug, K.C. Pan, and T.D. Streeter. “A computational method for optimal structural design. I. Piecewise uniform structures.” In: *International Journal for Numerical Methods in Engineering* 5.2 (1972), pp. 171–184. DOI: `10.1002/nme.1620050204`.

[69] E.J. Haug, K.C. Pan, and T.D. Streeter. “A computational method for optimal structural design II: continuous problems.” In: *International Journal for Numerical Methods in Engineering* 9.3 (1975), pp. 649–667. DOI: `10.1002/nme.1620090312`.

[70] S. Heimbs. “Virtual testing of sandwich core structures using dynamic finite element simulations.” In: *Computational Materials Science* 45.2 (2009), pp. 205–216. DOI: `10.1016/j.commatsci.2008.09.017`.

[71] A. Heinrichs, D. Siegel, P. Frank, P. Bomke, R. Naguschweski, and M. Frank. “Bionische Entwicklung einer additiv gefertigten A-Säulen-Verstärkung.” In: *Karosseriebautage Hamburg 2017*. Springer, 2017, pp. 43–56. DOI: `10.1007/s35725-017-0029-0`.

[72] M. Helou and S. Kara. “Design, analysis and manufacturing of lattice structures: an overview.” In: *International Journal of Computer Integrated Manufacturing* 31.3 (2018), pp. 243–261. DOI: `10.1080/0951192X.2017.1407456`.

[73] X. Huang, Z.H. Zuo, and Y.M. Xie. “Evolutionary topological optimization of vibrating continuum structures for natural frequencies.” In: *Computers & Structures* 88.5-6 (2010), pp. 357–364. DOI: `10.1016/j.compstruc.2009.11.011`.

[74] C. Hundertmark, R. Tinter, M. Ortelt, and M.J.B. Hauser. “Diatom-inspired plastic deformation elements for energy absorption in automobiles.” In: *Journal of Bionic Engineering* 12.4 (2015), pp. 613–623. DOI: `10.1016/S1672-6529(14)60151-7`.

[75] H. Jäger, R. Mastel, and M. Knaebel. *Technische Schwingungslehre. Grundlagen - Modellbildung - Anwendungen*. 9th ed. Wiesbaden (Germany): Springer Vieweg, 2016. DOI: `10.1007/978-3-658-13793-9`.

[76] B.N. Jensen. *MAX IV stability*. Presentation at the PETRA IV Meeting, Deutsches Elektronen-Synchrotron DESY (unpublished). Sept. 11, 2017.

[77] J.S. Jensen and N.L. Pedersen. “On maximal eigenfrequency separation in two-material structures: the 1D and 2D scalar cases.” In: *Journal of Sound and Vibration* 289.4-5 (2006), pp. 967–986. DOI: `10.1016/j.jsv.2005.03.028`.

[78] Z. Jihong and Z. Weihong. “Maximization of structural natural frequency with optimal support layout.” In: *Structural and Multidisciplinary Optimization* 31.6 (2006), pp. 462–469. DOI: `10.1007/s00158-005-0593-2`.

[79] A.J. Keane and A.P. Bright. “Passive vibration control via unusual geometries: experiments on model aerospace structures.” In: *Journal of Sound and Vibration* 190.4 (1996), pp. 713–719. DOI: `10.1006/jsvi.1996.0086`.

[80] R. Kienzler and R. Schröder. *Einführung in die Höhere Festigkeitslehre*. Berlin, Heidelberg (Germany): Springer, 2009. DOI: `10.1007/978-3-540-89325-7`.

[81] B. Klein. *FEM. Grundlagen und Anwendungen der Finite-Element-Methode im Maschinen- und Fahrzeugbau*. 9th ed. Wiesbaden (Germany): Vieweg+Teubner Verlag, 2012. DOI: `10.1007/978-3-8348-2134-8`.

[82] B. Klein and T. Gänsicke. *Leichtbau-Konstruktion. Dimensionierung, Strukturen, Werkstoffe und Gestaltung*. 11th ed. Wiesbaden (Germany): Springer Vieweg, 2019. DOI: `10.1007/978-3-658-26846-6`.

[83] M.A.R. Koehl and J.R. Strickier. "Copepod feeding currents: food capture at low Reynolds number 1." In: *Limnology and Oceanography* 26.6 (1981), pp. 1062–1073. DOI: `10.4319/lo.1981.26.6.1062`.

[84] L.A. Krog and N. Olhoff. "Optimum topology and reinforcement design of disk and plate structures with multiple stiffness and eigenfrequency objectives." In: *Computers & Structures* 72.4 (1999), pp. 535–563. DOI: `10.1016/S0045-7949(98)00326-5`.

[85] Marco Laumanns, Eckart Zitzler, and Lothar Thiele. "On the effects of archiving, elitism, and density based selection in evolutionary multi-objective optimization." In: *Evolutionary multi-criterion optimization. EMO 2001. Lecture Notes in Computer Science*. Ed. by E. Zitzler, K. Deb, L. Thiele, C.A. Coello Coello, and D. Corne. Berlin, Heidelberg (Germany), New York (USA): Springer, 2001, pp. 181–196. DOI: `10.1007/3-540-44719-9_13`.

[86] C.-M. Lee, V.N. Goverdovskiy, and A.I. Temnikov. "Design of springs with 'negative' stiffness to improve vehicle driver vibration isolation." In: *Journal of Sound and Vibration* 302.4-5 (2007), pp. 865–874. DOI: `10.1016/j.jsv.2006.12.024`.

[87] J.H. Lee and J.Y. Lee. "A light and scanning electron microscopic study on the marine diatom Roperia tesselata (roper) grunow." In: *Diatom Research* 5.2 (1990), pp. 325–335. DOI: `10.1080/0269249X.1990.9705123`.

[88] Z. Li, J. Zhang, J. Fan, Z. Wang, and L. Zhao. "On crushing response of the three-dimensional closed-cell foam based on voronoi model." In: *Mechanics of Materials* 68 (2014), pp. 85–94. DOI: `10.1016/j.mechmat.2013.08.009`.

[89] O.K. Lim and J.S. Lee. "Structural topology optimization for the natural frequency of a designated mode." In: *KSME International Journal* 14.3 (2000), pp. 306–313. DOI: `10.1007/BF03186423`.

[90] Y. Liu and M. Shimoda. "Non-parametric shape optimization method for natural vibration design of stiffened shells." In: *Computers & Structures* 146 (2015), pp. 20–31. DOI: `10.1016/j.compstruc.2014.08.003`.

[91] Z. Liu, J. Nudell, C. Preissner, J. Collins, and H. Cease. "Optimization for the APS-U magnet support structure." In: *Proceedings of the 9th Mechanical Engineering Design of Synchrotron Radiation Equipment and Instrumentation Conference* (Barcelona, Spain). Ed. by I. Costa, D. López, M. Prieto, and V.R.W. Schaa. Geneva (Switzerland): JACoW Publishing, 2016, pp. 254–256. DOI: `10.18429/JACoW-MEDSI2016-TUPE44`.

[92] F. Ljunggren and A. Ågren. "Development of a new damper to reduce resonant vibrations in lightweight steel joist floors." In: *Applied Acoustics* 63.11 (2002), pp. 1267–1280. DOI: `10.1016/S0003-682X(02)00025-7`.

[93] H.N. Lopes, R. Pavanello, and J. Mahfoud. "Topology optimization for the maximization of frequency separation margin." In: *Proceedings of VI International Symposium on Solid Mechanics (MecSol)*. Joinville (Brazil), 2017.

[94] D. Losic, G. Rosengarten, J.G. Mitchell, and N.H. Voelcker. "Pore architecture of diatom frustules: potential nanostructured membranes for molecular and particle separations." In: *Journal of Nanoscience and Nanotechnology* 6.4 (2006), pp. 982–989. DOI: `10.1166/jnn.2006.174`.

[95] J. Lou, L. Ma, and L.-Z. Wu. "Free vibration analysis of simply supported sandwich beams with lattice truss core." In: *Materials Science and Engineering: B* 177.19 (2012), pp. 1712–1716. DOI: `10.1016/j.mseb.2012.02.003`.

[96] J. Lou, B. Wang, L. Ma, and L. Wu. "Free vibration analysis of lattice sandwich beams under several typical boundary conditions." In: *Acta Mechanica Solida Sinica* 26.5 (2013), pp. 458–467. DOI: `10.1016/S0894-9166(13)60041-5`.

[97] J.H. Luo and H.C. Gea. "Optimal bead orientation of 3D shell/plate structures." In: *Finite Elements in Analysis and Design* 31.1 (1998), pp. 55–71. DOI: `10.1016/S0168-874X(98)00048-1`.

[98] Z.-D. Ma, H.-C. Cheng, and N. Kikuchi. "Structural design for obtaining desired eigenfrequencies by using the topology and shape optimization method." In: *Computing Systems in Engineering* 5.1 (1994), pp. 77–89. DOI: `10.1016/0956-0521(94)90039-6`.

[99] Y. Maeda, S. Nishiwaki, K. Izui, M. Yoshimura, K. Matsui, and K. Terada. "Structural topology optimization of vibrating structures with specified eigenfrequencies and eigenmode

shapes." In: *International Journal for Numerical Methods in Engineering* 67.5 (2006), pp. 597–628. DOI: `10.1002/nme.1626`.

[100] M. Maier. "Entwicklung einer systematischen Vorgehensweise für bionischen Leichtbau." PhD thesis. University of Bremen, 2015. URL: `https://media.suub.uni-bremen.de/handle/elib/910` (visited on 08/02/2021).

[101] M. Maier, D. Siegel, K.-D. Thoben, N. Niebuhr, and C. Hamm. "Transfer of natural micro structures to bionic lightweight design proposals." In: *Journal of Bionic Engineering* 10.4 (2013), pp. 469–478. DOI: `10.1016/S1672-6529(13)60241-3`.

[102] D. Mangra, S. Sharma, and C. Doose. "Performance of the Vibration Damping Pads in the APS Storage Ring." In: *Proceedings of the* 1st *International Workshop on Mechanical Engineering Design of Synchrotron Radiation Equipment and Instrumentation, Wurenlingen/Villigen, Switzerland* (Villingen, Switzerland). 2000. URL: `https://www.osti.gov/biblio/791142-RT6xyU/native/` (visited on 08/02/2021).

[103] J.R. Marlats, J.L. Giorgetta, and J.P. Daguerre. *SOLEIL strategy for beam position stability. Study of the overall stability: from ground to magnets*. Presentation at the Mechanical Engineering Design of Synchrotron Radiation Equipment and Instrumentation Conference. 2008. URL: `https://medsi.lbl.gov/files/page_137/Presentations_Papers/Beam_Stability_Vibration_and_Thermal_Effects/SOLEII_Strategy_for_Beam_Stability_-_JL._Giorgetta_-_PPT.pdf` (visited on 07/30/2021).

[104] I. Maskery, N.T. Aboulkhair, A.O. Aremu, C.J. Tuck, and I.A. Ashcroft. "Compressive failure modes and energy absorption in additively manufactured double gyroid lattices." In: *Additive Manufacturing* 16 (2017), pp. 24–29. DOI: `10.1016/j.addma.2017.04.003`.

[105] I. Maskery, A. Hussey, A. Panesar, A. Aremu, C. Tuck, I. Ashcroft, and R. Hague. "An investigation into reinforced and functionally graded lattice structures." In: *Journal of Cellular Plastics* 53.2 (2017), pp. 151–165. DOI: `10.1177/0021955X16639035`.

[106] I. Maskery, L. Sturm, A.O. Aremu, A. Panesar, C.B. Williams, C.J. Tuck, R.D. Wildman, I.A. Ashcroft, and R.J.M. Hague. "Insights into the mechanical properties of several triply periodic minimal surface lattice structures made by polymer additive manufacturing." In: *Polymer* 152 (2018), pp. 62–71. DOI: `10.1016/j.polymer.2017.11.049`.

[107] R. Meske, B. Lauber, and E. Schnack. “A new optimality criteria method for shape optimization of natural frequency problems.” In: *Structural and Multidisciplinary Optimization* 31.4 (2006), pp. 295–310. DOI: `10.1007/s00158-005-0550-0`.

[108] N. Meyners. *Girders, alignment, vibrations*. Presentation at the PETRA IV Workshop, Jesteburg, Deutsches Elektronen Synchrotron DESY (unpublished). Sept. 11, 2018.

[109] N. Meyners. *Vibration: PETRA III water on/off*. Presentation at the PETRA IV Tech. Forum, Deutsches Elektronen Synchrotron DESY (unpublished). Feb. 12, 2019.

[110] F. Mirtsch, N. Weinert, M. Pech, and G. Seliger. “Vault structures enabling sustainable products.” In: *13th International Conference on Life Cycle Engineering*. Vol. 3. Citeseer. 2006, pp. 629–634. URL: `http://citeseerx.ist.psu.edu/viewdoc/download?doi=10.1.1.421.3081&rep=rep1&type=pdf` (visited on 08/02/2021).

[111] S.G. Mosanenzadeh, H.E. Naguib, C.B. Park, and N. Atalla. “Design and development of novel bio-based functionally graded foams for enhanced acoustic capabilities.” In: *Journal of Materials Science* 50.3 (2015), pp. 1248–1256. DOI: `10.1007/s10853-014-8681-6`.

[112] D. Mousanezhad, R. Ghosh, A. Ajdari, A.M.S. Hamouda, H. Nayeb-Hashemi, and A. Vaziri. “Impact resistance and energy absorption of regular and functionally graded hexagonal honeycombs with cell wall material strain hardening.” In: *International Journal of Mechanical Sciences* 89 (2014), pp. 413–422. DOI: `10.1016/j.ijmecsci.2014.10.012`.

[113] T. Mukhopadhyay and S. Adhikari. “Free-vibration analysis of sandwich panels with randomly irregular honeycomb core.” In: *Journal of Engineering Mechanics* 142.11 (2016), p. 06016008. DOI: `10.1061/(ASCE)EM.1943-7889.0001153`.

[114] W. Nachtigall. *Bionik. Grundlagen und Beispiele für Ingenieure und Naturwissenschaftler*. 2nd ed. Berlin, Heidelberg (Germany): Springer, 2002. DOI: `10.1007/978-3-642-18996-8`.

[115] P.H. Nakasone and E.C.N. Silva. “Dynamic design of piezoelectric laminated sensors and actuators using topology optimization.” In: *Journal of Intelligent Material Systems and Structures* 21.16 (2010), pp. 1627–1652. DOI: `10.1177/1045389X10386130`.

[116] R. Nicoletti. “Linearization of embedded patterns for optimization of structural natural frequencies.” In: *Journal of the Brazilian Society of Mechanical Sciences and Engineering* 41.12 (2019), pp. 1–12. DOI: `10.1007/s40430-019-2040-0`.

[117] R. Nicoletti. "On the natural frequencies of simply supported beams curved in mode shapes." In: *Journal of Sound and Vibration* 485 (2020), p. 115597. DOI: `10.1016/j.jsv.2020.115597`.

[118] B. Niu, J. Yan, and G. Cheng. "Optimum structure with homogeneous optimum cellular material for maximum fundamental frequency." In: *Structural and Multidisciplinary Optimization* 39.2 (2009), pp. 115–132. DOI: `10.1007/s00158-008-0334-4`.

[119] M. Nourbakhsh, N. Morris, M. Bergin, F. Iorio, and D. Grandi. "Embedded sensors and feedback loops for iterative improvement in design synthesis for additive manufacturing." In: *International Design Engineering Technical Conferences and Computers and Information in Engineering Conference*. Vol. 1A. American Society of Mechanical Engineers. 2016, pp. 1–9. DOI: `10.1115/DETC2016-59627`.

[120] J. Nudell, Z. Liu, J. Preissner, J. Collins, and H. Cease. "Preliminary design and analysis of the FODO module support system for the APS-U storage ring." In: *Proceedings of the 9th Mechanical Engineering Design of Synchrotron Radiation Equipment and Instrumentation Conference* (Barcelona, Spain). Ed. by I. Costa, D. López, M. Prieto, and V.R.W. Schaa. Geneva (Switzerland): JACoW Publishing, 2016, pp. 83–86. DOI: `10.18429/JACoW-MEDSI2016-MOPE32`.

[121] N. Olhoff. "Optimal design of vibrating circular plates." In: *International Journal of Solids and Structures* 6.1 (1970), pp. 139–156. DOI: `10.1016/0020-7683(70)90086-7`.

[122] N. Olhoff. "Optimal design of vibrating rectangular plates." In: *International Journal of Solids and Structures* 10.1 (1974), pp. 93–109. DOI: `10.1016/0020-7683(74)90103-6`.

[123] N. Olhoff. "Optimization of vibrating beams with respect to higher order natural frequencies." In: *Journal of Structural Mechanics* 4.1 (1976), pp. 87–122. DOI: `10.1080/03601217608907283`.

[124] N. Olhoff. "Maximizing higher order eigenfrequencies of beams with constraints on the design geometry." In: *Journal of Structural Mechanics* 5.2 (1977), pp. 107–134. DOI: `10.1080/03601217708907308`.

[125] N. Olhoff, B. Niu, and G. Cheng. "Optimum design of band-gap beam structures." In: *International Journal of Solids and Structures* 49.22 (2012), pp. 3158–3169. DOI: `10.1016/j.ijsolstr.2012.06.014`.

[126] Robert Oshana. "4 - overview of digital signal processing algorithms." In: *DSP software development techniques for embedded and real-time systems*. Ed. by Robert Oshana. Embedded Tech-

nology. Burlington (USA): Newnes, 2006, pp. 59–121. DOI: `10.1016/B978-075067759-2/50006-5`.

[127] Z. Ozdemir, E. Hernandez-Nava, A. Tyas, J.A. Warren, S.D. Fay, R. Goodall, I. Todd, and H. Askes. “Energy absorption in lattice structures in dynamics: experiments.” In: *International Journal of Impact Engineering* 89 (2016), pp. 49–61. DOI: `10.1016/j.ijimpeng.2015.10.007`.

[128] A. Panesar, M. Abdi, D. Hickman, and I. Ashcroft. “Strategies for functionally graded lattice structures derived using topology optimisation for additive manufacturing.” In: *Additive Manufacturing* 19 (2018), pp. 81–94. DOI: `10.1016/j.addma.2017.11.008`.

[129] M.-Y. Park, Y. Park, and Y.-S. Park. “Raising natural frequencies of a structure via surface-grooving technique.” In: *Structural and Multidisciplinary Optimization* 34.6 (2007), pp. 491–505. DOI: `10.1007/s00158-007-0103-9`.

[130] N.L. Pedersen. “Maximization of eigenvalues using topology optimization.” In: *Structural and Multidisciplinary Optimization* 20.1 (2000), pp. 2–11. DOI: `10.1007/s001580050130`.

[131] N.L. Pedersen. “Optimization of holes in plates for control of eigenfrequencies.” In: *Structural and Multidisciplinary Optimization* 28.1 (2004), pp. 1–10. DOI: `10.1007/s00158-004-0426-8`.

[132] P. Pedersen and N.L. Pedersen. “An optimality criterion for shape optimization in eigenfrequency problems.” In: *Structural and Multidisciplinary Optimization* 29.6 (2005), pp. 457–469. DOI: `10.1007/s00158-004-0499-4`.

[133] M. Petyt. *Introduction to Finite Element Vibration Analysis*. 2nd ed. New York (USA): Cambridge University Press, 2010. DOI: `10.1017/CBO9780511761195`.

[134] R. Platzer. *EASy (Easy Alignment System). 6-Achs-Präzisionspositionierung*. Presentation at Deutsches Elektronen-Synchrotron DESY (unpublished). Aug. 26, 2020.

[135] J. Plocher and A. Panesar. “Effect of density and unit cell size grading on the stiffness and energy absorption of short fibre-reinforced functionally graded lattice structures.” In: *Additive Manufacturing* (2020), p. 101171. DOI: `10.1016/j.addma.2020.101171`.

[136] G. Pohl and W. Nachtigall. *Biomimetics for Architecture & Design. Nature - Analogies - Technology*. Switzerland: Springer International Publishing Switzerland, 2015. DOI: `10.1007/978-3-319-19120-1`.

[137] Z.-Q. Qu. *Model Order Reduction Techniques with Applications in Finite Element Analysis*. London (United Kingdom): Springer-Verlag London Ltd., 2004. DOI: `10.1007/978-1-4471-3827-3`.

[138] RAMPF Machine Systems GmbH & Co. KG. *EPUMENT® I Mineralguss für moderne Maschinenbetten und Gestellbauteile*. URL: `https://www.rampf-group.com/fileadmin/rampf-gruppe.de/media/machine_systems/downloads/Mineralguss-EPUMENT-DE.pdf` (visited on 08/02/2021).

[139] V. Ravindranath, S. Sharma, L. Doom, C. Channing, F. Lincoln, A. Jain, and P. Joshi. "Stability of NSLS-II girder-magnet assembly." In: *Diamond Light Source Proceedings*. Vol. 1. MEDSI-6. Cambridge University Press, 2010. DOI: `10.1017/S2044820110000675`.

[140] M. Rechberger, H. Paschke, A. Fischer, and J. Bertling. "New tribological strategies for cutting tools following nature." In: *Tribology International* 63 (2013), pp. 243–249. DOI: `10.1016/j.triboint.2012.09.008`.

[141] R. Röhlsberger, C.G. Schroer, R. Wanzenberg, S. Klumpp, and W. Wurth. "Light source upgrades at DESY: PETRA IV and FLASH2020+." In: *Synchrotron Radiation News* 32.1 (2019), pp. 27–31. DOI: `10.1080/08940886.2019.1559605`.

[142] F.E. Round, R.M. Crawford, and D.G. Mann. *Diatoms: Biology and Morphology of the Genera*. Cambridge (United Kingdom): Cambridge University Press, 1990.

[143] R.E. Ruland. *A Design Library of Magnet Supports - A Proposal*. SLAC, 2005. URL: `https://www.osti.gov/biblio/878783` (visited on 08/02/2021).

[144] M. Ruzzene. "Vibration and sound radiation of sandwich beams with honeycomb truss core." In: *Journal of Sound and Vibration* 277.4 (2004), pp. 741–763. DOI: `10.1016/j.jsv.2003.09.026`.

[145] E.-O. Saemann and R. Platzer. *Vermessungsprotokoll. Vermessung Steifigkeit EASy A2 (200_300)*. Tech. rep. unpublished. ZM1, DESY, Jan. 13, 2020.

[146] A.-M.M. Schmid, R.K. Eberwein, and M. Hesse. "Pattern morphogenesis in cell walls of diatoms and pollen grains: a comparison." In: *Protoplasma* 193.1-4 (1996), pp. 144–173. DOI: `10.1007/BF01276642`.

[147] T.L. Schmitz and K.S. Smith. *Mechanical Vibrations. Modeling and Measurement*. New York (USA): Springer, 2012. DOI: `10.1007/978-1-4614-0460-6`.

[148] C.G. Schroer, R. Röhlsberger, E. Weckert, R. Wanzenberg, I. Agapov, R. Brinkmann, and W. Leemans. *PETRA IV. Upgrade of PETRA III to the Ultimate 3D X-ray Microscope. Conceptual Design Resport*. Tech. rep. Deutsches Elektronen-Synchrotron DESY, A Research Centre of the Helmholtz Association, Nov. 2019. DOI: `10.3204/PUBDB-2019-03613`.

[149] C.G. Schroer et al. “PETRA IV: the ultralow-emittance source project at DESY.” In: *Journal of Synchrotron Radiation* 25.5 (2018), pp. 1277–1290. DOI: `10.1107/S1600577518008858`.

[150] D. Schwarz. *Auslegung von Blechen mit Sicken (Sickenatlas)*. Vol. 168. Forschungsvereinigung Automobiltechnik eV, 2002. URL: `https://publications.rwth-aachen.de/record/96309` (visited on 08/02/2021).

[151] Y. Seki, S.G. Bodde, and M.A. Meyers. “Toucan and hornbill beaks: a comparative study.” In: *Acta Biomaterialia* 6.2 (2010), pp. 331–343. DOI: `10.1016/j.actbio.2009.08.026`.

[152] Y. Seki, M.S. Schneider, and M.A. Meyers. “Structure and mechanical behavior of a toucan beak.” In: *Acta Materialia* 53.20 (2005), pp. 5281–5296. DOI: `10.1016/j.actamat.2005.04.048`.

[153] S. Sharma, B. Rusthoven, V. Ravindranath, and C. Doose. *Design of Accelerator Girder System for Vibration Suppression*. Presentation at the Workshop on Ambient Ground Motion and Civil Engineering for Low Emittance Electron Storage Ring, Hsinchu, Taiwan. 2005. URL: `https://www.yumpu.com/s/VjBOr4qhxEFPpWCg` (visited on 08/02/2021).

[154] Z.Y. Shi, S.S. Law, and L.M. Zhang. “Structural damage localization from modal strain energy change.” In: *Journal of Sound and Vibration* 218.5 (1998), pp. 825–844. DOI: `10.1006/jsvi.1998.1878`.

[155] M. Shimoda and Y. Liu. “Node-based free-form optimization method for vibration problems of shell structures.” In: *Computers & Structures* 177 (2016), pp. 91–102. DOI: `10.1016/j.compstruc.2016.08.011`.

[156] M. Shimoda, T. Nagano, T. Morimoto, Y. Liu, and J.-X. Shi. “Non-parametric free-form optimal design of frame structures in natural frequency problem.” In: *International Journal of Mechanical Sciences* 117 (2016), pp. 334–345. DOI: `10.1016/j.ijmecsci.2016.08.024`.

[157] M.J. Silva, W.C. Hayes, and L.J. Gibson. “The effects of non-periodic microstructure on the elastic properties of two-dimensional cellular solids.” In: *International Journal of Mechanical Sciences* 37.11 (1995), pp. 1161–1177. DOI: `10.1016/0020-7403(94)00018-F`.

[158] U. Simsek, T. Arslan, B. Kavas, C.E. Gayir, and P. Sendur. “Parametric studies on vibration characteristics of triply periodic minimum surface sandwich lattice structures.” In: *The International Journal of Advanced Manufacturing Technology* (2020), pp. 1–16. DOI: `10.1007/s00170-020-06136-6`.

[159] W. Soedel. "A natural frequency analogy between spherically curved panels and flat plates." In: *Journal of Sound and Vibration* 29 (1973), pp. 457–461. DOI: `10.1016/S0022-460X(73)80061-6`.

[160] S.V. Sorokin, S.V. Grishina, and O.A. Ershova. "Analysis and control of vibrations of honeycomb plates by parametric stiffness modulations." In: *Smart Materials and Structures* 10.5 (2001), pp. 1031–1045. DOI: `10.1088/0964-1726/10/5/320`.

[161] H.-C. Spatz, L. Köhler, and T. Speck. "Biomechanics and functional anatomy of hollow-stemmed sphenopsids. I. Equisetum giganteum (Equisetaceae)." In: *American Journal of Botany* 85.3 (1998), pp. 305–314. DOI: `10.2307/2446321`.

[162] C. Spura. *Technische Mechanik 2. Elastostatik. Nach fest kommt ab*. 13th ed. Berlin, Heidelberg (Germany): Springer Vieweg, 2019. DOI: `10.1007/978-3-658-19979-1`.

[163] B. Stanford, P. Beran, and M. Bhatia. "Aeroelastic topology optimization of blade-stiffened panels." In: *Journal of Aircraft* 51.3 (2014), pp. 938–944. DOI: `10.2514/6.2013-1871`.

[164] A.R. Studart. "Additive manufacturing of biologically-inspired materials." In: *Chemical Society Reviews* 45.2 (2016), pp. 359–376. DOI: `10.1039/C5CS00836K`.

[165] T. Sun, W. Tan, L. Chen, and A. Rollett. "In situ/operando synchrotron x-ray studies of metal additive manufacturing." In: *MRS Bulletin* 45.11 (2020), pp. 927–933. DOI: `https://doi.org/10.1557/mrs.2020.275`.

[166] W.P. Syam, W. Jianwei, B. Zhao, I. Maskery, W. Elmadih, and R. Leach. "Design and analysis of strut-based lattice structures for vibration isolation." In: *Precision Engineering* 52 (2018), pp. 494–506. DOI: `10.1016/j.precisioneng.2017.09.010`.

[167] B. Tampigny et al. "Thermal stability of the new ESRF extremely brilliant source." In: *Proceedings of the* 9^{th} *Mechanical Engineering Design of Synchrotron Radiation Equipment and Instrumentation Conference* (Barcelona, Spain). Ed. by I. Costa, D. López, M. Prieto, and V.R.W. Schaa. Geneva (Switzerland): JACoW Publishing, 2016. DOI: `10.18429/JACoW-MEDSI2016-WEAA03`.

[168] C. Tekoğlu, L.J. Gibson, T. Pardoen, and P.R. Onck. "Size effects in foams: experiments and modeling." In: *Progress in Materials Science* 56.2 (2011), pp. 109–138. DOI: `10.1016/j.pmatsci.2010.06.001`.

[169] L.H. Tenek and I. Hagiwara. "Eigenfrequency maximization of plates by optimization of topology using homogenization and mathematical programming." In: *JSME International Journal. Ser. C, Dynamics, Control, Robotics, Design and Manufacturing* 37.4 (1994), pp. 667–677. DOI: `10.1299/jsmec1993.37.667`.

[170] M. Terracciano, L. De Stefano, and I. Rea. “Diatoms green nanotechnology for biosilica-based drug delivery systems.” In: *Pharmaceutics* 10.4 (2018), p. 242. DOI: `10.3390/pharmaceutics10040242`.

[171] H. Thomas, M. Zhou, and U. Schramm. “Issues of commercial optimization software development.” In: *Structural and Multidisciplinary Optimization* 23.2 (2002), pp. 97–110. DOI: `10.1007/s00158-002-0170-x`.

[172] M.K. Thompson et al. “Design for additive manufacturing: trends, opportunities, considerations, and constraints.” In: *CIRP Annals* 65.2 (2016), pp. 737–760. DOI: `10.1016/j.cirp.2016.05.004`.

[173] T.D. Tsai and C.C. Cheng. “Structural design for desired eigenfrequencies and mode shapes using topology optimization.” In: *Structural and Multidisciplinary Optimization* 47.5 (2013), pp. 673–686. DOI: `10.1007/s00158-012-0840-2`.

[174] M. Upadhyay, T. Sivarupan, and M. El Mansori. “3D printing for rapid sand casting - a review.” In: *Journal of Manufacturing Processes* 29 (2017), pp. 211–220. DOI: `10.1016/j.jmapro.2017.07.017`.

[175] M.W.D. Van der Burg, V. Shulmeister, E. Van der Giesen, and R. Marissen. “On the linear elastic properties of regular and random open-cell foam models.” In: *Journal of Cellular Plastics* 33.1 (1997), pp. 31–54. DOI: `10.1177/0021955X9703300103`.

[176] A. Van Veelen, N. Koebernick, C.S. Scotson, D. McKay-Fletcher, T. Huthwelker, C.N. Borca, J.F.W. Mosselmans, and T. Roose. “Root-induced soil deformation influences Fe, S and P: rhizosphere chemistry investigated using synchrotron XRF and XANES.” In: *New Phytologist* 225.4 (2020), pp. 1476–1490. DOI: `10.1111/nph.16242`.

[177] VDI 6224 Blatt 3. *Bionik - Bionische Strukturopimierung im Rahmen eines ganzheitlichen Produktentstehungsprozesses*. Berlin (Germany): Beuth-Verlag, 2017.

[178] W.M. Vicente, Z.H. Zuo, R. Pavanello, T.K.L. Calixto, R. Picelli, and Y.M. Xie. “Concurrent topology optimization for minimizing frequency responses of two-level hierarchical structures.” In: *Computer Methods in Applied Mechanics and Engineering* 301 (2016), pp. 116–136. DOI: `10.1016/j.cma.2015.12.012`.

[179] H.N.G. Wadley and D.T. Queheillalt. “Thermal applications of cellular lattice structures.” In: *Materials Science Forum*. Vol. 539. Trans Tech Publications Ltd. 2007, pp. 242–247. DOI: `10.4028/www.scientific.net/MSF.539-543.242`.

[180] J.C. Wallach and L.J. Gibson. "Mechanical behavior of a three-dimensional truss material." In: *International Journal of Solids and Structures* 38.40 (2001), pp. 7181–7196. DOI: `10.1016/S0020-7683(00)00400-5`.

[181] C. Wang and F. Liao. "Topography optimization and parametric analysis of bead layout for sheet metal bracket." In: *SAE Technical Paper* (2010). DOI: `10.4271/2010-01-0266`.

[182] D. Wang, M.I. Friswell, and Y. Lei. "Maximizing the natural frequency of a beam with an intermediate elastic support." In: *Journal of Sound and Vibration* 291.3-5 (2006), pp. 1229–1238. DOI: `10.1016/j.jsv.2005.06.028`.

[183] D. Wang, J.S. Jiang, and W.H. Zhang. "Optimization of support positions to maximize the fundamental frequency of structures." In: *International Journal for Numerical Methods in Engineering* 61.10 (2004), pp. 1584–1602. DOI: `10.1002/nme.1124`.

[184] J. Wang, S.R. Sama, and G. Manogharan. "Re-thinking design methodology for castings: 3D sand-printing and topology optimization." In: *International Journal of Metalcasting* 13.1 (2018), pp. 2–17. DOI: `10.1007/s40962-018-0229-0`.

[185] J.-T. Wang, F. Jin, and C.-H. Zhang. "Estimation error of the half-power bandwidth method in identifying damping for multi-DOF systems." In: *Soil Dynamics and Earthquake Engineering* 39 (2012), pp. 138–142. DOI: `10.1016/j.soildyn.2012.02.008`.

[186] X.L. Wang and W.J. Stronge. "Micro-polar theory for a periodic force on the edge of elastic honeycomb." In: *International Journal of Engineering Science* 39.7 (2001), pp. 821–850. DOI: `10.1016/S0020-7225(00)00065-3`.

[187] Y. Wang, S. Jia, M. Wei, L. Peng, Y. Wu, and X. Liu. "Research progress on solidification structure of alloys by synchrotron X-ray radiography: A review." In: *Journal of Magnesium and Alloys* 8.2 (2020), pp. 396–413. DOI: `10.1016/j.jma.2019.08.003`.

[188] R. Wanzenberg et al. "Design status of the ultra-low emittance synchrotron facility PETRA IV." In: *AIP Conference Proceedings*. Vol. 2054. 1. AIP Publishing LLC. 2019, p. 030002. DOI: `10.1063/1.5084565`.

[189] B.T. Warwick, C.K. Mechefske, and I.Y. Kim. "Effect of stiffener configuration on bulkhead modal parameters." In: *International Design Engineering Technical Conferences and Computers and Information in Engineering Conference*. Vol. 51852. American Society of Mechanical Engineers. 2018. DOI: `10.1115/DETC2018-85385`.

[190] B.T. Warwick, C.K. Mechefske, and I.Y. Kim. "Topology optimization of a pre-stiffened aircraft bulkhead." In: *Structural and Multidisciplinary Optimization* 60.4 (2019), pp. 1667–1685. DOI: `10.1007/s00158-019-02284-w`.

[191] P. Willmott. *An Introduction to Synchrotron Radiation. Techniques and Applications*. 2nd ed. Hoboken, New Jersey (USA): John Wiley & Sons, Inc., 2019. DOI: `10.1002/9781119970958`.

[192] T. Wortmann and G. Nannicini. "Introduction to architectural design optimization." In: *City Networks*. Springer, 2017, pp. 259–278. DOI: `10.1007/978-3-319-65338-9_14`.

[193] J. Wu, N. Aage, R. Westermann, and O. Sigmund. "Infill optimization for additive manufacturing—approaching bone-like porous structures." In: *IEEE transactions on visualization and computer graphics* 24.2 (2017), pp. 1127–1140. DOI: `10.1109/TVCG.2017.2655523`.

[194] S. Xiang, G.-W. Kang, M.-S. Yang, and Y. Zhao. "Natural frequencies of sandwich plate with functionally graded face and homogeneous core." In: *Composite Structures* 96 (2013), pp. 226–231. DOI: `10.1016/j.compstruct.2012.09.003`.

[195] Y.M. Xie and G.P. Steven. "A simple approach to structural frequency optimization." In: *Computers & Structures* 53.6 (1994), pp. 1487–1491. DOI: `10.1016/0045-7949(94)90414-6`.

[196] B. Xu, Y.S. Han, L. Zhao, and Y.M. Xie. "Topology optimization of continuum structures for natural frequencies considering casting constraints." In: *Engineering Optimization* 51.6 (2018), pp. 941–960. DOI: `10.1080/0305215X.2018.1506771`.

[197] M. Xu and Z. Qiu. "Free vibration analysis and optimization of composite lattice truss core sandwich beams with interval parameters." In: *Composite Structures* 106 (2013), pp. 85–95. DOI: `10.1016/j.compstruct.2013.05.048`.

[198] N. Yaghoobi and B. Hassani. "Topological optimization of vibrating continuum structures for optimal natural eigenfrequency." In: *International Journal of Optimization in Civil Engineering* 7.1 (2017), pp. 1–12. URL: `http://ijoce.iust.ac.ir/article-1-280-en.html`.

[199] C. Yan, L. Hao, A. Hussein, and D. Raymont. "Evaluations of cellular lattice structures manufactured using selective laser melting." In: *International Journal of Machine Tools and Manufacture* 62 (2012), pp. 32–38. DOI: `10.1016/j.ijmachtools.2012.06.002`.

[200] J. Yang, G.-S. Lin, C.-Y. Mou, and K.-L. Tung. "Diatom-mimicking ultrahigh-flux mesoporous silica thin membrane with straight-through channels for selective protein and nanoparticle separations." In: *Chemistry of Materials* 31.5 (2019), pp. 1745–1751. DOI: `10.1021/acs.chemmater.8b05295`.

[201] R.J. Yang, C.J. Chen, and C.H. Lee. "Bead pattern optimization." In: *Structural optimization* 12.4 (1996), pp. 217–221. DOI: `10.2514/6.1996-3988`.

[202] S. Ying, G. Xu, C. Li, and Z. Mao. "Point cluster analysis using a 3d voronoi diagram with applications in point cloud segmentation." In: *ISPRS International Journal of Geo-Information* 4.3 (2015), pp. 1480–1499. DOI: `10.3390/ijgi4031480`.

[203] A.M. Zenkour. "A comprehensive analysis of functionally graded sandwich plates: part 2—buckling and free vibration." In: *International Journal of Solids and Structures* 42.18-19 (2005), pp. 5243–5258. DOI: `10.1016/j.ijsolstr.2005.02.016`.

[204] L. Zhang. *Beam stability consideration for low emittance storage ring*. Presentation at the Workshop on Ambient Ground Motion and Vibration Suppression for Low Emittance Storage Rings (GM 2017), Beijing, China. 2017.

[205] L. Zhang, M. Lesourd, and T. Lewis. "Vibration damping systems for magnet girder assembly at the ESRF." In: *Proceedings of the 2001 Particle Accelerator Conference*. Vol. 2. IEEE. 2001, pp. 1465–1467. DOI: `10.1109/PAC.2001.986715`.

[206] W. Zhang, C. Wu, C. Zhang, and Z. Chen. "Microstructure and mechanical property of turtle shell." In: *Theoretical and Applied Mechanics Letters* 2.1 (2012), p. 014009. DOI: `10.1063/2.1201409`.

[207] C. Zhao, G.P. Steven, and Y.M. Xie. "Evolutionary natural frequency optimization of thin plate bending vibration problems." In: *Structural and Multidisciplinary Optimization* 11.3 (1996), pp. 244–251. DOI: `10.1007/bf01197040`.

[208] J. Zhao, M. Zhang, Y. Zhu, X. Li, L. Wang, and C. Hu. "Concurrent optimization of additive manufacturing fabricated lattice structures for natural frequencies." In: *International Journal of Mechanical Sciences* 163 (2019), p. 105153. DOI: `10.1016/j.ijmecsci.2019.105153`.

[209] Z. Zheng, J. Yu, and J. Li. "Dynamic crushing of 2D cellular structures: a finite element study." In: *International Journal of Impact Engineering* 32.1 (2005), pp. 650–664. DOI: `10.1016/j.ijimpeng.2005.05.007`.

[210] H.X. Zhu, J.R. Hobdell, and A.H. Windle. "Effects of cell irregularity on the elastic properties of open-cell foams." In: *Acta Materialia* 48.20 (2000), pp. 4893–4900. DOI: `10.1016/S1359-6454(00)00282-2`.

[211] H.X. Zhu, J.R. Hobdell, and A.H. Windle. "Effects of cell irregularity on the elastic properties of 2D Voronoi honeycombs." In: *Journal of the Mechanics and Physics of Solids* 49.4 (2001), pp. 857–870. DOI: `https://doi.org/10.1016/S0022-5096(00)00046-6`.

[212] J.H. Zhu, W.H. Zhang, and K.P. Qiu. "Bi-directional evolutionary topology optimization using element replaceable method." In: *Computational Mechanics* 40.1 (2007), pp. 97–109. DOI: `10.1007/s00466-006-0087-0`.

[213] Z.H. Zuo, X. Huang, J.H. Rong, and Y.M. Xie. "Multi-scale design of composite materials and structures for maximum natural frequencies." In: *Materials & Design* 51 (2013), pp. 1023–1034. DOI: `10.1016/j.matdes.2013.05.014`.

APPRECIATION OF STUDENT WORK

Declaration according to the *General information for doctoral examinations* of the Faculty of Production Engineering of the University of Bremen:

The thesis contains results that originated from the supervision of the following student works:

- Selina K. Linnemann, internship report: *Untersuchung der dynamischen Eigenschaften von bio-inspirierten Gitterstrukturen unter schwingender Beanspruchung*, degree program 'Material Design - Bionics and Photonics' (bachelor) of the University of Applied Sciences Hamm-Lippstadt (2018-2019)
- Laura M. Lottes, master thesis: *Shape optimization of Plates to Improve Vibration Characteristics*, degree program 'Production Engineering - General Mechanical Engineering' (master) of the University of Bremen (2019)
- Selina K. Linnemann, bachelor study project: *Geometrieoptimierung eines Balkens zur gezielten Beeinflussung bestimmter Eigenfrequenzen mit Hilfe der Finite-Elemente-Methode*, degree program 'Material Design - Bionics and Photonics' (bachelor) of the University of Applied Sciences Hamm-Lippstadt (2019-2020)
- Oleksandr Savysko, master thesis: *Geometrieanpassung in Form der Eigenmoden zur Erhöhung von Eigenfrequenzen bei 3D-Magnetträgerstrukturen*. degree program 'Mechanical Engineering' (master) of the Otto von Guericke University Magdeburg (2020)

EIDESSTATTLICHE VERSICHERUNG

Hiermit erkläre ich, Simone Andresen, dass die vorliegende Dissertation mit dem Titel „Impact of Structural Components on Natural Vibrations“ gemäß der Promotionsordnung (Dr.-Ing.) der Universität Bremen für den Fachbereich 4 (Produktionstechnik) vom 20.08.2020 von mir ohne unerlaubte fremde Hilfe angefertigt worden ist.
Ich bestätige, dass ich keine anderen als die von mir angegebenen Quellen und Hilfsmittel benutzt habe. Darüber hinaus versichere ich, dass ich die den benutzten Werken wörtlich oder inhaltlich entnommenen Stellen als solche kenntlich gemacht habe.
Ich bestätige, dass meine vorliegende Arbeit nach den geltenden Prinzipien der guten wissenschaftlichen Praxis der Universität Bremen und der Deutschen Forschungsgemeinschaft verfasst ist. Die zu Prüfungszwecken beigelegte elektronische Version der Dissertation ist identisch mit der abgegebenen gedruckten Version.

Bremen, 06 August 2021

M.Sc. Simone Andresen